Structural Studies of Mid-Z Lanthanide Elements at High Pressure

Rachel Jane Husband

Doctor of Philosophy
The University of Edinburgh
January 2015

Abstract

Europium (Eu) metal is divalent at ambient pressure due to its half-filled $4f$ electron shell, unlike the majority of the lanthanide elements which are trivalent. Consequently, Eu does not fit in with the general trend of structural phase transitions observed in the trivalent lanthanide elements, and instead its behaviour is much more complex. Although long thought to undergo a pressure-induced valence transition to a mixed-state form, there have been surprisingly few structural studies on Eu's high-pressure behaviour - until 2011 there had been no structural studies since the early 1990s.

This thesis presents the results of extensive high-resolution angle-dispersive powder x-ray diffraction experiments on Eu up to a pressure of ∼70 GPa. The previously-reported transition to Eu-III at ∼17 GPa is found to be due to pressure-induced changes in a contaminant phase that appears to have been present in almost all previous studies, and not due to changes in Eu itself.

When care is taken in the sample loading process, it is possible to obtain non-contaminated samples. This made it possible to identify a transition to a new phase, Eu-IV, at 31.5 GPa. The diffraction patterns from this phase are extremely complex. However, collecting high-resolution diffraction data on 'clean' samples made it possible to resolve a large number of closely-spaced reflections, and to identify the large number of weak reflections that appear at the transition. Eu-IV was determined to have an incommensurately-modulated crystal structure, the first of this type to be observed in a lanthanide element at high pressure.

On further compression above 38 GPa, Eu transforms to another new phase, Eu-V, which has also been determined to have an incommensurately-modulated crystal structure. Eu-V has the same superspace group as Eu-IV, but the modulation vector differs in direction and magnitude. The transition to Eu-V is accompanied by an increase in modulation amplitudes and the appearance of

higher-order satellite reflections, suggesting a complex modulation wave. This is the first incommensurate-incommensurate transition to be observed in the non-host-guest elements at high pressure.

Angle-dispersive powder x-ray powder diffraction experiments have also been performed on europium's trivalent neighbour, samarium (Sm), up to ∼50 GPa. The distorted-fcc phase has been confirmed to have the rhombohedral $hR24$ structure first observed in Pr. Evidence of a path-dependent transition to a new phase, Sm-VII, is observed on annealing followed by pressure decrease. A similar transition to another new phase, Sm-VII′, was observed on heating to 428 K at 25.5 GPa. The diffraction patterns from Sm-VII and Sm-VII′ are extremely similar, but subtle differences in their diffraction patterns suggest that they correspond to different structures.

Lay Summary

The majority of the metallic elements adopt simple, high-symmetry structures at ambient pressure. These consist of a highly-ordered arrangement of atoms, which can be described by a crystal lattice that is periodic in three dimensions. It may be expected that close-packed structures, such as face-centred cubic (fcc) and hexagonal close-packed (hcp), would be favoured at high pressures due to the increase in density. However, many of these elements transform to low-symmetry, complex structures on compression. In particular, a number have been observed to adopt incommensurately-modulated structures at high pressure. In these structures, atoms are displaced from their average positions by a modulation wave, the wavelength of which is an irrational multiple of the lattice periodicity.

Diamond-anvil cells (DACs) can be used to compress materials to over a million times atmospheric pressure. In these devices, a small sample is compressed between the tips of two diamond anvils. The atomic arrangement of materials at extreme pressures can then be probed using the intense x-ray beams provided by synchrotron sources.

In this work, the high-pressure crystal structures of the lanthanide elements europium (Eu) and samarium (Sm) have been investigated using angle-dispersive x-ray powder diffraction techniques. The high-pressure structural behaviour of Eu has been found to be remarkably different from that of the other lanthanide elements. Two new high-pressure phases of Eu are reported, both of which have an incommensurately-modulated crystal structure.

Declaration

I declare that this thesis was composed by myself, that the work contained herein is my own except where explicitly stated otherwise in the text, and that this work has not been submitted for any other degree or professional qualification except as specified.

Parts of this work have been published in [1] [2] [3] [4] [5].

(*Rachel Jane Husband, January 2015*)

Acknowledgements

Firstly, I would like to thank my supervisor Malcolm McMahon for providing guidance and support over the course of my Ph.D, and Ingo Loa for all of his helpful advice. I would like acknowledge Lars Lundegaard, Olga Degtyareva and Graham Stinton for collecting the preliminary data that contributed towards this work. I would like to thank the members of the McMahon group for help on the many beamtimes I have attended. In particular, Emma McBride, Graham Stinton, Keith Munro and Richard Briggs. I would also like to thank my office mates over the last four years for their continuous support. In particular, Julian Schmehr, William Whitley and Chris O'Neill.

I would also like to acknowledge the beamline staff at DLS, PETRA-III and the ESRF, and thank for all of their help in ensuring that these experiments were successful. In particular, Heribert Wilhelm, Annette Kleppe and Dominik Daisenberger at I15, Hanns-Peter Liermann and Zuzana Konôpková at P02.2, and Michael Hanfland at ID09a. I would also like to thank Simon Macleod of AWE for use of pressure cells and equipment. I'm also grateful to the mechanical workshop at Edinburgh for their engineering and technical support.

I would like thank the Scottish Doctoral Training Centre in Condensed Matter Physics for financial support, and for giving me the opportunity to travel to so many exciting places over the last four years.

Contents

List of Figures

List of Tables

Chapter 1

Introduction

1.1 Complex Structures in the Elements at High Pressure

At ambient pressure, the majority of the metallic elements adopt high-symmetry structures, such as the body-centred cubic (bcc), face-centred cubic (fcc) and hexagonal close-packed (hcp) structures. However, many of these elements transform to low-symmetry, complex structures on compression [21]. In particular, a number of the elements undergo pressure-induced structural transitions to incommensurately-modulated or incommensurate composite 'host-guest' crystal structures, both of which are examples of aperiodic crystals. Unlike periodic crystals, aperiodic crystals lack translational symmetry along one or more directions, but still exhibit long-range order. The periodic table in figure 1.1 highlights the elements which adopt incommensurate composite and incommensurately-modulated structures at high pressures. Incommensurate composite structures have been observed in group 1 [22–24], group 2 [25, 26] and group 15 elements [27, 28], as well as in the transition metal Sc [29]. Incommensurately-modulated structures have been observed in group 16 [30, 31] and group 17 [32, 33] elements, as well as the group 15 element P [34].

Experimentally, it is possible to compress samples to extreme pressures through the use of diamond-anvil cells (DACs). In these devices, pressure is generated by compressing a sample between the tips of two diamond anvils. Pressures of $\sim$400 GPa have been achieved using conventional DACs equipped with bevelled

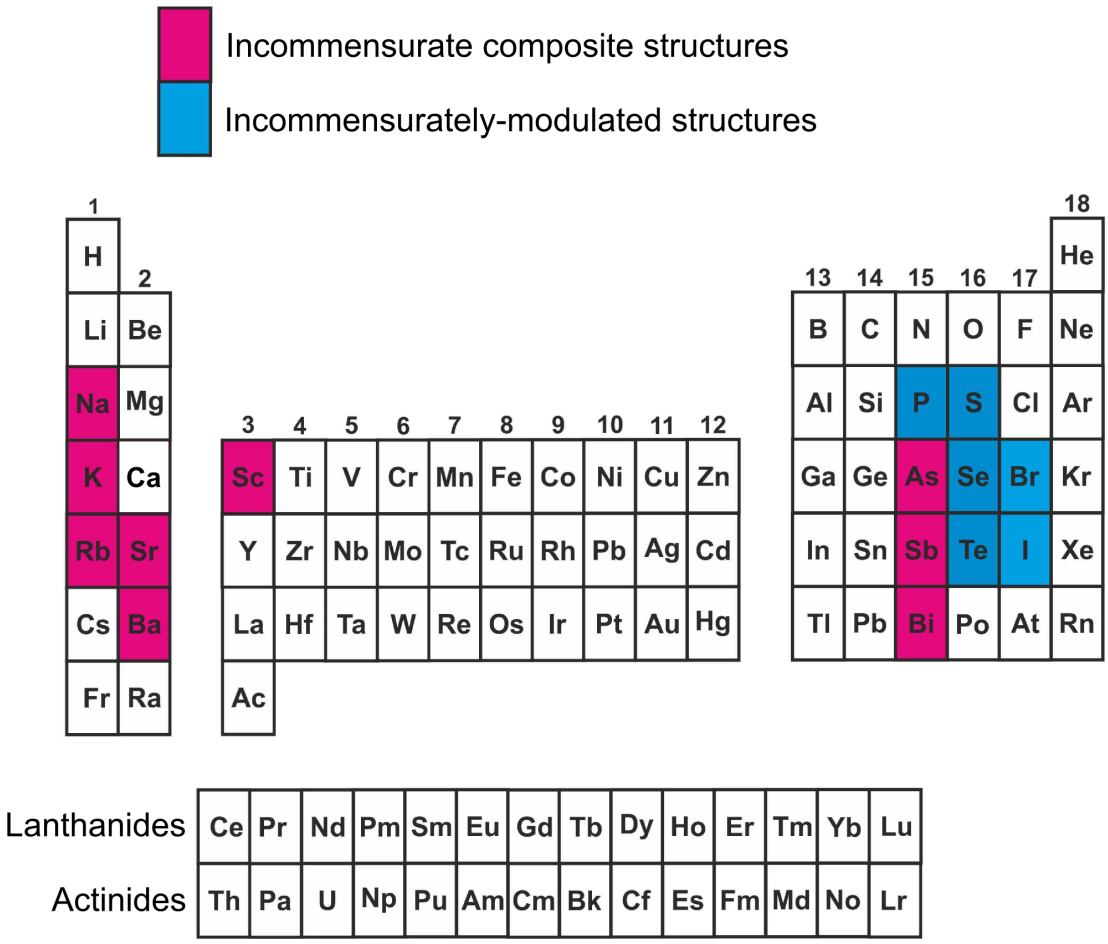

Figure 1.1: Periodic table highlighting the elements which were previously reported to adopt composite 'host-guest' structures (pink) and incommensurately-modulated structures (blue) at high pressures.

diamonds [35], and pressures exceeding 600 GPa have been achieved using micro-semi-balls made of nanodiamond as second-stage anvils within conventional diamond-anvil cells [36].

X-ray diffraction performed on samples contained with DACs can be used to determine the structure of materials at high pressures. However, structural determination of high-pressure phases is complicated by the fact that it often difficult to obtain single-crystals, making it necessary to rely on powder x-ray diffraction. In powder x-ray diffraction, the three-dimensional information available from single-crystal studies is collapsed onto one-dimension. This can often result in overlap of Bragg reflections with similar d-spacings, which is particularly problematic when dealing with diffraction patterns from complex structures.

Due to the small sample size required to reach high pressures in DACs, intense

sources of x-rays are required in order to obtain high-quality diffraction data. Initial x-ray diffraction studies therefore relied on energy-dispersive techniques, as this utilised the white beam available from synchrotron sources to maximise the x-ray flux. However, the resolution of energy-dispersive diffraction patterns is poor, and it is not possible to obtain accurate Bragg intensities, making it difficult to determine atomic positions within the unit cell [37]. The development of angle-dispersive x-ray diffraction techniques using area detectors and synchrotron radiation in the early 1990s [38, 39] offered significantly higher resolution and improved powder averaging in comparison with energy-dispersive techniques. Data collected using this new approach then made it possible to identify subtle features in the diffraction patterns that could not be identified using energy-dispersive techniques. The structures of many high-pressure phases were then revealed to be more complex than initially thought [21].

This thesis describes the results of angle-dispersive x-ray powder diffraction studies on europium (Eu) and samarium (Sm) metals at high pressure. Eu is an unusual member of the lanthanide series, which does not exhibit the common series of structural phase transitions observed in the majority of the lanthanide elements under pressure, and instead its behaviour is remarkably different. Initial x-ray diffraction studies reported the appearance of additional reflections in the diffraction patterns collected above ∼17 GPa [13,14], which was taken as evidence of a pressure-induced transition to a new phase, Eu-III. However, despite the fact that this transition was initially reported in 1985 [13], a structural solution for Eu-III was not proposed until 2012, when Bi *et al.* reported a series of phase transitions up to 92 GPa [15]. Their interpretation of the structural behaviour of Eu above 18 GPa has been found to be inconsistent with the work described in this thesis. Instead, Eu has been found to transform to a new phase, Eu-IV, which has an incommensurately-modulated crystal structure. On further compression, Eu has been found to transform to another new phase, Eu-V, which also has an incommensurately-modulated crystal structure. This is the first observation of an incommensurately-modulated to incommensurately-modulated transition to be observed in the elements at high pressure, and the first observation of an incommensurate structure in the lanthanide elements.

The high-pressure behaviour of Eu is often compared with that of its trivalent neighbours, Sm and gadolinium (Gd), with the aim of producing a unified phase diagram of all the lanthanide elements [40]. Although the high-pressure structural behaviour of Sm is consistent with the general trend observed in the 'regular'

members of the lanthanide series, previous x-ray diffraction studies do not provide a complete description of its structural behaviour under pressure. The work presented in this thesis provides definitive structural assignments for the high-pressure phases of Sm. Additionally, a path-dependent structural transition to a new phase, Sm-VII, is observed on annealing followed by pressure decrease. A similar transition to another new phase, Sm-VII′, is observed on heating. This suggests that, despite the fact that the high-pressure structural behaviour of the 'regular' lanthanide elements is often thought to be well known, surprises still remain.

Chapter 2

Experimental Techniques

2.1 Introduction

This thesis describes the results of angle-dispersive x-ray powder diffraction experiments performed at high pressure. In this chapter, an introduction to this experimental technique is given. The chapter is split into five main sections. Firstly, a brief description of the device used to obtain high pressures, the diamond-anvil cell (DAC), is given in section 2.2. Secondly, an introduction to crystals is given in section 2.3, leading up to the description of incommensurately-modulated crystal structures according to the superspace formalism. Thirdly, an introduction to the theory of x-ray diffraction is given in 2.4. The data analysis methods are then outlined in section 2.5. Finally, an overview of the incommensurately-modulated crystal structures that have been observed in the elements at high pressures is given in section 2.6. This chapter is predominantly to serve as an overview of the techniques utilised in this thesis, while the precise experimental details of individual experiments will be given at the beginning of the appropriate chapter.

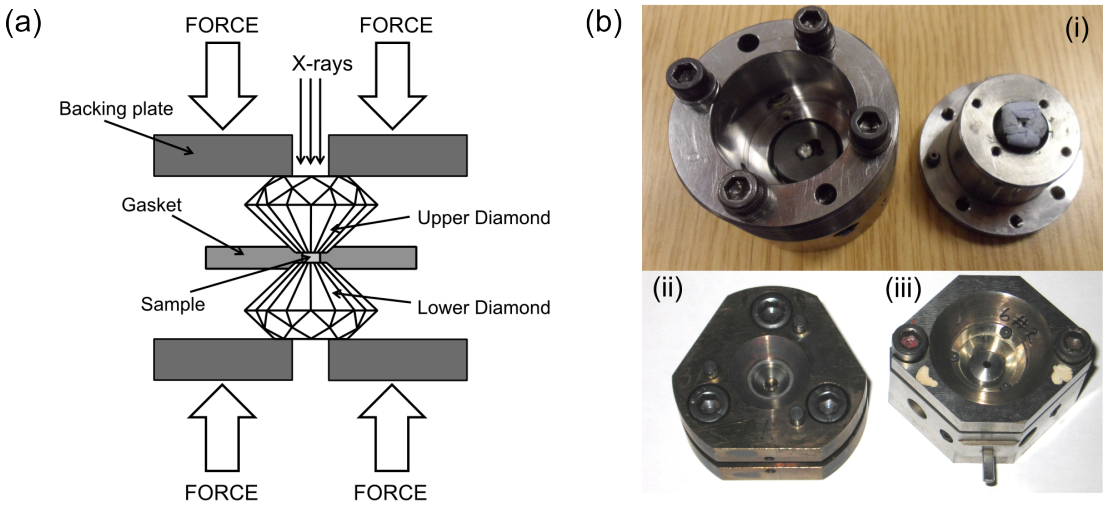

Figure 2.1: (a) A schematic of a diamond-anvil pressure cell (DAC).
(b) Pictures of (i) an open Livermore pressure cell, (ii) a closed MB pressure cell and (iii) a closed DXR pressure cell.
.

2.2 High-Pressure Techniques

2.2.1 Diamond-Anvil Cells

The device used to reach high pressures is the diamond-anvil pressure cell (DAC). This consists of two opposing diamond anvils, each of which is attached to a backing seat. The sample is contained between the two diamond tips by the use of a metallic gasket material. A force is then applied to drive the diamonds together in order to increase the pressure of the sample according to pressure = force/area. By making the diamond culets very small, it is possible to reach very high pressures. A schematic illustrating the basic principle of a DAC is shown in figure 2.1(a).

In the cell preparation process, the gasket is first indented to the required thickness. This is typically 15–30 μm, depending on the culet size, sample material and required pressure. A hole is drilled in the centre of the indent to act as the sample chamber. The sample, as well as a pressure calibrant and pressure-transmitting medium (if required), are loaded into the sample chamber and the cell is closed. A description of the pressure calibrants and pressure-transmitting media used in this thesis are described in sections 2.2.2 and 2.2.3, respectively. The lanthanide metals, in particular europium, oxidise easily. For this reason, all samples were loaded in a glovebox in a dry argon atmosphere.

A number of different types of diamond-anvil pressure cells were used in the work described in this thesis: Merrill-Bassett (MB) [41] cells equipped with tungsten carbide Boehler-Almax (BA) seats, Diacell x-ray (DXR) cells equipped with conventionally-cut beryllium (Be) seats, and Livermore type cells [42] equipped with conventionally-cut tungsten carbide seats. Pictures of each of these cells are shown in figure 2.1(b) for comparison.

In conventionally-cut diamond anvil and seats, the lower part of the anvil sits on a flat seat above a conical aperture. The seats are typically made of Be due to its high x-ray transmission. However, in the Boehler-Almax (BA) design, the lower part of the anvil is cut in a conical shape, which then sits in an indent which is cut into the seat, as described in reference [6]. This is illustrated in figures 2.2(a) and (b), which show schematics of a conventionally-cut diamond anvil and seat, and a BA design diamond anvil and seat, respectively. The BA design offer a number of advantages over the conventional design. In particular, it allows for a larger opening aperture ($\pm 37°$), which is a significant advantage in single crystal studies as it allows access to a much larger volume of reciprocal space. Additionally, the conical design provides additional support to the diamond, resulting in increased stability. The anvils which are used are also much smaller, and consequently cheaper, than conventional anvils, and absorption due to the anvils is consequently reduced.

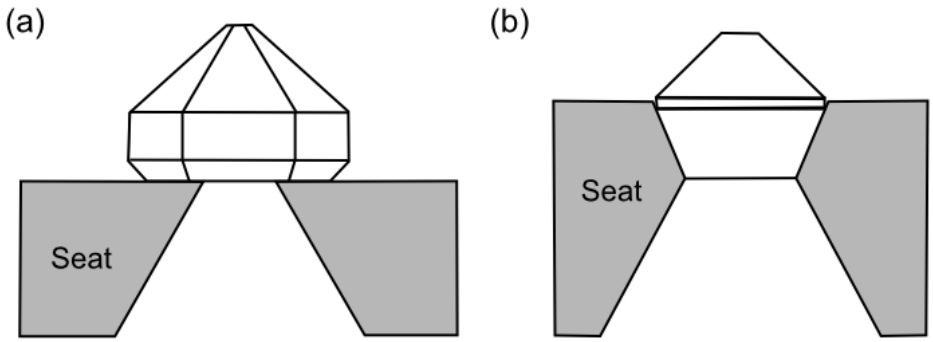

Figure 2.2: Schematic of (a) a conventionally-cut diamond-anvil and seat and (b) a conical-cut, BA design diamond-anvil and seat. Figures are modified from reference [6].

The MB cells can routinely reach pressures of $\sim$35 GPa when equipped with diamonds with 300 μm culets, with no resulting damage to the diamonds. The DXR cells can routinely reach pressures of $\sim$50 GPa when equipped with diamonds with 300 μm culets, and $\sim$70 GPa when equipped with diamonds with 200 μm culets, with no resulting damage to the diamonds.

The Livermore type cells [42] are gas membrane driven piston-cylinder cells. In this design, the diamond is mounted on a slot that is cut into the seat. The use of a slot aperture is a disadvantage for single crystal studies, as it limits the access to reciprocal space. It can also be disadvantageous in powder diffraction studies, as only a fraction of the Debye-Scherrer rings can be detected. This is a particular issue when dealing with samples with pronounced preferred orientation. The use of a gas membrane is also essential for high-temperature experiments, as it allows the pressure to be changed remotely, while also enabling the application of uniform pressure. These cells can routinely reach pressures of ∼70 GPa when equipped with diamonds with 200 μm culets, with no resulting damage to the diamonds.

The majority of the advantages of the different cell types, in particular the choice of seats, is only a factor for single crystal diffraction studies, and not so important in powder diffraction experiments. In particular, the size of the opening angle is not as important in powder diffraction experiments, where the cell is typically not oscillated more than ±5°. For this reason, in the experiments performed in this thesis, the choice of cell type used was predominantly determined by the maximum pressure of interest.

2.2.2 Pressure Calibration

Two standard methods of pressure-calibration have been used in this work: the ruby fluorescence method, and the use of an internal pressure standard. A brief description of each of these methods is given in this section.

The Ruby Fluorescence Technique

One of the most commonly used methods of pressure determination is the ruby fluorescence technique, which was first described by Forman *et al.* in 1972 [43]. Ruby (Cr^{3+}-doped Al_2O_3) has a set of two fluorescent emission lines, R_1 and R_2, which are due to electronic transitions in the Cr^{3+} ions. These occur at 692.86 and 694.25 nm, respectively, at ambient pressure. The wavelengths of these electronic transitions depend on the environment of the Cr^{3+} ions, and therefore exhibit a pressure-induced wavelength shift. It is therefore possible to determine the pressure of the sample from the shift of the emissions lines. Although it is possible to determine the pressure from the wavelength shift of

either R_1 or R_2, the R_1 line is used most frequently.

A small ruby sphere, of about 5–10 μm in size, is placed in the sample chamber. The ruby must be small enough that it will not become trapped between the two diamond anvils as the gasket becomes thinner at higher pressure, as this will result in an anomalously large pressure reading. The fluorescence is then excited by a laser, and the emission spectrum is recorded. The pressure is then determined from the position of the R_1 emission line. The calibration used throughout this thesis is that by Mao *et al.* [44], which is given in equation 2.1, where P is the pressure in megabars, $A = 19.04$ Mbar, $B = 7.665$, $\Delta\lambda$ is the wavelength shift and λ_0 is the wavelength of R_1 at ambient pressure. This calibration is valid up to 80 GPa, although subsequent studies have extended the calibration to higher pressures [45, 46].

$$P = \frac{A}{B}\left\{\left[1 + \left(\frac{\Delta\lambda}{\lambda_0}\right)\right]^B - 1\right\} \tag{2.1}$$

A significant advantage of using a fluorescent material as a pressure calibrant is that it is possible to determine the pressure without the need to collect x-ray diffraction data, which is not possible with an internal pressure standard. One of the main advantages of the use of ruby as the fluorescent material is that it has an intense fluorescence signal, and the pressure-induced wavelength shift of the R_1 line is relatively large. However, the R_1 and R_2 emission lines are affected by the presence of non-hydrostatic stress, which can result in peak broadening due to the presence of a pressure gradient, as well as a change in the splitting of the R_1 and R_2 emission lines [47]. Ruby also has a number of disadvantages for use at high temperatures. The R_1 emission line exhibits a relatively large temperature-dependent wavelength shift, and so a large uncertaintly in the temperature reading can result in a large uncertainty in the pressure [48]. Additionally, significant line broadening is observed with temperature, until the R_1 and R_2 lines can no longer be resolved above $\sim$550 K [48]. For this reason, the pressure in all of the high temperature experiments described in this thesis was determined using an internal pressure standard.

Internal Pressure Standard

The second method of pressure determination is the use of an internal pressure standard, in which the equation of state (EOS) is already well known. The volume of the standard is determined using x-ray diffraction, and the pressure is determined from the known EOS. Typically transition metals, which do not undergo any pressure-induced structural transitions, are used. It is also important to ensure that the standard does not react with the sample material. One of the main disadvantages of this method is the presence of diffraction peaks from the standard. Although these can be avoided using a small x-ray beam, this becomes increasingly more difficult at high pressures. This is a particular disadvantage when indexing complex diffraction patterns, due to the possibility of overlap of peaks from the pressure marker with those from the sample.

In some of the work described in this thesis, Ta was used as a pressure-marker. One advantage of using Ta is that, although it is a relatively strong x-ray scatterer, it adopts the body-centred cubic structure, and so has a relatively small number of diffraction lines. In some samples, a small grain of Ta, of about 10–20 μm in size, was included in the sample chamber. In other samples, a piece of 1 μm thick Ta foil was placed between the diamond and the gasket material. The pressures of both samples were determined using the ambient-temperature pressure-volume relation of Ta measured by Hanfland *et al.* [49], and a thermal correction based on the results of Dorogokupets and Oganov [50] was applied for the high-temperature experiments. In all cases, the volume of Ta was determined using the maximum number of Ta Bragg reflections that could be identified in the diffraction pattern.

The ambient pressure lattice parameter of Ta depends on the amount of hydrogen absorbed in the production process, with the lattice parameters exhibiting a linear dependence on the amount of hydrogen present [51]. A small difference in the ambient-pressure atomic volume can result in a significant change in the calculated pressure from the EOS. For example, the lattice parameters determined for the Ta powder and the Ta foil used in different samples differed by $\sim$0.002 Å, which results in a pressure difference of almost 1 GPa at 50 GPa for the same unit cell volume of Ta. The ambient-pressure atomic volume of Ta was therefore determined at the beginning of each experiment for the Ta calibrant used.

2.2.3 Pressure-Transmitting Media

In a diamond-anvil cell, pressure is generated by the application of a uniaxial force on the two diamond anvils, and the sample is contained radially by the gasket material. As a result, the uniaxial stress can be larger than the radial stress, resulting in non-hydrostatic conditions. The presence of non-hydrostatic stress can result in peak broadening of diffraction peaks, as well as systematic *hkl*-dependent peak shifts. It can thus also contribute to uncertainties in the pressure reading. When ruby is used as a pressure marker, non-hydrostatic conditions can result in peak broadening of the fluorescence lines, and a change in the splitting of the R_1 and R_2 emission lines. When an internal pressure calibrant is used, the presence of uniaxial stress will mean that the crystal planes in the sample that are parallel to the diamond culets will have a smaller spacing than those that are perpendicular. However, diffraction from these planes is not possible using transmission geometry in a DAC, and so the presence of non-hydrostatic stress therefore results in the pressure being underestimated.

In order to minimise non-hydrostatic stress, samples can be loaded surrounded by an inert material, called the pressure-transmitting medium (PTM), which ideally supports no shear. However, all materials will inevitably become non-hydrostatic above a certain pressure, and so have a hydrostatic limit. However, the work presented in this thesis deals with samples that are extremely reactive, and in order to minimise any possible sources of contaminanation, the majority of samples were loaded without a PTM. A number of samples were loaded in He or in mineral oil, which have been reported to be hydrostatic up to 30 GPa [52] and 0.9 GPa [53], respectively.

2.2.4 Resistive Heating

High-pressure high-temperature experiments were carried out using resistively-heated membrane-driven diamond anvil cells. In this set-up, external resistive heaters are used to heat the cell body, and heat is transferred to the sample by the thermal conductivity of the cell body, the diamond anvils and the gasket. The use of membrane-driven cells enables the pressure to be controlled *in situ*. MB cells were heated using an external ring heater (Watlow Ltd.), and Livermore-type cells were heated using a purpose-built Cu heating block. A picture of the Cu heating block mounted on beamline I15 at Diamond Light source is shown

in figure 2.3. In both cases, the temperature was determined using a K-type thermocouple placed on the back of one of the diamond anvils. The uncertainty in temperature was estimated to be no more than 10 K.

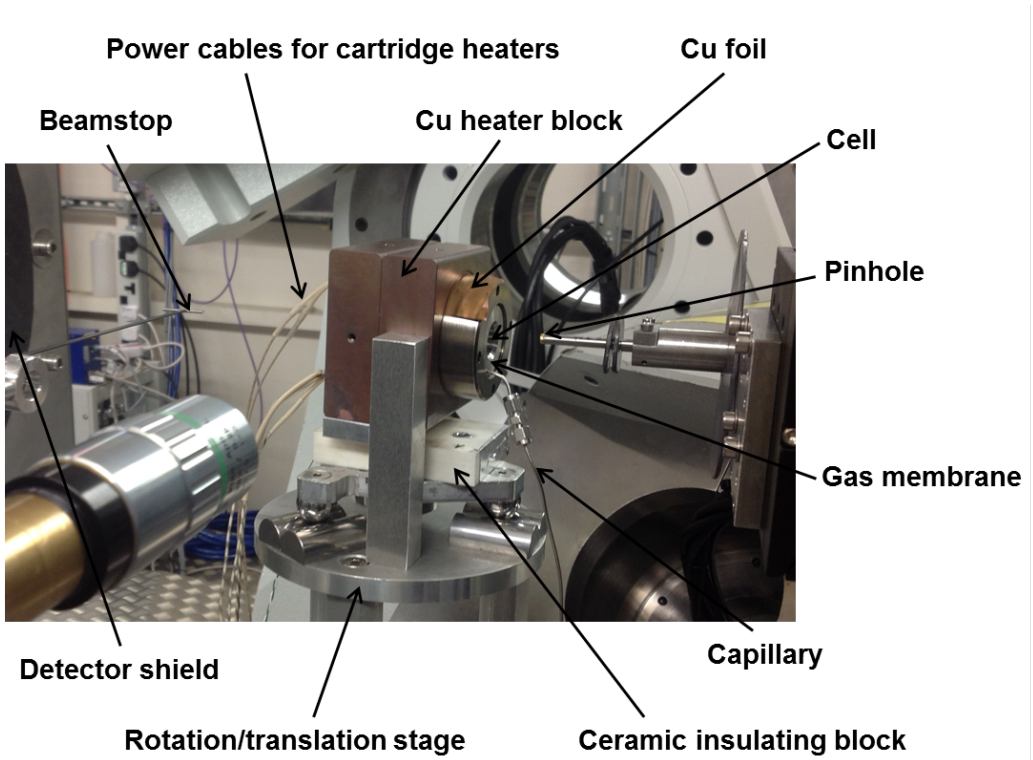

Figure 2.3: The Cu heater block mounted on beamline I15 at Diamond Light Source. Four cartridge heaters are inserted into holes drilled into the face of the Cu block that faces the detector. Several sheets of Cu foil are inserted between the cell and the Cu block to maximise thermal contact, and the block is mounted on a ceramic block to prevent heating of the rotation/translation stage. The gas membrane, which is used to increase the pressure in situ, is connected to the gas regulator via a capillary

.

The maximum temperature reached in the studies described in this thesis was limited to 449°C, in order to prevent damage to the cell body and the diamond anvils due to oxidation. Alternative methods have been developed to reach higher temperatures using resistive heating, such as the method described in reference [42]. In this case, the sample is heated using miniature heaters round the diamond anvils and the cell is kept in vacuum to prevent oxidation of the diamonds.

2.3 Crystals

In this section, an brief description of periodic crystals is first given in section 2.3.1, followed by a description of symmetry and space groups in section 2.3.2. An introduction to incommensurately-modulated crystals, followed by their description according to the superspace formalism in section 2.3.3. Finally, a description of the symmetry of incommensurately-modulated crystal structures and an introduction to superspace groups is given in section 2.3.4.

2.3.1 Periodic Crystals

A crystal is a solid in which the atoms are arranged in a way which exhibits long-ranged periodic order in one or more dimensions. Periodic crystals possess translational symmetry and, consequently, they also possess long-range order. It is therefore possible to identify a set of identical points in the crystal that are indistinguishable from each other due to symmetry. These form an infinite array of discrete points which define the Bravais lattice, which is also referred to as the crystal, or direct lattice. This is described mathematically by equation 2.2, where R is a lattice vector, $\vec{a}$, $\vec{b}$ and $\vec{c}$ are the primitive lattice vectors and u, v and w are integers which run from 0 to ∞.

$$\vec{R} = u\vec{a}_1 + v\vec{a}_2 + w\vec{a}_3 \tag{2.2}$$

The lattice vectors $\vec{a}_1$, $\vec{a}_2$ and $\vec{a}_3$ form a parallelogram which defines a volume called the unit cell. The unit cell can then be translated through all points in the crystal lattice to fill all space. The position of an atom within the unit cell is given by equation 2.3, where x_1, x_2 and x_3 are fractional coordinates with respect to the basis vectors $\vec{a}_1$, $\vec{a}_2$ and $\vec{a}_3$.

$$\vec{x} = x_1\vec{a}_1 + x_2\vec{a}_2 + x_3\vec{a}_3 \tag{2.3}$$

The Fourier transform of the direct lattice is the Reciprocal lattice, as defined by equation 2.4, where h, k and l are integers. The reciprocal lattice vectors, $\vec{G}_{hkl}$, are defined in terms of three basis vectors $\vec{a}_1^*$, $\vec{a}_2^*$ and $\vec{a}_3^*$, which are derived from the direct lattice vectors according to equations 2.5.

$$\vec{G}_{hkl} = h\vec{a}_1^* + k\vec{a}_2^* + l\vec{a}_3^* \tag{2.4}$$

$$\begin{aligned} \vec{a}_1^* &= 2\pi \frac{\vec{a}_2 \times \vec{a}_3}{\vec{a}_1 \cdot (\vec{a}_2 \times \vec{a}_3)} \\ \vec{a}_2^* &= 2\pi \frac{\vec{a}_3 \times \vec{a}_1}{\vec{a}_1 \cdot (\vec{a}_2 \times \vec{a}_3)} \\ \vec{a}_3^* &= 2\pi \frac{\vec{a}_1 \times \vec{a}_2}{\vec{a}_1 \cdot (\vec{a}_2 \times \vec{a}_3)} \end{aligned} \tag{2.5}$$

2.3.2 Symmetry of Periodic Crystals

The following section gives an introduction to the symmetry of periodic crystals, following the descriptions given in chapter 1 of reference [54] and section 2.1 of reference [19].

Periodic crystals are typically classified according to the number and type of symmetry elements that are present. A symmetry operation is an operation that transforms the object to a state that is indistinguishable from the initial state. This can be an inversion through a point, a rotation around an axis, or a reflection in a plane. The reference point about which these transformations take place (point, axis or plane) is called the symmetry element. All objects also have the identity operator, which leaves the object unchanged, and so at least one symmetry element is always present. The set of symmetry elements that are present in an object defines the point group.

For a finite-sized object, there are an infinite possible number of point groups. However, the periodicity of a crystal results in a limited number of allowed symmetry elements. For example, periodic crystals may only have 1-, 2-, 3-, 4- and 6-fold rotational axes. This results in a total of 32 unique combinations of symmetry operations that can be present in a three-dimensional periodic crystal, which form the set of 32 possible three dimensional crystallographic point groups. These can be classed into 7 crystal systems: triclinic, monoclinic, orthorhombic, tetragonal, trigonal, hexagonal, and cubic, according to their point groups.

The unit cell is usually chosen to reflect the symmetry of the lattice. A crystal can then be described in one of 7 lattice systems (triclinic, monoclinic,

orthorhombic, tetragonal, rhombohedral, hexagonal, and cubic), each of which imposes constraints on the unit cell. The exception to this is the triclinic lattice, where no restrictions are placed on the lattice vectors. Note that the trigonal crystal system can be described in both the rhombohedral and hexagonal lattice systems.

The 7 lattice systems can be combined with centring operations (body, face, base and rhombohedral centring) to produce the 14 Bravais lattices. When combined with the 32 crystallographic point groups, this describes 73 symmorphic space groups. The translational symmetry present in crystals also introduces a further set of symmetry elements, which involve either a rotation or reflection followed by a translation, and the set of 11 enantiometic pairs must also be included. This defines a total of 230 space groups, which describe the unique set of symmetry operations that can be present within a crystal.

Space groups are identified either by their unique number, or by their associated Hermann-Mauguin symbol. The first character of the Hermann-Mauguin symbol is a letter that defines the centring (P = primitive, I = body, F = face, C = base, R = rhombohedral). The remaining symbols define the symmetry elements that are present along one, two or three symmetry directions, depending on the lattice type. For example, only one symmetry direction is present in a monoclinic lattice, whereas orthorhombic, tetragonal, hexagonal and cubic each contain three.

The symmetry elements present within a crystal define a set of symmetry-equivalent atomic positions, called Wyckoff positions. There are two types of Wyckoff positions: general positions, which are points that are left invariant only by the identity operator, and special positions, which are left invariant by at least two symmetry operations (one of which is the identity operator). Special positions therefore lie on one of the symmetry elements. The number of atoms generated by a single atom placed at a given Wyckoff position is called the site multiplicity, where it is clear that a general position will have a higher multiplicity than any special position. Each space group has an associated set of Wyckoff positions, which are identified by their Wyckoff symbol. This consists of the site multiplicity followed by a letter than identifies it from other positions within the same space group.

The transformation of atoms within a crystal can be described mathematically by equation 2.6, where R is a 3×3 rotation matrix and $\vec{v}$ describes a translation.

$$\begin{pmatrix} x_1' \\ x_2' \\ x_3' \end{pmatrix} = R \begin{pmatrix} x_1 \\ x_2 \\ x_3 \end{pmatrix} + \begin{pmatrix} v_1 \\ v_2 \\ v_3 \end{pmatrix} \tag{2.6}$$

2.3.3 Aperiodic Crystals

There exists a class of crystals that do not possess transitional symmetry, but still exhibit long-range order. These called aperiodic crystals. There are three known classes of aperiodic crystals: incommensurately-modulated crystals, composite crystals, and quasicrystals. This thesis deals entirely with incommensurately-modulated crystals structures, and so the remainder of this section will focus this type of structure. Following the description of incommensurately-modulated structures given in the textbook by S. van Smaalen [55], this section first gives an introduction to modulated structures, followed by an overview of the description of incommensurately-modulated structures within the superspace formalism.

Modulated Crystals

Modulated structures consist of an average structure, where the atoms in the structure are displaced away from their average position in a way that can be described by a periodic modulation function. The average structure is defined in the same way as a conventional three-dimensional crystal, with a lattice defined by equation 2.2 and atomic positions defined by equation 2.3. However, in order to distinguish them from those in the modulated structure, the fractional coordinates in the average structure will be labelled as $\vec{\overline{x}}$.

The displacement of an atom from its average position, $\vec{\overline{x}}$, is described by a modulation function, $\vec{u}$. This function is periodic in $\overline{x}_4 = \vec{q} \cdot \vec{\overline{x}} + t$, where $\overline{x}_4$ is the 4^{th} superspace component and t is the initial phase of the wave. The position of this atom in the modulated structure is then given by $\vec{\overline{x}} + \vec{u}$. The modulation vector is a wave function, with a characteristic wavevector $\vec{q} = q_1\vec{a}_1^* + q_2\vec{a}_2^* + q_3\vec{a}_3^*$, or (q_1, q_2, q_3) in the basis of $\vec{a}_1^*$, $\vec{a}_2^*$ and $\vec{a}_3^*$. When any of components of $\vec{q}$ are irrational, the structure is incommensurate.

Atoms can be displaced along any direction, and so the modulation function is a three-dimensional vector $\vec{u} = (u_1, u_2, u_3)$ in the basis of $\vec{a}_1$, $\vec{a}_2$ and $\vec{a}_3$, where

each component is periodic in $\overline{x}_4$. As with all periodic functions, it is possible to expand each component as a Fourier series according to equation 2.7, where $i = 1, 2, 3$ labels the vector components. In general, only a small number of the Fourier components will be non-zero due to symmetry constraints.

$$u_i = \sum_{n=1} A_i^n \cos 2\pi n\overline{x}_4 + B_i^n \sin 2\pi n\overline{x}_4 \tag{2.7}$$

Diffraction from aperiodic crystal structures generates sharp Bragg spots in a similar way to periodic crystals. In modulated crystal structures, the Bragg peaks can be indexed according to 4 integers (h, k, l, m) according to equation 2.8. Reflections with $m = 0$ are referred to as main reflections, and are the same as those that would be observed from the average structure. Reflections with $m \neq 0$ are referred to as mth-order satellite reflections, which sit at $\pm m\vec{q}$ from the main Bragg reflections. These are usually less intense than the main Bragg reflections, and generally only low order satellites are observed.

$$\vec{H} = h\vec{a}_1^* + k\vec{a}_2^* + l\vec{a}_3^* + m\vec{q}^* \tag{2.8}$$

An incommensurately-modulated crystal structure with a modulation vector $\vec{q} = (q_1, 0, 0)$ is illustrated in figure 2.4(a). In this example, the atoms are displaced away from their average position in the $\vec{a}_1$ direction, with the modulation function $u_1 = A_1 \sin 2\pi q_1 x_1$. The $(hk0)$ plane of the corresponding reciprocal lattice is illustrated in figure 2.4(b), where only first-order ($|m| = 1$) satellite reflections are shown.

The Superspace Formalism

It is possible to describe modulated structures by defining the average structure and modulation function, as described in the previous section. However, a significant problem with this approach is that it is not easy to deal with symmetry. The concept of symmetry is important when refining crystal structures as it identifies relationships between refineable parameters, such as the Fourier amplitudes in the modulation function. Consequently, the concept of superspace was developed by de Wolff *et al.* [56] as a solution to this problem.

The reciprocal lattice in three-dimensional space, as defined by equation 2.8,

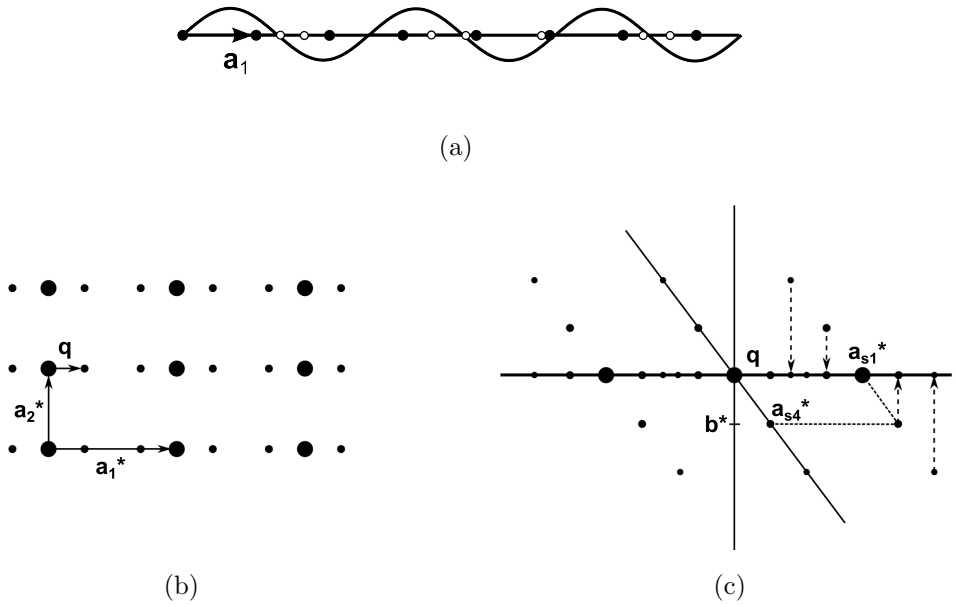

Figure 2.4: (a) An incommensurately-modulated structure with a modulation vector $\vec{q} = (q_1, 0, 0)$ and a modulation function $u_1 = A_1 \sin 2\pi q_1 x_1$. The position of the atoms in the average structure are shown by the solid symbols. The position of the atoms in the modulated structure are shown by the open circles, and the modulation function is shown to scale.
(b) The $(hk0)$ plane in reciprocal space showing the reciprocal lattice of the modulated structure described in (a). The reciprocal lattice is defined by equation 2.8, where only first-order ($|m| = 1$) satellite reflections are shown.
(c) The $(h00m)$ plane in reciprocal superspace showing the superspace reciprocal lattice of the modulated structure described in (a). The observed reciprocal lattice, as described in (b), is a projection of the superspace reciprocal lattice onto physical space, which is shown by the thick horizontal line. The superspace reciprocal lattice is defined by equations 2.9 and 2.10, where up to second order ($|m| = 2$) satellite reflections are shown.
Figures are modified from chapter 2 of reference [7].

can be thought of as a projection of the superspace reciprocal lattice $\vec{H}_s$, which exists in four-dimensional space, onto real space. In order to describe this mathematically, it is necessary to construct a dimensionless basis vector, $\vec{b}$, which is perpendicular to physical space, with a corresponding reciprocal vector $\vec{b}^*$. A set of 4 superspace reciprocal lattice vectors, $\vec{a}^*_{s1}$, $\vec{a}^*_{s2}$, $\vec{a}^*_{s3}$ and $\vec{a}^*_{s4}$, can then be constructed according to equations 2.9 and 2.10. The first 3 superspace reciprocal lattice vectors are the same as the reciprocal lattice vectors $\vec{a}^*_1$, $\vec{a}^*_2$ and $\vec{a}^*_3$ described in the precious section. However, in the superspace formalism the 4th superspace reciprocal lattice vector also contains a component along $\vec{b}^*$. The projection of superspace reciprocal lattice points with $m \neq 0$ onto physical space then define

the satellite reflections. The superspace reciprocal lattice is then constructed according to equation 2.11.

$$\vec{a}^*_{si} = \vec{a}^*_i \qquad i = 1, 2, 3 \tag{2.9}$$

$$\vec{a}^*_{s4} = \vec{a}^*_4 + \vec{b}^* \tag{2.10}$$

$$\vec{H}_s = h\vec{a}^*_{s1} + k\vec{a}^*_{s2} + l\vec{a}^*_{s3} + m\vec{a}^*_{s4} \tag{2.11}$$

The superspace reciprocal lattice for an incommensurately-modulated structure with a modulation vector $\vec{q} = (q_1, 0, 0)$ is shown in figure 2.4(c), where both first and second order satellite reflections are included. Dotted lines indicate the projection of the $m \neq 0$ reflections onto physical space to generate satellite reflections. The observed reciprocal lattice is then consistent with that shown in figure 2.4(b).

Using the fact that the direct and reciprocal lattice superspace vectors are related by $\vec{a}^*_{si} \cdot \vec{a}_{si'} = \delta_{ii'}$, it is then possible to construct the set of direct superspace lattice vectors, as defined by equations 2.12 and 2.13. These define the unit cell in superspace. The position of a point within the unit cell is defined by (x_{s1}, x_{s2}, x_{s3}, x_{s4}), which are fractional coordinates in the basis of $\vec{a}_{s1}$, $\vec{a}_{s2}$, $\vec{a}_{s3}$ and $\vec{a}_{s4}$.

$$\vec{a}_{si} = \vec{a}_i - q_i\vec{b} \qquad i = 1, 2, 3 \tag{2.12}$$

$$\vec{a}_{s4} = \vec{b} \tag{2.13}$$

The superspace unit cell of the incommensurately-modulated structure illustrated in figure 2.4(a) is shown in figure 2.5(a). The fractional superspace coordinates for the average structure, $\vec{\overline{x}}$, and for the modulated-structure, $\vec{x}$, are indicated. It can be seen from the diagram that $x_{si} = x_i$ for $i = 1, 2, 3$ for all points in superspace. From geometry, it can be seen that for a point in physical space, $x_{s4} = \vec{x} \cdot \vec{q}$. In this case the modulation vector only has one non-zero component, q_1, and so $x_{s4} = q_1 x_2$. For points at a distance t from physical space, $x_{s4} = \vec{x} \cdot \vec{q} + t$. The 4^{th} superspace coordinate of the average structure, $\overline{x}_4$, can then be idenfied with the argument of the modulation function, $\vec{u}(\overline{x}_4)$, that was introduced in

section 2.3.3.

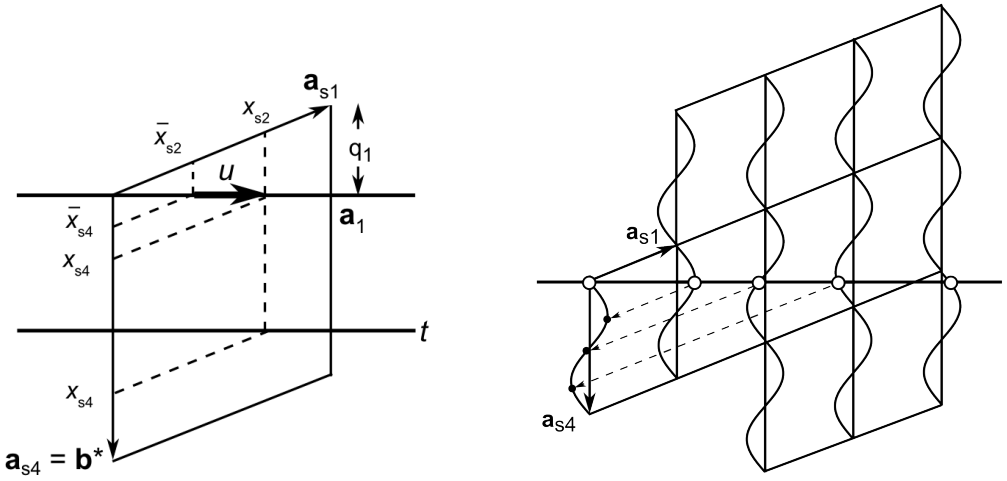

(a) (b)

Figure 2.5: A unit cell in superspace corresponding to an incommensurately-modulated structure with $\vec{q} = (q_1, 0, 0)$, where the unit cell is defined by the lattice vectors $\vec{a}_{s1}$ and $\vec{a}_{s4}$, and the solid horizontal line represents physical space. $\vec{a}_1$ is the lattice vector of the average structure in physical space, and $\vec{u}$ is the displacement of the atom away from its average position due to the modulation. Fractional superspace coordinates for the average structure, $\bar{\vec{x}}$, and for the modulated structure, $\vec{x}$, are shown on the diagram. From geometry, it can be seen that all points in physical space have $x_{s4} = q_1 x_2$, and points at a distance t from physical space have $x_{s4} = q_1 x_2 + t$.
(b) The direct superspace lattice corresponding to the structure described in (a). The grid lines show the superspace lattice, the solid horizontal line represents physical space and the strings represent atoms in superspace. The position of the atoms in physical space are determined by the intersection of each string with physical space, as shown by the open circles. Atoms in physical space can be translated by an integer multiple of $\vec{a}_{s1}$ into the first unit cell, as shown by the dotted arrows. This produces the generalised electron density in superspace, as shown by the solid circles.
Figures are modified from chapter 2 of reference [7].

Following the description of the direct superspace lattice, the next step is to formulate a description of atoms in superspace. This can be done by an extension of the description of a modulated structure in real space given in section 2.3.3, where the position of an atom the modulated-structure is given by $\vec{x} = \bar{\vec{x}} + \vec{u}$. In order to describe the modulation along one direction, the modulation function can be superimposed over the row of atoms, as illustrated in the example shown in figure 2.4(a), so that the atomic positions in the real structure are given by the points at which the modulation function intersects physical space. For each atom, the modulation wave is rotated by 90°, so that on average it is perpendicular to physical space, using the atomic position in the modulated structure as a

pivot. This is repeated for each atom in the structure, generating a series of parallel 'strings'. These strings are the representation of atoms in superspace. For example, performing this for the structure illustrated in figure 2.4(a) produces the set of strings shown in figure 2.5(b). The wavelength of the modulation wave then defines the repeat unit of the structure, and so defines the length of $\vec{a}_{s4}$, and consequently also defines the length of $\vec{b}$. From this, the periodicity of the lattice in four dimensions can clearly be observed.

Additionally, each string has an associated electron density. Due to the periodicity of the lattice in superspace, it is possible to map each of the atoms in physical space onto a point on one string by a translation of an integer multiple of superspace lattice vectors. This is illustrated in figure 2.5(b) by the dashed arrows. When this is performed for each of the atoms in the structure, it generates a string of generalised electron density in superspace. For a commensurately-modulated structure, atoms will lie on a set number of positions on the string. However, for an incommensurately-modulated structure, each atom will lie at a different point on the string. Finally, this string of electron density can be translated through all unit cells.

Following this description, all of the structural information can be contained within one unit cell in superspace. Consequently, structural parameters are often plotted as a function of t, where $0 < t < 1$ runs over the length of one unit cell along $\vec{b}^*$.

2.3.4 Symmetry of Aperiodic Crystals

The three-dimensional translational symmetry present in regular periodic crystals is lost in incommensurately-modulated crystals. Although translational symmetry is still present in the directions perpendicular to the modulation vector, translational symmetry is lost in the direction of the modulation vector.

In periodic crystals, atomic positions can be transformed according to $\vec{x}' = \vec{x} + \vec{R}_{uvw}$, where $\vec{R}_{uvw}$ is a lattice vector. Although translational symmetry is not present in incommensurately-modulated structures, it can be recovered by introducing a phase factor. Atoms in an incommensurately-modulated structure can then be transformed according to $\vec{x}' = \vec{x} + \vec{R}_{uvw} - \vec{q}.\vec{R}_{uvw}$. Symmetry in incommensurately-modulated structures can also be observed in direct lattice defined within the superspace formalism.

The symmetry of incommensurately-modulated crystals can be observed in their diffraction patterns, which contain sharp Bragg spots. From the diffraction pattern, it is also possible to identify symmetry elements in the same way as for periodic crystals. That is, symmetry operations that transform main reflections onto main reflections, and satellite reflections onto satellite reflections. The main Bragg reflections from incommensurately-modulated structures are the same as the reflections from the average structure. The diffraction pattern therefore has the same point group as the average structure, and the transformation of coordinates of the average structure can be expressed mathematically by equation 2.6.

A symmetry operation can image satellite reflections onto $\pm\vec{q}$, or alternatively onto a satellite reflection corresponding to a different main reflection. This is expressed mathematically by equation 2.14, where R is a symmetry operator that describes a symmetry operation present in the average structure, q is the modulation vector, and $\vec{n}^*$ is a reciprocal lattice vector. The factor ϵ can take values of ± 1.

$$qR - \epsilon q = \vec{n}^* \tag{2.14}$$

The transformation of coordinates in superspace can be described mathematically by equation 2.15, where R_s is a 4×4 matrix defined by equation 2.16 and $\vec{v}_s$ describes a translation. Components v_{s1}, v_{s2} and v_{s3} define screw axes and glide planes in physical space, in the same way as in periodic crystals. However, v_{s4} describes a translation perpendicular to physical space. Note that a non-zero v_{s4} component is only possible for $\epsilon = 1$, and not for $\epsilon = -1$. The value of v_{s4} is typically identified by a symbol ($0 = 0$, $s = 1/2$, $t = 1/3$, $\overline{t} = -1/3$, $q = 1/4$, $\overline{q} = -1/4$, $h = 1/6$ and $\overline{h} = -1/6$).

$$\begin{pmatrix} x'_{s1} \\ x'_{s2} \\ x'_{s3} \\ x'_{s4} \end{pmatrix} = R_s \begin{pmatrix} x_{s1} \\ x_{s2} \\ x_{s3} \\ x_{s4} \end{pmatrix} + \begin{pmatrix} v_{s1} \\ v_{s2} \\ v_{s3} \\ v_{s4} \end{pmatrix} \tag{2.15}$$

$$R_s = \begin{pmatrix} R_{11} & R_{12} & R_{13} & 0 \\ R_{21} & R_{22} & R_{23} & 0 \\ R_{31} & R_{32} & R_{33} & 0 \\ n_1^* & n_2^* & n_3^* & \epsilon \end{pmatrix} \tag{2.16}$$

The symbol for a superspace group consists of three components. Firstly, the space group of the average structure. This is followed by the modulation vector, indicating which components are equal to zero. Finally, the values for v_{s4} for each symmetry element in the space group symbol are given. If all of these are equal to 0, then they are omitted from the symbol. For example, the superspace group $C2/c(q_1 0 q_3)0s$ has an average structure with the $C2/c$ space group, and the modulation vector is in the a-c plane. The 2-fold rotation has $v_{s4} = 0$ and the c-glide has $v_{s4} = 1/2$.

There are a total of 756 superspace groups in (3+1)-dimensions. It should be noted that this is not equivalent to the number of space groups in 4-dimensions, of which there are 4783. In practice, the superspace group of an incommensurately-modulated crystal structure can be identified by the consideration of systematic absences, in a similar way to three-dimensional structures. A list of the superspace groups, along with the systematic absences, is given in reference [20].

2.3.5 Pearson Notation

In this thesis, Pearson notation will commonly be used to refer to particular crystal structures. In this notation, 3 symbols are used to identify the crystal structure type. The first symbol is a lowercase letter that refers to the lattice system (a = triclinic, m = monoclinic, o = orthorhombic, t = tetragonal, h = hexagonal/rhombohedral, c = cubic), the second is an uppercase letter that refers to the lattice centring (P, I, F, C, R), and finally a number that gives the number of atoms in the conventional unit cell. Note that information on the space group is *not* included in the Peason symbol. For incommensurately-modulated crystal structures, a prefix of i- is included before the Pearson symbol to indicated that the structure is incommensurate, where the Pearson symbol is that of the average structure.

2.4 X-ray Diffraction

The following section gives an overview of the technique of x-ray diffraction. Firstly, a brief introduction to the underlying theory is given in section 2.4.1, based on the description in chapter 6 of reference [8] and chapter 1 of reference [57]. This is followed by a description of x-ray powder diffraction (section 2.4.2), high pressure x-ray diffraction (section 2.4.3) and synchrotron x-ray diffraction (section 2.4.4). The methods that were used to analyse the diffraction data are described in section 2.5.

2.4.1 Theory of X-ray Diffraction

The Bragg formalism

In the Bragg description [8], the periodic distribution of atoms within a solid is described as a set of parallel planes. Each set of planes is defined by a set of three integers, h, k and l, which describe how the planes intersect the three lattice vectors, $\vec{a}$, $\vec{b}$ and $\vec{c}$. These are called Miller indices, and they are specific to the choice of unit cell (and hence the choice of lattice vectors). The plane closest to the origin (but not the one that goes through the origin) then crosses the lattice vectors at $\vec{a}/h$, $\vec{b}/k$ and $\vec{c}/l$.

X-rays are specularly reflected by the atoms in each of the planes, and non-zero diffracted intensity will only be observed at angles in which the waves reflected from adjacent planes interfere constructively. This is illustrated in figure 2.6(a), which shows the reflection of two incoming x-ray beams from a set of lattice planes defined by h, k, and l, where $\vec{k}$ is the wave vector of the incoming beam and $\vec{k}'$ is the wave vector of the outgoing wave. The condition for constructive interference is given by equation 2.17, where n is the order of the reflection, d_{hkl} is the spacing between lattice planes, and θ is the angle between the incoming wave and the normal to the lattice planes.

$$n\lambda = 2d_{hkl}\sin\theta \tag{2.17}$$

According to conventional notation, (hkl) describes a set of planes, $[hkl]$ describes the direction normal to this set of planes, and $\{hkl\}$ describes the set of planes

that are equivalent due to the symmetry of the lattice. In practice, the nth order reflection can be treated as a reflection from the (nh, nk, nl) set of planes.

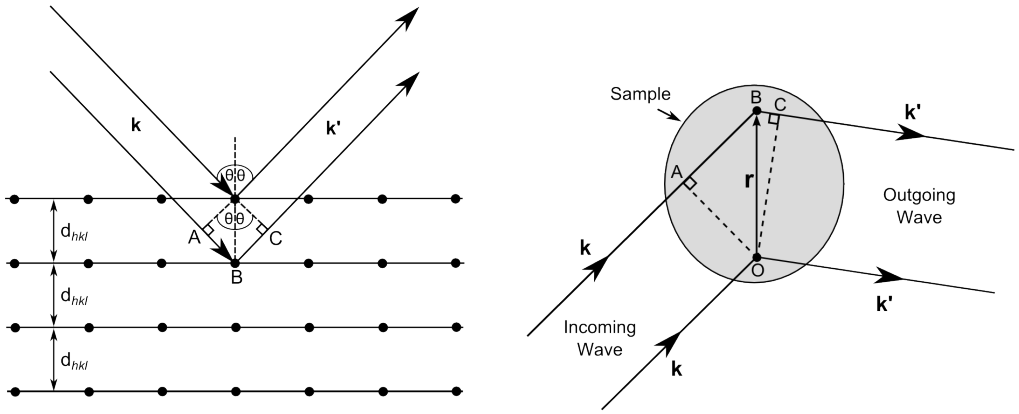

(a) (b)

Figure 2.6: (a) Reflection of two incoming x-ray beams from lattice planes (hkl) within a crystal. From simple geometry, it can be seen that the path difference between waves reflecting from two consecutive planes is give by $AB + BC = 2d_{hkl} \sin\theta$. The condition for constructive interference is then given by $n\lambda = 2d_{hkl} \sin\theta$, also known as Bragg's law.
(b) Two incoming waves with wave vectors $\vec{k} = 2\pi\vec{\hat{n}}/\lambda$ scattering from points O and B in a crystal, where O and B are separated by $\vec{r}$. The path difference between the two waves is given by $AB + BC = \vec{r} \cdot (\vec{\hat{n}}' - \vec{\hat{n}})$.

Laue Formalism and the Reciprocal Lattice

An alternative description of diffraction is given by the von Laue formalism [8]. Unlike the Bragg formalism, it is not necessary to consider planes of atoms within the crystal. Instead, the Laue formalism can be derived from the consideration of an incoming wave scattering from two points within the crystal. This can then be extended to consider scattering from all points in a crystal lattice.

Consider an incoming wave $\vec{k} = 2\pi\vec{\hat{n}}/\lambda$ scattering from two points in a crystal, O and B, which are separated by $\vec{r}$, as illustrated in figure 2.6(b). As we are only considering elastic scattering, the magnitude of the incoming and outgoing waves is the same, and the outgoing wave has the wavevector $\vec{k}' = 2\pi\vec{\hat{n}}'/\lambda$. The path difference between the two incoming waves is given by $AB + BC = \vec{r} \cdot (\vec{\hat{n}} - \vec{\hat{n}}')$. The condition for constructive interference is then given by $\vec{r} \cdot (\vec{\hat{n}}' - \vec{\hat{n}}) = m\lambda$, where m is an integer. Multiplying each side of this equation by $2\pi/\lambda$ allows it to be rewritten as $\vec{r} \cdot (\vec{k}' - \vec{k}) = 2\pi m$. Defining the difference between the incoming

and outgoing waves as $\vec{K} = \vec{k}' - \vec{k}$, where $\vec{K}$ is the scattering vector, the condition for constructive interference can then be written as $\vec{r} \cdot \vec{K} = 2\pi m$.

This can then be extended to consider scattering from the array of points in a Bravais lattice. This gives a set of three equations that must be satisfied in order for constructive interference to be achieved, given by equations 2.18a, 2.18b and 2.18c, where h, k and l are integers. These are known as the Laue equations, and they define the conditions for which diffraction will occur. The directions of the diffracted beams are then given by the set of vectors $\vec{K}$ that satisfy all three equations simultaneously.

$$\vec{K} \cdot \vec{a} = 2\pi h \tag{2.18a}$$

$$\vec{K} \cdot \vec{b} = 2\pi k \tag{2.18b}$$

$$\vec{K} \cdot \vec{c} = 2\pi l \tag{2.18c}$$

The set of vectors that satisfy these conditions correspond to the reciprocal lattice vectors, $\vec{G}_{hlk}$, as defined by equation 2.4 in section 2.3.1. Diffraction is then observed only when the scattering vector is equal to a reciprocal lattice vector.

The scattering amplitude, $S(\vec{G}_{hkl})$, at a given scattering vector $\vec{K} = \vec{G}_{hkl}$, is given by equation 2.19, where the sum is over all atoms in the system. The position of the n^{th} atom in the crystal can be written as $\vec{R}_n = (X_p + x_q)\vec{a} + (Y_p + y_q)\vec{b} + (Z_p + z_q)\vec{c}$, where ($X_p$, Y_p, Z_p) give the position of p^{th} lattice point and (x_q, y_q, z_q) give the position of the q^{th} atom in the unit cell, with respect to the basis vectors $\vec{a}$, $\vec{b}$ and $\vec{c}$. The sum over all atoms can then be rewritten as two separate sums: one sum over all the lattice vectors p, and one sum over all of the atoms in the unit cell q, as shown in equation 2.20.

$$S(\vec{G}_{hkl}) = \sum_n f_n \exp i\vec{G}_{hkl} \cdot \vec{R}_n \tag{2.19}$$

$$= \sum_p \exp\left[2\pi i(hX_p + kY_p + lZ_p)\right] \sum_q f_q exp[2\pi i(hx_q + ky_q + lz_q)] \tag{2.20}$$

$$= \sum_p \exp\left[2\pi i(hX_p + kY_p + lZ_p)\right] F(\vec{G}_{hkl}) \tag{2.21}$$

$$F(\vec{G}_{hkl}) = \sum_q f_q \exp\left[2\pi i(hx_q + ky_q + lz_q)\right] \tag{2.22}$$

The scattering amplitude, $S(\vec{G}_{hkl})$, can then be written it terms of the structure factor, $F(\vec{G}_{hkl})$, which is defined according to equation 2.22. Bragg reflections which have zero intensity can then be determined from the exponent. The intensity of each Bragg peak is then proportional to the the scattering amplitude squared, $|S(\vec{G}_{hkl})|^2$. The atomic form factor, f_q, is the ratio of the scattering amplitude from the atom compared to the scattering from a single electron, as given by equation 2.23. The scattering from a single atom is given by the Fourier transform of the atomic electron density. The atomic form factor has a maximum at $\theta = 0°$, where it is equal to the number of electrons in the atom, and decreases for higher values of θ.

$$f_q(\vec{K}) = -\frac{1}{e}\int_V \rho(\vec{r}) \exp 2\pi i\vec{K} \cdot \vec{r} d\vec{r} \tag{2.23}$$

The Ewald Construction

The Laue condition states that in order for diffraction to occur, the scattering vector $\vec{K}$ must be equal to one the reciprocal lattice vectors $\vec{G}_{hkl}$. In order to determine whether or not this condition is fulfilled, it is useful to consider the Ewald construction.

In the Ewald construction [8], the incoming wave vector $\vec{k}$ is drawn so that it terminates on one of the reciprocal lattice points $\vec{G}_{hkl}$. A sphere of radius $|\vec{k}|$ is then drawn, with the origin of $\vec{G}_{hkl}$ as the centre of the sphere. This is illustrated in figure 2.7(a). As we are considering the case where $|\vec{k}| = |\vec{k}'|$, the Laue condition will then not be fulfilled unless a reciprocal lattice point lies on the surface of the sphere. When this is the case, it is possible to draw $\vec{k}'$ pointing from the centre of the sphere to the reciprocal lattice point on the surface of the sphere. This results in $\vec{K}$ being equal to a reciprocal lattice vector.

For the majority of incoming wave vectors $\vec{k}$ and orientations of the reciprocal lattice, this condition will not be fulfilled. In order to determine the reciprocal lattice of a particular lattice, different techniques can be employed. The work in this thesis has been performed using angle-dispersive x-ray diffraction. In

this technique, the wavelength of the x-ray beam (and hence also the radius of the Ewald sphere) is kept constant. The crystal, and consequently also the reciprocal lattice, is then rotated around a fixed axes. Reciprocal lattice points then intersect the surface of the Ewald sphere at particular lattice orientations, fulfilling the diffraction condition.

Alternatively, it is possible to perform energy-dispersive x-ray diffraction. In this case, the wavelength of the incoming x-ray beam is varied, which corresponds to changing the size of the Ewald sphere while the orientation of the reciprocal lattice remains fixed. Reciprocal lattice points then pass through the surface of the Ewald sphere as the diameter of the sphere is varied. However, x-ray absorption is energy-dependent, and so it is not possible to determine accurate Bragg intensities. Consequently, it is difficult to obtain accurate atomic positions from this method.

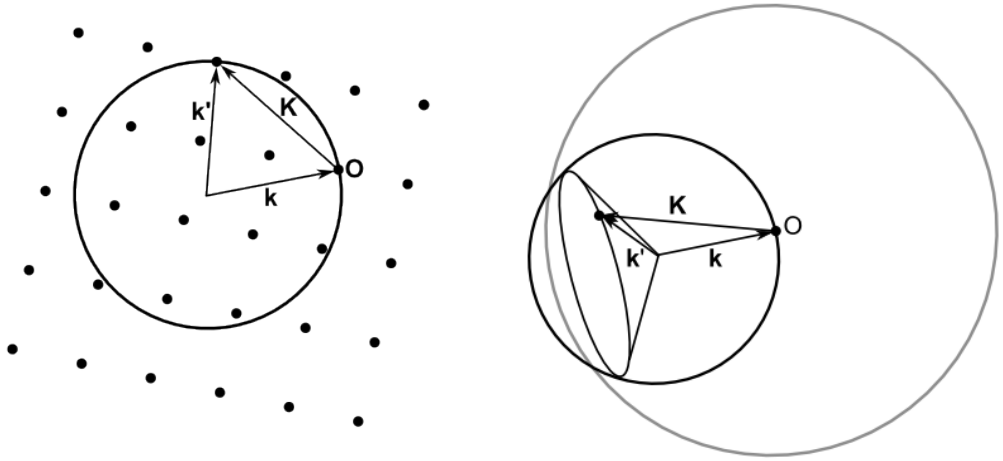

(a) (b)

Figure 2.7: (a) The Ewald sphere construction for a single crystal. The wave vector of the incoming x-ray beam, $\vec{k}$, is drawn so that it terminates at one of the reciprocal lattice points. A sphere is drawn with the initial point of $\vec{k}$ as the origin of the sphere. This defines the Ewald sphere. The Bragg condition is satisfied for reciprocal lattice points that lie on the surface of the sphere, when the scattering vector $\vec{K} = \vec{k}' - \vec{k}$ is equal to a reciprocal lattice vector, $\vec{G}_{hkl}$.
(b) The Ewald sphere construction for a powder sample. The wave vector of the incoming x-ray beam, $\vec{k}$, defines the Ewald sphere (black). The reciprocal lattice is rotated around all possible angles, in order to consider all possible orientations of the crystallites. Each reciprocal lattice point then defines a sphere in reciprocal space (grey). The Bragg condition is satisfied for all points in which $\vec{K}$ lies on the circle where the two sphere intersect, and the wave vectors of the scattered waves, $\vec{k}'$, define a cone of scattered intensity.
Figures are modified from chapter 6 of reference [8].

2.4.2 X-ray Powder Diffraction

X-ray powder diffraction is performed on a sample which ideally contains a large number of randomly orientated crystallites. The diffraction pattern which is obtained is then the same as summing up the patterns from each of the individual crystallites. In practice, the sample is usually oscillated during the exposure in order to improve the powder averaging.

The conditions for constructive interference can be easily be determined using the Ewald construction. The incident wave vector, $\vec{k}$, and hence the Ewald sphere, remain fixed. The reciprocal lattice is then rotated around all possible angles, to consider all possible orientations of the crystallites. Each reciprocal lattice point with $K < 2k$ will then intersect the Ewald sphere in a circle, and the scattered vectors $\vec{k}'$ lie on a cone. This is illustrated in figure 2.7. Consequently, diffraction from a powder sample produces cones of diffracted intensity. Each of these cones then intersects the 2D flat detector in a circle, which is known as a Debye-Scherrer ring. A powder diffraction pattern therefore consists of a set of Debye-Scherrer rings.

The main disadvantage of powder diffraction is that the three-dimensional information that is collected in single crystal diffraction is projected onto one-dimension. For each sample reflection, the only information that can be determined is the d-spacing, and no information can be gathered about the orientation of the Bragg reflection in reciprocal space. This is a particular problem when dealing with complex diffraction patterns, where large numbers of diffraction peaks can result in peak overlap. High-resolution diffraction data are therefore required in order to resolve closely-spaced reflections.

2.4.3 High-Pressure X-ray Diffraction

Due to the fact that diamonds are transparent to x-rays, it is possible to perform x-ray diffraction experiments on samples contained within a DAC. High-pressure x-ray diffraction experiments introduce a number of complications compared with those performed at ambient pressure. Access to reciprocal space is limited by the opening angle of the cell, which is a particular issue when dealing with single crystals. Obtaining a single crystal of a material at high pressure can be problematic. Many pressure-induced structural transitions are accompanied

by a volume-collapse, which reduces the chances of retaining a single crystal of the higher pressure phase. In some cases, it is possible to grow a single crystal at high pressure. For example, this has been achieved by annealing the sample at temperatures just below the melting temperature [58], or by the slow pressurisation of the sample across the phase transition under hydrostatic conditions [59]. However, the success of these methods is sample-dependent, and in many cases it is not possible to obtain a single crystal. In these cases, it is therefore necessary to rely on powder diffraction for structure solution.

As discussed in section 2.4.2, determining the crystal structure from powder diffraction data is much more difficult than from single crystal diffraction. Additional complications are introduced when performing x-ray powder diffraction experiments at high pressure. In particular, the quality of the diffraction patterns can be affected by the presence of non-hydrostatic stress, which can result in both *hkl*-dependent peak shifts and peak broadening. This is especially problematic when dealing with complex structures, where high-resolution patterns are required in order to resolve closely-spaced reflections. Non-hydrostatic stress can be minimised through the use of a pressure-transmitting medium, as discussed in section 2.2.3.

A highly collimated x-ray beam is essential for high-pressure x-ray diffraction experiments, in order to avoid reflections from the gasket material. This becomes increasingly more important with increasing pressure, as smaller diamond culets must be used to obtain the required pressure. This is extremely important when indexing complex structures based on powder diffraction, as it introduces the possibility of peak overlap between gasket and sample reflections.

2.4.4 Synchrotron X-ray Diffraction

Synchrotrons are brilliant sources of x-rays, where electrons are accelerated to relativistic velocities to generate intense x-ray beams. Synchrotrons operate based the principle that an accelerating charged particle emits electromagnetic radiation. All synchrotrons have the same underlying set up. Bunches of electrons are first generated in an electron gun, and are then accelerated in a linear accelerator (linac) using a pulsed electric field. These bunches are then injected into a booster synchrotron, where they are further accelerated to relativistic velocities until they reach the energy at which the synchrotron operates (3 GeV for Diamond Light Source (DLS), 6 GeV at the European Synchrotron Radiation

Facility (ESRF) and PETRA III). When the electrons have reached the required energy, they are passed into the storage ring.

The storage ring consists of straight sections connected by bending magnets (24 straight sections at DLS, 32 straight sections at the ESRF). The magnets force the electrons into a curved trajectory, and radiation is emitted at each bending magnet as the path of the electrons curves due to the magnetic field. The spectrum of radiation emitted from bending magnets covers a large continuous band, with an angular distribution equal to the bending angle of the magnet. In order to generate a more intense, collimated x-ray beam, insertion devices are used. These sit in the straight sections of the electron path.

Two types of insertion devices are used: multipole wigglers and undulators. Both of these consist of a periodic arrangement of dipole magnets with alternating polarity. This produces a magnetic field in the direction perpendicular to the electron trajectory, the strength of which varies periodically along the electron path. This causes the electrons to oscillate with a wavelength dictated by the spacing of the magnets, and a cone of electromagnetic radiation is produced with every oscillation. The wavelength of emitted radiation is related to the magnetic wavelength, given by the spacing between magnets. The maximum displacement of the electron due to the oscillation is related to the strength of the magnetic field, and the angle of the radiated cone is related to the angle of deflection.

Insertion devices are characterised by a factor K, which is proportional to the on-axis magnetic field, B_0, and the magnetic period, λ_0. The full expression for K is given in equation 2.24, where m_0 is the rest mass of an electron and γ is the Lorentz factor [60]. Wigglers have a high magnetic field and a smaller number of magnets than undulators, and are characterised by $K > 1$. The emitted radiation is a superposition of the radiation emitted in each oscillation, with an angular distribution that is determined by the deflection angle of the electrons.

$$K = \frac{ecB_0\lambda_0}{2\pi\gamma m_0 c^2} = 93.4 B_0 \lambda_0 \tag{2.24}$$

Undulators have a larger number of dipole magnets, and consequently a smaller magnetic wavelength, and are characterised by $K \approx 1$. This results in a smaller magnetic field, and so the angle of deflection of the electrons is smaller than in a wiggler. The angle of deflection of the electron is of the same magnitude of the angle of emitted radiation, which means that the radiation emitted from

each oscillation interferes constructively. This results in a narrow cone of emitted radiation, with peaks of maximum intensity at specific wavelengths, which are related to the magnetic wavelength. The intensity of the emitted radiation can be tuned by opening and closing the undulator gap, in accordance with the experiment that is being performed.

The beam of x-rays generated from the insertion device pass into one of the beamlines, at which the experiments are performed. Firstly, the x-rays pass through an optics hutch, in which the beam is focussed using mirrors. Angle-dispersive x-ray diffraction experiments are performed at a fixed-wavelength, and so a monochromator is used to select the required wavelength. The monochromator usually consists of pairs of high-quality single crystals, which are orientated so that the required wavelength satisfies the Bragg condition. In some beamlines, the beam is then focussed using Kirkpatrick-Baez (KB) mirrors. These are a pair of curved horizontal and vertical mirrors with a common focal point centred on the sample.

Synchrotrons are extremely useful in the field of high pressure, in which a highly collimated, intense x-ray beam is required in order to look at small samples. Consequently, there are a number of dedicated high pressure beamlines at different synchrotron sources. The experiments detailed in this thesis have been performed at three dedicated high-pressure beamlines, located at three different synchrotron sources. These are beamline ID09a at the ESRF, beamline I15 at DLS and P02.2 at PETRA-III. A brief description of these beamlines are given below. In particular, the differences between the different experimental stations are highlighted.

ID09a comprises an undulator, and the resulting x-ray beam is vertically focused by a spherical mirror and horizontally by a bent Si (111) monochromator. The bent Si crystal results in a range of d-spacings within the crystal, and so a narrow spread of wavelengths satisfy the Bragg condition. The beam diameter ranges from 10–30 μm. Data are then collected using a Mar555 area detector.

I15 uses a multipole wiggler, and the wavelength is selected by a Si (111) double crystal monochromator, which enables the wavelength to be tuned between 20–80 keV. The resulting x-ray beam is then focussed both vertically and horizontally by large KB mirrors. The beam diameter can be focussed to a minimum diameter of 30 μm. Data are then collected using a Mar345 image plate detector.

P02.2 uses an undulator. The wavelength is selected by a Si (111) and Si (311)

double crystal monochromator, which allows a number of wavelengths to be selected (8.6, 25.6, 42.9, 60 and 77.1 keV). The x-ray beam is focussed by KB mirrors and a compound refractive lens (CRL), which results in a beam size of $2{\times}2$ μm^2. Data are then collected using a Mar345 image plate detector.

Although there are subtle differences between the different beamlines, the basic experimental set-up is the same. A photo of a Livermore DAC cell mounted on the I15 beamline at DLS is shown in figure 2.8. The DAC cell is mounted on a translation/rotation stage on the beamline. The pinhole is used to reduce the size of the x-ray beam, and the beamstop stops the direct beam from hitting the detector.

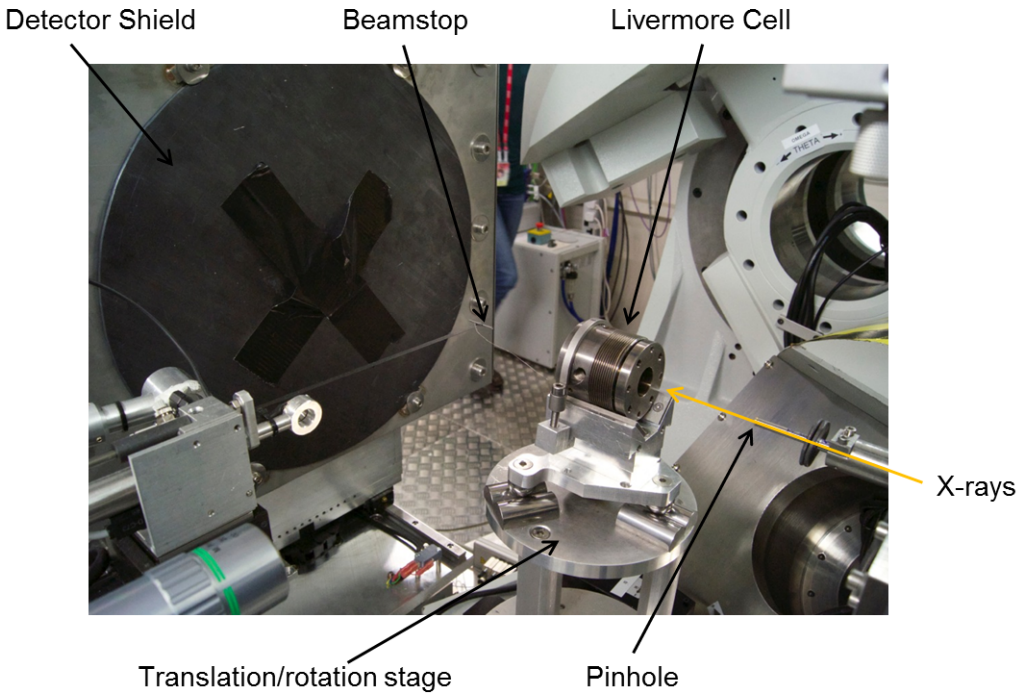

Figure 2.8: A Livermore DAC cell mounted on the I15 beamline at Diamond Light Source.

.

2.5 Data Analysis

In all cases, the two dimensional diffraction images were integrated using the Fit2D software [61, 62] to produce one-dimensional diffraction profiles. Analysis

of integrated diffraction profiles can be classed into two main categories: indexing of new crystal structures, and structural refinement. The method used to index periodic structures is described in section 2.5.1, and the general procedure used to index incommensurately-modulated structures is described in section 2.5.2. Structural refinements based on integrated diffraction profiles were performed using the Le Bail and Rietveld methods, which are outlined in section 2.5.3.

2.5.1 Indexing Periodic Structures

In the work described in this thesis, a number of new crystal structures have been identified. The diffraction profiles corresponding to these new structures have been indexed using the DICVOL software [63], which was used to determine the crystal type and lattice parameters. The only input parameters that are required are the d-spacings of the sample reflections, and the volume range of the unit cell that is to be considered. The software varies the unit cell lengths and angles in real space in order to search for solutions, where crystal systems are considered in order of decreasing symmetry. The intervals over which these parameters are allowed to vary are then reduced using the dichotomy method until a solution is obtained. In general, a number of solutions are generated, in particular when searching for monoclinic solutions.

Although the DICVOL software determines the crystal type and unit cell dimensions, it does not determine the space group. This is done through the consideration of the systematic absences, as discussed in section 2.3.2. These are tabulated in reference [19]. In general, the presence of any lattice centring is first considered, before the presence of additional symmetry elements. Further systematic absences can be introduced if atoms lie on special positions, which can enable the identification of the site symmetry of the atoms. In principle, there are a number of methods that can be used to determine the atomic positions within the unit cell. However, in all of the work described in this thesis it was possible to determine the atomic arrangement based on the density restrictions, which made it possible to determine the site symmetry of the atoms. Refineable atomic coordinates can then be determined from a Rietveld refinement.

2.5.2 Indexing Incommensurately-Modulated Structures

When indexing incommensurately-modulated crystal structures, the unit cell of the average structure must first be determined. It is therefore necessary to first classify reflections as either main ($m = 0$) or satellite ($m \neq 0$) reflections, which can be particularly problematic when dealing with powder diffraction data.

Once the main reflections are identified, the average structure can be determined in the same way as for periodic structures. The SUPERCELL software [64] can then be used to search for possible modulation vectors. The symmetry of the average structure imposes restrictions on the allowed directions of the wave vector, which can be used to limit the search. Finally, the superspace group can be determined. Systematic absences of satellite reflections must be taken into consideration, as this indicates the presence of translational symmetry perpendicular to physical space. The entire set of nonequivalent (3+1)-dimensional superspace groups are tabulated in reference [20]. In general, there will be a number of possible descriptions of the structure, and care must be taken when comparing two similar structures.

2.5.3 Structural Refinements

Le Bail [65] and Rietveld [66] refinements are methods in which to optimise a set of parameters in order to determine the best structural model. These are not methods of structure solution, and the starting model must be close to the final solution in order to find the global minimum. Both of these approaches are least-squares refinements in which the best fit between the entire observed and calculated pattern is obtained by varying a set of parameters. This is done by minimising the residual, which is given by $S_y = \sum_i w_i(y_i - y_{ci})^2$, where $w_i = 1/y_i$, y_i is the observed intensity at point i, and y_{ci} is the calculated intensity at point i [55].

In a Le Bail refinement it is possible to refine the lattice parameters (a, b, c, α, β and γ), peak shapes and overall background in order to determine the best fit. However, the atomic positions are not taken into consideration, and the calculated intensities do not depend on the structural model. A Le Bail refinement is therefore performed to determine the lattice parameters and space group of the structure, before the atomic positions are considered. In a Rietveld refinement,

the peak intensities are derived from the atomic positions. In addition to the parameters that can be optimised in a Le Bail refinement, the atomic positions, atomic displacement parameters and preferred orientation can also be refined in a Rietveld refinement. Note that in most cases the symmetry restrictions imposed by the space group significantly reduce the number of refinable parameters.

In order to assess the quality of the fit based on the refinement, it is conventional to use one of the following: the profile R-factor (R_p), the weighted-profile R-factor (R_{wp}) or χ^2. The expressions for each of these quantities are given by equations 2.25 to 2.27, where R_{exp} is the best possible value of R_{wp} [55]. It is worth noting that the R-factor of a Le Bail refinement will always be lower than that of a Rietveld refinement, as the intensities in a Le Bail refinement do not depend on the structural model.

$$R_p^2 = \frac{\sum_i (y_i - y_{ci})^2}{\sum_i y_i^2} \tag{2.25}$$

$$R_{wp}^2 = \frac{\sum_i w_i (y_i - y_{ci})^2}{\sum_i w_i y_i^2} \tag{2.26}$$

$$\chi^2 = \frac{\sum^2 w_i (y_i - y_{ci})^2}{N - P} = \frac{R_{wp}^2}{R_{exp}^2} \tag{2.27}$$

The background can modelled as a polynomial (typically a Legendre polynomial), where the number of terms can be defined. Alternatively, the background can be defined manually. The peak shapes are typically described by a pseudo-Voigt function, which is a weighted sum of Gaussian and Lorenzian functions. Mathematically, this can be described as $PV = \eta L + (1 - \eta)G$, where η is the mixing parameter [67]. The definitions of the Gaussian (G) and Lorenzian (L) functions are given in equations 2.28 and 2.29, respectively, where η is the full-width half-maximum (FWHM) and $\Delta 2\theta$ is the displacement from the Bragg angle [55].

$$G = \frac{2}{\Gamma}\sqrt{\frac{\ln 2}{\pi}} exp\left[-4 \ln 2 \left(\frac{\Delta 2\theta}{\Gamma}\right)^2\right] \tag{2.28}$$

$$L = \frac{2}{\pi\Gamma}\left[\frac{1}{1 + 4(\Delta 2\theta/\Gamma)^2}\right] \tag{2.29}$$

However, instead of refining η and Γ, it is possible to instead refine the parameters Γ_G and Γ_L, which are the FWHM of G and L, respectively. Γ_G can itself be described by the Caglioti formula, which is given in equation 2.30, and Γ_L can be described by equation 2.31. The pseudo-Voigt peak shapes are therefore described by 5 independent parameters, W, V, U, X and Y, each of which can be refined.

$$\Gamma_G^2 = W + V\tan\theta + U\tan^2\theta \tag{2.30}$$

$$\Gamma_L = X\tan\theta + Y/\cos\theta \tag{2.31}$$

It is also possible to account for preferred orientation. This can be included in the refinement using one of a number of preferred orientation functions, P_K. In particular, the March function has been shown to display the best overall performance for general use [68]. This function is given by equation 2.32, where α is the angle between $[hkl]$ and the preferred-orientation vector, and r is a refineable parameter.

$$P_K = (r^2\cos^2\alpha + (1/r)\sin^2\alpha)^{-3/2} \tag{2.32}$$

A further set of refineable parameters are introduced when dealing with incommensurately-modulated structures. These are the components of $\vec{q}$, as well as the modulation amplitudes A_i^n and B_i^n, as defined by equation 2.7. Symmetry requirements imposed by the superspace group will limit the number of refineable components of both the modulation vector and modulation amplitudes. In addition, generally only low-order satellite reflections are observed, which further reduces the number of modulation amplitudes that should be considered.

There are a number of programs available for performing Rietveld refinements. In the work described in this thesis, Le Bail and Rietveld refinements were performed using the Jana software [69], as it allows for the refinement of incommensurately-modulated structures.

2.6 Incommensurately-Modulated Structures in the Elements at High Pressure

U is the only element that adopts an incommensurately-modulated crystal structure at ambient pressure. The α-U structure, which is stable at ambient temperature, displays an incommensurate modulation below 43 K [70]. This transition is driven by a Peierls-like transition that is related to Fermi surface nesting of the narrow f-electron bands [71].

However, although U is unique in adopting an incommensurately-modulated structures at ambient pressure, a number of elements adopt these types of structures at high pressures. The first two high-pressure elemental incommensurately-modulated structures to be discovered, iodine phase-V and Te-III, were reported almost simultaneously. Iodine phase-V, which has an F-centred orthorhombic average structure with the modulation vector along the a axis [33]. Phase V, which has a very small pressure-stability range (23.3–25.5 GPa), is observed in the intermediate pressures between the lower-pressure molecular phase I and the higher-pressure monatomic phase II. Interestingly, the incommensurate modulation of phase-V results in a continuous range of interatomic distances within the crystal, the shortest of which is longer than the bond length of the molecular crystal but shorter than the nearest-neighbour distance in the monatomic crystal. Bromine has also been found to adopt this structure immediately before molecular dissociation [32], suggesting that the formation of this phase is an important part of the dissociation process.

Te-III has an I-centred monoclinic average structure with the wave vector pointing along the b axis [72]. Again, this structure can be considered in terms of interatomic distances. The modulated structure results in closest-contact distances of $\sim$0.2 Å shorter than the nearest-neighbour distance in the unmodulated structure, with the closest-contact distance remaining constant within error in the 5.5–23.3 GPa range, while the nearest-neighbour distance in the unmodulated structure decreased by $\sim$4.5%. The same incommensurate structure is also observed in Se and in S [30, 72]. First-principles calculations on S identified a soft phonon mode in the undistorted phase and evidence of pronounced Fermi-surface nesting, suggesting that the formation of this structure was due to a one-dimensional charge-density wave instability [73]. Inelastic x-ray scattering experiments on Te-III found a pronounced anomaly in the phonon

branch at wave vectors close to that of the modulation vector, and first principles calculations determined this to be related to a soft phonon in the average structure [31]. The same study also calculated the Fermi surface and found evidence of effective nesting, which they comment is surprising for a simple 3D metal. They therefore concluded that the formation of this structure is also due to a charge-density wave instability.

An incommensurately-modulated structure was also observed in P between 107 and 137 GPa [34], where the possibility of incommensurate modulation was first suggested from first-principles calculations [74]. This structure, phase IV, has a C-centred orthorhombic average structure with a modulation vector along the c axis.

Structures can be easily and definitely identified as incommensurately-modulated from single crystal diffraction data, as each of the main Bragg reflections are surrounded by satellite reflections at $\pm\vec{q}$. However, identifying a structure as incommensurately-modulated from powder diffraction data can be difficult. In iodine phase V, pairs of weak $m = \pm 1$ satellite reflections were observed to approach the corresponding $m = 0$ reflection as the magnitude of the modulation vector decreased on compression, enabling the satellite reflections to be easily identified. However, although the average structure of Te-III was determined from powder diffraction, the fact that it is incommensurate was not realised until the collection of single crystal diffraction data [72]. A further difficulty arises in the cases when the intensity of some satellite reflections is comparable to that of the main reflections, such as in phase IV of P [34], making it difficult to classify reflections as main or satellite reflections.

Chapter 3

The Lanthanide Elements

3.1 Introduction

The lanthanide series is the group of 15 elements running from lanthanum with atomic number 57 to lutecium with atomic number 71, which are characterised by the gradual filling of the $4f$ electron shell. The members of the series can be categorised into a group of 'regular' trivalent members, with similar physical properties, and a small group of irregular members (Ce, Eu and Yb), whose behaviour is remarkably different. This thesis describes the high-pressure structural behaviour of two neighbouring lanthanide elements, divalent Eu and trivalent Sm, as determined from powder x-ray diffraction.

This chapter presents a review of the high-pressure behaviour of the lanthanide elements. Firstly, an overview of the high-pressure structural behaviour of the trivalent lanthanide elements is given in section 3.2, including a description of electronic changes observed at high pressure. This is followed by a description of the high-pressure behaviour of divalent Eu in section 3.3. An in depth description of the previous high-pressure x-ray diffraction studies on Eu is given in the introduction of chapter 4, and a description of the previous high-pressure x-ray diffraction studies Sm is given in the introduction to chapter 7.

3.2 The Trivalent Lanthanide Elements

The 'regular' lanthanide elements are trivalent at ambient pressure, with the electronic structure [Xe]$6s^2 5d^1 4f^n$. Their electronic structure therefore differs only by the number of electrons in the $4f$ shell. The $4f$ electrons are highly-localised, and the interaction between neighbouring atoms is mostly governed by the $6s$ and $5d$ conduction electrons. When the $4f$ electrons are not considered, these elements are isoelectronic. Consequently, their behaviour is remarkably similar.

A common structural trend is observed across the series at ambient pressure, with the lighter elements (La–Nd, excluding Ce) exhibiting the dhcp structure, samarium alone exhibiting the Sm-type structure, and the heavy lanthanides (Gd–Tm) exhibiting the hcp structure. The opposite trend (hcp $\rightarrow$ Sm-type $\rightarrow$ dhcp) is observed in each individual element under pressure, with transitions to the fcc structure and then to a distorted-fcc (dfcc) phase observed on further compression. At even higher pressures, these elements transform to low-symmetry phases. This transition is sometimes accompanied by a volume collapse associated with $4f$ electron delocalisation [9].

The trivalent lanthanide elements are therefore said to exhibit a common sequence of structural phase transitions under pressure (hcp $\rightarrow$ Sm-type $\rightarrow$ dhcp $\rightarrow$ fcc $\rightarrow$ dfcc $\rightarrow$ low-symmetry "collapsed"), and their high-pressure structural behaviour is often thought to be well known. Considerable effort has gone into resolving the high-pressure structural behaviour of the light lanthanide elements, in particular Ce and Pr. However, the same cannot be said of the heavier rare earth elements, where the structural assignment of the dfcc and 'collapsed' phases rely heavily on analogy with other members in the series. Additionally, subtle structural differences between different members of the series suggest that their behaviour may not be as similar as initially thought, and surprises still remain.

A summary of the most up-to-date understanding of the high-pressure structural behaviour of the trivalent lanthanide elements up to 150 GPa is shown in figure 3.1, where the transition pressures are taken from reference [9]. Details of individual structures, and a discussion of interesting features observed in individual elements, are given in section 3.2.

In the following section, a brief description of the common structures observed

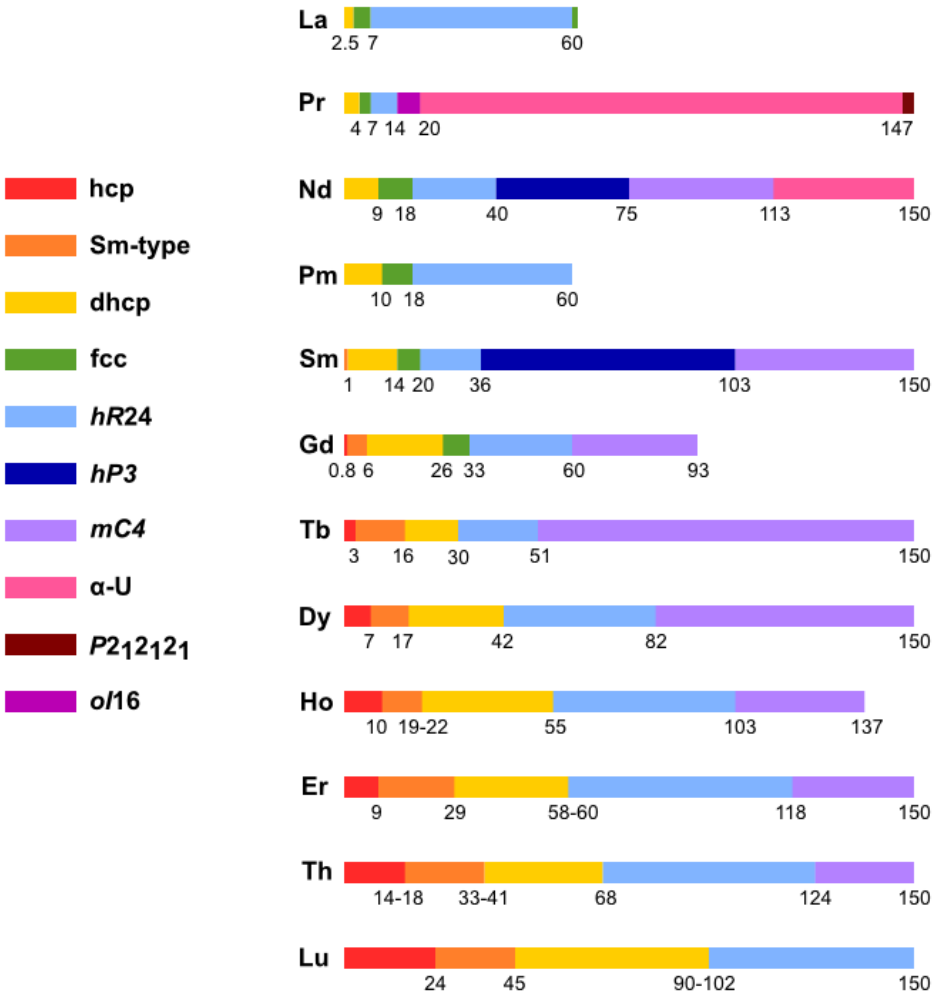

Figure 3.1: A summary of the high-pressure structural behaviour of the trivalent lanthanide elements up to 150 GPa. Transition pressures are taken from [9] and references therein.

in the trivalent lanthanide elements at high pressures is given. This is split into three sections: close-packed structures, distorted-fcc structures, and finally low-symmetry structures. Structural details, as well as a description of the associated electronic behaviour, are discussed in each section.

3.2.1 Close-Packed Structures

The lower-pressure crystal structures [hcp, double-hcp (dhcp), Sm-type and fcc] are close-packed, and differ only by the stacking sequence of the close-packed

layers. Details of the stacking sequence, space group, and atomic positions of these structures are given in table 3.1. Note that the hcp, dhcp and Sm-type structures are described in a trigonal space group, with $a = b \neq c$, $\alpha = \beta = 90°$ and $\gamma = 120°$, whereas fcc is described in a cubic space group, with $a = b = c$ and $\alpha = \beta = \gamma = 90°$.

Structure	Stacking sequence	Space group	Atomic Positions
hcp	AB	$P6_3/mmc$	$2c$ ($\frac{1}{3}$, $\frac{2}{3}$, $\frac{1}{4}$)
dhcp	ABAC	$P6_3/mmc$	$2a$ (0, 0, 0) and $2c$ ($\frac{1}{3}$, $\frac{2}{3}$, $\frac{1}{4}$)
Sm-type	ABABCBCAC	$R\bar{3}m$	$3a$ (0, 0, 0) and $6c$ (0, 0, $\frac{2}{9}$)
fcc	ABC	$Fm\bar{3}m$	$4a$ (0, 0, 0)

Table 3.1: Structural details of the close-packed structures observed in the trivalent lanthanide elements.

The fact that a common structural trend (hcp $\rightarrow$ dhcp $\rightarrow$ Sm-type $\rightarrow$ fcc) is observed with decreasing atomic number, and also in each individual element with increasing pressure, suggests that there is a common feature influencing the crystal structure in both cases. Johansson and Rosengren [40] showed that the crystal structure that is adopted is related to the parameter $F = R_{ws}/R_I$, where R_{ws} is the Wigner Seitz radius and R_I is the ionic radius, where F increases across the series, and decreases in each individual element on compression. Duthie and Pettifor [75] later showed that this quantity is related to the number of d electrons. These transitions are therefore driven by an increase in the occupancy of the d-band.

3.2.2 The Distorted-fcc Phase

At higher pressures, a transition from the fcc to the distorted-fcc (dfcc) phase is observed [9, 14]. This is accompanied by two distinct changes in the diffraction patterns: the splitting of some of the fcc reflections into multiple reflections as the unit cell distorts away from cubic, and the appearance of superlattice reflections as the atoms move away from their fcc positions. These two features are not necessarily observed simultaneously, and in many cases the superlattice reflections are observed before splittings are resolved. It should be noted that single-phase fcc patterns are not observed in the heavy lanthanide elements Tb [76], Dy [77], Ho [78] and Er [79], and instead these elements were reported to transform directly to the dfcc phase.

There are many different ways in which to distort the cubic unit cell, each of which results in a different set of splittings of the fcc reflections in the diffraction pattern. For example, stretching (or compressing) the unit cell along the [100] direction will split the (200) fcc reflection into a doublet, and further distorting the unit cell along the [010] direction will split the (200) fcc reflection into a triplet. Alternatively, stretching (or compressing) the fcc unit cell along the [111] direction will split the (111) fcc reflection into a doublet while leaving the (200) unaffected. It is therefore very important to be able to resolve closely-spaced split-fcc reflections in order to correctly index the structure. The splitting of the first 8 fcc peaks for a number of distorted-fcc structures is shown in figure 3.2. It is also necessary to construct the correct supercell of the original structure to account for the superlattice reflections.

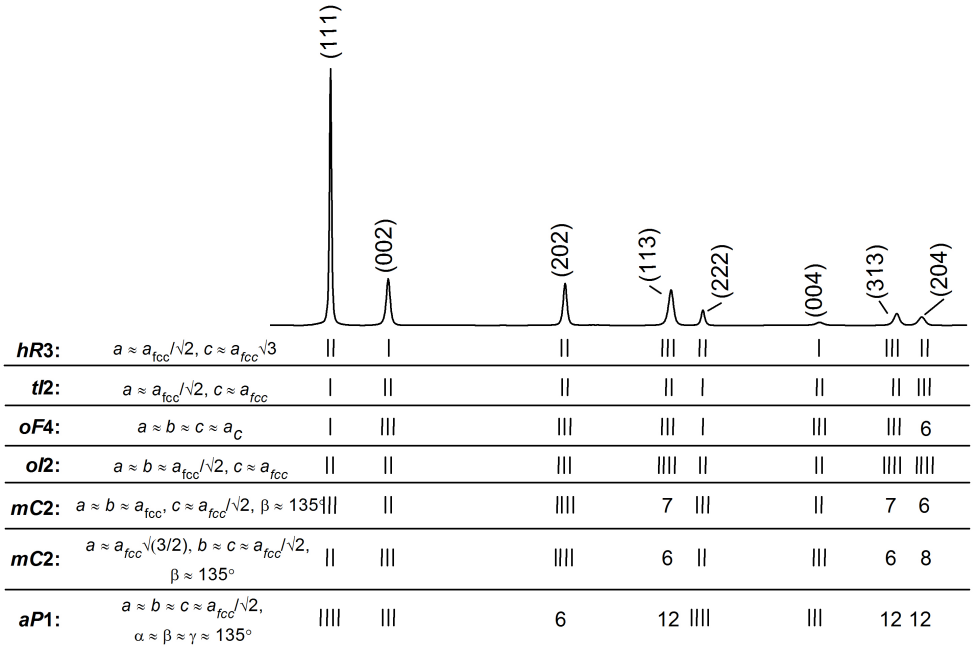

Figure 3.2: Integrated diffraction profile corresponding to fcc Sm (upper). The tick marks indicate the splitting of the fcc diffraction peaks for a selection of distorted-fcc structures as the unit cell is distorted away from cubic [10]. The relationship of the structures to fcc, along with their Pearson symbol, are given at the left hand side, where a_{fcc} is the lattice parameter of the fcc structure.

The lanthanide element in which the the dfcc phase is observed at the lowest pressure is Pr, where the fcc $\rightarrow$ dfcc transition occurs at 7.4 GPa [11]. Consequently, this phase has been the focus of an extensive number of x-ray diffraction studies, and a number of different crystal structures were proposed. Details of the candidate structures are given in Table 3.2, including their relationship to the fcc structure. A detailed discussion of previous x-ray

diffraction studies is given in reference [11]. Due to lack of an overall agreement between different studies, the structure of this phase remained disputed until Evans *et al.* [11] performed high-resolution powder diffraction experiments to definitively determined the dfcc phase to have the $hR24$ structure initially proposed by Hamaya *et al.* [80] However, the $mC4$ structure could only be ruled out due to the observation of a small number of weak reflections (the (101), (210) and $(\bar{3}01)$ $hR24$ reflections), which could not be described by this structure. Evans *et al.* also found that a good fit was obtained with the $hP4$ structure. However, this structure predicted a number of additional reflections and peak splittings that were not observed in the patterns.

Table 3.2: Candidate structures for the dfcc phases of praseodymium. The $mC16$ and $oI16$ structures were proposed for Pr-VII, and the remaining structures were proposed for Pr-VI.

Structure	Spacegroup	Relationship to fcc	Atomic Positions
$oP16$ [81]	$Pmmm$	$a \approx b \approx a_{fcc}/\sqrt{2}$	Not given
$hP6$ [82, 83]	$P3_121$	$a \approx a_{fcc}/\sqrt{2}$	$6c$
	or $P3_221$	$c \approx 2\sqrt{3}a_{fcc}$	
$hR24$ [80]	$R\bar{3}m$	$a \approx \sqrt{2}$	$6c$, $18h$
		$c \approx 2\sqrt{3}$	
$oC8(1)$ [84]	$Cmmm$	$a \approx 2a_{fcc}$	$4g$, $4j$
		$b \approx c \approx a_{fcc}/\sqrt{2}$	
$oC8(2)$ [84]	$Cmma$	$a \approx 2a_{fcc}$	$4a$, $4g$
		$b \approx c \approx a_{fcc}/\sqrt{2}$	
$mC16$ [85]	$C2/m$	$a \approx \sqrt{6}a_{fcc}$	$4i$, $4i$, $8j$
		$b \approx c \approx \sqrt{2}a_{fcc}$	
$oI16$ [11]	$Ibam$	$a \approx 2a_{fcc}$	$8g$, $8j$
		$b \approx c \approx a_{fcc}/\sqrt{2}$	

The $hR24$ structure, which has the $R\bar{3}m$ space group and atoms in the $6c$ $(0,0,z_1)$ and $18h$ $(x,-x,z_2)$ Wykoff positions, is associated with the softening of the TA phonon mode at the L point of the Brillouin zone [80]. The relationship between $hR24$ and fcc is given by $\vec{a} \approx -\vec{a}_{fcc} + \vec{b}_{fcc}$ and $\vec{c} \approx 2(\vec{a}_{fcc} + \vec{b}_{fcc} + \vec{c}_{fcc})$, which is illustrated in figure 3.3(a). The $hR24$ structure is therefore a $2 \times 2 \times 2$ supercell of fcc in the hexagonal setting. The $hR24$ structure is then equivalent to fcc when $c/a = \sqrt{6}$, $z_1 = 0.25$, $z_2 = 0.25$ and $x = 0.5$.

Above 13.7 GPa, Evans *et al.* found that their diffraction patterns could no longer be described by the $hR24$ structure, indicating a transition to a new phase, Pr-VII. This second dfcc phase was determined to have the $Ibam$ space group, and atoms in the $8g$ $(0,\ y_1,\ 1/4)$ and $8j$ $(x,\ y_2,\ 0)$ Wyckoff positions ($oI16$ in

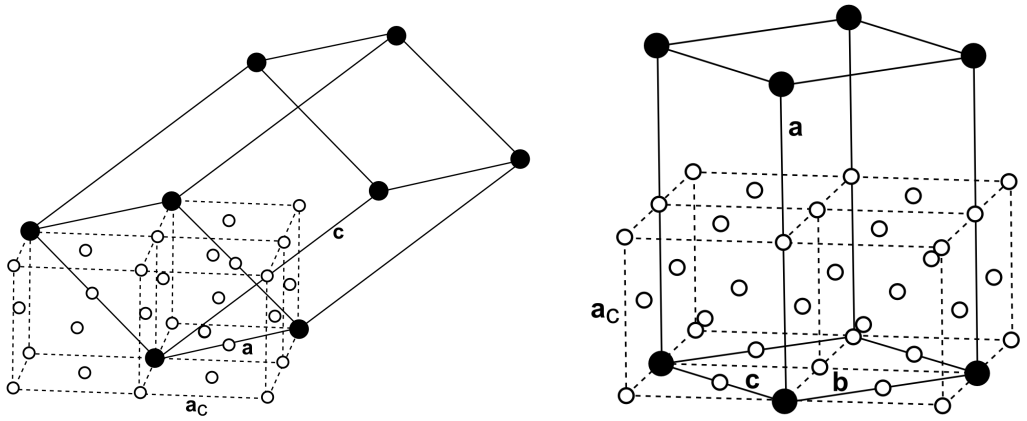

(a) (b)

Figure 3.3: The relationship between fcc and the (a) $hR24$ and (b) $oI16$ structures, where the $hR24$ figure has been modified from reference [11]. The solid lines show the unit cells of the $hR24$ and $oI16$ structures, respectively, and the solid circles show the corner atoms in the respective structures. The dashed lines show the unit cell of the fcc structure, and the open circles show the fcc atoms.

Pearson notation). This structure is equivalent to fcc when $a = b/\sqrt{2} = c/\sqrt{2}$, $x = y_1 = 1/4$ and $y_2 = 0$. The relationship between the $oI16$ and fcc structures is illustrated in figure 3.3(b). The $hR24$–$oI16$ transition is sluggish, occurring over the 13.7–19.9 GPa pressure range. The corresponding changes in the diffraction profiles are subtle, and the transition was identified by the observation of a change in the relative intensity of the (006)/(202) and (0,0,12)/(404) doublets. Evidence of a transition to the *Ibam* structure was also observed in Nd [11] and La [86], raising the question of whether or not this phase is also present in other members of the series.

With the exception of Sm, the dfcc phases of the remaining trivalent elements have also been reported to have the $hR24$ structure [11, 76–79, 87–89]. However, in many cases the structural assignment is performed by analogy with the dfcc phase of Pr. Rietveld refinements based on this structure have only been shown for Gd [88], Dy [90], Er [79] and Tm [89], and the weak peaks that rule out the $mC4$ structure have only been explicitly mentioned in the case of Nd [11]. However, there is evidence to suggest that the $hR24$ structural assignment may not always be correct. In their high-pressure x-ray diffraction measurements on Dy, Shen *et al.* [91] observed (002) fcc reflection to split into a doublet. This cannot be explained by the $hR24$ structure, in which the (002) reflection would remain a singlet, as shown in figure 3.2. They therefore determined the dfcc phase to have the C-centred orthorhombic structure, $oC8(1)$, with the space group $Cmmm$,

which was previously considered by Porsch and Holzapfel [84]. Note that Shen *et al.* refer to this structure using the Peason symbol $oS8$, which is equivalent to $oC8$. The splitting of the (002) reflection can be seen in the diffraction profiles of Dy shown in the later study by Samundrala and Vohra [90]. However, the authors index the patterns based on the $hR24$ structure and do not comment on the fact that this structure cannot account for this splitting.

Krüger *et al.* [14] reported the pressure dependence of the c/a ratio of the dfcc phase for all the trivalent lanthanides up to Tb. In this study, the dfcc phase was indexed based on a trigonal structure with the space group $P3_221$ in all cases. In Pr, Nd and Sm, the c/a ratio was reported to decrease by over 1.5%, which is significantly larger than the distortion reported for La, Gd and Tb, in which the c/a ratio remained close to the cubic value. However, if the data points from Pr and Nd that occur in the pressure regions after the transition to the $oI16$ structure are disregarded, the remaining points would suggest that the c/a distortion of these elements is similar to that of La, Gd, and Tb. Krüger *et al.* also plotted the pressure dependence of the (105) superlattice reflection for the same elements (Pr–Tb), where the intensity was normalised with respect to that of the K_α fluorescence peak. In general, the superlattice reflections were observed before the splitting of the fcc reflections could be resolved. However, in Sm the c/a ratio had already increased away from the fcc value even at the lowest pressure.

With the exception of the work by Krüger *et al.*, the pressure-dependence of the lattice parameters of the $hR24$ structure have only been reported for Pr and Ho, and only a few data points were shown for the latter [11, 78]. Evans *et al.* [11] reported the c/a ratio of $hR24$-Pr to increase from $\sqrt{6} = 2.449$ at 7.5 GPa to 2.487 at 13.42 GPa, corresponding to stretching the fcc structure along the [111] direction. Cunningham *et al.* determined the c/a ratio of $hR24$-Tb to be 2.381 ($<\sqrt{6}$) at 40.2 GPa [76], corresponding to *compressing* the fcc structure along the [111] direction. However, in the paper by Cunningham *et al.* there is a clear error in the indexing of the $hR24$ reflections on the diffraction profile, as the (01,11) reflection is reported to have a longer d-spacing than the (226) reflection, which is inconsistent with the lattice parameters quoted for this phase. The c/a ratio of $hR24$-Ho was reported to decease to $<\sqrt{6}$ on pressure increase, but then increase to $>\sqrt{6}$ on pressure decrease, suggesting that there is some hysteresis on pressure cycling [78]. The pressure-dependence of the $hR24$ structure therefore does not appear to be the same in different elements.

3.2.3 Post-dfcc Phases

On further compression, the majority of the trivalent lanthanide elements transform from the dfcc phase to low-symmetry phases. A number of different structures are observed across this series, as can be seen in figure 3.1, and the general trend differs between the light and heavy members of the series. Pr transforms from Pr-VII to the α-U structure, also observed in Ce. Nd and Sm transform to the hexagonal $hP3$ structure, before transforming to the monoclinic $mC4$ structure on further compression. The 'heavy' lanthanides (Gd to Tm) have been reported to transform directly from $hR24$ to the $mC4$ structure.

The $mC4$ structure has the $C2/m$ space group, with atoms in the $4i$ (x, 0, z) Wyckoff positions, and the $hP3$ structure has either the $P3_121$ or $P3_221$ space group, with atoms in the $3a$ ($-x$, $-x$, 0) Wyckoff positions in both cases. Again, these structures are both distortions of the fcc structure. The relationship between $hP3$ and fcc is given by $\vec{a} \approx -1/2\vec{a}_{fcc}+1/2\vec{b}_{fcc}$ and $\vec{c} \approx \vec{a}_{fcc}+\vec{b}_{fcc}+\vec{c}_{fcc}$, as illustrated in figure 3.4(a), and the two structures are equivalent when $c/a = \sqrt{6}$. The relationship between $mC4$ and fcc is given by $\vec{a} \approx 1/2\vec{a}_{fcc} - 1/2\vec{b}_{fcc} - \vec{c}_{fcc}$, $\vec{b} \approx 1/2\vec{a}_{fcc}+1/2\vec{b}_{fcc}$ and $\vec{c} \approx 1/2\vec{a}_{fcc}-1/2\vec{b}_{fcc}+\vec{c}_{fcc}$, as illustrated in figure 3.4(a), and the two structures are equivalent when $a = c = \sqrt{3/2}a_{fcc}$, $b = \sqrt{1/2}a_{fcc}$ and $\beta = 109.471°$.

3.2.4 Pressure-Induced Changes in Electronic Behaviour

The high-pressure high-temperature bevahiour of Ce is vastly different from that of the 'regular' trivalent lanthanide elements, and it exhibits a number of unusual physical properties. At 0.3 GPa, Ce undergoes an isostructural volume-collapse transition between the γ and α phases, both of which have the fcc structure [92]. This transition involves a volume collapse of 16.5 % at ambient temperature, with the percentage volume change decreasing with increasing temperature. The γ-α phase boundary also ends in a critical point, making Ce the *only* element with a solid-solid phase transition that ends in a critical point [93]. Above 5.5(2) GPa at 295 K, Ce transforms either to the α-U or $mC4$ structures, depending on the method of sample production and preparation [12].

Due to its unusual phase diagram, Ce has been the subject of a large number of both experimental and theoretical studies. In particular, the isostructural

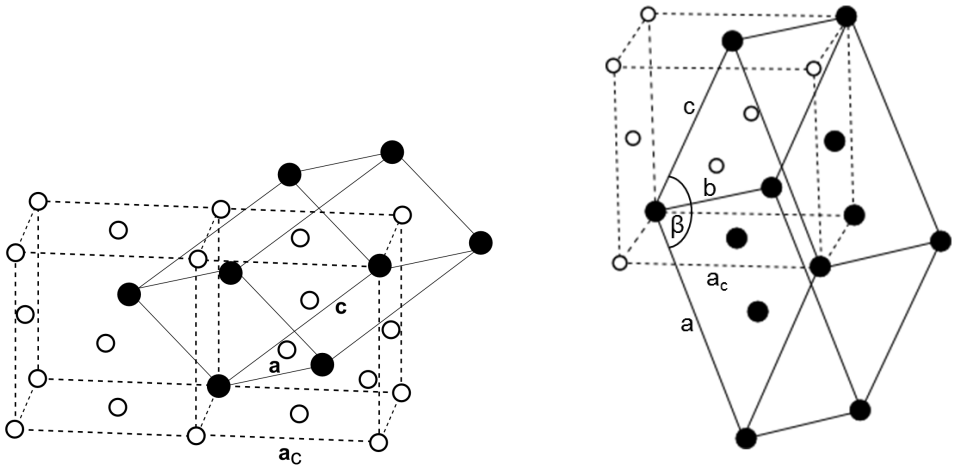

(a) (b)

Figure 3.4: The relationship between fcc and the (a) $hP3$ and (b) $mC4$ structures, where the figures have been modified from references [11] and [12], respectively. The solid lines show the unit cells of the $hP3$ and $mC4$ structures, and the solid circles show the atoms in the respective structures. The dotted lines show the unit cell of the fcc structure, and the open circles show the fcc atoms.

transition, which is unique amongst the elements, provides a benchmark for understanding the physics that governs the behaviour of the $4f$ electrons. The mechanism which drives this transition is still under debate, with the main theoretical descriptions being the Kondo volume-collapse [94], where the approach of the $4f$ level to the Fermi level leads to an increase in the Kondo transition temperature [95], and the Mott transition [96], where the $4f$ electrons go from being localised to itinerant.

With the exception of Nd, Sm, La and Pm, volume-collapse transitions are also observed in the 'regular' trivalent lanthanide elements under pressure. However, it should be noted that due to the limited pressure range over which La and Pm have been studied (60 GPa in each case), it is possible that volume-collapse transitions will be observed in these elements at higher pressures. Unlike Ce, the volume collapse is not associated with an isostructural transition, but with the transition to the post-dfcc low-symmetry phase. The heavier trivalent lanthanides (Gd–Ho) undergoing a volume collapse over the $hR24 \rightarrow mC4$ transition [76, 79, 88–90, 97], Pr over the $hR24 \rightarrow \alpha$-U transition [11] and Lu over the dhcp $\rightarrow hR24$ transition [98]. The volume changes associated with these transitions are much smaller than that observed in Ce, ranging from 1.5% in Dy and Tm to 8.3% in Pr.

These transitions are often associated with changes in the nature of the $4f$ electrons from localised to itinerant. The delocalised $4f$ electrons would then participate in bonding, resulting in a lower atomic volume, and an associated volume-collapse at the transition. At this point, the electron shells would also be far from spherical, resulting in the adoption of low-symmetry structures. A comparison can be made with the actinide series, where the $5f$ electrons in the lighter members (up to Pu) are delocalised, whereas the heavier members have localised $5f$ electrons [96]. Consequently, the heavier members have a larger atomic volume than the lighter members of the series. The elements Pa–Pu also exhibit low-symmetry structures, whereas the heavier elements adopt high-symmetry structures .

However, recent studies have suggested that the origin of the volume-collapse observed at the dfcc $\rightarrow$ post-dfcc transition is not the same for all the members of the lanthanide series. Fabbris *et al.* concluded that, out of the options considered in their study (valence transition model, Mott-Hubbard model, Kondo volume collapse model, $s \rightarrow d$ charge transfer), the mechanism behind the volume collapse in Gd was $s \rightarrow d$ charge transfer, whereas in Tb it was thought to be due to a Kondo volume collapse [95]. The volume collapse in Dy was also thought to be most likely due to a Kondo volume-collapse [99].

La, which is the first member of the lanthanide series, does not have any $4f$ electrons, exhibits a novel reentrant transition (fcc $\rightarrow$ $hR24$ $\rightarrow$ fcc) under pressure [100]. The observation of the $hR24$ phase in this element was taken as evidence that the transition to this phase is not driven by changes in the behaviour of the $4f$ electrons. The behaviour of Y should also be considered, as Y is isostructural with the trivalent lanthanide elements when the $4f$ electrons are not considered. Y exhibits the common series of structural phase transitions (hcp $\rightarrow$ dhcp $\rightarrow$ Sm-type $\rightarrow$ fcc $\rightarrow$ dfcc) below 50 GPa, transforming to the $mC4$ structure above 99(4) GPa, where this transition is accompanied by a 2.6 % volume collapse [101]. Again, the dfcc phase is reported to have the $hR24$ structure, although a Rietveld refinement is not shown. The (002) fcc reflection, which should remain a singlet in the $hR24$ structure, is also very broad, questioning the $hR24$ structural assignment. The observation of a volume-collapse transition in Y questions the validity of the assumption that it is related to $4f$ electron delocalisation. Instead, it was suggested that this case the transition is related to the transfer of electrons from the s and p bands to the $4f$ band [101].

The fact that changes in the nature of the electronic structure are often

inferred from structural changes highlights the importance of precise structural determination. The report of a large volume collapse (16.7 %) at the dfcc $\rightarrow$ α-U transition in Pr [102] was found to be due to misindexing of the $hR24$ diffraction patterns, with the later study reporting a volume collapse of only 8.3 % [11]. The report of an unphysical increase in volume over the $hR24 \rightarrow$ Pr-VII transition [103] was thought to be due to misindexing of the Pr-VII diffraction patterns [11]. High-resolution powder x-ray diffraction studies are therefore *essential* in order to definitively determine structural assignments of high-pressure phases.

3.3 Europium

Due to its half-filled $4f$ electron shell, europium (Eu) is divalent at ambient pressure, with the electronic structure [Xe]$6s^2 4f^7$. Similar to the trivalent lanthanide elements, the $4f$ electrons are highly localised, and do not participate in bonding, and so the interaction between neighbouring atoms is largely governed by the conduction electrons. Eu has one less conduction electron than each of the trivalent lanthanide elements, and so one less electron is participating in bonding. Eu therefore has a significantly larger atomic volume than would be expected to be in keeping with the general trend observed across the series [13]. This is illustrated in figure 3.5, which shows the molar volumes of the lanthanide elements at ambient pressure. Eu also has a significantly lower bulk modulus than those of the trivalent lanthanide elements due to its weaker metallic bonding [13].

The trivalent electronic configuration of Eu, [Xe]$6s^2 5d^1 4f^6$, is expected to become more stable than the divalent state at high pressure [40]. A transition from a divalent to a trivalent state is therefore expected to occur when the energy gain from an additional electron involved in metallic binding is *greater* than the energy required to excite an electron from the $4f$ to $5d$ electronic levels. A number of different transition pressures have been calculated. Using a pseudopotential method, Johansson and Rosengren [40] determined the transition to a fully trivalent state predicted to occur at 24.5(2) GPa. A later study by Min *et al.* [104] used the linearised muffin-tin orbital method to determine this transition to occur at 70.6 GPa, although they commented that this pressure should be considered as an upper limit. However, these calculations only considered a transition from a fully-divalent to a fully-trivalent state. Rosengren and Johansson [105] also considered the possibility of Eu transforming to a mixed-valent state. That is,

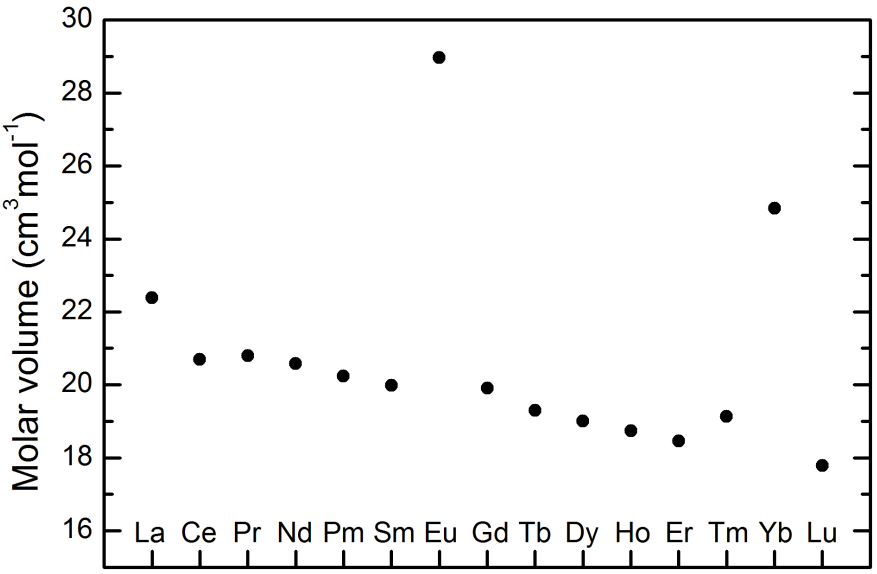

Figure 3.5: Molar volume of the lanthanide elements at ambient pressure, illustrating the anomalously large molar volumes of Eu and Yb. The figure is adapted from reference [13]

when the divalent and trivalent states lie close enough in energy that neither is favoured. The electronic structure then fluctuates between the two integral $4f$ occupations, and the result is that the average $4f$ occupation (and therefore also the valence) is non-integer. Note that this is due to the $4f$ occupation, and consequently the valence, of individual atoms fluctuating in time. Rosengren and Johannson determined the valence of Eu to increase from 2 on compression above 18 GPa, reaching a fully-trivalent state at 35 GPa. However, these calculations were performed assuming that Eu adopts the bcc structure in this pressure range, which is not the case. Takemura *et al.* [13] also commented that a transition back to a divalent state is expected even higher pressures, introducing the possibility that Eu will never become fully trivalent.

In their neutron diffraction study, Nereson *et al.* [106] reported that the Eu magnetic moments are antiferromagnetically ordered below 91 K at ambient pressure, with a helical spin structure along the [100] direction, with a period of $3.5a$ at T_N. The divalent [Xe]$6s^2 4f^7$ electronic configuration is magnetic, and the trivalent [Xe]$6s^2 5d^1 4f^6$ is nonmagnetic. A transition to a trivalent state would therefore be expected to be accompanied with the loss of magnetic ordering at low temperature. The observation of magnetism under pressure would therefore be taken as evidence that Eu retains a strongly divalent character. The high-pressure resistivity study by Bundy and Dunn [107] reported an abrupt change in dR/dT between 75–90 K up to 12.5 GPa, which suggests that the magnetic

ordering persists up to this pressure. Above 25 GPa, a different discontinuity in dR/dT was observed at ∼150 K. Although the nature of this transition is unknown, it introduces the possibility of magnetic ordering being present in the higher pressure phase. A broad bend in the $R(T)$ curves was also observed in the 60–70 K region above 25 GPa, which was suggested to be due to a sluggish phase transition, or due to changes in the electron scattering conduction mechanism with temperature.

Room temperature L_{III} x-ray absorption measurements by Röhler [108] determined the valence of Eu to increase smoothly on compression. However, the valence was observed to saturate at 2.64 at 24 GPa, and Eu has not fully transformed to the trivalent state by 34 GPa, the highest pressure reached in this study. Mössbauer measurements by Farrell *et al.* [109] later reported the valence of Eu to increase on compression up to 14 GPa at 44 K, and estimated an overall change in the occupancy of the $4f$ shell of about ∼0.4 electrons. The same study also reported the magnitude of the magnetic moment to decrease over the same pressure range.

However, a more recent study by Bi *et al.* [110] combined the results of various experimental studies [x-ray absorption near edge structure (XANES), x-ray magnetic circular dichroism (XMCD) and Synchrotron Mössbauer Spectroscopy (SMS)] with the results of electronic structure calculations to determine that Eu remains nearly divalent up to at least 87 GPa, and magnetic up to at least 50 GPa. The changes in the XANES spectra that were previously attributed to a transition to a mixed-valent state [108] were also observed in this study. However, these were determined to be due to electronic and structural changes due to the bcc to hcp transition, and not due to any valence change. The previously reported shift in the Mössbauer isomer shift on compression to 14 GPa [109], also thought to be due to a valence change, was again observed. However, the authors determined this shift to be due to changes in the atomic volume, and hence an increase in the s electron density at the Eu nucleus, and not due to changes in the $4f$ electron occupation.

Johansson and Rosengren predicted that if it was possible to obtain Eu in a metallic, trivalent state, it would be superconducting [40]. Bundy and Dunn saw no evidence of superconductivity in their resistance measurements up to 40 GPa and down to 2.3 K [107]. However, a later study by Debessai *et al.* reported Eu to be superconducting above 80 GPa [111]. The critical temperature, T_c, was found to increase at a rate of 18 mK/GPa, from 1.8 K at 80 GPa to 2.75 K

at 142 GPa, the highest pressure reached in this study. T_c remained much lower than that of the other superconducting lanthanide elements, where T_c lies between 10–20 K at extreme pressure. Debessai *et al.* suggested that the anomalously low critical temperature may be due to the fact that Eu adopts an unfavourable crystal structure, or due to the presence of low-lying magnetic states resulting in Van Vleck paramagnetism, or that Eu is not yet fully trivalent at this pressure.

A valence transition is also expected to have an influence on the structural properties. The promotion of an electron from the $4f$ state to the conduction band would result in a change in the electronic bonding, and so a volume collapse would be expected following a transition to the trivalent state. An abrupt change in the valence would then be expected to be accompanied by volume-collapse, where as a continuous valence change would be expected to be accompanied by changes in the compressibility. On transforming to a trivalent state, it is then expected that Eu will adopt one of the common high-pressure crystal structures observed in the lanthanide elements at high pressure [40].

The description of lanthanide elements is known to be particularly challenging for density functional theory due to the presence of the highly-localised $4f$-electrons [112]. For this reason, the majority of computational studies on Eu have focused on its behaviour at ambient pressure, in particular the magnetic behaviour, and only a small number have focused on its high pressure behaviour. Using the augmented-plane-wave approach within the local-density approximation, Nixon and Papaconstantopoulos [113] determined the pressure-induced bcc–hcp structural transition to occur at 10.6 GPa, which is lower than the experimental value of 12.5 GPa. This study also determined the electron-phonon coupling constant to increase on compression, and predicted the onset of superconductivity between 60–90 GPa, in agreement with experiment. However, these calculations were performed on the hcp, bcc and fcc structures as the high-pressure structure of Eu remained unknown at this time.

The high-pressure behaviour of Eu should naturally be compared with that of the heaviest lanthanide element, ytterbium (Yb), which is also divalent at ambient pressure due to its fully-filled $4f$ electron shell. Yb also exhibits an anomalously large atomic volume (as can be seen in figure 3.5) and compressibility, than would be expected to be in keeping with the trend observed in the trivalent lanthanide elements [13]. Yb exhibits the fcc structure at ambient pressure, transforming to the bcc structure at 4 GPa, and to the hcp structure above 26 GPa. On further compression, Yb transforms to a second fcc phase above 53 GPa and finally to

the $hP3$ phase above 98(5) GPa [114]. Yb has also been reported to undergo a pressure-induced valence transition. L_{III} x-ray absorption measurements [115] determined Yb to be divalent in the bcc phase, with its valence increasing on compression of the hcp phase, before becoming trivalent in the hcp phase. It is also worth noting that the higher-pressure $hP3$ structure is also observed in the trivalent lanthanides Sm and Nd at high pressures.

Eu and Yb are isoelectronic with the group II element barium (Ba) when the $4f$ electrons are not considered. Consequently, the high-pressure behaviour of Eu and Yb is often compared with that of the alkaline earth metals. At low pressures, the high-pressure structural behaviour of Eu and Yb is in keeping with the common trend observed in the group II elements on compression (fcc–bcc–hcp). These transitions are associated with an increase in the d-like character of the conduction band, as the energy of the s band increases on compression due to orthogonality requirements [116]. However, the bulk moduli of Eu and Yb are both still slightly smaller than would be expected to be in keeping with the general trend observed in the group II elements as a function of molar volume [13].

3.4 Conclusions

In this chapter, the previous work on the high-pressure lanthanide elements was discussed. The 'regular' trivalent lanthanide elements undergo a common series of phase transitions under pressure (hcp $\rightarrow$ Sm-type $\rightarrow$ dhcp $\rightarrow$ fcc $\rightarrow$ dfcc $\rightarrow$ low-symmetry), and consequently their high-pressure structural behaviour is often throught to be well known. However, structural assignement often relies on analogy with other members of the series, in particular for the dfcc and low-symmetry phases. However, the diffraction patterns from different distorted-fcc structures are similar, and it has been shown for Pr that great care has to be taken in order to definatively determine the structure of the dfcc phase [11].

The transition to the low-symmetry structures is sometimes accompanied by a volume-collapse transition that is often attributed to the delocalisation of the $4f$ electrons. However, it has been shown that this is not the case in Gd, where the transition is associated with $s \rightarrow d$ charge transfer [95]. The fact that changes in the nature of the electronic behaviour is often inferred from structural changes highlight the importance of precise structural determination.

Eu is divalent at ambient pressure, and as such its behaviour is strikingly different from that of the trivalent lanthanide elements. The trivalent electronic configuration was predicted to be stable at high pressures, and a number of transition pressures were determined. Although initial experimental studies reported the valence of Eu to increase on compression [108, 108], a more recent study reported Eu to remain divalent up to at least 87 GPa [110].

Chapter 4

The Structure of Eu-III

4.1 Introduction

The experimental results of the high-pressure x-ray diffraction experiments on Eu metal are split into 3 chapters. This chapter starts with a discussion of the previous x-ray diffraction studies on Eu at high pressure. The experimental details for all three chapters (4, 5 and 6) are then described. Finally, the results from the initial Eu studies are presented.

Despite the observation of interesting behaviour of Eu at high pressure, and the conflicting nature of the reports, there have been remarkably few studies into its high-pressure structural behaviour. Eu does not exhibit the common structural sequence observed in the trivalent lanthanide elements at high pressure, and instead its behaviour is significantly different. Previous x-ray diffraction studies found that Eu exhibits the bcc structure at ambient pressure, transforming to the hcp structure above 12.5 GPa [13–15]. In the x-ray diffraction study by Takemura and Syassen [13], they reported the appearance of a number of weak reflections in their diffraction patterns above 18 GPa in addition to those from the hcp phase [13]. On further compression, the relative intensity of the hcp and non-hcp reflections was observed to remain constant up to 30 GPa, the highest pressure reached in this study. On subsequent pressure decrease, the strongest of the new reflections was observed in all the hcp patterns until the hcp–bcc transition at 12.5 GPa, although no evidence of any extra reflections was seen in the bcc patterns. They therefore concluded that the non-hcp reflections were not from

a separate phase, and that their appearance was not due to a pressure-induced chemical reaction. Instead, the appearance of the additional reflections was taken as evidence of a transition to a new phase, Eu-III, above 18 GPa. The integrated diffraction profile of Eu at 27.1 GPa, taken from this study [13], is shown in figure 4.1(a), where the two most intense non-hcp reflections are indicated. The structure of Eu-III was not determined, although it was thought to be closely related to hcp. The authors also noted that it is possible to describe all the reflections in the pattern with a $1 \times 1 \times 18$ supercell of the hcp structure, although this structure predicts a large number of reflections that were not observed.

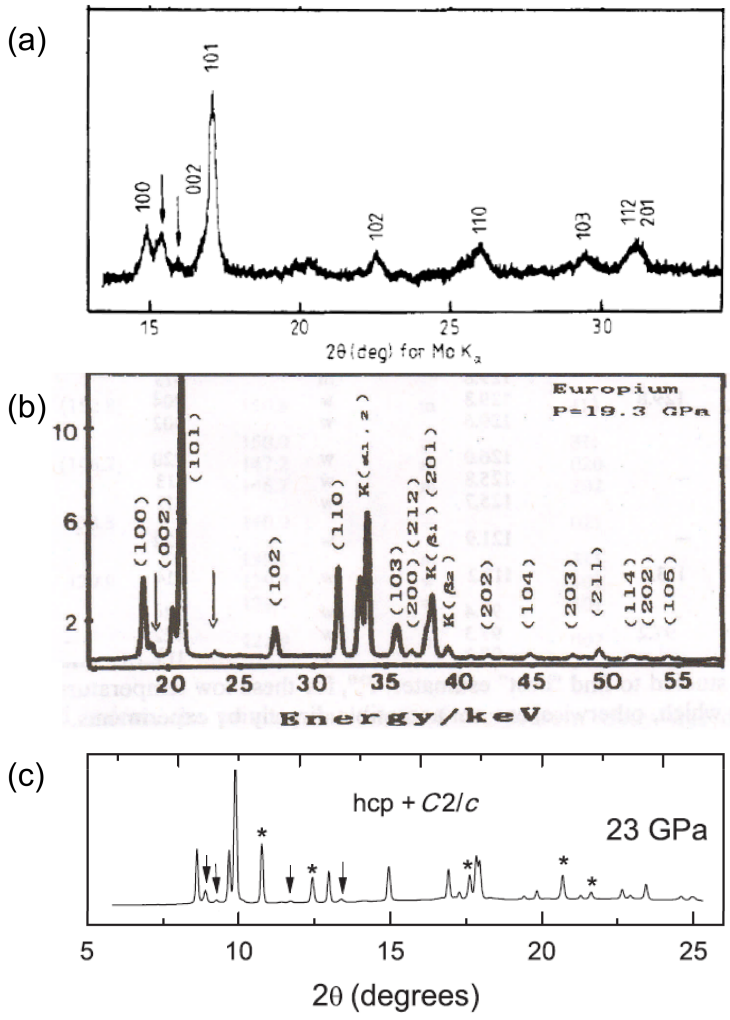

Figure 4.1: Integrated diffraction profiles of Eu-III at (a) 27.1 GPa, (b) 19.3 GPa and (c) 23 GPa, as reported in previous diffraction studies. The figures were adapted from references [13], [14] and [15], respectively. The arrows indicate the weak reflections that are observed in addition to those from hcp above ∼17 GPa.

Subsequent diffraction studies also reported the appearance of the weak reflections

on compression. Grosshans and Holzapfel [117] did not observe their appearance until a much higher pressure of 32 GPa. This behaviour was identified as the transition to Eu-III, although no diffraction profiles were shown. Krüger *et al.* also reported the weak reflections to appear above 17 GPa, with further changes in the diffraction patterns observed above 32 GPa [14]. The integrated diffraction profile of Eu at 19.3 GPa, taken from this study, is shown in figure 4.1(b). The two non-hcp reflections which are highlighted in this pattern are in similar positions to those observed by Takemura and Syassen. Grosshans and Holzapfel [118], who determined the equation of state of Eu up to ∼42 GPa, also reported the observation of the Eu-III phase above ∼17 GPa, although no diffraction patterns were shown in the study.

Although this behaviour was initially reported in 1985, no structural solutions were proposed for Eu above 18 GPa until 2012. In an x-ray diffraction study, supported by *ab initio* structure prediction calculations, Bi *et al.* [15] reported a series of high-pressure phase transitions and structural assignments of Eu up to 92 GPa. They also observed the appearance of the additional reflections above 18 GPa, as highlighted in the diffraction pattern at 23 GPa shown in figure 4.1(c), taken from reference [15]. Two regions of phase mixture were proposed to exist from 18 to 66 GPa: a mixture of hcp and a C-centred monoclinic structure with the space group $C2/c$ from 18 to 41 GPa, and a mixture of the same monoclinic structure and an orthorhombic structure with the space group $Pnma$ from 41 to 66 GPa. On further compression, the orthorhombic structure was reported to be stable up to 92 GPa, the maximum pressure reached in this study.

However, the structural assignments in the 18–92 GPa region are highly questionable. Although the quality of the diffraction data shown in this paper is high, insufficient reasoning is given to justify their structural models. In particular, no fits are shown of the hcp and $C2/c$ structures to the data in the 18–41 GPa region, despite the fact that refinements are shown for all other proposed structural solutions. It is therefore not possible to comment on how well this structure describes their data in this pressure region. The lattice parameters of the $C2/c$ structure are also not reported for this pressure range. However, personal correspondence with the author found that the lattice parameters were determined to be $a = 3.17$ Å, $b = 5.29$ Å, $c = 9.63$ Å and $\beta = 104.7°$ at 37 GPa. The atomic positions in the $C2/c$ structure were not determined, and the number of atoms in the unit cell was not given. However, a comparison of the volume per unit cell of the $C2/c$ and $Pnma$ structures at 55 GPa indicates that the $C2/c$

unit cell should contain 8 atoms. Although a refinement based on the $C2/c$ and $Pnma$ structures is shown to the 55 GPa pattern, the fit to the $C2/c$ structure is performed using a Le Bail refinement, whereas the fit to the $Pnma$ structure based on the 75 GPa is performed using a Rietveld refinement. From the fit to the 75 GPa profile it can be seen that, although this structure can account for the majority of the features in the pattern, there are a number of weak features that it cannot describe.

Bi *et al.* determined a different structural sequence as a result of their first-principles structure searches: bcc $\rightarrow$ hcp $\rightarrow$ $C2/c$ $\rightarrow$ $Fdd2$ $\rightarrow$ Pnma $\rightarrow$ $C2/c$ $\rightarrow$ hcp, with transition pressures of 10, 16, 22, 34, 46 and 80 GPa, respectively. Searches were performed using both a random searching algorithm, an unpublished genetic algorithm and using the evolutionary algorithm code USPEX, searching for structures with up to 8, 30 and 4 atoms per unit cell, respectively. The $C2/c$, $Fdd2$ and $Pnma$ structures are close in enthalpy in the 16–45 GPa region, and the authors comment that it is possible that the $C2/c$ structure may not be observed experimentally above 46 GPa due to enthalpy barriers of formation. The structural details of the $Fdd2$ structure are not given, although the authors comment that the unit cell is large, with 40 atoms per unit cell, and the corresponding diffraction pattern contains high-intensity low-angle reflections that are not observed in the diffraction patterns.

Despite the observation of unusual behaviour of Eu at high pressure, there has been only one study of its high-pressure, high-temperature behaviour, in which the melt curve was determined, although only to 7 GPa [119]. Large areas of the phase diagram of this unusual element therefore remain completely unknown. In the small pressure range in which the melt curve is known, a maximum was observed in the bcc phase at about 3.5 GPa and 722 K.

In order to investigate the high pressure structural behaviour of Eu, angle-dispersive x-ray powder diffraction experiments have been performed up to ~ 70 GPa. The results of these studies can be separated into three distinct sections, the experiments and results of which will be discussed separately.

Firstly, we report that the behaviour initially attributed to a phase transition to Eu-III is not due to any changes in Eu itself, but rather due to pressure-induced changes in a contaminant phase. Additionally, this contaminant phase undergoes a structural transition, which is accompanied by a change in stoichiometry. The observation of this transition was essential in the process of identifying the

presence of the contaminant. Details of the this work have been published in J. Phys. Conf. Ser. [5] and High Press. Res. [3].

The presence of these contaminant phases greatly complicated initial x-ray diffraction studies. However, loading non-contaminated samples has enabled us to proposed an alternative description of the structural behaviour of Eu above 18 GPa. In the second section, we report a transition to an incommensurately-modulated crystal structure, Eu-IV, above 31.5 GPa. This is the first observation of an incommensurate structure in the lanthanide series. Details of this work have been published in Phys. Rev. Lett. [4].

Finally, we report a structural transition to a second incommensurately-modulated crystal structure, Eu-V, above 38 GPa. Eu-V has the same superspace group as Eu-IV, but the wavevector has a different direction and magnitude. This is the first observation of an incommensurately-modulated to incommensurately-modulated transition in the elements at high pressure. Details of this work have been published in Phys. Rev. B [2].

4.2 Experimental Details

This section describes the experimental details of the work described in this chapter, and also the experimental details of the work described in subsequent chapters 5 and 6.

Eu samples were loaded into diamond-anvil cells equipped with W or Re gaskets in a dry argon atmosphere ($<$ 1 ppm O_2 and $<$ 1 ppm H_2O). A total of ten contaminated samples were considered, seven of which were loaded in a mineral oil pressure-transmitting medium (PTM) (samples 1–7), two of which were loaded in a He PTM samples (8–9), and the remaining sample was loaded without a PTM (sample 10). With the exception of the sample loaded without a PTM, a small ruby sphere was included as a pressure calibrant. The pressure was subsequently determined using the ruby fluorescence method described in section 2.2.2 of chapter 2. The ruby spectrum was recorded before and after each exposure to account for the possibility of a pressure drift. No pressure marker was included in the sample loaded without a PTM, and the pressure was determined from the d-spacing of at least 1 sample reflection using a calibration determined from samples 8 and 9.

Ambient-temperature diffraction data were collected on two non-contaminated samples, which will subsequently be referred to as samples 11 and 12. In order to minimise any possible sources of contamination, the non-contaminated samples were loaded quickly in a well-maintained glove box (< 0.1 ppm O_2, < 0.1 ppm H_2O) without a PTM and without a pressure calibrant. The pressure was determined using the calibration determined from samples 8 and 9.

Two additional Eu samples were loaded in cells equipped with W gaskets for the high-temperature experiments. In one of these samples, a small grain of Ta powder was included as a pressure marker (sample 13), and in the other sample a piece of 1 μm thick Ta foil was placed between the sample and one of the diamond anvils (sample 14). Then pressure was determined from the equation of state of Ta, as described in section 2.2.2. Both of these samples were loaded without a PTM. The cells containing these samples were heated using the purpose-built Cu heating block described in section 2.2.4. The temperature was measured using a K-type thermocouple placed on the back of one of the diamonds, and the uncertainty in temperature was estimated to be no more than 10 K. A summary of all of the Eu samples used in the work described in this chapter, as well as chapters 5 and 6, is given in table 4.1.

Sample	**Pressure Calibrant**	**PTM**
1–7	Ruby	Mineral oil
8–9	Ruby	Helium
10–12	No pressure marker	No PTM
13	Ta powder	No PTM
14	1 μm thick Ta foil	No PTM

Table 4.1: A description of the Eu samples used in the work described in chapters 4, 5 and 6.

Angle-dispersive powder x-ray diffraction data were collected at the 9.5HPT beamline at the SRS, on station ID09a at the ESRF, on beamline I15 at DLS and on beamline P02.2 at PETRA-III, using monochromatic x-ray beams collimated to 30μm (9.5HPT), 10 μm (ID09a) and 30 μm (I15), and focused to 2×2 μm^2 (P02.2). Data were collected using a mar555 area detector (ID09a), a mar345 image plate detector (I15) and a Perkin Elmer area detector (P02.2). Preliminary experiments on contaminated samples were performed on the 9.5HPT beamline before the start of my PhD. However, the majority of the experiments, including

all experiments on non-contaminated samples, and all of the data analysis, were performed over the course of my PhD.

The 2D diffraction images were integrated using the FIT2D [61, 62] software to produced 1D diffraction profiles. Indexing was performed using the DICVOL [63] and SUPERCELL [64] indexing programs, and Le Bail and Rietveld refinements were performed with the Jana software [69].

4.3 Experimental Results

4.3.1 Identification of the Cubic Contaminant

In all of our samples, the bcc–hcp transition was observed at 12.5 GPa in agreement with previous studies [13–15]. In most of our samples, the appearance of the additional weak reflections was observed above 17 GPa. However, in a number of samples the reflections were observed at lower pressures, although always after the transition to the hcp phase. When the pressure was increased above 31.5 GPa, significant changes in the diffraction patterns were observed, indicating a transition to a new phase, Eu-IV. This will be discussed in detail in chapter 5, and the current chapter will focus on the behaviour of Eu below this pressure.

In agreement with Takemura and Syassen [13], the relative intensity of the hcp and non-hcp reflections was observed to remain constant in the 18-31.5 GPa region, supporting their conclusion that the new reflections are not due to a sluggish transition to a new phase. An attempt to index our data using the $1 \times 1 \times 18$ hcp supercell discussed in this study found that, although this structure can account for the most intense of the non-hcp reflections, it cannot account for all of the weak reflections that appear above $\sim$18 GPa. It also generates a large number of reflections (>60) that are not observed. Attempts to index the entire set of reflections as a single phase using the DICVOL software were also unsuccessful. However, the relative intensity of the hcp and extra peaks was observed to vary between different samples. This suggested that the non-hcp reflections are from a separate phase.

The pressure of sample 1 was increased to 38 GPa, and the sample was annealed for 3 hours at 473 K. On subsequent pressure decrease, although we observed

the reappearance of the hcp reflections below 31.5 GPa, as expected, we did not observe the reappearance of the non-hcp reflections. Instead, a new set of reflections were observed in the diffraction profiles. This is illustrated in figure 4.2, which shows the integrated diffraction profiles of Eu at 19.2 GPa, and after pressure cycling and annealing at 30.2 GPa. The arrows indicate the most intense of the non-hcp reflections in each of the patterns, and it is clear that a different set of reflections is present in each case. In particular, fewer non-hcp reflections are present in the 30.2 GPa pattern. This suggested the presence of two phases in the sample, one of which is hcp, and that the non-hcp phase had undergone a phase transition.

The DICVOL program was used to index the non-hcp reflections as a separate phase. A reasonably good fit was obtained using a cubic unit cell with $a_P = 4.713$ Å, where P refers to the fact that the cell is primitive. However, although this unit cell could account for most of the non-hcp reflections, it cannot account for the peaks at 19.6° and 24.3°. An almost identical set of d-spacings is generated from an I-centred cubic structure with $a_I = \sqrt{2}a_P$. The diffraction profiles of these two structures can only be distinguished by the observation of the (321), (251) and (361) I-centred reflections (plus higher-order reflections) that cannot be described by the primitive unit cell. A Le Bail refinement based on the I-centred cubic structure to the diffraction pattern at 30.2 GPa found that this structure can account for all the non-hcp reflections observed in the pattern, including the peaks at 19.6° and 24.3°, which are identified as the (251) and (361) reflections, respectively. The (321) reflection has the same d-spacing as the (102)-hcp reflection and so cannot be identified. We therefore determined this phase to have an I-centred cubic unit cell with $a_I = 6.665$ Å.

In order to determine the space group, it is necessary to consider the set of allowed reflections for I-centred cubic space groups, which are given in Table 4.2. The (002) and (006) refections are not observed, satisfying the condition that $l = 4n$ for $(00l)$ reflections, which determines the space group to be either $I4_132$, $I\bar{4}3d$, or $Ia\bar{3}d$. Additionally, the (222), (330), (334), (442) and (226) reflections are absent, which satisfies the $2h + l = 4n$ condition for (hhl) reflections, and determines the space group to be either $I\bar{4}3d$ or $Ia\bar{3}d$. Finally, the $Ia\bar{3}d$ space group can be ruled out due to the observation of the (103) and (105) reflections, which do not satisfy the $k, l = 2n$ condition for $(0kl)$ reflections, but do satisfy the $k + l = 2n$ condition. The space group is therefore uniquely identified as $I\bar{4}3d$ (no. 220).

For the $I\bar{4}3d$ structure to coexist with hcp, the density of the two structures is

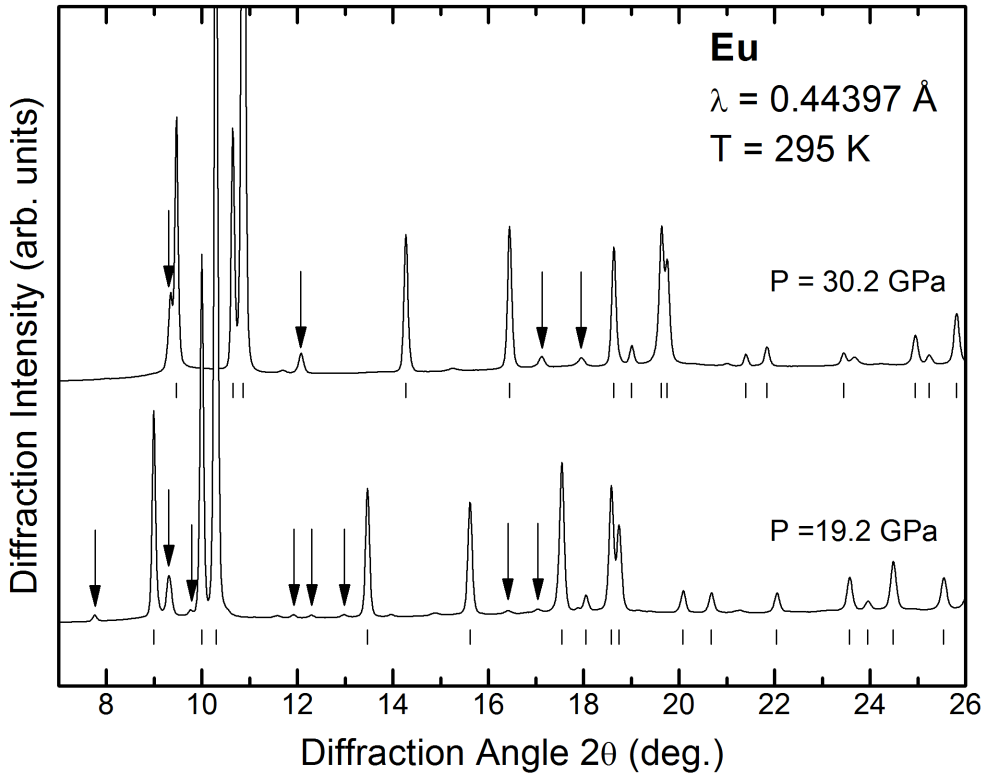

Figure 4.2: Integrated diffraction profiles of Eu at 19.2 GPa (lower) and 30.2 GPa (upper). The pressure of sample was increased to 38 GPa and the sample was annealed for 3 hours at 473 K between the collection of the 19.2 GPa and 30.2 GPa profiles. The tick marks below the profiles show the position of the hcp reflections. The arrows show the most intense of the non-hcp reflections that are present in each pattern.

Reflection conditions				**Space groups**
hkl	$0kl$	hhl	$00l$	
$h+k+l$	$k+l$	l	l	$I23$, $I2_13$, $Im\bar{3}$
				$I432$, $I\bar{4}3m$, $Im\bar{3}m$
$h+k+l$	$k+l$	l	$l=4n$	$I4_132$
$h+k+l$	$k+l$	$2h+l=4n;\ l$	$l=4n$	$I\bar{4}3d$
$h+k+l$	k,l	l	l	$Ia\bar{3}$
$h+k+l$	k,l	$2h+l=4n;\ l$	$l=4n$	$Ia\bar{3}d$

Table 4.2: Systematic absenses corresponding to the set of I-centred cubic space groups, reproduced from reference [19].

expected to be the same at the same pressure. This determines the number of atoms in the $I\bar{4}3d$ structure to be 12, the lowest site multiplicity in this space group, as higher multiplicities corresponded to a considerably larger density than that of hcp Eu. An excellent fit was obtained with the Eu atoms in the 12a ($\frac{3}{8}$,

0, $\frac{1}{4}$) Wyckoff positions, and an equally good fit was obtained with the atoms in the 12b ($\frac{7}{8}$, 0, $\frac{1}{4}$) positions, where the 12a and 12b positions are related by an inversion centre. This structure will subsequently by referred to by its Pearson symbol, $cI12$, where 12 is the number of Eu atoms per unit cell.

A two-phase hcp/$cI12$ Rietveld refinement to the diffraction pattern of Eu at 31.2 GPa is shown in figure 4.3. The inset highlights the (251) $cI12$ reflection, which determines the structure to be I-centred, and also the (105) $cI12$ reflections, which rules out the $Ia\overline{3}$ and $Ia\overline{3}d$ space groups. The refined lattice parameters of the hcp phase at 31.2 GPa are a = 3.0978(2) Å and c = 4.7744(4) Å, corresponding to a volume per atom of 19.840(3) Å^3. The refined lattice parameter of the $cI12$ phase is a = 6.667(2) Å, corresponding to a volume per Eu atom of 24.69(2) Å^3. The $cI12$ structure is therefore *less* dense than hcp at the same pressure, with a volume per Eu atom that is 4.85(2) Å^3 larger than that of hcp-Eu. As it is extremely unlikely that the application of pressure would stabilise a structure that is less dense that the lower-pressure phase, this suggested that the cubic phase does not consist of pure Eu, but rather it is a contaminant that was present in the sample. The Rietveld refinement using Eu atoms alone is excellent, suggesting that the additional atoms must be very weakly scattering in comparison with Eu, and the small difference in the volume per atom suggests that the impurity atom(s) must be very small.

4.3.2 Identification of the Rhombohedral Contaminant

Having identified the transformed patterns to consist of hcp plus the $cI12$ contaminant phase, this suggested that the original patterns must also consist of hcp plus a different contaminant phase. An attempt was made to index the non-hcp reflections that appear above ∼18 GPa as a separate phase. However, in many of our samples the intensity of the additional reflections was very low, and in many cases only 4–6 non-hcp reflections were observed. Initial attempts to index this phases were therefore unsuccessful.

Sample 2 was left for one month at 25.5 GPa in order to investigate changes over time. Interestingly, the intensity of the non-hcp reflections was observed to increase significantly in comparison with the patterns collected previously. This is illustrated in figure 4.4, which shows the integrated diffraction profiles of Eu at 25.5 GPa, and one month later at 26.1 GPa. Consequently, this enabled a larger number of weak reflections to be identified than was possible in the initial

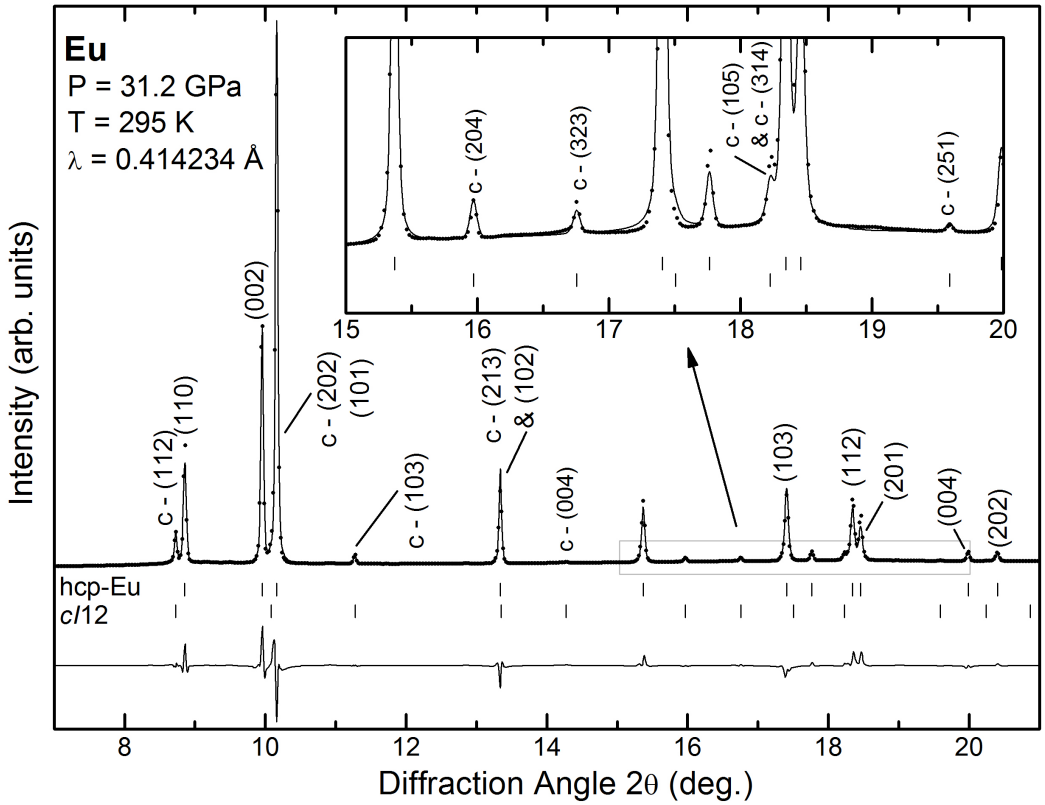

Figure 4.3: A two-phase Rietveld refinement of hcp-Eu plus the $cI12$ contaminant to the diffraction pattern of Eu at 31.2 GPa. The points show the experimental data, and the solid line shows the fit. The tick marks show the position of the hcp reflections (upper) and the $cI12$ contaminant (lower), and the residuals are shown below the tick marks. The inset illustrates the excellent fit to the weak $cI12$ reflections. The corresponding Miller indices are given above the profile, where 'c' indicates reflections from the $cI12$ contaminant phase. In particular, the observation of the (251)-$cI12$ reflection determines the structure to be I-centred, and the observation of the (103) and (105)-$cI12$ reflections rule out the $Ia\bar{3}$ and $Ia\bar{3}d$ space groups.

data. The fact that two distinct phases were present could also be seen in the two-dimensional diffraction image. The Debye Scherrer rings corresponding to the non-hcp reflections had become spotty, whereas those from the hcp phase remained smooth. This is illustrated in figure 4.5, which shows a portion of the two-dimensional diffraction image and corresponding integrated diffraction profile of Eu at 26.5 GPa.

Bi *et al.* indexed their diffraction patterns in the 18–41 GPa region as a mixed phase consisting of hcp plus a monoclinic structure with space group $C2/c$. However, the $C2/c$ structure could not describe the non-hcp reflections in our diffraction patterns, and another solution was required. The DICVOL software was used to search for solutions in the 10–200 Å^3 volume range, where a total of 8 reflections were used in the search. A good fit was obtained in the $P2/m$

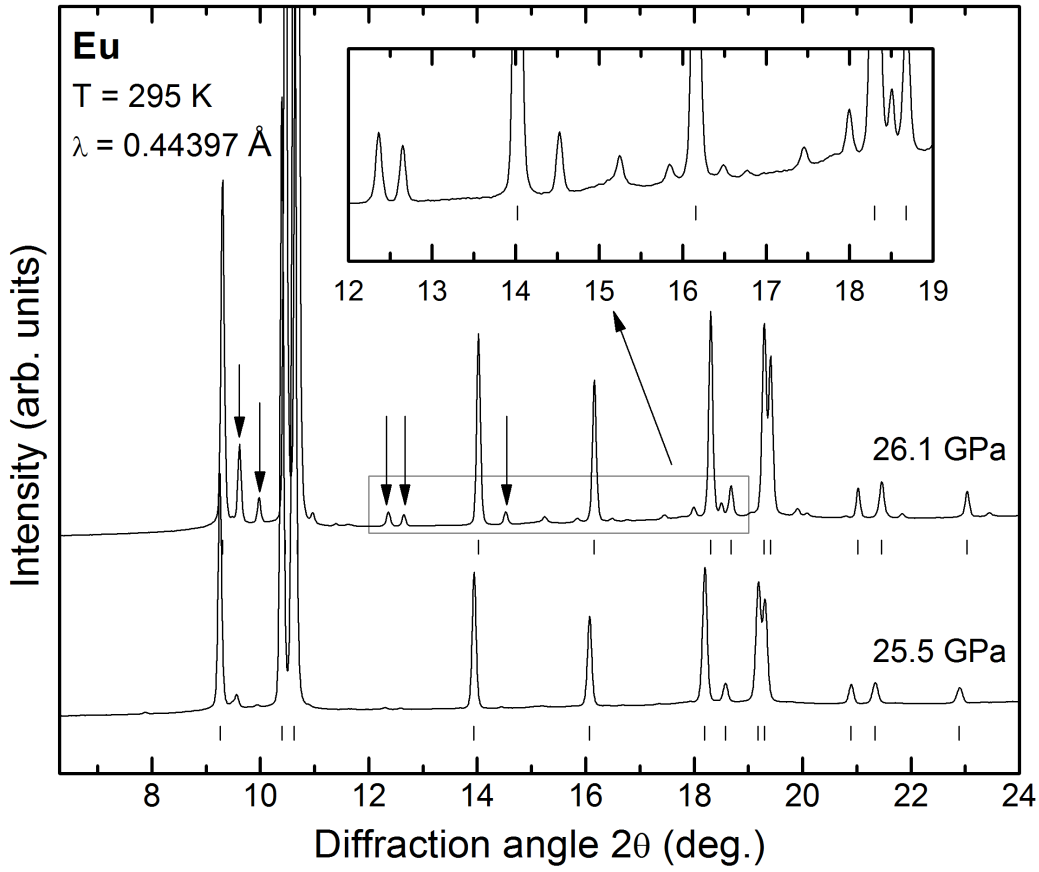

Figure 4.4: Integrated diffraction profiles of Eu at 25.5 GPa (lower) and at 26.1 GPa (upper), where the 26.1 GPa pattern was collected after the cell was left for one month after the collection of the 25.5 GPa pattern. The tick marks below the patterns show the peaks from the hcp phase. The intensity of the non-hcp reflections increased significantly between the two data collections. The arrows above the top profile show the non-hcp peaks that were observed by Takemura and Syassen [13], and the inset illustrates the large number of additional peaks that can be identified in our data pattern.

space group with refined lattice parameters $a = 4.4748(8)$ Å, $b = 4.6430(4)$ Å, $c = 3.2289(4)$ Å and $\beta = 92.95(1)°$. However, although this structure can account for all of the non-hcp reflections observed in the pattern, it also predicts a large number of reflections that are not observed, and the observed reflections do not satisfy the allowed reflection conditions for any of the higher-symmetry monoclinic space groups.

A further search was performed in the 200–500 Å^3 volume range using the same 8 reflections. This generated a hexagonal unit cell with $a = 9.291$ Å and $c = 5.381$ Å, the volume of which is 6 times larger than that of the initial monoclinic solution. Although a good fit is obtained with most hexagonal space groups, all of these predict an even larger number of unobserved reflections than the smaller

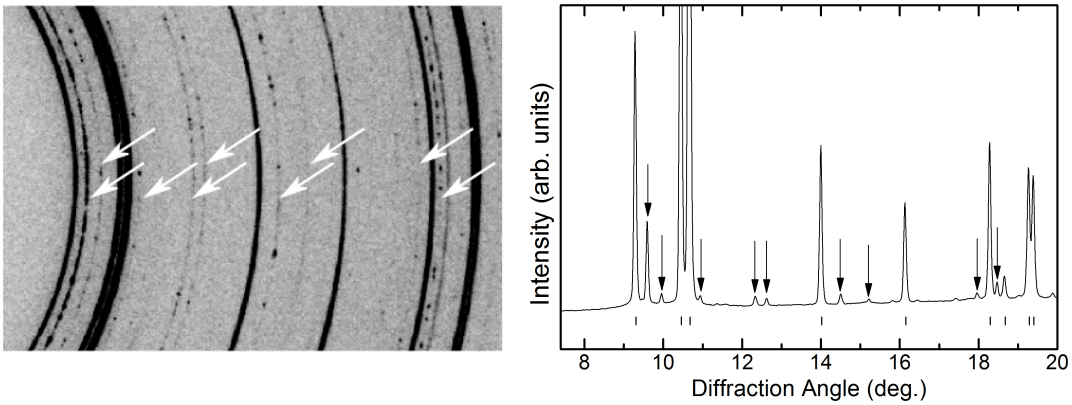

(a) (b)

Figure 4.5: (a) The 2D diffraction image of Eu at 26.5 GPa and (b) the corresponding integrated diffraction profile. The arrows in (a) show the spotty Debye Scherrer rings from the non-hcp reflections and the arrows above the profile in (b) show the same peaks in the integrated profile.

monoclinic cell. However, all of the observed reflections satisfy the condition $h - k + l = 2n$, determining the lattice to be rhombohedral. Additionally, the absence of the (003), (2-21), (5-51) and (8-81) reflections fulfills the condition $l = 2n$ for $(hh\overline{2h}l)$ reflections, determining the space group to be either $R3c$ or $R\overline{3}c$. A Le Bail refinement to this structure in these space groups found that they can account for all of the reflections observed in the pattern, and that they only predict a small number (8) of reflections that are not observed.

Density requirements restricts the number of Eu atoms in the rhombohedral structure to 18 per hexagonal unit cell (6 in the rhombohedral setting). A good fit was obtained in the $R\overline{3}c$ space group with the atoms in the 18e (x, 0, 0) Wyckoff positions. An equivalent structure was obtained in the $R\overline{3}c$ space group with atoms in the 18b (x, y, z) Wyckoff positions. We therefore determined the space group to be $R\overline{3}c$ (no. 167). This structure will subsequently be referred to by its Pearson symbol, $hR6$, where 6 refers to the number of Eu atoms in the rhombohedral setting.

A two-phase hcp/$hR6$ Rietveld refinement of structure to the diffraction profile of Eu at 26.1 GPa is shown in figure 4.6. The refined structural parameters are $a = 9.293(4)$ Å and $c = 5.381(4)$ Å with atoms in the (0.800(4), 0, 0) positions. The inset illustrates that the $hR6$ structure can account for the large number of non-hcp reflections that are observed in the pattern. The volume per Eu atom of hcp at 26.1 GPa is 21.05(1) Å^3, while the $R\overline{3}c$ structure at the same pressure is less dense, with a volume/atom of 22.36(1) Å^3.

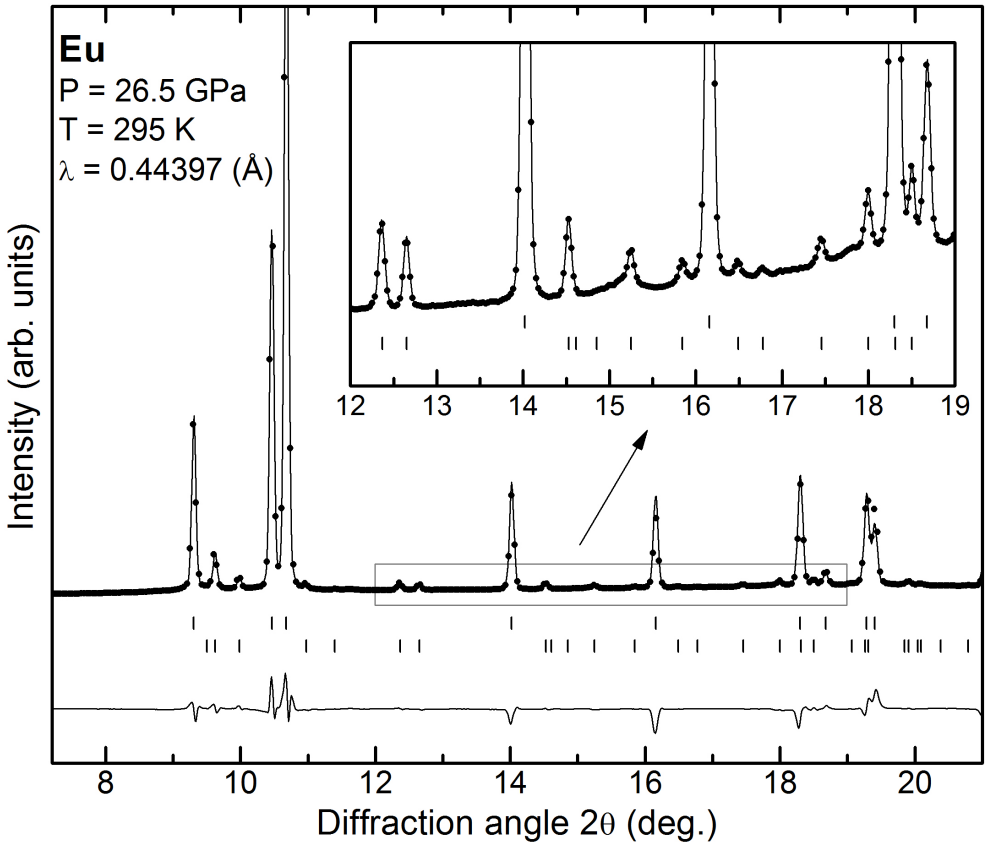

Figure 4.6: A two-phase Rietveld refinement of hcp plus the $hR6$ structure to the diffraction profile of Eu at 26.1 GPa. The points show the experimental data and the solid line shows the fit. The tick marks below the profile show the calculated peak positions, and the residuals are shown below the tick marks. The inset illustrates that the $hR6$ structure can account for the large number of weak reflections that are observed in the pattern.

4.3.3 Non-Contaminated Samples

In order to confirm that the $hR6$ and $cI12$ phases do not consist of purely Eu, but are in fact impurities phases, we attempted to load a sample that does not show any traces of contamination in the diffraction patterns. As it was not immediately clear at what point in the loading process the contamination had occurred, efforts were made to minimise any possible sources of contamination. All samples were loaded in a high-quality glovebox (< 0.1 ppm O_2 and < 0.1 ppm H_2O), and when the samples were cut from the bulk sample, care was taken to completely cut away all surface layers so that the material looked shiny and metallic. Newly cut surfaces of the Eu samples were observed to discolour when left in the glovebox for a short amount of time, and so samples were loaded as quick as possible to minimise the contact between the sample surface and the atmosphere. In order

to minimise any further sources of contamination, samples was loaded without a pressure marker and without a PTM.

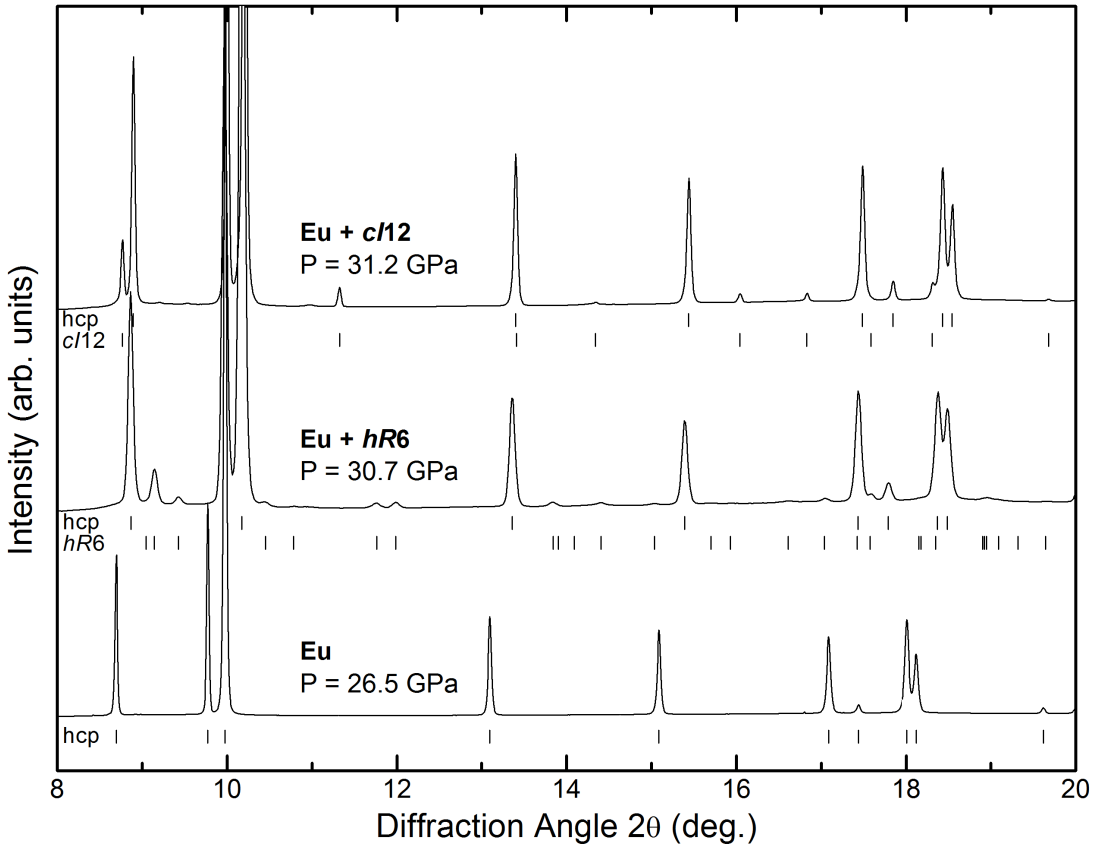

Figure 4.7: Integrated diffraction patterns of a non-contaminated Eu sample at 26.5 GPa (lower), Eu plus the $hR6$ contaminant at 30.7 GPa (middle) and Eu plus the $cI12$ contaminant at 31.2 GPa (upper). The tick marks below the 26.5 GPa pattern show the position of the hcp reflections. The tick marks below the 30.7 GPa pattern show the position of the hcp reflections (upper) and the $hR6$ reflections (lower). The tick marks below the 31.2 GPa pattern show the positions of the hcp reflections (upper) and the $cI12$ reflections (lower).

In the majority of samples, the additional reflections were still observed above 17 GPa. However, in sample 11, we did not observe the appearance of any additional reflections, and instead Eu remained in the hcp phase up to 31.5 GPa. A comparison of the integrated diffraction patterns collected from this 'clean' Eu sample at 26.5 GPa, Eu plus the $hR6$ contaminant at 30.7 GPa and Eu plus the $cI12$ contaminant is shown in figure 4.7. This confirms that the observation of the additional non-hcp reflections above 17 GPa was not due to changes in Eu, but rather due to pressure-induced changes in a contaminant phase that was present in the sample. It should then be noted that both the 'clean' and contaminated samples were taken from the same bulk Eu sample, and so the contamination is more likely to have occurred during the cell loading procedure than to be an

intrinsic problem with sample purity.

4.4 Discussion

Having solved the structures of the $cI12$ and $hR6$ contaminant phases, it was then possible to go back and fit data collected in earlier studies. A plot of the volume per Eu atom against pressure for Eu and the $hR6$ and $cI12$ contaminant phases is shown in figure 4.8. In the majority of patterns only a small number (4–6) of $hR6$ reflections were observed, and it was not possible to perform a Rietveld refinement of the $hR6$ structure to the data. The lattice parameters were therefore determined from the d-spacings of at least 4 reflections. At pressures greater than 31.5 GPa, Eu is in the higher-pressure Eu-IV phase, which is discussed in detail in chapter 5. The pressure at which the $hR6$–$cI12$ transition occurs will also be discussed in this chapter, where the mixed-phase Eu-IV/$hR6$ and Eu-IV/$cI12$ diffraction patterns can be described in full.

It is clear from figure 4.8 that the volume per Eu atom of $cI12$ is significantly *larger* than that of $hR6$: the $cI12$ phase is 19.7% less dense than hcp Eu at 31.2 GPa, whereas the $hR6$ phase is only 6.7% less dense at 30.7 GPa. This suggests that the stoichiometry of the two contaminant phases is not the same. The transition from $hR6$ to $cI12$ is therefore both a structural and stoichiometric transition, where the ratio of non-Eu atoms to Eu atoms increases.

The pressure dependence of the lattice parameters of the $hR6$ and $cI12$ contaminant phases are shown in figure 4.9. The a and c lattice parameters of the $hR6$ contaminant decrease smoothly as a function of pressure, with a decreasing from 10.086(5) Å at 13.6 GPa to 9.111(4) Å at 31.6 GPa, and c decreasing from 5.624(4) Å at 13.6 GPa to 5.320(3) Å at 31.6 GPa. The c/a axial ratio shows an overall increase with increasing pressure, although there is a slight deviation from this trend at low pressures. The use of a PTM does not appear to have an influence on the pressure dependence of any of the structural parameters. The a lattice parameter of the $cI12$ contaminant decreases smoothly with pressure, from 6.6963(1) Å at 29.4 GPa to 6.5853(15) Å at 37.49 GPa. All data on this phases were collected on samples loaded with a mineral oil PTM, and so it is not possible to determine if the use of a PTM has any influence.

Takemura and Syassen [13] noted that they did not observe any additional

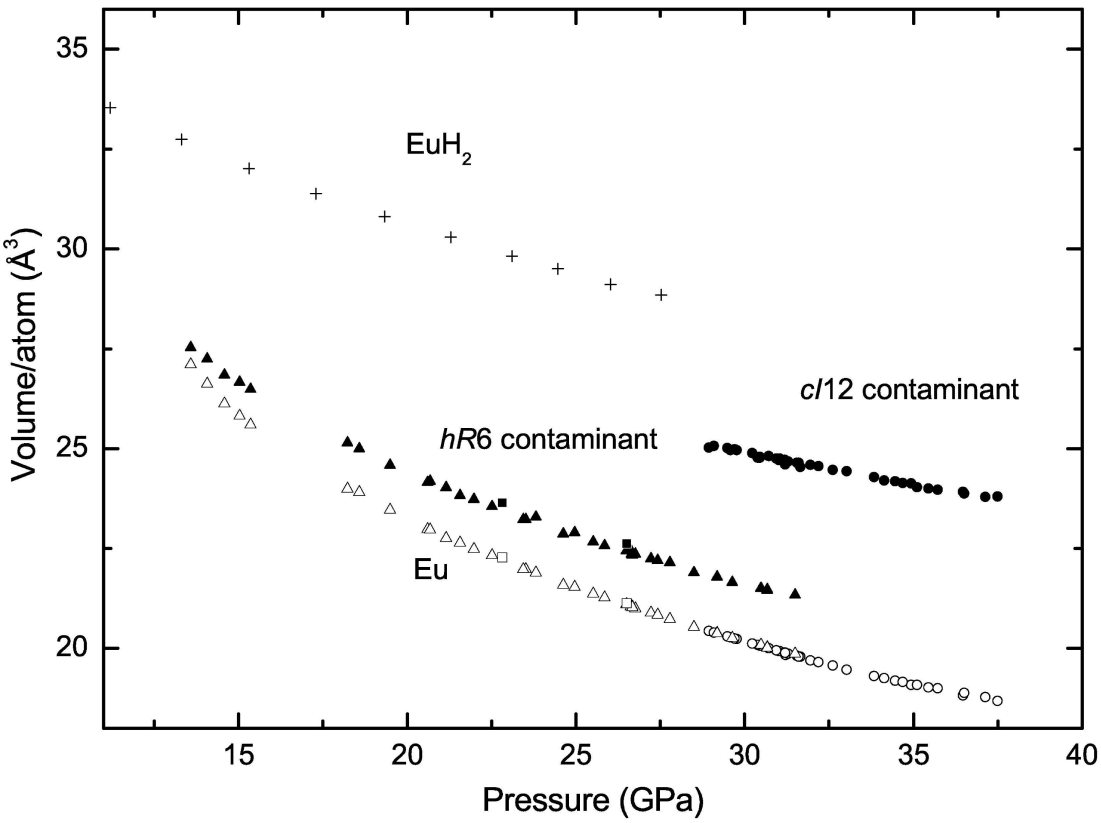

Figure 4.8: Volume per Eu atom against pressure for Eu and the $hR6$ and $cI12$ contaminant phases. The Eu volumes were obtained by Rietveld fits to the diffraction patterns, and the volumes for the contaminant phases were determined from the d-spacings of 4 to 11 reflections. The solid triangles show data for the $hR6$ phase measured on samples loaded with a pressure-transmitting medium, and the open triangles show data for the hcp phase at the same pressures, as obtained from mixed-phase profiles. The solid circles show data for the $cI12$ phase measured on samples loaded with a pressure-transmitting medium, and the open circles show data for the hcp phase at the same pressures, as obtained from mixed-phase profiles. The solid squares show data for the $hR6$ phase measured on the sample loaded without a PTM, and the open squares show data for the hcp phase at the same pressures, as obtained from mixed-phase profiles. The estimated uncertainties in the atomic volumes as obtained from the least-squares fits are smaller than the equivalent of the symbol size. The crosses show data for EuH_2, as taken from reference [16]

reflections in their bcc patterns collected on pressure decrease, and this was taken as evidence that a pressure-induced chemical reaction had not taken place. However, we did observe additional reflections on decompression to the bcc phase, although they could not be indexed based on the $hR6$ structure, introducing the possibility of a transition to yet another contaminant phase.

The fact that the contaminant peaks are not observed below a certain pressure introduces the possibility of a pressure-induced reaction between Eu and one of

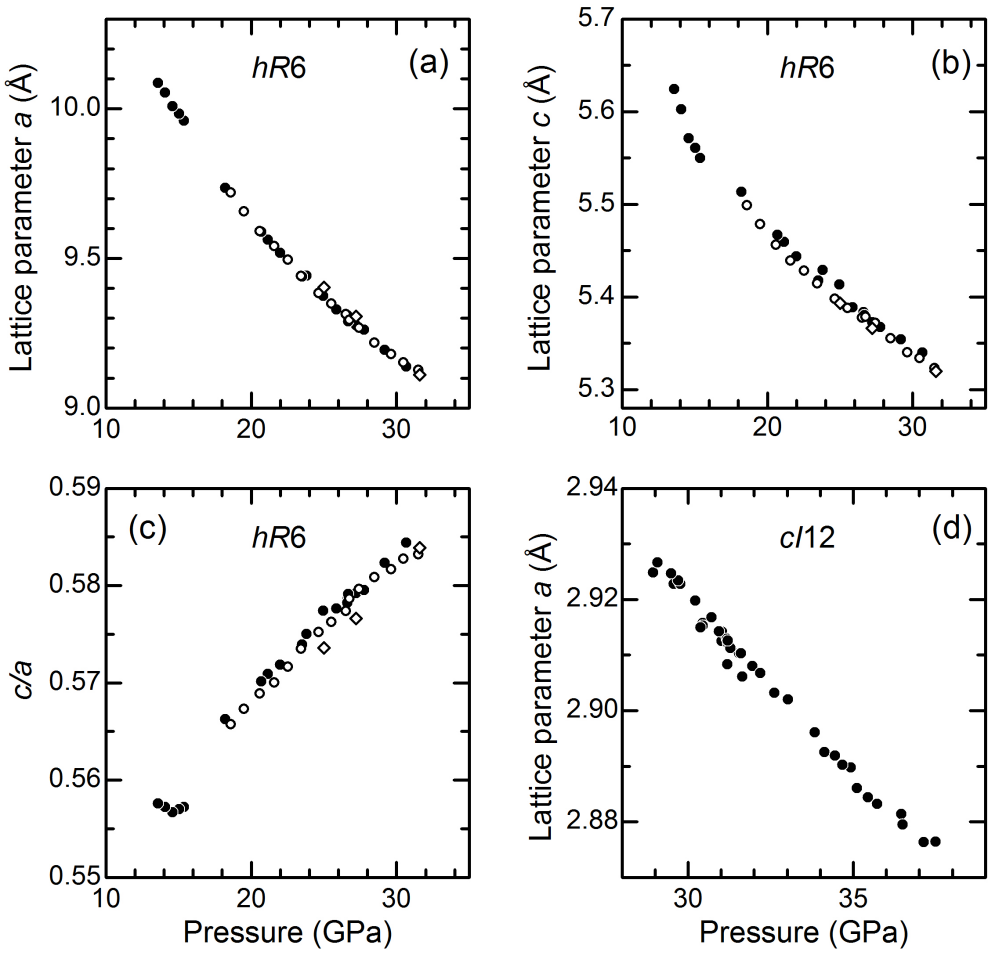

Figure 4.9: Pressure dependence of (a) lattice parameter a, (b) lattice parameter c and (c) c/a axial ratio of the $hR6$ contaminant phase, and the pressure dependence of (d) the lattice parameter a of the $cI12$ contaminant phase. Structural parameters were determined from the d-spacings of 4–11 reflections. The solid circles show data measured on samples loaded with a mineral oil PTM, the open circles show data measured on samples loaded with a He PTM and the open diamonds show data for measured on a sample loaded without a PTM. In all cases, the estimated uncertainties are smaller than the symbol size and so are not shown.

the cell components, such as the PTM, gasket material or pressure calibrant. However, the contaminant peaks have been observed in samples loaded in different PTMs (mineral oil, He and without a PTM) using several different gasket materials (Re and W) and pressure markers (ruby, Ta and no pressure marker). We also observed no damage to the diamond culets in these experiments, suggesting that there was no reaction between Eu and the diamonds.

An obvious source of contamination would be due to oxidation of the Eu sample during the loading procedure. However, the structures of $hR6$ and $cI12$ do not match any of the reported high-pressure structures for Eu oxides, either

for EuO or Eu_2O_3 [120, 121]. Also, the volume per Eu atom of the $hR6$ contaminant is only 1.31(14) Å^3 greater than that of pure Eu at 26.1 GPa, which is significantly smaller volume difference than observed in either of the Eu oxides. The equation of state of EuO was determined up to 8.5 GPa by McWhan *et al.* [122]. Extrapolating this to higher pressures gives a volume per Eu atom of 28.650 Å^3 at 26.1 GPa, which is 7.6 Å^3 greater than that of hcp-Eu at the same pressure. The volume per Eu atom of Eu_2O_3 was reported by Jiang *et al.* to be 68.151 Å^3 at 13.1 GPa, which is 40.96 Å^3 greater than that of hcp-Eu at that pressure.

The small difference in the volume per Eu atom between the hcp and $hR6$ structures suggests that the $hR6$ is most likely a hydride, EuH_x. However, the structures of the contaminants also do not match any of the reported structures for Eu hydrides. High pressure x-ray diffraction studies on europium hydride were performed by Matsuoka *et al.* [16], where a sample of Eu in H_2 was compressed up to 50 GPa, and a sample of EuH_2 in He was compressed up to 28 GPa. The data for EuH_2 are included in figure 4.8 for comparison with our data. A transition to EuH_2 was observed in the Eu in H_2 sample at 2.7 GPa, and so no data is available on EuH_x with $x < 2$. Extrapolating these data to 30 GPa gives a volume per H atom of 4.1 Å^3. Comparing this with the difference in the volume per Eu atom of 4.8 Å^3 between $cI12$ and hcp-Eu at the same pressure, suggests that the density of the $cI12$ phase could be explained by it being EuH_x, with $x \approx 1.2$ at 30.5 GPa. A similar comparison gives a value of $x \approx 0.3$ for $hR6$ at the same pressure. Figure 4.8 also suggests that both contaminant phases are less compressible than Eu, which is consistent with results by Matsuoka *et al.* on other Eu hydrides.

Although it is possible to load clean samples that do not show the $hR6$ phase above 17 GPa, of the large number of samples loaded over the course of our studies, the majority were contaminated. The relative intensity of the contaminant reflections varied between difference samples. A two-phase Rietveld refinement to the patterns with the most intense contaminant reflections determined the contaminant contant to be ∼4% for both the $hR6$ and $cI12$ phases, although in most samples the reflections from the contaminant phases were much less intense. Interestingly, it was noted that the diffraction profiles from a 'clean' sample at 37 GPa, which did not initially contain diffraction peaks from the $hR6$ phase, contained very strong diffraction peaks from this phase after the sample was heated for 2.5 h at 373 K. This suggests that what may initially appear to be a pure Eu sample may in fact still contain impurities. Similar behaviour was

observed in the high-pressure high-temperature studies described in section 6.2.3, where the impurity reflections were also observed to become more intense over the time that the sample was heated.

Understanding the behaviour of such contaminant phases is vital for high pressure studies, in particular for work carried out at high temperatures. Future studies on the valence or superconductivity of Eu at high pressures should be combined with diffraction studies to ensure that the sample is not contaminated. In particular, it is not sufficient to simply collect a diffraction pattern at low pressures, but it is necessary to collect at least one pattern above 17 GPa in order to determine the quality of the sample. This then questions the quality of the samples used in previous studies. Of particular note, previous L_{III} x-ray absorption measurements showed evidence of hysteresis on decompression below 22 GPa [108]. This was compared with the x-ray diffraction study by Takemura and Syassen [13], in which the reflections from the contaminant phase were observed to remain in the diffraction patterns on decompression below 18 GPa. Although Bi *et al.* [110] initially saw no evidence of Eu^{3+} impurities in their Mössbauer spectra, we have shown that the contaminant is in a mixed-valent state, and that it undergoes a valence transition at the $hR6$–$cI12$ transition. In their room temperature resistivity measurements, Bundy and Dunn [107] reported a small, but reproducible, step in the resistance of Eu at 18 GPa. It should also be noted that Debessai *et al.* [111] found that they did not observe evidence of superconductivity in one of their samples due to oxidation as a consequence of exposure to air. As we have found that loading samples without any evidence of the $hR6$ contaminant is much more difficult than loading samples without any oxide present, the presence of this contaminant phase may then offer a possible explanation for the anomously low value of T_c that was reported in this study.

4.5 Conclusions

In conclusion, we have determined that the appearance of weak reflections in the diffraction patterns collected above 17 GPa that were initially attributed to a transition to Eu-III are *not* due to changes in Eu itself, but are due to changes in a contaminant that was present in previous studies. The $hR6$ contaminant has been observed to undergo a transition to a body-centred cubic phase, $cI12$, following pressure cycling and annealing. The volume per Eu atom of the $cI12$ contaminant is significantly larger than that of the $hR6$ contaminant at the same

pressure, suggesting that the two phases have different stoichiometries or chemical compositions. Comparison of the volume per Eu atom with that reported recently for EuH_2 suggests that the $cI12$ phase might be a Eu hydride, EuH_x, with $x \approx 1.2$, and that $hR6$ may be a subhydride, with $x \approx 0.3$.

Chapter 5

The Structure of Eu-IV

5.0.1 Introduction

In the previous chapter (4), it was shown that all of the previous high-pressure x-ray diffraction studies on Eu [13–15] were complicated by the presence of an impurity phase, evidence of which is not observed in the diffraction patterns until pressures above ∼17 GPa. Consequently, the previous observation of the contaminant reflections above this pressure was mistakingly attributed to a structural changes in Eu itself. However, in section 4.3.3 it was shown that if great care is taken in the sample loading process, it is possible to obtain non-contaminated samples. In such samples, no additional reflections were observed in the diffraction profiles collected above 17 GPa, and Eu remains in the hcp phase up to 31.5 GPa.

Structural assignments for Eu above ∼17 GPa have only been proposed in one previous study, when Bi *et al.* [15] combined the results from powder x-ray diffraction experiments with *ab initio* structure prediction calculations to determine a series of structural assignments up to 92 GPa. A critical evaluation of this work was given in section 4.1 of chapter 4. In summary, they determined their diffraction patterns in the 18–35 GPa region to correspond to a mixture of hcp plus a monoclinic structure with space group $C2/c$, and their patterns in the 35–66 GPa region to correspond to a mixture of the same $C2/c$ structure plus an orthorhombic structure with space group $Pnma$. The $Pnma$ structure was reported to remain stable up to 92 GPa, the highest pressure reached in this study. However, it is now evident that the diffraction patterns in this

study contained reflections from the $hR6$ contaminant phase, which were wrongly indexed based on the $C2/c$ structure. This then questions the validity of their structural assignments, as it introduces the possibility of misidentifying peaks from the contaminant phase as those from pure Eu.

In order to investigate the structural behaviour of Eu above 31.5 GPa, angle-dispersive powder x-ray diffraction experiments have been performed on a non-contaminated Eu sample up to 37 GPa. Eu has been found to transform to a new phase, Eu-IV, at 31.5 GPa. This phase has an incommensurately-modulated crystal structure; the first structure of this type to be observed in the lanthanide elements. The majority of this work has been published in Phys. Rev. Lett. [4].

5.0.2 Experimental Results

The experimental results in this chapter directly follow on from those described in chapter 4. The experimental details of this work are given in section 4.2.

Transition to Eu-IV

In section 4.3.3, it was shown that when great care was taken to minimise the chances of contamination by loading high-purity Eu samples quickly without a pressure-transmitting medium (PTM) and without a pressure calibrant, it was possible to obtain the non-contaminated sample 11. Angle-dispersive powder x-ray diffraction data were collected on this up to 37 GPa the maximum pressure that could be reached with this cell before gasket failure. In this sample, no additional reflections were observed in the diffraction patterns collected above 17 GPa, and instead the sample remained in the hcp phase up to 31.5 GPa. Above this pressure, significant changes in the diffraction profiles were observed, which was taken as evidence of a transition to a new phase, Eu-IV. This is illustrated in figure 5.1, which shows the integrated diffraction profiles of Eu in the hcp phase at 30.6 GPa, and after the transition to the Eu-IV phase at 33.9 GPa. The changes in the diffraction profiles can be described by two distinct features. Firstly, a large number of the hcp reflections split into doublets or triplets. This is illustrated in figure 5.1(d), which illustrates the splitting of the (101)-hcp reflection into a triplet. Simultaneously, a large number of additional weak reflections (> 30) appeared, some of which are highlighted in figures 5.1(b) and (c).

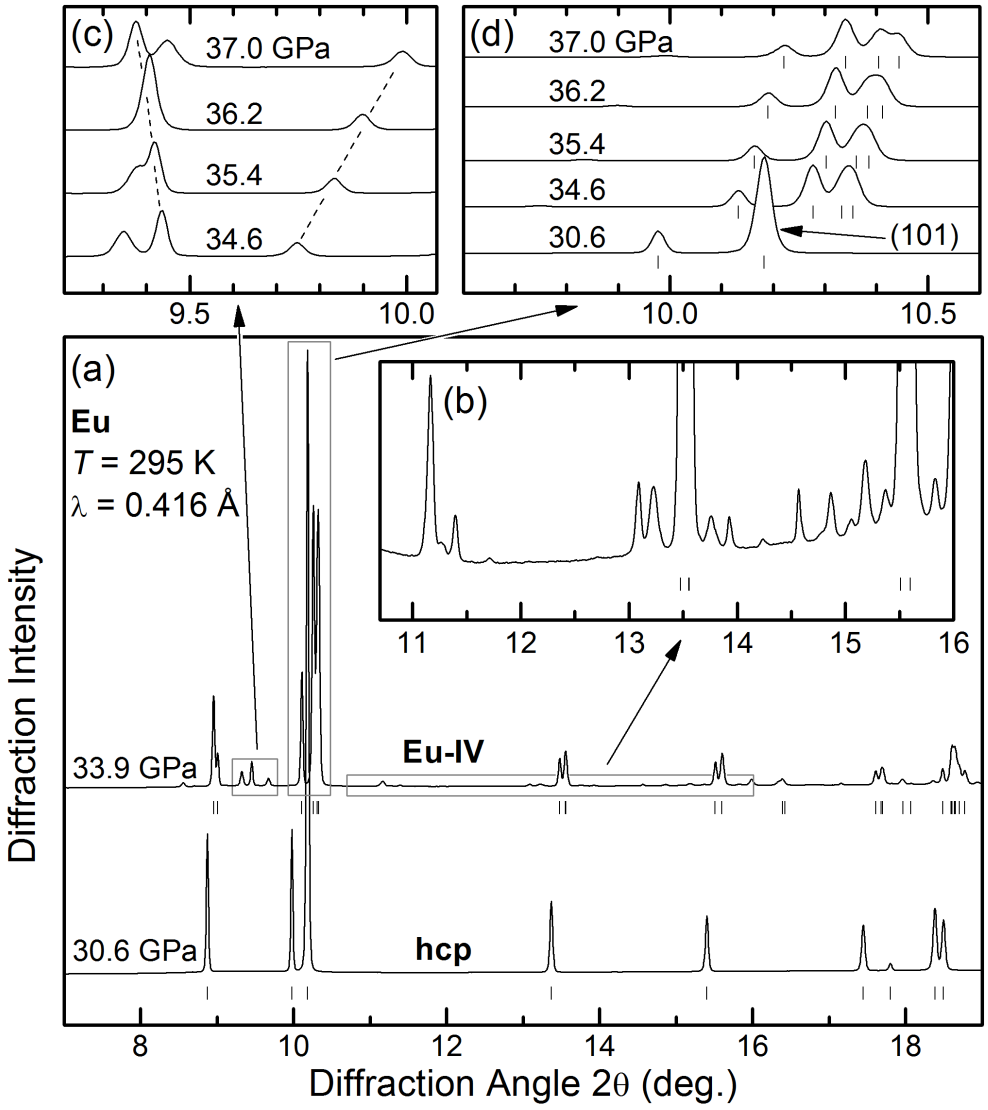

Figure 5.1: (a) Integrated diffraction profiles of Eu in the hcp phase at 30.6 GPa (lower) and in the Eu-IV phase at 33.9 GPa (upper). The tick marks below the profiles show the calculated peak positions of the hcp structure (lower) and the $mC4$ structure (upper). (b) The large number of weak reflections that appear at the transition, which cannot be accounted for by the $mC4$ structure. (c) The movement of one of the weak reflections to lower angles (higher d-spacing) with increasing pressure. (d) The splitting of the (101)-hcp reflection into a triplet, as the $mC4$ structure distorts away from hcp.

The splitting of the hcp reflections into doublets and triplets suggests a transition to a distorted-hcp structure. The first consideration was the $Pnma$ structure proposed by Bi *et al.* for pressures above ∼35 GPa, which is an orthorhombic distortion of hcp. The relationship between $Pnma$ and hcp is given by $\vec{a}_o \approx \vec{a}_h$, $\vec{b}_o \approx \vec{a}_h + 2\vec{b}_h$ and $\vec{c}_o \approx \vec{c}_h$, where o labels the lattice vectors of the orthorhombic structure and h labels the lattice vectors of hcp. The two structures are equivalent when the axial b/a ratio is equal to $\sqrt{3}$, and distorting the b/a ratio away from

this value will result in the splitting of some of the hcp reflections. A Le Bail refinement of the orthorhombic structure to the 33.9 GPa diffraction profile found that, although this structure can account for the splitting of some of the hcp reflections, it cannot account for all of them, and the overall quality of the fit is poor. In particular, it cannot account for the splitting of the (101)-hcp reflection into a triplet.

The fact that the orthorhombic *Pnma* structure does not account for all the split reflections suggests that it is necessary to consider lower-symmetry structures. The DICVOL [63] program was then used to search for an alternative solution. A good fit was obtained with a monoclinic structure with $a \approx 3.1$ Å, $b \approx 5.3$ Å, $c \approx 4.7$ Å, and $\beta \approx 90.3°$. All observed reflections satisfy $h+k = 2n$, determining the structure to be C-centred. There are only two C-centred monoclinic space groups: $C2/m$ (number 12) and $C2/c$ (number 15). The presence of the c-glide introduces a further reflection condition, which is that only $h0l$ and $00l$ reflections with $l = 2n$ are present. The absence of the (001), (003), (201) and $(\overline{2}01)$ reflections therefore suggests that the space group is $C2/c$. Density considerations determined the number of atoms in the unit cell to be 4, the lowest multiplicity that is possible in this space group, and a good fit was obtained with the atoms in the $4e$ $(0, y, \frac{1}{4})$ Wyckoff positions. The Pearson symbol for this structure is $mC4$, which shall be used to refer to it from this point onwards. It should be noted that this structure is *not* related to the monoclinic $C2/c$ structure proposed by Bi *et al.* for pressures above 18 GPa. A Rietveld refinement based on the $mC4$ structure to the 33.9 GPa diffraction pattern gives lattice parameters of $a = 3.0838(5)$ Å, $b = 5.3002(7)$ Å, $c = 4.7239$ Å and $\beta = 90.39(1)°$, and the atomic coordinate $y = 0.341(2)$. The calculated peak positions are shown below the 33.9 GPa pattern in figure 5.1(a), and also under the patterns in panels (b) and (d). Crucially, this structure can account for the splitting of the (101)-hcp reflection into a triplet, as illustrated in figure 5.1(d).

Although the $mC4$ structure can account for all of the split-hcp reflections, it cannot account for any of the weak additional reflections that appear at the transition, such as those illustrated in figure 5.1(b). Attempts to index the additional reflections as an extra phase using the DICVOL software were unsuccessful. The possibility of indexing them using a supercell of the $mC4$ structure was also considered. However, the absence of any low-angle reflections in the diffraction profiles suggested the unit cell is small. Additionally, it was noted that while *all* of the split-hcp reflections move to *higher* angles (shorter

d-spacings) with increasing pressure, a number of the weak reflections move to *lower* angles (longer d-spacings). The pressure-dependence of the d-spacings of 19 non-$mC4$ reflections, with respect to their d-spacings at 33.9 GPa (d_0), are shown in figure 5.2(a). These reflections are identified in the diffraction profile of Eu at 33.9 GPa in figure 5.2(b), where reflections were chosen that can be clearly identified over the entire pressure range. A total of 6 reflections move to longer d-spacings on pressure increase, while the remaining reflections move to shorted d-spacings. The behaviour of reflection 3 is illustrated in figure 5.1(c). It is therefore not possible to describe the non-$mC4$ reflections as superlattice reflections of the $mC4$ structure.

The possibility that the structure is incommensurately-modulated was then considered. That is, that the weak reflections are satellite reflections corresponding to an incommensurate modulation in the average $mC4$ structure. A detailed description of incommensurately-modulated structures within the superspace formalism is give in section 2.3.3, and the problems associated with indexing these types of structures are discussed in section 2.5.2. Having already identified the average structure, the SUPERCELL program was then used to index the non-$mC4$ reflections as satellite reflections corresponding to the modulation wave vector in the a–c plane, with $q_1 \sim 0.8$ and $q_3 \sim 0.6$. The superspace group was then determined to be $C2/c(q_1 0 q_3)00$. The Pearson symbol for this structure is i-$mC4$, where i indicates that the structure is incommensurate, and $mC4$ is the Pearson symbol of the average structure.

All of the Bragg reflections in the pattern can then be indexed with 4 Miller indices $(hklm)$ according to $\vec{G} = h\vec{a}^* + k\vec{b}^* + l\vec{c}^* + m\vec{q}$, where $\vec{a}^*$, $\vec{b}^*$ and $\vec{c}^*$ are the reciprocal lattice vectors of the unmodulated $mC4$ structure. The displacement of each atom in the modulated structure from its position in the average structure is given by the modulation function $\vec{u}(\overline{x}_4)$, where $\overline{x}_4 = \vec{q}\cdot\vec{r}_0$ is the fourth superspace component and r_0 is the position of the atom in the average crystal structure. As the modulation function is periodic in $\overline{x}_4$, it is possible to expand it as a Fourier series according to equation 5.1, where α labels the crystallographic axes $\vec{a}$, $\vec{b}$ and $\vec{c}$. Note that this means that although the wave vector is in the $\vec{a} - \vec{c}$ plane, the atoms are displaced from their average positions along the directions of all three lattice vectors.

$$u_\alpha(\overline{x}_4) = \sum_{n=1}^{\infty} [A_{n\alpha} \cos 2\pi n\overline{x}_4 + B_{n\alpha} \sin 2\pi n\overline{x}_4] \tag{5.1}$$

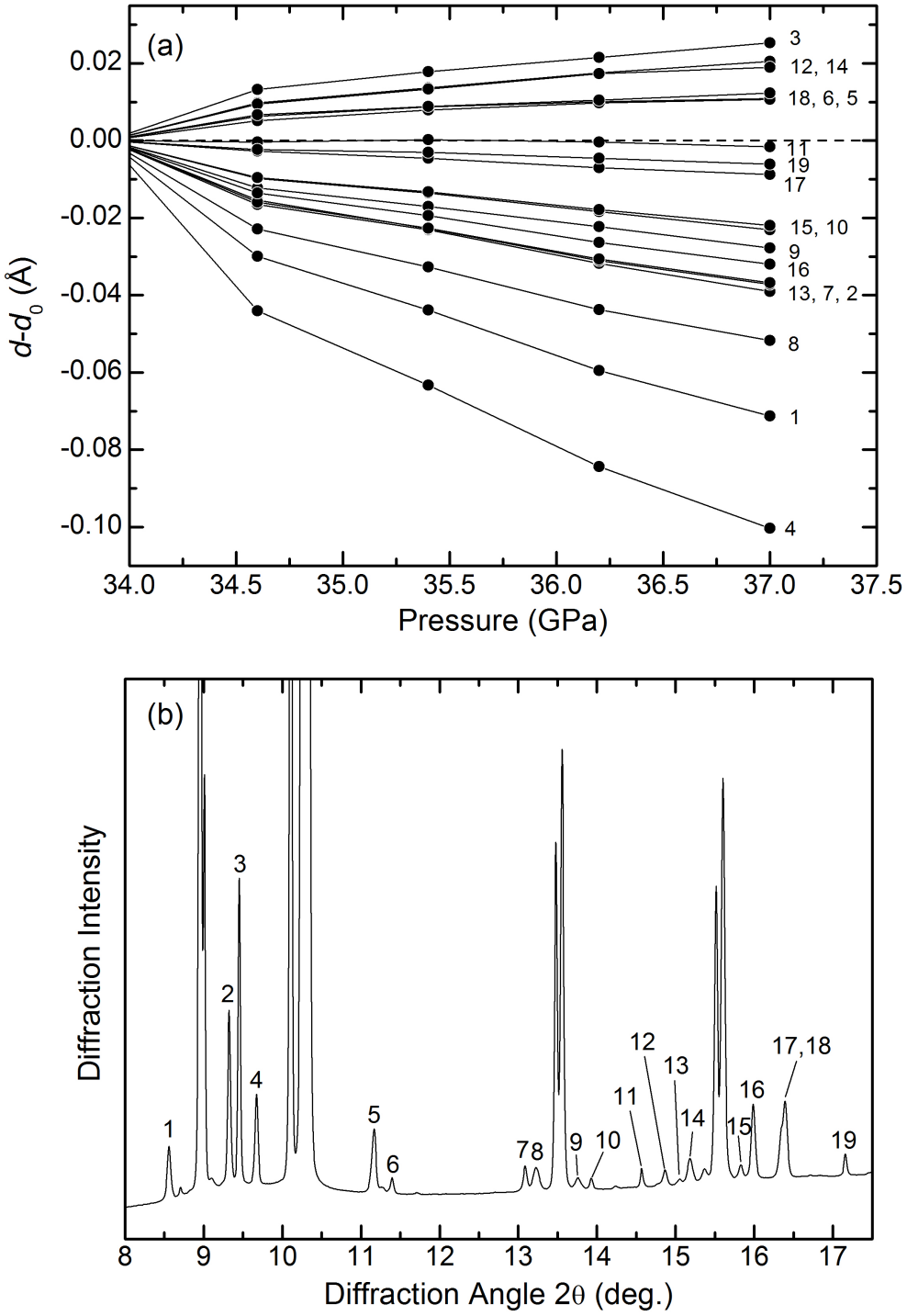

Figure 5.2: (a) Pressure dependence of the d-spacings of a selection of weak Eu-IV reflections (1–19) with respect to those at 33.9 GPa (d_0).
(b) Identification of these reflections in the diffraction profile of Eu at 33.9 GPa.

A Rietveld refinement of the *i*-$mC4$ structure based on the diffraction pattern of Eu at 33.9 GPa is shown in figure 5.3, where only first-order ($m = \pm 1$) satellite reflections are considered. This structure can account for *all* of the reflections in the pattern, both the split-hcp reflections and the additional reflections that

appear at the transition. An excellent fit is obtained, with $R_{wp} = 2.5\%$ and $R_p = 4.2\%$. The refined lattice parameters are $a = 3.0835(1)$ Å, $b = 5.2994(2)$ Å, $c = 4.7239(1)$ Å, with monoclinic angle $\beta = 90.400(2)^\circ$ and atomic coordinate $y = 0.342(1)$. The refined wave vector components are $q_1 = 0.8095(2)$ and $q_3 = 0.5908(2)$, with modulation amplitudes of $B_{1a} = -0.034(2)$, $A_{1b} = 0.016(1)$, and $B_{1c} = 0.040(1)$. All other first-order modulation amplitudes are equal to zero due to symmetry restrictions of the $C2/c(q_1 0 q_3)00$ superspace group.

Eu-IV is the first incommensurate structure to be observed in the lanthanide elements, and the first incommensurately-modulated crystal structure to be observed in the elements at high pressure in which the modulation vector is not along one of the crystallographic axes. Schematic views of the unmodulated $mC4$ and the incommensurately-modulated i-$mC4$ crystal structures are shown in figure 5.4, where the modulation amplitudes are shown to scale. The very close relation to the hcp structure can clearly be seen in the views of the structures in the a–b plane, shown in figures 5.4(a) and (b).

The i-$mC4$ structure gives an excellent fit to the diffraction patterns collected up to 37 GPa, the highest pressure that was reached with this cell. Once the structure was determined, it was possible to also fit the data collected on contaminated sample 1 up to 38 GPa. Although reflections from the $cI12$ contaminant were present in all of the diffraction patterns collected from this sample, these were easily identified over the whole pressure range. Above 38 GPa, the diffraction patterns could no longer be described by the i-$mC4$ structure, which was taken as evidence of a transition to a new phase, Eu-V. This will be discussed in detail in chapter 6.

The pressure-dependence of the lattice parameters a, b, c, β and the atomic coordinate y across the hcp $\rightarrow$ i-$mC4$ transition are shown in figures 5.5(a)–(e), where hcp is described in the orthohexagonal setting. The relationship between the hexagonal and orthohexagonal settings of hcp is given by $\vec{a}_o = \vec{a}_h$, $\vec{b}_o = \vec{a}_h + 2\vec{b}_h$ and $\vec{c}_o = \vec{c}_h$, where o labels the orthohexagonal lattice vectors and h labels the hexagonal unit vectors. The description of Eu-IV in the $C2/c(q_1 0 q_3)00$ superspace group setting therefore enables a direct comparison with hcp in the orthohexagonal setting, as the $\vec{a}$ and $\vec{c}$ lattice vectors of i-$mC4$ and orthohexagonal hcp are directly related. On compression, the lattice parameters a, b and c vary smoothly over the transition from hcp to i-$mC4$. The monoclinic angle β increases from 90° in the hcp phase, reaching a maximum value of 90.47(2)° at 37.5 GPa. The atomic coordinate y remains close to the hcp value of

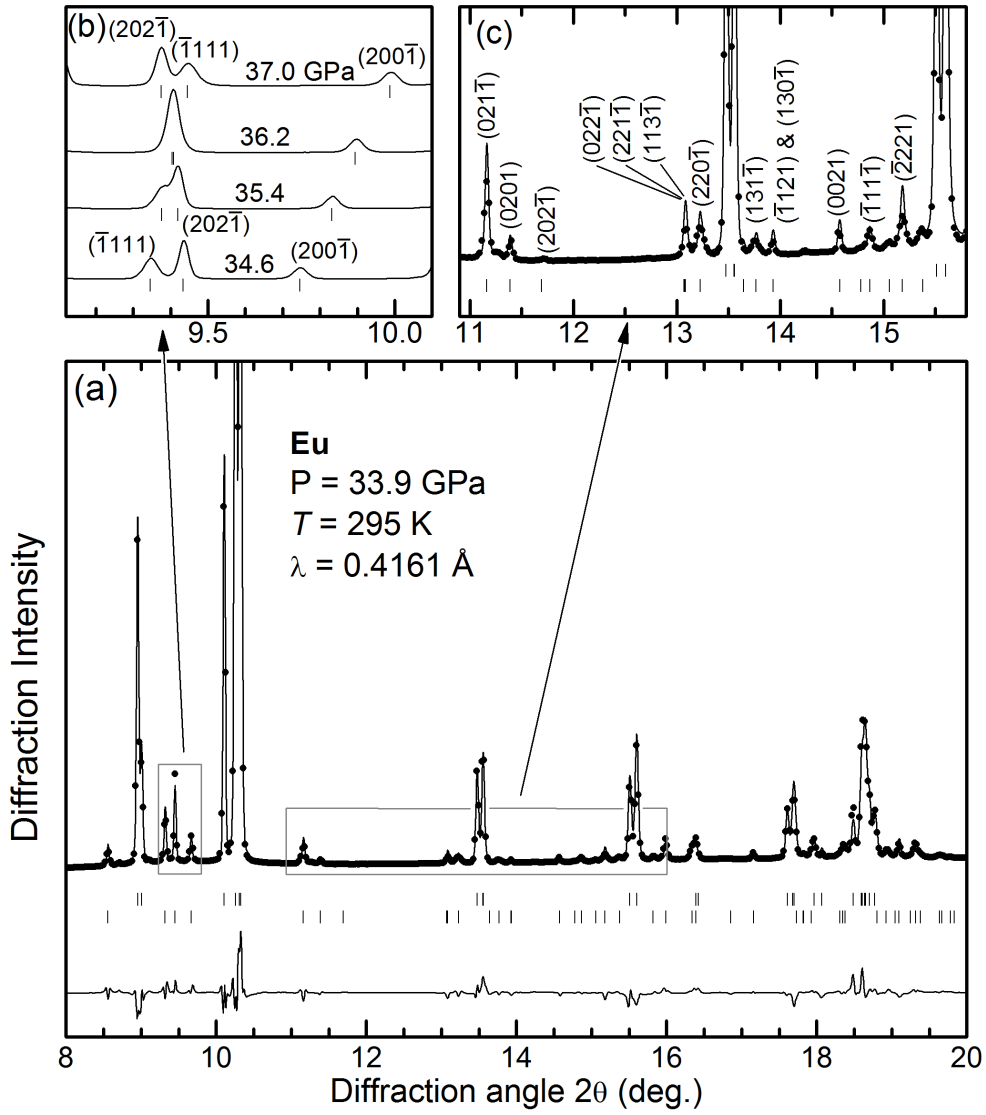

Figure 5.3: (a) Rietveld refinement of the *i*-$mC4$ structure based on the diffraction pattern of Eu at 33.9 GPa. The points show the experimental data and the solid line shows the fit. The tick marks below the profile show the calculated peak positions of the main (upper) and first-order satellite reflections (lower), and the residuals are shown below the tick marks. This structure can account for all of the weak reflections that appear at the transition, as illustrated in panel (c), including those that move to longer *d*-spacings with increasing pressure, such as the (202$\bar{1}$) reflection illustrated in panel (b).

$y = 1/3$, although there is a systematic difference in the values determined from each of two samples. However, it is most likely that this arises from different preferred orientation in the samples. The most intense reflection in the diffraction patterns collected from sample 1 was saturated on the detector, and so the results from sample 11 are more reliable.

The pressure dependence of the c/a and b/a axial ratios are shown in figures 5.6(a)

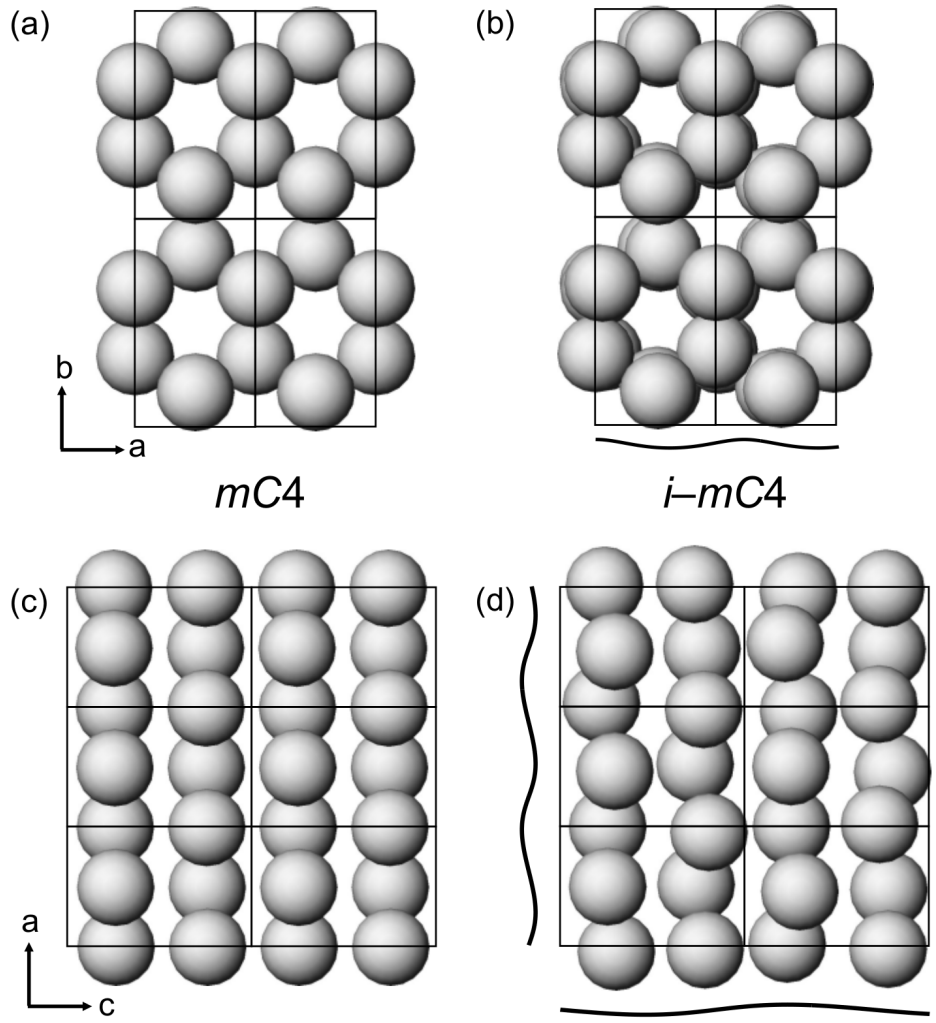

Figure 5.4: Schematic views of the unmodulated $mC4$ and the incommensurately-modulated i-$mC4$ crystal structures at 33.9 GPa. Four unit cells viewed along the c direction of (a) $mC4$ and of (b) i-$mC4$. Six unit cells viewed along the b direction of (c) $mC4$ and of (d) i-$mC4$. Projections of the modulation function $\vec{u}(\overline{x}_4)$ onto the ab and ac planes, evaluated along the crystallographic axes, are shown besides the crystal structures in (b) and (d), respectively. The modulation function along the b axis is zero and therefore not shown.

and (b), respectively. In an ideal close-packed hcp structure, the c/a axial ratio is equal to $\sqrt{8/3} = 1.633$. The c/a ratio of hcp Eu is already smaller than the close-packed value at 13.7 GPa, where $c/a = 1.5903(15)$. The c/a ratio is observed to decrease on compression, before flattening out at $\sim$1.54 above $\sim$25 GPa. Following the transition to i-$mC4$, a steep decrease in the c/a ratio is observed, reaching a minimum of 1.5247(5) at 37.5 GPa. The b/a ratio is observed to decrease from the hcp value of $\sqrt{3}$ following the transition to Eu-IV, reaching 1.7119(6) at 37.5 GPa.

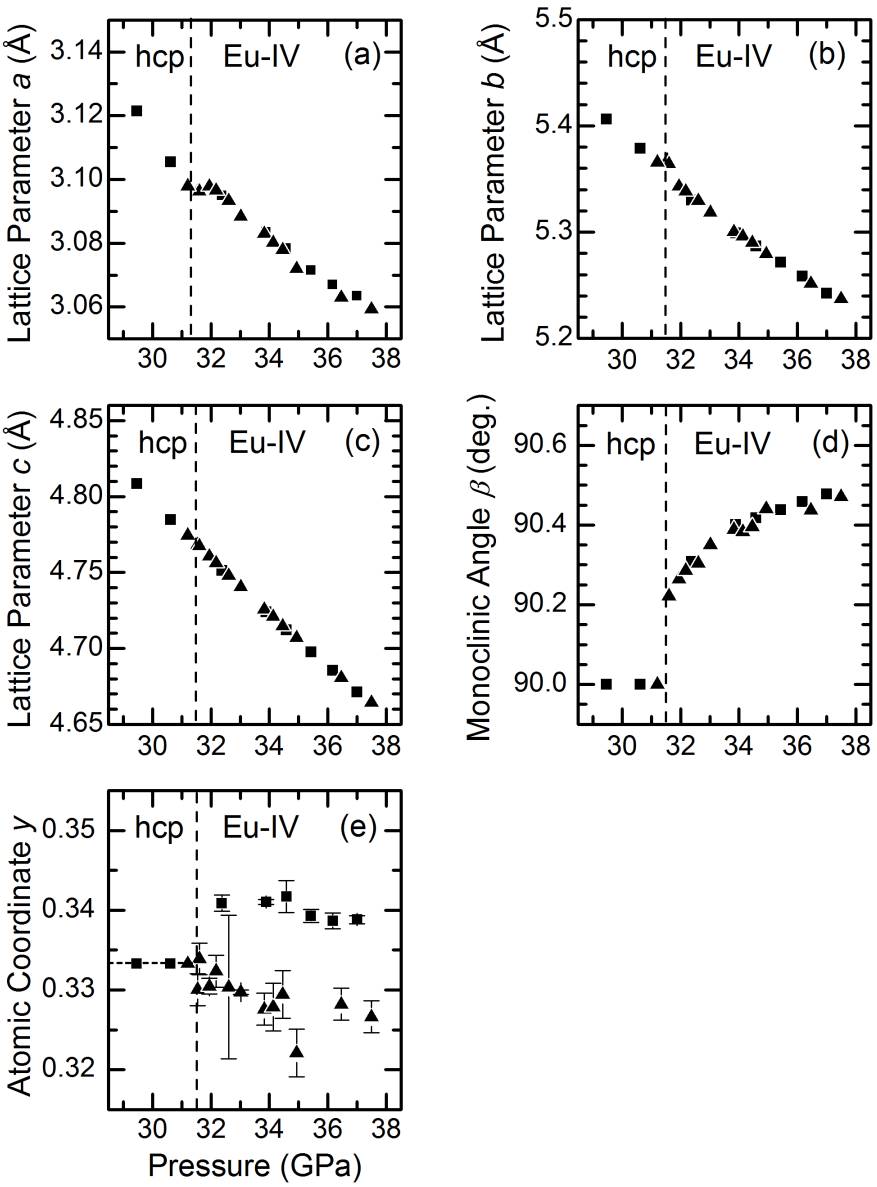

Figure 5.5: Structural parameters of Eu as a function of pressure, as determined from Rietveld refinements to the diffraction profiles. The solid squares show data collected on sample 11 and the solid triangles show data collected on sample 1. The hcp structure is described in the orthohexagonal setting, where the monoclinic angle β is equal to 90°, the atomic coordinate y is equal to 1/3, and b/a is equal to $\sqrt{3}$. With the exception of y, the estimated uncertainties are smaller than the symbol size and so have not been included.

The pressure dependence of the wave vector components q_1 and q_3, and the modulation amplitudes B_{1a}, A_{1b} and B_{1c}, are shown in figures 5.7(a)–(e). The wave vector component q_1 is observed to decrease on compression, passing smoothly through $q_1 = 0.8 = 4/5$, which corresponds to a commensurate modulation in this direction. The wave vector component q_3 is also observed

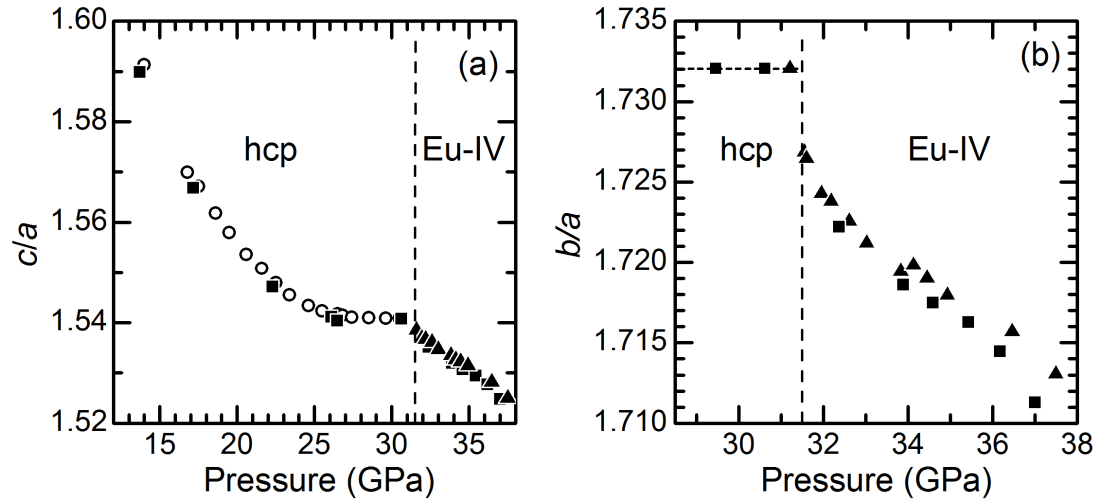

Figure 5.6: The c/a and b/a axial ratios of Eu as a function of pressure, as determined from Rietveld refinements to the diffraction profiles. The solid squares show data collected on sample 11, the solid triangles show data collected on sample 1, and the open circles show data collected on sample 9. The b/a ratio is equal to $\sqrt{3}$ in the hcp phase, where hcp is described in the orthohexagonal setting. The estimated uncertainties are smaller than the symbol size and so have not been included.

to decrease with increasing pressure, although the magnitude of change is much smaller than that observed in q_1. The magnitudes of all three modulation amplitudes ($|B_{1a}|$, $|A_{1b}|$ and $|B_{1c}|$) are observed to increase with increasing pressure.

It is interesting to consider the high pressure behaviour of Eu in terms of interatomic distances. Each atom in the hcp structure has two near-neighbour shells due to the non-ideal c/a ratio, and each atom in the hypothetical unmodulated $mC4$ structure would have a total of five near-neighbour shells. However, the presence of the incommensurate modulation in the i-$mC4$ structure results in a wide spread of near-neighbour distances, as each atom in the structure is displaced by a different amount in each unit cell.

It is possible to consider the entire set of interatomic distances present in the structure by plotting the interatomic displacements as a function of t in the range $0 < t < 1$, where t is the phase of the modulation. This is shown for pressures of 32.4 and 37.0 GPa in figures 5.8(a) and (b), respectively, where the near-neighbour distances of the unmodulated $mC4$ structure are also shown for comparison. Interestingly, the closest-contact distance in the i-$mC4$ structure is 3.87 % smaller at 37.0 GPa than at 32.4 GPa, whereas the nearest-neighbour distance in the $mC4$ structure has only decreased by 1.24 %. Extrapolating the lattice parameters of

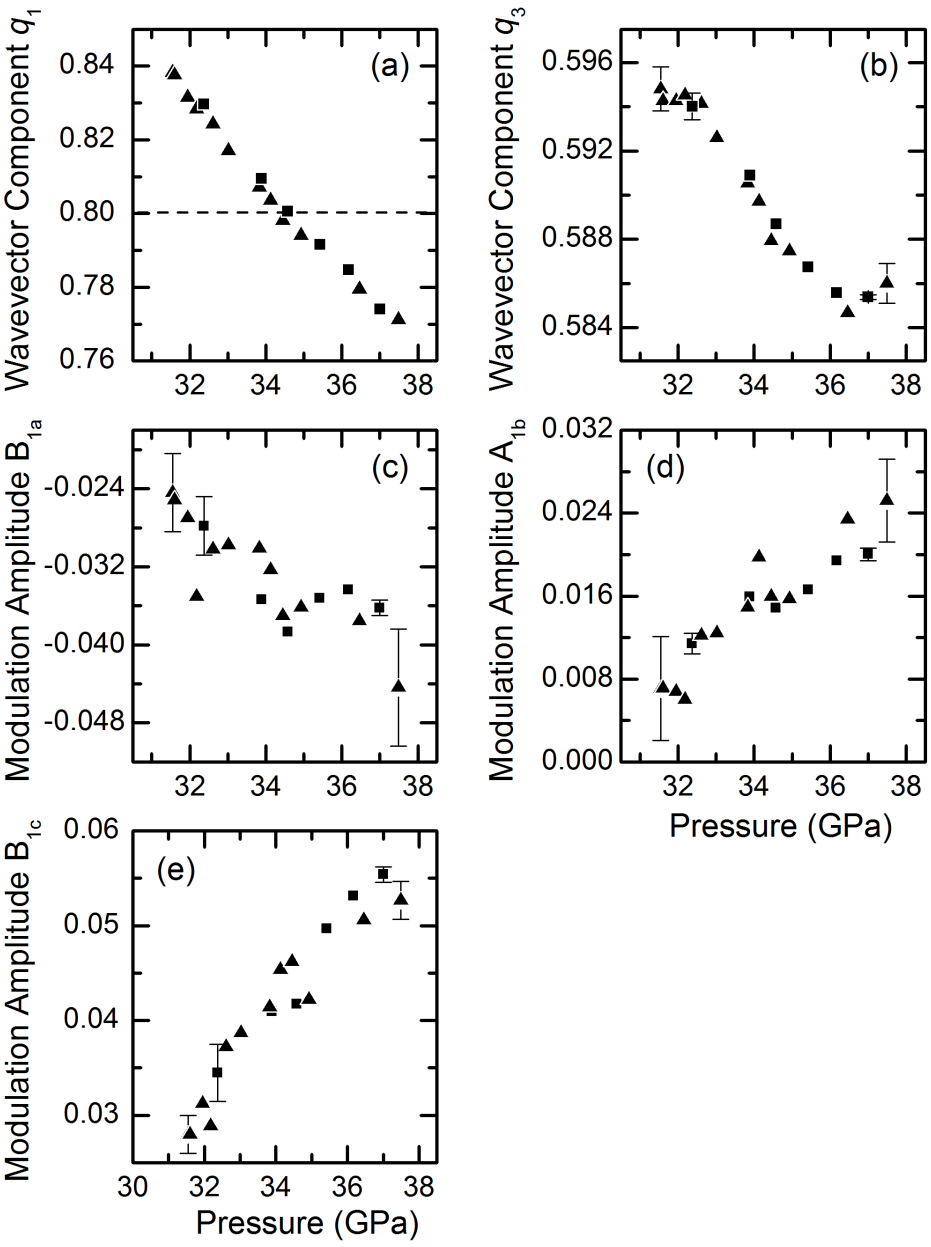

Figure 5.7: Wave vector components (a) q_1 and (b) q_3, and modulation amplitudes (c) B_{1a}, (d) A_{1b} and (e) B_{1c} of the i-$mC4$ structure as a function of pressure, as determined from Rietveld refinements to the Eu diffraction profiles. The solid squares show data collected on sample 11 and the solid triangles show data collected on sample 1. Representative error bars are shown on selected data points. The estimated uncertainties of q_1 are smaller than the symbol size and so have not been included. q_1 is observed to pass smoothly through the value of $q_1 = 0.8 = 4/5$, which corresponds to a commensurate modulation in this direction, as indicated by the dotted line in panel (e).

the hcp structure to higher pressures finds that the nearest-neighbour distance would decrease by 2.14 % over the same pressure range. This is different from

what was observed in the incommensurately-modulated Te-III [72], where the closest-contact distance remains constant within error within the pressure range over which this structure was observed, whereas the nearest-neighbour distance in the unmodulated structure decreased by ∼4.5%.

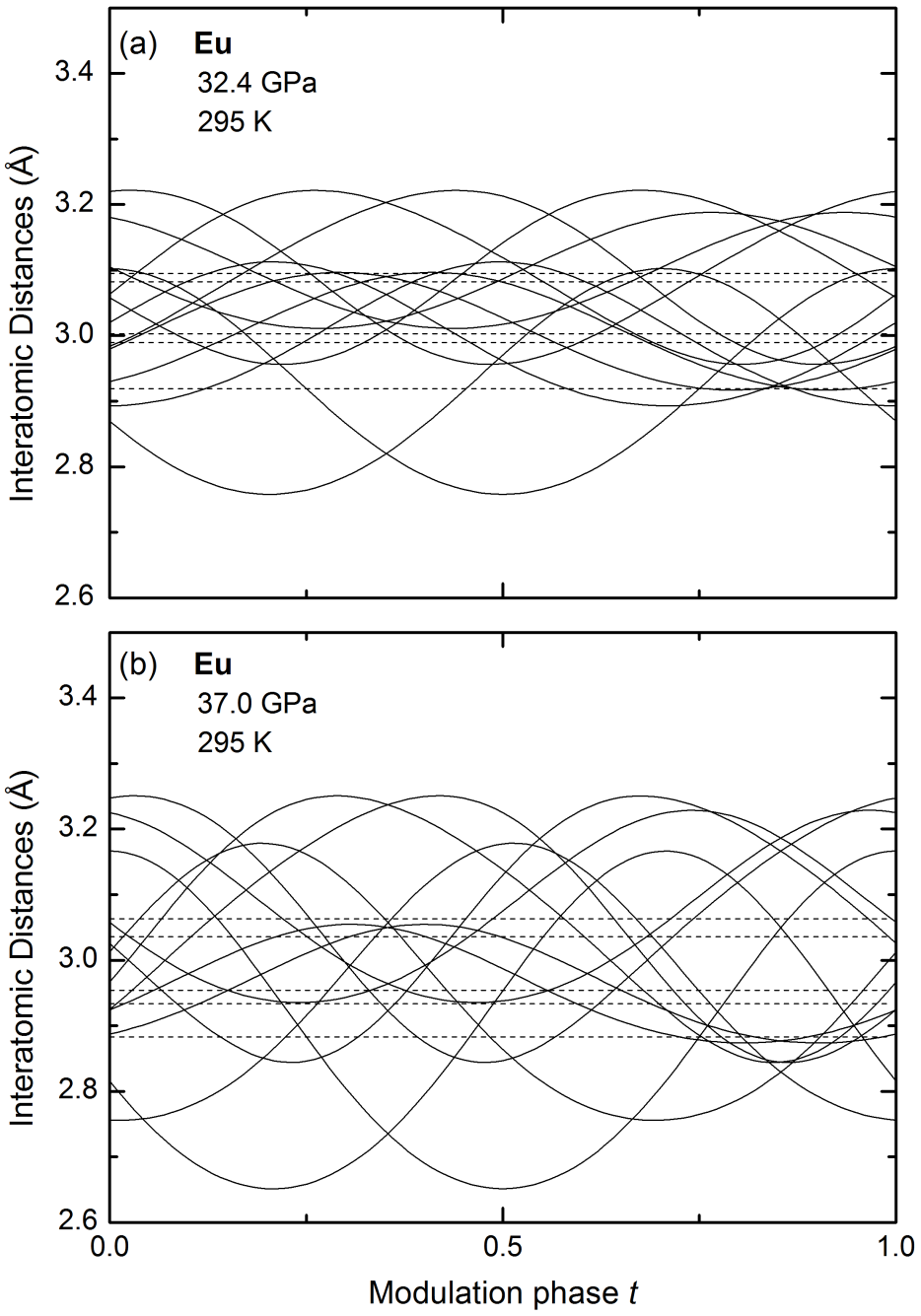

Figure 5.8: Interatomic distances as a function of the modulation phase t for the i-$mC4$ structure at (a) 32.5 GPa and (b) 37.0 GPa. The dotted lines show the near-neighbour distances of the unmodulated $mC4$ structure.

This behaviour can also be seen in the plot of the pressure-dependence of the interatomic distances in Eu as a function of pressure, which is shown in

figure 5.9(a). The range of interatomic distances that are present due to the modulation are indicated by the shaded area. It is clear that the closest-contact distance in the modulated *i*-$mC4$ structure decreases more rapidly on compression than the nearest-neighbour distance in the hypothetical unmodulated $mC4$ structure. The range of interatomic distances present in the *i*-$mC4$ structure is also observed to increase with pressure, from 0.46 Å at 32.5 GPa to 0.60 Å at 37 GPa. This is therefore unlike the behaviour observed in the incommensurately-modulated phase-IV of phosphorus, in which the width of the distribution of interatomic distances was reported to be ∼0.08 Å between 113 and 137 GPa [34].

The pressure-dependence of the maximum atomic displacements in the *i*-$mC4$ structure, with respect to the atomic positions in the $mC4$ structure, are shown in figure 5.9(b). δ_1, δ_2 and δ_3 are the maximum atomic displacements along the $\vec{a}$, $\vec{b}$ and $\vec{c}$ directions, respectively, which are given by $B_{1a}|\vec{a}|$, $A_{1b}|\vec{b}|$ and $B_{1c}|\vec{c}|$. Despite the decrease in the unit cell dimensions with increasing pressure, the maximum atomic displacements increase due to the increase in the modulation amplitudes.

In their energy-dispersive x-ray diffraction study of Eu up to 40 GPa, Krüger *et al.* [14] reported changes in their diffraction patterns collected above 32 GPa. It is therefore likely that these were evidence of the phase transition to the incommensurate phase. In particular, the extra reflections observed in that study are in the correct positions to be the most intense satellite reflections of *i*-$mC4$, but the limited resolution made it impossible to resolve the splitting of the hcp reflections and other details. Bundy and Dunn observed a step in the electrical resistance of Eu near 28 GPa at room temperature [107], which may also be related to the transition from hcp to the *i*-$mC4$ phase at 31.5 GPa. The transition to the $Pnma$ structure reported by Bi *et al.* [15] above ∼35 GPa can also be identified with the hcp → *i*-$mC4$ transition at 31.5 GPa. Although Bi *et al.* determine the transition pressure to be slightly higher than was determined in this work, there is evidence in their 35 GPa diffraction profile that the hcp reflections have already split into multiple peaks. This suggests that the transition to Eu-IV has already began at this pressure.

5.0.3 Origin of the Modulation Wave

Having identified an incommensurately-modulated crystal structure in Eu at high pressure, it would be desirable to be able to identify the mechanism driving

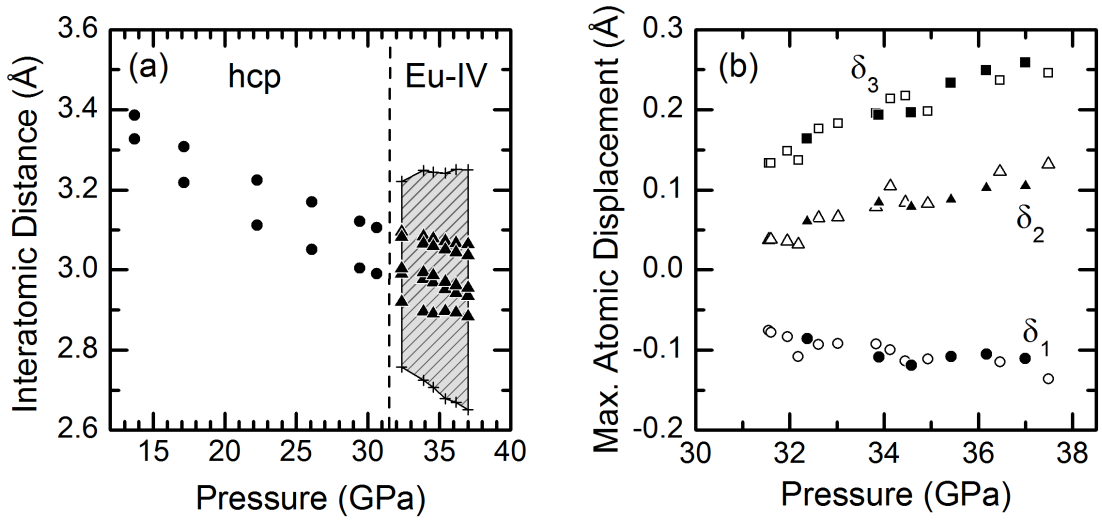

Figure 5.9: (a) Interatomic distances in Eu as a function of pressure, as determined from Rietveld refinements to the diffraction profiles. The solid circles show the 2 sets of near-neighbour distances in the hcp phase, and the solid triangles show the 5 sets of near-neighbour distances in the unmodulated $mC4$ structure. The crosses show the shortest and longest near-neighbour distances observed in the modulated i-$mC4$ structure, and the range of near-neighbour distances which are present due to the modulation are indicated by the shaded area.
(b) The pressure-dependence of the maximum atomic displacements in the modulated i-$mC4$ structure, with respect to the atomic positions in the average $mC4$ structure. δ_1 (circles), δ_2 (triangles) and δ_3 (squares) are the maximum atomic displacements along the $\vec{a}$, $\vec{b}$ and $\vec{c}$ directions, respectively. The open and closed circles show data collected on samples 1 and 10, respectively.

the formation of the modulation wave. That is, to look for the presence of pronounced nesting between parallel areas of the Fermi surface, or the associated phonon softening at wave vectors equal to that of the nesting vector, in the average structure, or to look for the presence of strong electron-phonon coupling. First-principles calculations on the high-pressure incommensurately-modulated phase of sulphur, S-IV, found evidence of Fermi-surface nesting, and identified a soft-phonon in the average structure [73]. A soft-phonon and pronounced Fermi-surface nesting was also identified in the average structure of the incommensurately-modulated Te-III [31].

However, in order to be able to perform meaningful calculations on the high-pressure phases of Eu, it is first necessary to be able to accurately describe the lower-pressure phases. The description of the lanthanide elements is known to be challenging for density-functional theory calculations. The overlap between the $4f$ orbitals on neighbouring atoms is very small, and the electrons are highly localised. If the $4f$ electrons are treated as valence states, the resulting orbitals

are overextended, which results in overbinding due to the additional electrons involved in bonding. Min *et al.* [104] performed total energy calculations of Eu at ambient pressure using the linearised muffin-tin orbital method, where the $4f$ states were treated as regular valence states within the local density approximation (LDA), which determined a value for the Wigner-Seitz radius that is 13% smaller than the experimental value when the $4f$ electrons were considered to be paramagnetic, and 5% smaller when they were considered to be ferromagnetic. The origin of this overbinding lies in the fact that the Coulomb correlation is not accounted for in the LDA. Alternatively, the $4f$ electrons can be treated as core states. Min *et al.* also performed total energy calculations with the $4f$ treated as cores states within the LDA. In this case, all electrons were still considered self-consistently, but the interatomic f-d hybridisation and the f-f direct hopping interaction was neglected. This determined a value for the Wigner-Seitz radius that is only 0.9% larger that the experimental value in both the paramagnetic and ferromagnetic states.

Bi *et al.* [15] performed computational structure searches on Eu at high pressure, and determined a sequence of structural transitions up to 100 GPa: bcc $\rightarrow$ hcp $\rightarrow$ $C2/c$ $\rightarrow$ $Fdd2$ $\rightarrow$ Pnma $\rightarrow$ $C2/c$ $\rightarrow$ hcp. Nonpolarised calculations were performed using the projector-augmented wave (PAW) method within the frozen core approximation, where the $4f$ electrons were treated as core states within the PAW potential, and the generalised gradient approximation (GGA). The lattice parameter was determined to be 3.5% larger than the experimental value, which is a significant improvement on the calculations in which the $4f$ electrons were treated as valence states. The bcc–hcp transition was determined to occur at 10 GPa, which is in fair agreement with the experimental transition pressure of 12.5 GPa. However, the high-pressure lattice parameters were not reported, and so it is not possible to compare with experiment.

In an attempt to identify the origin of the incommensurate modulation in Eu-IV, density-functional theory calculations were performed by I. Loa of the University of Edinburgh. Firstly, the equation of state and the lattice parameters of the bcc and hcp structures were calculated using the same approach as Bi *et al.* (PAW, frozen-core, GGA), with the $4f$ electrons treated as core states. The bcc–hcp transition was determined to occur at 9 GPa, which is in good agreement with the transition pressure determined by Bi *et al.* The pressure-dependence of the calculated and experimental values of the c/a axial ratio of hcp-Eu are shown in figure 5.10. Experimentally, the c/a ratio was observed to decrease from 1.59 at

13 GPa, and level off at 1.54 at ∼28 GPa. The calculations determined a much more dramatic decrease in c/a, with was calculated to reach 1.34 at 20 GPa. An even more dramatic decrease in c/a was observed with the calculations were performed within the LDA. The failure of this method to reproduce the experimentally-observed behaviour suggests that treating the $4f$ electrons as core states is not an adequate way in which to describe the electronic behaviour of Eu at high pressures. Nevertheless, structural optimisations of the unmodulated $mC4$ structure were performed up to 100 GPa. Although these determined an orthorhombic distortion above 13 GPa, the monoclinic angle, γ, was within ±0.1 of 90° over the whole pressure range.

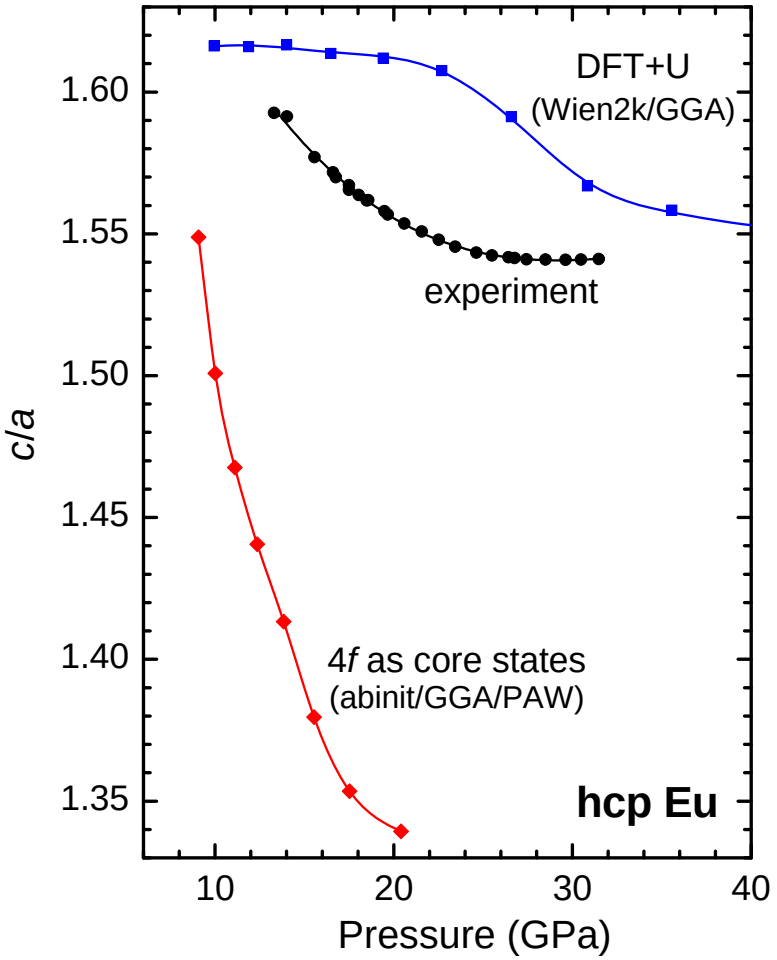

Figure 5.10: The c/a axial ratio of hcp-Eu against pressure. The red diamonds show data calculated with the $4f$ electrons treated as core states, the blue squares show data calculated in the DTF+U scheme, and the black circles show experimental data reported in this chapter. Calculations were performed by I. Loa at the University of Edinburgh, and the figure is taken from the supplementary material of reference [4]. Further details of the calculations are given in the text.

Additionally, spin-polarised calculations were performed in the GGA using the

DTF+U approach in the full-potential augmented plane-wave plus local orbital code, WIEN2K. In this method, an onsite Coulomb parameter, U, is introduced to take into account the on-site repulsion due to the localised electrons. The ambient-pressure volume was determined to be 3% larger than the experimental value, which is in good agreement. The calculated pressure-dependence of the c/a axial ratio is also shown in figure 5.10. The c/a ratio was determined to decrease with increasing pressure, levelling off at 1.55, in good agreement with experiment. However, the steep decrease was determined to occur at a higher pressure than observed experimentally, so that the whole curve is shifted by $\sim$13 GPa. Although the hcp phase was determined to be have a lower enthalpy than the bcc phase at all pressures, the enthalpy difference is very small below 10 GPa, so that the two phases are almost degenerate. By shifting up the energy of the hcp phase by 10 meV/atom, the experimentally-observed transition pressure is recovered.

The DTF+U approach clearly provides a better description of the behaviour of Eu at high pressure than treating the $4f$ electrons as core states. However, there are still discrepancies between the calculated lattice parameters and those determined from experiment. Providing an accurate description of $4f$ electrons in Eu under pressure therefore provides a challenge for future work, and is essential in order to be able to investigate the mechanism driving the formation of the modulation wave in the i-$mC4$ structure.

5.0.4 Transition in the Contaminant Phase

In section 4.3.1, the transition from the $hR6$ to the $cI12$ contaminant phase was identified. Evidence of the $cI12$ phase was first observed in the diffraction patterns after sample 1 was annealed for 4 hours at 38 GPa 473 K and the pressure was decreased below 31.5 GPa. However, due to the complexity of the diffraction profiles of Eu above 31.5 GPa, it was not possible to identify the exact point at which the transition occurred.

In order to determine the at which point this transition occurs, the pressure of sample 2 was increased to 37.7 GPa. The transition from hcp Eu to Eu-IV was observed at 31.5 GPa, as expected, and the 33.6 GPa pattern could be indexed based on a two-phase mixture of Eu-VI plus $hR6$. On further pressure increase to 36 GPa, the clear change in the pattern was observed, and the 36 GPa pattern could then be indexed based on a two-phase mixture of Eu-IV and $cI12$. The transition in the contaminant is most noticeable at low diffraction angles, due

to the high degree of overlap with Eu-VI reflections at higher angles. This is illustrated in figure 5.11, which shows the low-angle sections of the diffraction profiles of Eu-IV plus $hR6$ at 33.6 GPa, and Eu-VI plus $cI12$ at 36 GPa. The transition pressure was therefore determined to be 34.8(12) GPa.

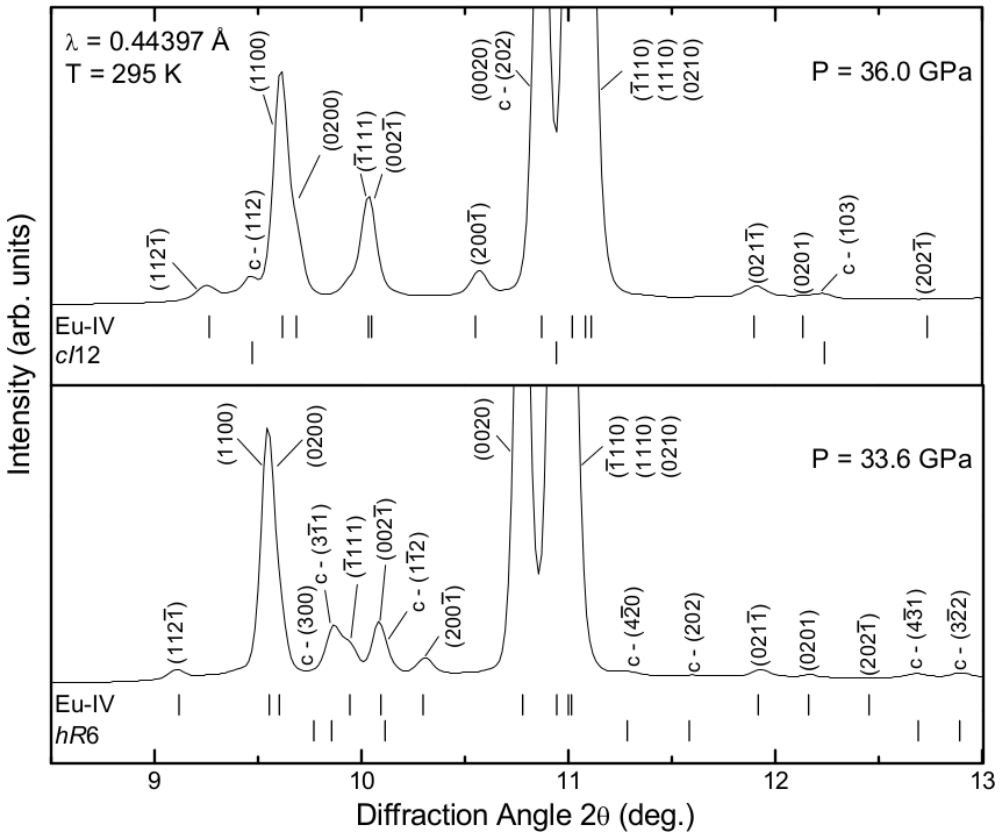

Figure 5.11: X-ray powder diffraction profiles of Eu-IV plus the $hR6$ contaminant at 33.6 GPa (lower profile), and Eu-IV plus the $cI12$ contaminant at 36.0 GPa (upper profile). The tick marks beneath the profiles show the calculated peak positions of the three phases. The corresponding Miller indices are given above the profiles, using $(hklm)$ notation for the incommensurate phases. c indicates reflections from the contaminant phase.

Although the transition at 31.5 GPa was identified in initial studies, the complex patterns obtained from Eu-IV made it impossible to index this phase with the presence of contaminant reflections. In particular, the hcp $\rightarrow$ i-$mC4$ and $hR6 \rightarrow$ $cI12$ transitions occur at very similar pressures. Additionally, two of the most intense i-$mC4$ satellite reflections appear at very similar d-spacings as the most intense of the $hR6$ reflections.

5.0.5 Conclusions

Angle-dispersive powder x-ray diffraction measurements on a non-contaminanted Eu sample have identified a transition to a new phase, Eu-IV, above 31.5 GPa. This phase has an incommensurately-modulated crystal structure with a C-centred monoclinic average structure and a modulation wave vector in the $a - c$ plane. This is the first structure of this type to be observed in a lanthanide element, and the first incommensurately-modulated structure to be observed in the elements at high pressure in which the modulation wave vector is not along one of the crystallographic axes. It would be desirable to be able to identify the mechanism driving the formation of the modulation wave. However, Eu is known to be challenging for DFT calculations due to the presence of the localised $4f$-electrons. This therefore remains a challenge for future computational studies.

Chapter 6

The Structure of Eu-V

6.1 Introduction

In order to investigate the structural behaviour of Eu above 38 GPa, angle-dispersive powder x-ray diffraction experiments have been performed on a non-contaminated Eu sample up to 46 GPa, the results of which are discussed in section 6.2.1. A transition to a second new phase, Eu-V, is observed above 38 GPa. This phase also has an incommensurately-modulated crystal structure with the same superspace group as Eu-IV, but the modulation wave vector has a different magnitude and direction. This is the first example of an incommensurately-modulated to incommensurately-modulated transition in the elements at high pressure.

Having identified the structure of Eu-V, it was then possible to go back and analyse data collected on a contaminated sample up to ∼70 GPa, the results of which are discussed in section 6.2.2. However, significant peak broadening observed on compression above ∼40 GPa make it increasingly difficult to determine accurate lattice parameters.

In addition, high-temperature high-pressure *in situ* powder x-ray diffraction experiments were performed up to 449 K, the results of which are described in section 6.2.3. Consequently, an initial estimate of the phase boundaries of the bcc, hcp, and incommensurate phases has been made.

The majority of the work described in this chapter has been published in Phys.

Rev. B [1].

6.2 Experimental Results

6.2.1 The Structure of Eu-V

Angle-dispersive powder x-ray diffraction data were collected on sample 1 up to a maximum pressure of 40.1 GPa. The *i*-$mC4$ structure gives an excellent fit to the diffraction profiles collected in the 31.5–38 GPa region, as discussed in chapter 5. However, this structure cannot explain the patterns collected at higher pressures. This suggested a transition to a new phase, Eu-V, above 38 GPa. Similar behaviour was observed in sample 8, which was loaded with a He pressure-transmitting medium (PTM).

Initial attempts to index this new phase were unsuccessful. However, analysis of data from these samples was complicated by the presence of the $cI12$ contaminant reflections. The diffraction profiles from Eu above 31.5 GPa are extremely complex, and great care must be taken in order to find a unique structural solution for the new phases. It was therefore essential to collect data on non-contaminated samples to avoid misidentification of contaminant peaks as those from pure Eu, particularly as the behaviour of the contaminant phase has only been established up to 38 GPa.

A sample was therefore loaded without a pressure marker and without a PTM with the aim of obtaining another non-contaminated sample (sample 12). Angle-dispersive powder x-ray diffraction data were collected from this sample on beamline I15 at Diamond Light Source up to a maximum pressure of 46 GPa, the highest pressure that could be reached with the pressure cell. No evidence of the $hR6$ contaminant reflections were observed in the diffraction patterns collected above 17 GPa, and Eu remained in the hcp phase up to 31.5 GPa, confirming that the sample was 'clean'. Above this pressure, changes in the diffraction profile characteristic of the transition to Eu-IV were observed. Further data were then collected in $\sim$1 GPa steps so that subtle changes in the diffraction patterns could be identified.

In agreement with the work described in chapter 5, the *i*-$mC4$ structure gives an excellent fit to the diffraction patterns collected in the 31.5–38 GPa region. The

highest-pressure single-phase i-$mC4$ pattern at 38 GPa is shown in figure 6.1, where only first order ($m = \pm 1$) satellite reflections are observed. A Rietveld refinement of the i-$mC4$ structure based on the diffraction profile of Eu at 38 GPa gives lattice parameters of $a = 3.0508(4)$ Å, $b = 5.2196(4)$ Å, $c = 4.6524(4)$ Å and $\beta = 90.541(9)°$, and the atomic coordinate $y = 0.3264(9)$, with wave vector components $q_1 = 0.7684(5)$ and $q_3 = 0.5864(4)$ and modulation amplitudes of $B_{1a} = -0.048(4)$, $A_{1b} = 0.0292(15)$, and $B_{1c} = 0.0557(14)$. These parameters are in agreement with the structural parameters that were determined for this phase in chapter 5.

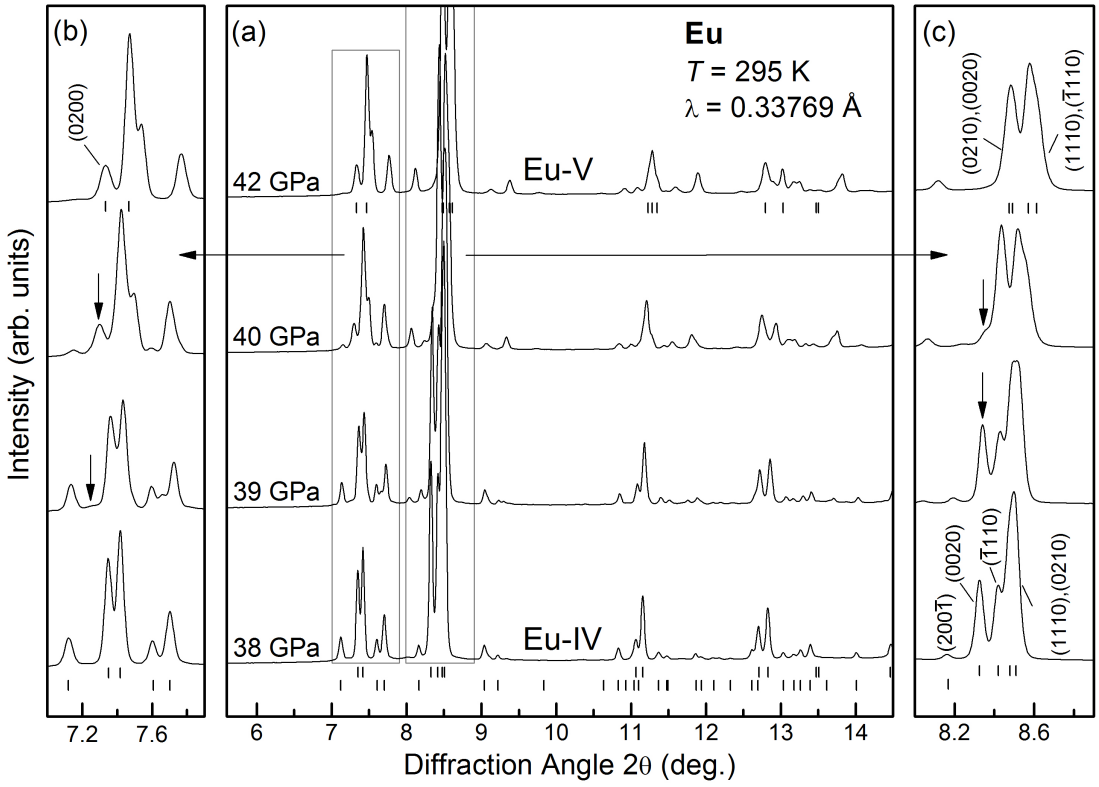

Figure 6.1: (a) X-ray powder diffraction profiles of Eu at 38, 39, 40 and 42 GPa illustrating the transition from Eu-IV to Eu-V. The 38 GPa profile can be indexed as single-phase Eu-IV, the 39 and 40 GPa profiles are mixed-phase, and the 42 GPa profile is single-phase Eu-V. The tick marks below the 38 GPa pattern show the calculated peak positions of the main (upper) and satellite (lower) reflections from i-$mC4$, and the tick marks below the 42 GPa pattern show the positions of the $mC4(2)$ reflections. The indices above the 42 GPa profile correspond to describing the $mC4(2)$ structure with $\beta < 90°$. (b) Enlargement showing the behaviour of the growth of the (0200) Eu-V reflection over the transition. This reflection is not present in the i-$mC4$ diffraction pattern. (c) Enlargement showing the behaviour of the (0020), ($\bar{1}$110), (1110) and (0210) i-$mC4$ reflections over the transition. The arrows indicates the disappearance of the (0020) i-$mC4$ reflection.

Above 38 GPa, we observed changes in the diffraction profiles which meant that

they could no longer be described by the *i-mC*4 structure. This was taken as evidence of a transition to a new phase, Eu-V, which was complete by 42 GPa. This is illustrated in figure 6.1(a), which shows diffraction patterns from Eu in the Eu-IV phase at 38 GPa, in the mixed-phase region at 39 and 40 GPa, and in the Eu-V phase at 42 GPa. The changes in the diffraction profiles during the transition can be characterised by three distinct features. Firstly, we observed the appearance of a set of new reflections that cannot be accounted for by the *i-mC*4 structure. Secondly, the intensity of the *i-mC*4 satellite reflections began to decrease until they had completely disappeared by 42 GPa. Finally, subtle changes in the main *i-mC*4 reflections were also observed. In particular, the intense (0020) *i-mC*4 main reflection was observed to decrease in intensity until it had completely disappeared by 42 GPa, as illustrated in figure 6.1(c).

Additional data from sample 12 were collected on beamline P02.2 at PETRA-III and in a second experimental run on I15, where the pressure was first decreased in order to observe the transition back into the Eu-IV phase, and then increased again to transform back into the Eu-V phase. In this case, we observed the Eu-IV $\rightarrow$ EuV transition at a slightly lower pressure, and the lowest-pressure single-phase Eu-V pattern was collected at 40.3 GPa. These additional data sets were considered alongside the original data collected on I15 during the process of indexing the patterns from the new phase. However, the short wavelength used at P02.2 ($\sim$0.29 Å) means that the splitting of the reflections could not be resolved as clearly as in the data collected at the other beamlines, where longer wavelengths were used ($\sim$0.34 Å at I15 and $\sim$0.41 Å at ID09a). For this reason, data from this run are not included in the plots of structural parameters included later in this chapter.

Attempts to index all of the reflections from Eu-V based on a crystal structure with a three-dimensional space group were unsuccessful. However, it was noted that the overall diffraction profile of the new phase is very similar to that of Eu-IV. In addition, a large number of weak reflections appear at the transition. This suggested the possibility that Eu had transformed to a second incommensurately-modulated crystal structure, and that the new set of reflections are satellite reflections.

In order to index the Eu-V patterns based on an incommensurately-modulated crystal structure, it is first necessary to identify the main diffraction peaks so as to determine the average structure. However, although there is clear distinction between main ($m = 0$) and satellite ($m \neq 0$) reflections in the diffraction

patterns from the Eu-IV phase, the reflections in the Eu-V patterns cannot be distinguished with the same certainty. The main *i*-$mC4$ reflections in the Eu-IV patterns can be identified by two distinct features. Firstly, they are much more intense than the surrounding satellite reflections. Secondly, they result from a continuous splitting of the hcp reflections as Eu transforms from hcp to the lower-symmetry monoclinic Eu-IV structure. However, these features are not so easily identifiable in the Eu-V patterns. The positions of some of the main *i*-$mC4$ reflections can be clearly identified over the course of the Eu-IV to Eu-V transition, and we therefore assumed these also to correspond to main reflections of the new phase. As noted previously, at least one of the main *i*-$mC4$ reflections, (0020), disappears at the transition, suggesting that there is a change in the average structure. A further complication is introduced by the fact that some of the new reflections that appear at the transition have an intensity comparable to that of the main Eu-IV reflections, and it is not immediately obvious if these are main or satellite reflections from the new phase.

However, the changes in the main *i*-$mC4$ reflections at the transition to Eu-V are subtle. It was therefore initially assumed that the average structure of both phases is similar. The DICVOL program [63] was therefore used to index a subset of the reflections based on a similar monoclinic unit cell, ensuring that all of the reflections previously identified as main Eu-V reflections were accounted for. The best fit was obtained using a monoclinic structure with space group $C2/c$ (number 15) with the atoms in the $4e$ (0, y, 0.25) Wyckoff positions. A Rietveld refinement of this structure to the 42 GPa diffraction profile gives lattice parameters of $a = 2.9756(18)$ Å, $b = 5.278(6)$ Å, $c = 4.564(4)$ Å and $\beta = 90.34(7)°$, with the atomic coordinate $y = 0.337(5)$. This structure will be referred to as $mC4(2)$, where the 2 distinguishes it from the average Eu-IV structure, $mC4$.

The positions of the main $mC4(2)$ reflections are shown by the tick marks under the 42 GPa diffraction profile of Eu in figure 6.1. This structure can account for the set of reflections originally identified as the main Eu-IV reflections, and also at least one of the new reflections that appeared at the transition. For example, the growth of the (0200) Eu-V reflection is shown in figure 6.1(b), which is not directly related to any of the peaks in the Eu-IV pattern.

The program SUPERCELL [64] was then used to index the remaining reflections as satellite reflections corresponding to a modulation vector in the $a - c$ plane, (q_1, 0, q_3), with $q_1 \approx 0.59$ and $q_3 \approx 0.59$. Analysis of systematic absences found the superspace group to be $C2/c(q_1 0 q_3)0s$ [*i*-$mC4(2)$, where again the (2)

distinguishes this from the Eu-IV *i*-$mC4$ structure]. This setting of *i*-$mC4(2)$ will subsequently be referred to as setting (a). Note that in all settings discussed here, the only parameters that differ are the monoclinic angle β and the wave vector component q_3. For this reason, these components will be labelled as β_a and q_{3a} in setting (a).

A Rietveld refinement of the *i*-$mC4(2)$ structure to the diffraction profile of Eu at 42 GPa is shown in figure 6.2, where only first order ($m = \pm 1$) satellite reflections have been considered. The refined structural parameters are $a = 2.9761(1)$ Å, $b = 5.2808(2)$ Å, $c = 4.5613(2)$ Å, $\beta_a = 90.373(3)^\circ$ and the atomic coordinate $y = 0.3377(3)$, with wave vector components $q_1 = 0.5869(1)$ and $q_{3a} = 0.5877(1)$ and modulation amplitudes of $A_{1a} = 0.0611(8)$, $B_{1b} = 0.0424(6)$, and $A_{1c} = 0.0679(4)$. As with Eu-IV, all other first-order Fourier components are equal to zero due to symmetry conditions imposed by the $C2/c(q_1 0 q_3)0s$ superspace group.

However, the $C2/c(q_1 0 q_3)0s$ superspace group is a non-standard setting. The s indicates that the c-glide includes a centring component along the $\vec{a}_{s4}$ direction in superspace, as explained in section 2.3.4. It order to compare the structure of Eu-V with that of Eu-IV, it is then necessary to transform from $C2/c(q_1 0 q_3)0s$ to the standard $C2/c(q_1 0 q_3)00$ superspace group setting. This can be done by considering the systematic absences of the two settings, which are given in table 6.1. The s changes the allowed reflection conditions for $h0lm$ and $00lm$ reflections from $l = 2n$ to $l+m = 2n$, with all other reflection conditions remaining the same.

Space groups	**Reflection conditions**		
	$hklm$, $0klm$	$h0lm$, $h00m$	$0k0m$
	$hk0m$	$00lm$	
$C2/c(q_1 0 q_3)00$	$h + k = 2n$	$h = 2n$	$k = 2n$
		$l = 2n$	
$C2/c(q_1 0 q_3)0s$	$h + k = 2n$	$h = 2n$,	$k = 2n$
		$l + m = 2n$	

Table 6.1: The systematic absences for the $C2/c(q_1 0 q_3)00$ and $C2/c(q_1 0 q_3)0s$ superspace groups, where n is an integer, as taken from references [19] and [20].

In the $C2/c(q_1 0 q_3)0s$ superspace group, each of the Bragg reflections can be indexed according to $\vec{H} = h\vec{a}^* + k\vec{b}^* + l_a\vec{c}^* + m(q_1\vec{a}^* + q_{3a}\vec{c}^*)$. It is possible to make the transformation $l_a = l_b + m$. This gives:

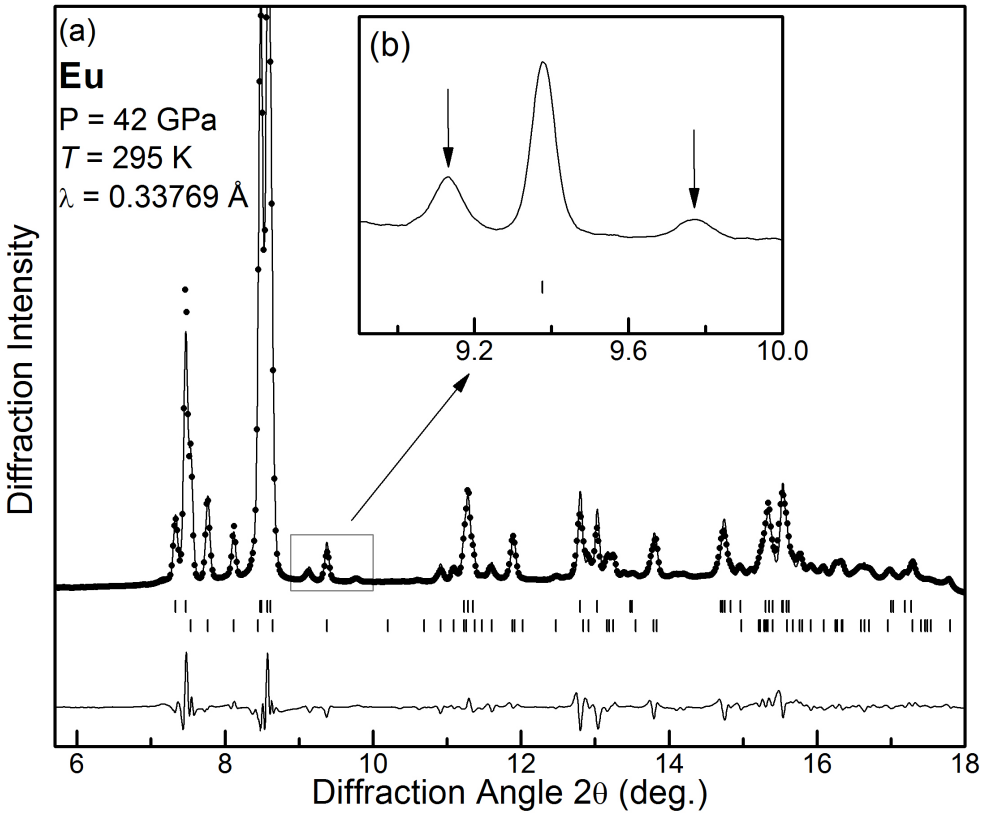

Figure 6.2: Rietveld refinement of the i-$mC4(2)$ structure based on the diffraction profile of Eu at 42 GPa, where only first order ($m = \pm 1$) satellite reflections have been considered. In panel (a), the points show the experimental data, and the solid line shows the fit. The tick marks below the profile show the calculated peak positions of the main (upper) and satellite (lower) reflections, and the residuals are shown below the tick marks. Inset (b) illustrates the most intense reflections that cannot be accounted for by main or first-order satellite reflections, which are indicated by the arrows above the profile. In this case, the solid line shows the experimental data.

$$\begin{aligned} \vec{H} &= h\vec{a}^* + k\vec{b}^* + (l_b + m)c^* + m(q_1\vec{a}^* + q_{3a}\vec{c}^*) \\ &= h\vec{a}^* + k\vec{b}^* + l_b\vec{c}^* + m(q_1\vec{a}^* + (q_{3a} + 1)\vec{c}^*) \\ &= h\vec{a}^* + k\vec{b}^* + l_b\vec{c}^* + m(q_1\vec{a}^* + q_{3b}\vec{c}^*) \end{aligned}$$

The reflection conditions for $C2/c(q_1 0 q_3)00$ are then recovered. That is, the condition $l_b = 2n$ ensures the condition $l_a + m = 2n$ is also fulfilled. The average structure, $mC4(2)$, is the same in both settings, as is the wave vector component q_1, but the transformation $q_{3b} = q_{3a} + 1$ has been made. The modulation vector for this superspace group is then ($\sim$0.59, 0, $\sim$1.59). This setting will subsequently be referred to as setting (b), with $\beta_b > 90°$ and $q_{3b} \approx 1.59$. It is also possible to make the transformation $l_a = l_c - m$, which gives a modulation wave vector of $q_{3c} = q_{3a} - 1 \approx -0.41$. This will subsequently be referred to as setting (c), with

$\beta_c > 90°$ and $q_{3c} \approx -0.41$.

The equivalence of settings (a)–(c) can be easily seen by considering the reciprocal lattice for the i-$mC4(2)$ structure in the $(h0l)$ plane in reciprocal space. This is illustrated in figures 6.3(a)–(c). The systematic absences of the $C2/c(q_1 0 q_3)0s$ superspace group mean that satellite reflections are observed for some of the main reflections that are absent, and satellite reflections are not observed for some of the main reflections that are present, as shown in figure 6.3(a). The equivalence of the wave vector components $q_{3b} \approx 1.59$ and $q_{3c} \approx -0.41$ in the $C2/c(q_1 0 q_3)00$ superspace group can be seen in figures 6.3(b) and (c). Note that if the C-centring was not present, all wave vector components that differ by integer values are equivalent.

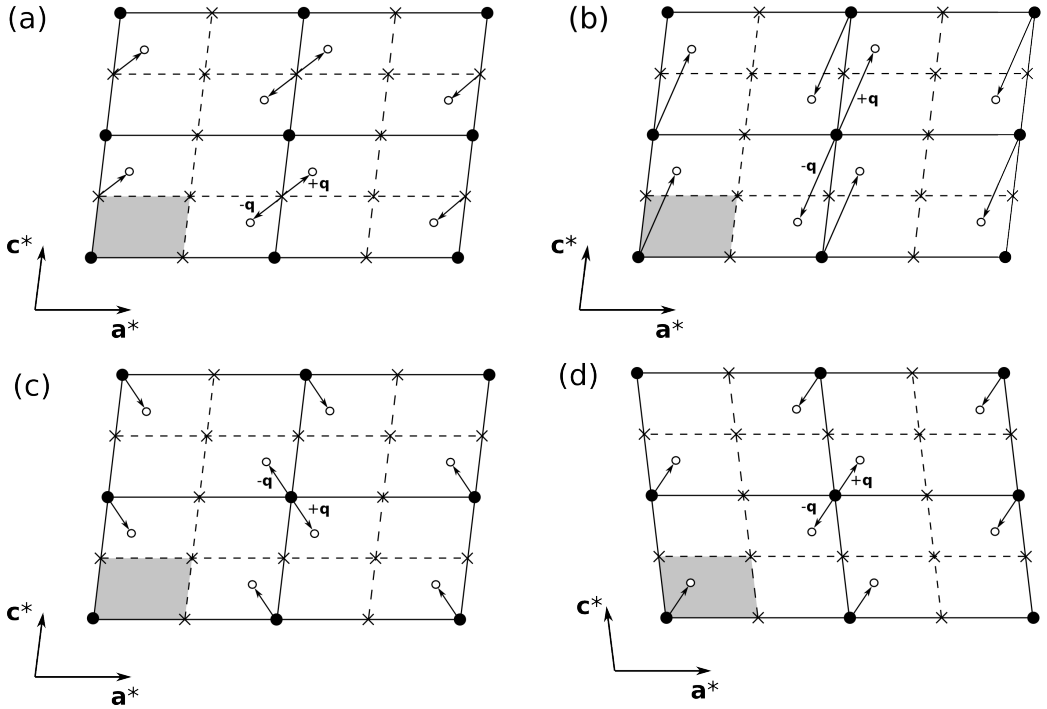

Figure 6.3: Different settings of the i-$mC4(2)$ structure in the $(h0l)$ plane in reciprocal space. A summary of the different settings is given in table 6.2.
(a) Setting (a) with $\beta_b > 90°$, $q_1 \approx 0.59$ and $q_{3a} \approx 0.59$.
(b) Setting (b) with $\beta_b > 90°$, $q_1 \approx 0.59$ and $q_{3b} = q_{3a} + 1 \approx 1.59$.
(c) Setting (c) with $\beta_c > 90°$, $q_1 \approx 0.59$ and $q_{3c} = q_3 - 1 \approx -0.41$.
(d) Setting (d) with $\beta_d < 90°$, $q_1 \approx 0.59$ and $q_{3d} = 1 - q_3 \approx 0.41$.
The solid symbols show the main Bragg reflections, the open circles show the first-order satellite reflections, and the crosses show the positions of the main Bragg reflections that are not observed due to the allowed reflection conditions.

The (a)–(c) settings are all descriptions of the i-$mC4(2)$ structure with $\beta > 90°$. It is also possible to describe this structure in setting (d), with $\beta_d = 180° - \beta_a <$

90°. Again, the wave vector components of this setting can be determined by considering the $(h0l)$ plane in reciprocal space, illustrated in figure 6.3(c). From this, it can be seen that q_1 remains the same, but $q_{3d} = 1 - q_{3a}$. A summary of the 4 settings of *i*-$mC4$, (a)–(d), is given in table 6.2.

Setting	**Superspace group**	**Monoclinic angle**	q_3
(a)	$C2/c(q_1 0 q_3)0s$	$\beta_a > 90°$	q_{3a}
(b)	$C2/c(q_1 0 q_3)00$	$\beta_b > 90°$	$q_{3b} = q_{3a} + 1$
(c)	$C2/c(q_1 0 q_3)00$	$\beta_c > 90°$	$q_{3c} = q_{3a} - 1$
(d)	$C2/c(q_1 0 q_3)00$	$\beta_d < 90°$	$q_{3d} = 1 - q_{3a}$

Table 6.2: Equivalent settings of the *i*-$mC4(2)$ structure. The lattice parameters a, b and c, and the modulation wave vector component q_1, are the same in each setting. The equivalence of these descriptions in the $(h0k)$ plane in reciprocal space is illustrated in figure 6.3. Unless it is explicitly stated, the *i*-$mC4(2)$ structure will be described in setting (b) throughout this chapter.

The *i*-$mC4$ was described with $\beta > 90°$. In order to compare the structure of *i*-$mC4(2)$ with *i*-$mC4$, it is therefore necessary to also describe it with $\beta > 90°$. For this reason, the *i*-$mC4(2)$ structure will predominantly be described in setting (b) from this point onward. A Rietveld refinement of the *i*-$mC4(2)$ structure in setting (b) to the 42 GPa profile gives structural parameters of $a = 2.9761(3)$ Å, $b = 5.2809(7)$ Å, $c = 4.5613(6)$ Å, $\beta_a = 90.372(10)°$ and the atomic coordinate $y = 0.3371(9)$, with wave vector components $q_1 = 0.5869(3)$ and $q_{3a} = 1.5877(4)$ and modulation amplitudes of $B_{1a} = 0.061(3)$, $A_{1b} = -0.041(2)$, and $B_{1c} = 0.0667(15)$. Note that this is equivalent to the Rietveld refinement shown in figure 6.2(a).

The *i*-$mC4(2)$ structure with first-order satellite reflections gives a reasonable fit to the diffraction pattern at this pressure. However, there are a small number of weak reflections that are not accounted for, the most intense of which are highlighted in figure 6.2(b). In order to test if these arise from higher-order satellite reflections, a single exposure of sample 12 was collected at ID09a following the pressure cycling described previously. A Rietveld refinement of the *i*-$mC4(2)$ structure to this 40.3 GPa pattern is shown in figure 6.4, where up to third-order ($m = \pm 3$) satellite reflections have been considered. The inclusion of second- and third-order satellite reflections results in an improved fit ($R_p = 5.6\%$ and $R_{wp} = 8.9\%$) in comparison with a refinement in which only first-order satellite reflections are considered ($R_p = 6.5\%$ and $R_{wp} = 10.3\%$). A larger

number of second-order satellite reflections (≈12) are observed in this pattern, as well as a number of third-order satellite reflections, as illustrated in figure 6.4(b). Crucially, this structure can also explain a number of extremely weak satellite reflections at low angles, as illustrated in figure 6.4(c), which were not observed in the original data collected at I15 and which were therefore not used in the determination of the *i*-$mC4(2)$ structure model. The parameters of the final solution for the *i*-$mC4(2)$ structure at 40.3 GPa are therefore a = 2.9886(3) Å, b = 5.2987(3) Å, c = 4.5720(4) Å, β = 90.328(8)°, and y = 0.3365(9), with a modulation wave vector of [0.5863(3), 0, 1.5865(2)]. The refined modulation amplitudes are B_{1a} = 0.042(5), A_{1b} = 0.0363(2), B_{1c} = 0.0693(19), B_{2a} = 0.035(6), A_{2b} = 0.008(3), B_{2c} = 0.019(3), B_{3a} = 0.018(11), A_{3b} = 0.008(4), and B_{3c} = 0.004(4). It should be stressed that, although the values determined for the third-order modulation amplitudes are small, the third-order satellites are clearly visible in the diffraction profile, as highlighted in figures 6.4(b) and (c).

The pressure dependencies of the lattice parameters (a, $b/\sqrt{3}$, c, c/a, b/a and vol/atom), across the transition from hcp to *i*-$mC4$ and then to *i*-$mC4(2)$, are shown in figures 6.6(a)–(f). Again, the hcp structure is described in the orthohexagonal setting. For this reason, the pressure dependence of a and $b/\sqrt{3}$ are shown in the same panel for comparison. Discontinuities are observed in all of the lattice parameters and their ratios (a, $b/\sqrt{3}$, c, c/a, b/a) across the *i*-$mC4$ to *i*-$mC4(2)$ transition, although no discontinuity was observed in the volume. In particular, the b/a ratio was observed to decrease away from $\sqrt{3}$ following the transition to *i*-$mC4$, and then increase away from $\sqrt{3}$ following the transition to *i*-$mC4(2)$, as shown in figure 6.6.

The pressure dependencies of the modulation wave vector components (q_1 and q_3) and the modulation amplitudes (B_{1a}, A_{1b} and B_{1c}), across the transition from *i*-$mC4$ to *i*-$mC4(2)$, are shown in figures 6.7(a)–(e). The *i*-$C4(2)$ structure has been described in setting (a), as this corresponds to a value of q_{3a} that is similar to that of q_3 in *i*-$mC4$. A discontinuous jump is observed in q_1, going from 0.7658(5) at 38 GPa in the Eu-IV phase to 0.5872(4) at 42 GPa in the Eu-V phase. The wave vector component q_3 is observed to vary smoothly over the transition, going from 0.5865(3) at 38 GPa in the Eu-IV phase to 0.5877(3) at 42 GPa in the Eu-V phase. However, the increase of q_3 above ∼36 GPa in the Eu-IV phase is much more pronounced than what was observed in the value of q_3 determined from samples 1 and 11 in the previous section (figure 5.5). The sign of the B_{1a} and A_{1b} changes over the transition, with B_{1a} going from -0.044(3) to 0.0286(15) and

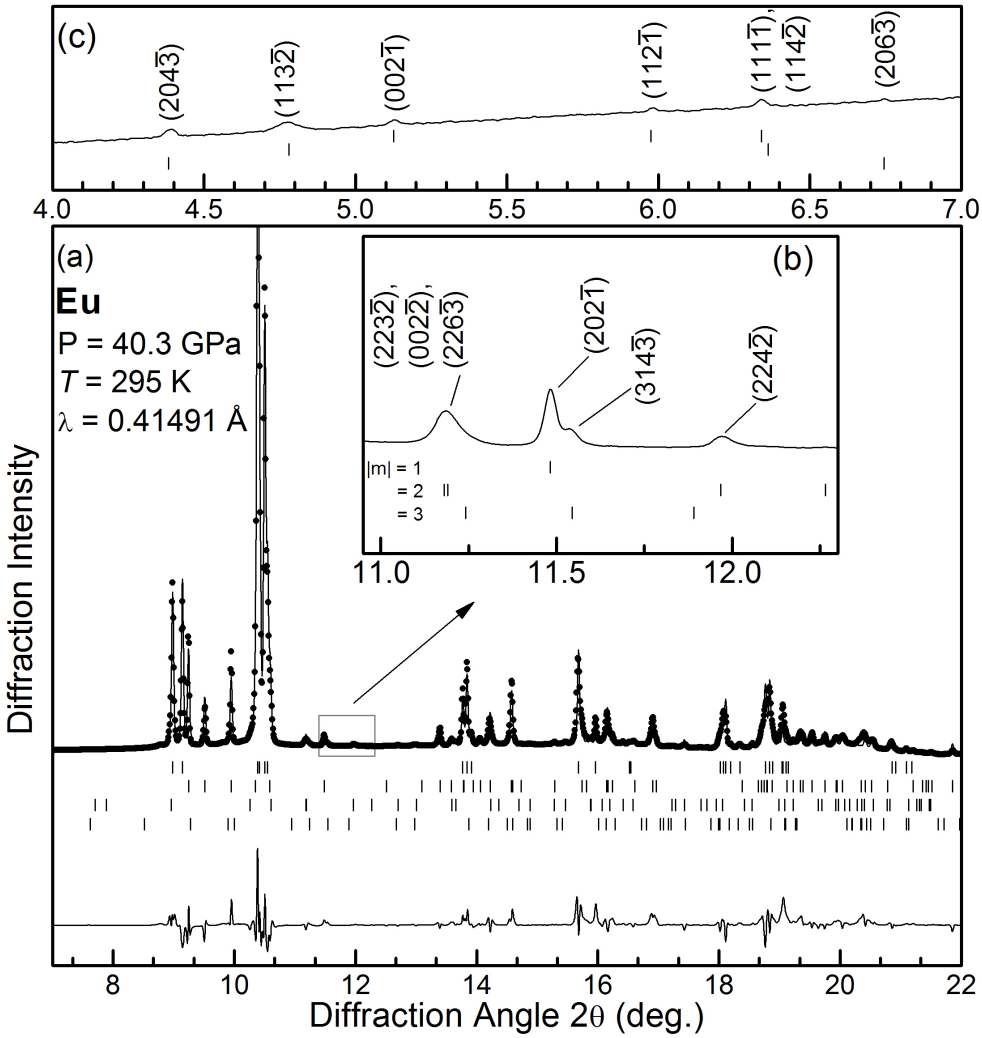

Figure 6.4: Rietveld refinement of the i-$mC4(2)$ structure to the 40.3 GPa diffraction profile of Eu, where up to third order ($m = \pm 3$) satellite reflections have been considered. The points show the experimental data, and the solid line shows the fit. The tick marks below the profile show the calculated peak positions of the main (upper) and satellite (lower) reflections, and the residuals are shown below the tick marks. Inset (b) illustrates weak reflections that cannot be described as main or first-order satellite reflections, but can be accounted for when up to third-order satellite reflections are considered. Inset (c) illustrates a number of extremely weak low-angle satellite reflections that can be described by this structure. In insets (b) and (c), the solid line shows the experimental data. The indices correspond to describing the i-$mC4(2)$ structure in setting (b).

A_{1b} going from 0.056(2) to -0.0390(10). An increase in B_{1c} is observed across the transition, going from 0.0549(13) at 38 GPa in the Eu-IV phase to 0.068(12) at 42 GPa in the Eu-V phase.

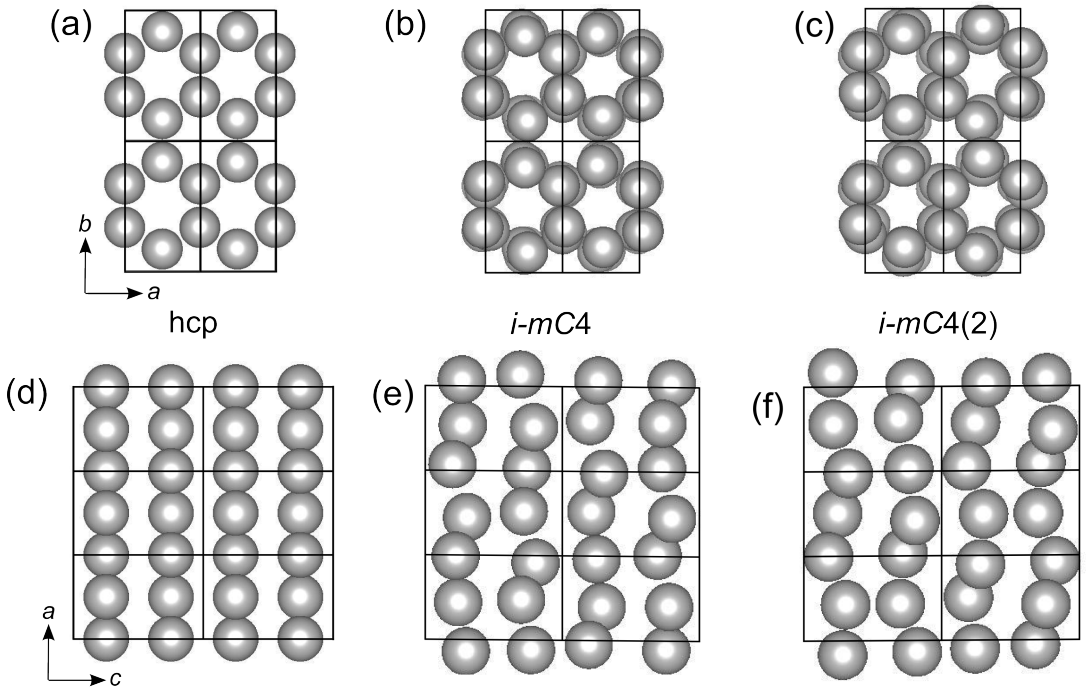

Figure 6.5: Schematic views of the hcp, *i*-$mC4$ (Eu-IV) and *i*-$mC4(2)$ (Eu-V) structures at <31.5, 38 and 41 GPa, respectively. Four unit cells viewed along the c direction of the (a) hcp, (b) *i*-$mC4$ and (c) *i*-$mC4(2)$ structures, and one unit cell viewed along the b direction of the (d) hcp, (e) *i*-$mC4$ and (f) *i*-$mC4(2)$ structures. The modulation amplitudes are drawn to scale.

6.2.2 Higher Pressures

Having solved the structure of Eu-V, it was then possible to go back and fit the patterns collected on samples that also contained diffraction peaks from the $cI12$ contaminant phase. One single-phase Eu-V pattern was collected from sample 1 at 40.1 GPa, and the *i*-$mC4(2)$ structure gives an excellent fit to this pattern when up to $m = \pm 2$ satellite reflections are considered.

The maximum pressure reached in any of the studies was obtained in sample 8, which was loaded with a He PTM. Data from this sample were collected up to 70.1 GPa in ∼1 GPa steps. However, the pressure of the sample jumped from 19.6 GPa, where the sample was in the hcp phase, to 32.5 GPa, where the sample had already transformed to Eu-IV. Analysis of this data was complicated by the fact that contaminant reflections from at least one impurity phase, in addition to those from the $cI12$ contaminant phase, were present. The highest-pressure single-phase Eu-IV pattern was collected at 38.5 GPa, a mixed-phase Eu-IV/Eu-V pattern was collected at 39.4 GPa, and the first single-phase Eu-V pattern

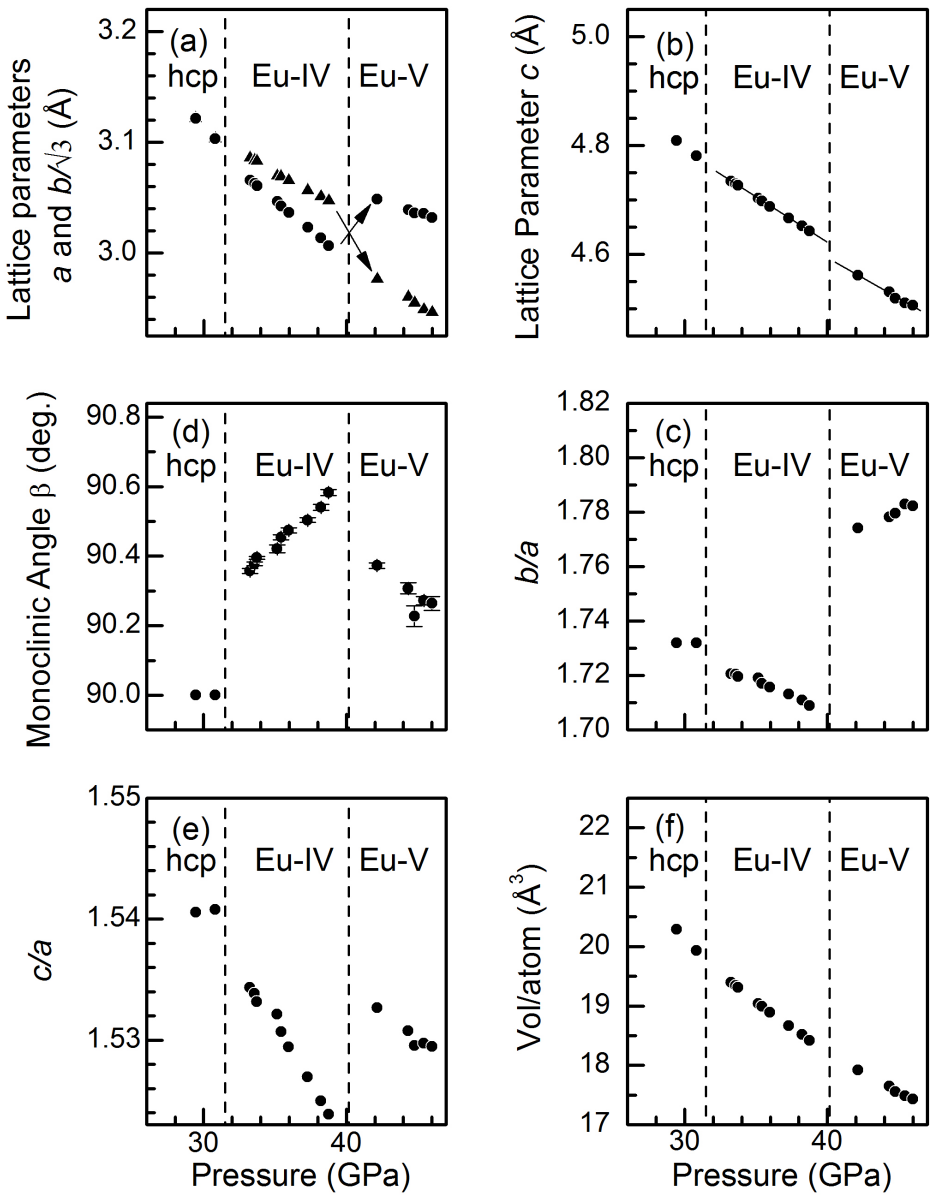

Figure 6.6: Lattice parameters of Eu as a function of pressure, across the transition from hcp to *i*-$mC4$ (Eu-IV) and then to *i*-$mC4(2)$ (Eu-V). The hcp structure is described in the orthohexagonal setting, where the b/a axial ratio is equal to $\sqrt{3}$. For this reason, the pressure dependence of a (triangles) and $b/\sqrt{3}$ (circles) are both shown in panel (a), in order to illustrate the distortion of the structure from hcp. The arrows on panel (a) and the lines on panel (b) are added as guides to the eye. The lattice parameters were obtained from Rietveld fits to the diffraction profiles. With the exception of β, the error bars are smaller than the symbol size and so have been omitted.

was collected at 40.5 GPa. The transition to Eu-V pattern was observed at a slightly lower pressure than initially observed in sample 12, where the first Eu-V pattern was collected at 42 GPa. However, it should be noted that following pressure-cycling, the first Eu-V pattern was collected at a slightly lower pressure

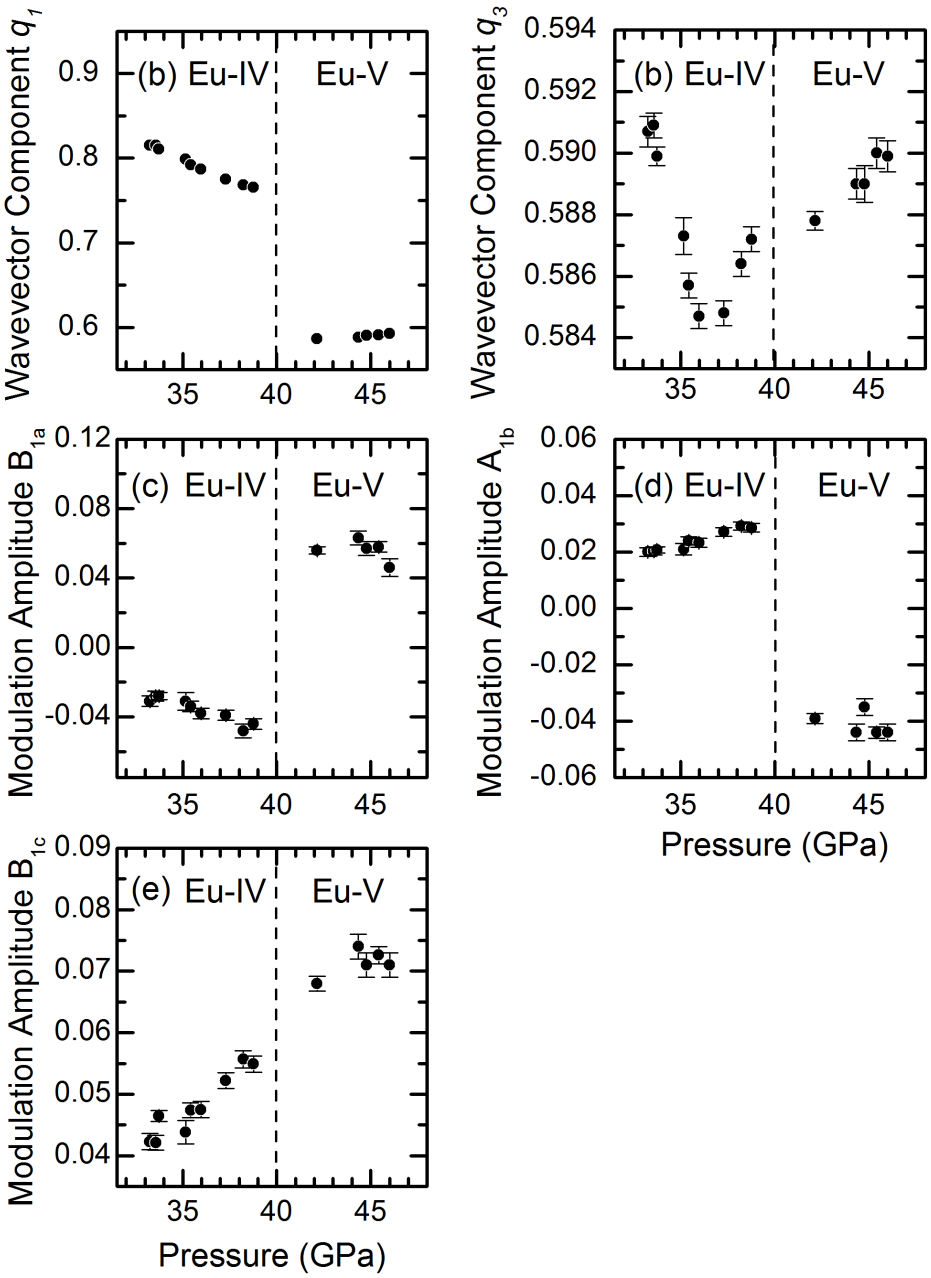

Figure 6.7: Modulation wave vector components (q_1 and q_3) and modulation amplitudes (B_{1a}, A_{1b} and B_{1c}) of Eu as a function of pressure, across the transition from *i*-$mC4$ (Eu-IV) to *i*-$mC4(2)$ (Eu-V). All parameters were obtained from Rietveld fits to the diffraction profiles. With the exception of q_3, the *i*-$mC4(2)$ structure is described in setting (b). However, q_3 is described in setting (a), as q_{3a} has a similar value to q_3 of *i*-$mC4$. The estimated uncertainties in q_1 are smaller than the symbol size and so have been omitted.

of 40.3 GPa.

The *i*-$mC4(2)$ structure provides a good fit to the diffraction patterns collected up to ∼50 GPa. However, this structure has a large number of refinable parameters

(a, b, c, β, q_1, q_3) that are determined by the peak positions in the diffraction profile, and accurate peak positions of at least seven reflections are required in order to determine the the unit cell dimensions and wave vector components. The diffraction profiles from this phase are extremely complex, with a large number of closely-spaced reflections, and very high-resolution data are required in order to resolve individual peaks. Despite the use of a helium pressure medium, significant broadening of the sample reflections above ∼40 GPa made it increasingly difficult to determine accurate unit cell dimensions. This can be seen in figure 6.8, which shows selected integrated diffraction profiles of Eu collected on sample 8 up to the maximum pressure. The calculated peak positions of the *i*-$mC4(2)$ structure, as determined from a Rietveld refinement, are shown under the 45.7 GPa pattern, where only first-order satellite reflections have been considered.

No dramatic changes are observed in the diffraction profiles collected up to ∼70 GPa, and the overall shape of the patterns is similar. However, it should be noted that the *i*-$mC4$ and *i*-$mC4(2)$ diffraction profiles are very similar, and the transition was identified by relatively subtle changes in the diffraction profiles. The possibility of similar transitions occurring at higher pressures therefore cannot be ruled out. However, it is noted that above 47.1 GPa, the (0001) reflection is observed to split into a doublet, with the splitting increasing at higher pressures, as highlighted in figure 6.8. This cannot be accounted for by the *i*-$mC4(2)$ structure when up to third-order satellite reflections are considered. However, there are reflections from at least two contaminant phases present in the diffraction patterns collected at lower pressures. The possibility that the apparent splitting is actually due to the presence of a contaminant reflection with a similar d-spacing to that of the (0001) reflection therefore cannot be ruled out. However, a simultaneous change in the the relative intensities of the (1100) and (113$\bar{1}$) reflections is observed, which is also highlighted in figure 6.8. Taken together, these changes provide evidence for a possible further structural transition at 47.1 GPa. High-resolution diffraction data collected on a non-contaminated sample should therefore be collected in order to determine if the changes in the diffraction profiles are due to a structural transition in Eu itself, or simply due to the presence of sample contaminants.

Unless Eu transforms to a higher-symmetry structure, the determination of the structural behaviour at pressure exceeding ∼50 GPa will be extremely challenging due to the complexity of the diffraction patterns and the increasing broadness of the diffraction peaks. It is noted that *ab initio* structure-prediction calculations

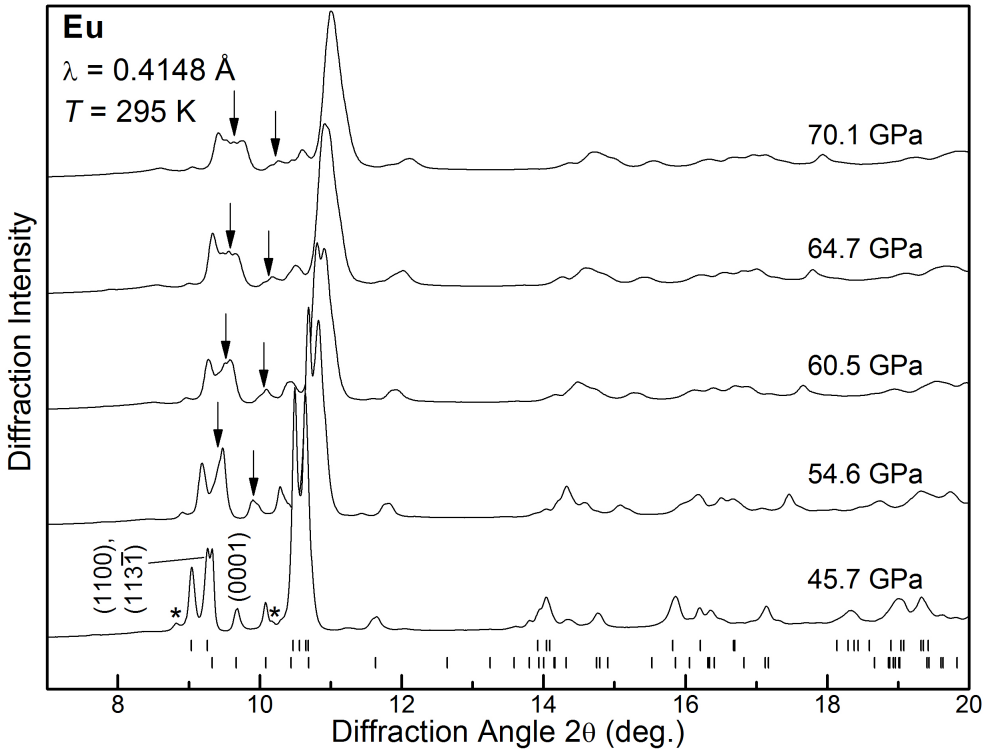

Figure 6.8: X-ray powder diffraction profiles of Eu at 45.7, 54.6, 60.5, 64.7 and 70.1 GPa collected from a sample loaded with a He PTM. The tick marks below the 45.7 GPa profile show the calculated peak positions of the main (upper) and first order satellite (lower) reflections, as determined from a Rietveld refinement of the *i*-$mC4(2)$ structure to this profile. The asterisks above the 45.7 GPa pattern indicate contaminant reflections from the $cI12$ contaminant phase. Significant peak broadening is observed at pressures above ∼45 GPa, and so it is not possible to reliably determine the lattice parameters of Eu above this pressure. The arrows indicate the splitting of the (0001) reflection into a doublet, and the simultaneous change in the relative intensity of the (1100) and (113$\bar{1}$) reflections, with increasing pressure. The splitting of the (0001) reflection cannot be described by the *i*-$mC4(2)$ structure.

by Bi *et al.* [15] determined the hcp structure to be the most stable structure of Eu above 90 GPa, which would easily be identifiable in the diffraction profiles. It is also interesting to consider the behaviour of divalent Ba, as its behaviour is often compared with that of Eu [13, 123], as the two elements are isoelectronic when the $4f$ electrons are not considered. Ba, which undergoes the bcc → hcp transition at 5 GPa, adopts a series of complex structures on further compression, before transforming to a second hcp structure above 45 GPa [26, 124, 125].

The compressibility of Eu up to 46 GPa is shown in figure 6.9. Eu is extremely compressible, and the relative volume, V/V_0, is equal to 0.363 at 46 GPa. With the exception of the bcc → hcp transition, no measurable volume discontinuities were observed up to the maximum pressure.

$$P = \frac{3B_0}{2}\left[\left(\frac{V_0}{V}\right)^{\frac{7}{3}} - \left(\frac{V_0}{V}\right)^{\frac{5}{3}}\right]\left\{1 + \frac{3}{4}(B_0' - 4)\left[\left(\frac{V_0}{V}\right)^{\frac{2}{3}} - 1\right]\right\} \tag{6.1}$$

$$P = P_R\frac{3B_0}{2}\left[\left(\frac{V_R}{V}\right)^{\frac{7}{3}} - \left(\frac{V_R}{V}\right)^{\frac{5}{3}}\right]\left\{1 + \frac{3}{4}(B_0' - 4)\left[\left(\frac{V_R}{V}\right)^{\frac{2}{3}} - 1\right]\right\} \tag{6.2}$$

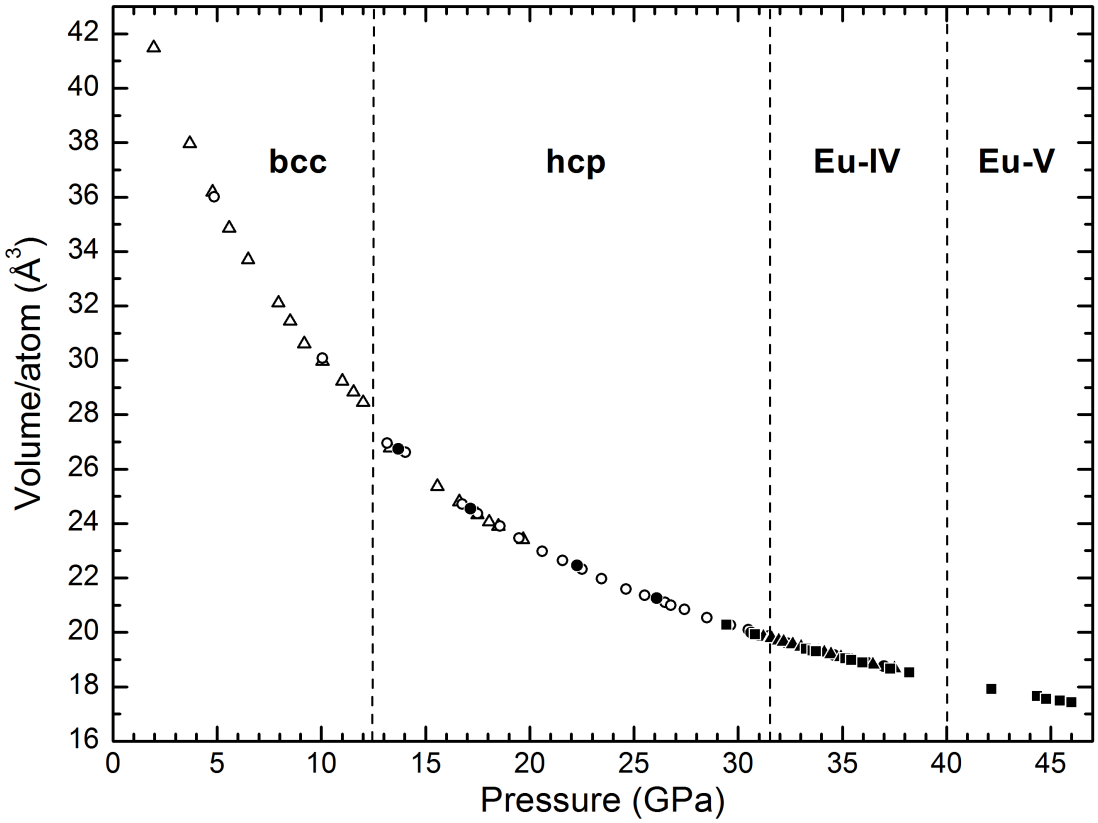

Figure 6.9: Volume per atom against pressure for Eu at ambient temperature. The Eu volumes were obtained from Rietveld fits to the diffraction patterns. The solid triangles show data collected on sample 1, the solid circles show data collected on sample 11, the solid triangles show data collected on sample 12, the open triangles show data collected on sample 8, and the open circles show data collected on sample 9. Samples 1, 11 and 12 were loaded without a PTM, and samples 8 and 9 were loaded with a He PTM. The estimated uncertainties in the atomic volumes are smaller than the symbol size and so have not been included.

A summary of the structural parameters of bcc, hcp, Eu-IV and Eu-V at selected pressures is given in table 6.10, as determined from Rieveld refinements to the diffraction profiles. No evidence of any of the crystal structures that have been observed in the trivalent lanthanides at high pressures have been observed, supporting the idea that Eu has not become trivalent by ∼70 GPa. Min *et*

al. [104] determined that a divalent to trivalent transition would involve a 7 % volume collapse. However, this would only be the case if a fully-divalent to fully-trivalent transition would occur, not a transition through mixed-valent state.

6.2.3 High-Temperature Studies

High-temperature high-pressure powder x-ray diffraction data were collected on samples 13 and 14 on beamline I15, and additional data from sample 14 were collected on beamline ID09a. In these experiments, the pressure of the sample was increased at constant temperature with the aim of determining the position of the high-temperature phase boundaries, in particular that between the hcp and incommensurate phases. Data were collected at three different temperatures: 363, 428 and 449 K. The 363 and 428 K data were each collected during a single run, and the 449 K data were collected in one run from each of the two samples. The pressure of sample 13 was increased to above 17 GPa at room temperature before the sample was heated, and no evidence of any peaks from the $hR6$ contaminant phases were observed in the diffraction profiles. However, reflections from the contaminant appeared in the patterns collected at elevated temperatures, and the intensity of these reflections was observed to increase as the sample was heated. Peaks from either the $hR6$ or $cI12$ contaminant phases were observed in all of the diffraction patterns collected from sample 14 above 17 GPa, and again the reflections were observed to grow as the sample was heated.

The results of the high-temperature studies are summarised in figure 6.11. The bcc $\rightarrow$ hcp transition, which is known to occur at 12.5 GPa at ambient temperature, was determined to occur between 11.1 and 13.6 GPa at 449 K. It is therefore tentatively suggest that the bcc $\rightarrow$ hcp phase boundary is close to vertical. The hcp $\rightarrow$ Eu-IV transition, which occurs at 31.5 GPa at ambient pressure, was determined to occur between 32.4 and 36.4 GPa at 363 K, and between 39.8 and 41.3 GPa at 428 K. This suggests that the pressure range over which the hcp phase is stable increases with increasing temperature.

At 363 K, the Eu-IV $\rightarrow$ Eu-V transition was observed to occur between 39.8 and 41.3 GPa at 313 K, which is again a slightly higher pressure than that observed at room temperature, where the transition was observed to start between 38 and 39 GPa. The Eu-IV $\rightarrow$ Eu-V phase boundary was also crossed at 428 K. However, the pressure of the sample jumped from 41.4 GPa in the Eu-IV phase to 59.5 GPa in the Eu-V phase, and the transition pressure was therefore not determined at

Phase	**Space group**	**Pressure**	**Lattice parameters**	**Atomic coordinates**	**Modulation vector**
bcc	$Im\bar{3}m$	10.1 GPa	$a = 3.9186(1)$ Å	(0, 0, 0)	–
hcp	$P6_3/mmc$	18.7 GPa	$a = 3.2748(2)$ Å	$(\frac{1}{3}, \frac{2}{3}, \frac{1}{4})$	–
			$c = 5.1153(2)$ Å		
Eu-IV	$C2/c(q_1 0 q_3)00$	33.9 GPa	$a = 3.0835(1)$ Å	$(0, 0.342(1), \frac{1}{4})$	$q_1 = 0.8095(2)$
			$b = 5.2994(2)$ Å		$q_3 = 0.5908(2)$
			$c = 4.7239(1)$ Å		
			$\beta = 90.400(2)°$		
Eu-V	$C2/c(q_1 0 q_3)00$	40.3 GPa	$a = 2.9886(3)$ Å	$(0, 0.3365(9), \frac{1}{4})$	$q_1 = 0.5863(3)$
			$b = 5.2987(3)$ Å		$q_3 = 1.5865(2)$
			$c = 4.5720(4)$ Å		
			$\beta = 90.328(8)°$		

Figure 6.10: Summary of the lattice parameters of Eu in the bcc, hcp, Eu-IV and Eu-V phases at selected pressures, as determined from Rietveld fits to the diffraction profiles.

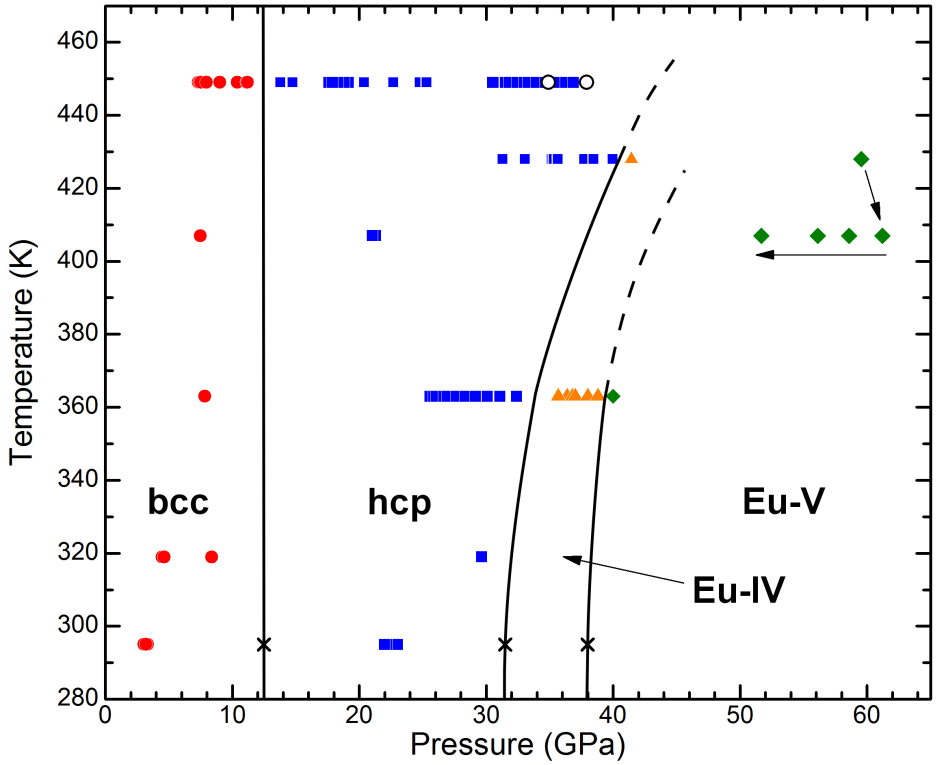

Figure 6.11: Phase diagram of Eu to 449K. The red circles show the points in the bcc phase, the blue squares show the points in the hcp phase, the orange diamonds show the points in the Eu-IV phase, and the green diamonds show the points in the Eu-V phase. The crosses show the room temperature transition pressures, and the open circles show the two points at which diamond failure occurred. The lines show an estimate of the phase boundaries. The data were collected on compression at constant temperature, with the exception of the data collected on Eu-V at 407 K, as indicated by the arrows.

this temperature. However, this does confirm that the Eu-V is stable up to at least 428 K.

An attempt was made to cross the hcp $\rightarrow$ incommensurate phase boundary at 449 K in both samples. However, somewhat surprisingly, in both cases the diamonds failed before we observed the transition to the incommensurate phase, and the highest-pressure hcp patterns were collected at 34.9 and 37.9 GPa, respectively, in the two samples.

There has been only one study of the high-pressure, high-temperature behavior of Eu, in which the melting curve was determined, although only to 7 GPa [119], and large areas of the phase diagram of Eu remain completely unknown. In the small pressure range in which the melting curve is known, a maximum was observed in the melting temperature of the bcc phase at about 3.5 GPa and 722 K. It is natural to compare the phase diagram of Eu with that of divalent Ba, which is

shown in figure 6.12. Ba also exhibits a maximum in its melting temperature in the bcc phase [17]. At higher pressures, Ba exhibits a deep minimum in the melting curve at 7.7 GPa, close to the bcc–hcp transition. Given the similarities in their electronic structure, it is possible that this unusual melting behavior is also present in Eu. In Ba, the pressure range over which the lower-pressure hcp phase, Ba-II, is stable increases with increasing temperature, with the Ba-II $\rightarrow$ Ba-IV transition occurring at $\sim$15 GPa at 573 K, compared with 12 GPa at room temperature [17]. This suggests that the pressure range over which the complex Ba-IV phase is stable decreases with increasing temperature, similar to what is observed in Eu.

It is noted that in previous high-pressure high-temperature experiments on K [126] and Te [127], diamond failure was consistently observed in different sample runs on sample melting. In K, this was found to be due to a reaction between the sample and the Re gasket that occurred on sample melting. Similar behavior was observed in Te on melting at $\sim$3 GPa and $\sim$750 K. The fact that the diamonds failed at moderate pressures and temperatures in both of these Eu samples, and also that diamond failure was observed at very similar pressures and temperatures in each case ($\sim$37 GPa, 449 K), suggests the possibility of a reaction between the Eu and the diamonds, or between Eu and the gasket material, in this region of P-T space. This introduces the possibility of a minimum in the melting curve of Eu in this region of P-T space. Future studies using different gasket materials are required in order to investigate the behavior of Eu in this region.

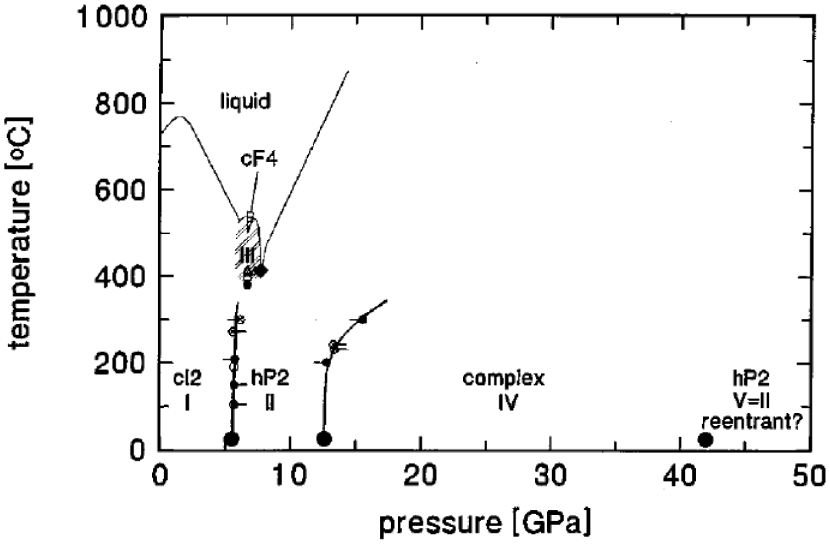

Figure 6.12: Phase diagram of Ba, taken from reference [17].

There have been very few studies of the high-temperature behaviour of any of the

elemental high-pressure incommensurately-modulated structures. The pressure-range in which incommensurately-modulated Te-III is stable was observed to reduce dramatically with increasing temperature, decreasing from about 25 GPa at room temperature to about 10 GPa at ∼625 K [127]. Instead, the commensurate Te-IV phase, which is not observed at room temperature, is observed at high-temperatures, with its stability range increasing with increasing temperature. This phase has the β-Po structure, which is related to the average structure of Te-III, but with higher-symmetry. It may then be the case that incommensurately-modulated structures are not stable at elevated temperatures. However, a recent paper found that the high-pressure incommensurate composite structure of rubidium, Rb-IV, which is observed between 16.6(3) and 19.6(2) GPa at room temperature [24], is *not* observed at 10 K [128], introducing the question of whether these phases are only stable over a small temperature range.

6.3 Conclusions

Angle-dispersive powder x-ray diffraction experiments have been performed on Eu up to ∼70 GPa. Eu transforms from the incommensurately-modulated Eu-IV to a new phase, Eu-V, which also has an incommensurately-modulated crystal structure [i-$mC4(2)$]. Eu-V has the same superspace group as Eu-IV, but the modulation wave vector has a different direction and magnitude. Discontinuities in the lattice parameters and wave vector components were observed at the transition, determining the transition to be first-order. This is the first incommensurately-modulated to incommensurately-modulated transition to be observed in the elements at high pressure.

Despite the unusual complex structures that have been observed in Eu at high pressure, it is one of the few remaining elements about which nothing is known beyond 100 GPa. However, the complexity of the diffraction patterns and the increasing broadness of the diffraction peaks means that the determination of the structural behaviour at pressures exceeding ∼50 GPa will be extremely challenging unless Eu transforms to a higher-symmetry structure. Extremely high-resolution diffraction data collected on non-contaminated samples will be required for further investigations in order to determine the structural behaviour of Eu at above this pressure. In particular, to determine the structure of Eu above 84 GPa, in the superconducting region [111].

High-temperature high-pressure *in situ* x-ray diffraction measurements on Eu up to 449 K and 61.2 GPa have provided an initial estimate of the phase boundaries of the bcc, hcp, Eu-IV and Eu-V phases. The pressure-range over which the hcp phase is stable has been found to increase with increasing temperature. Diamond failure was observed at similar pressures and temperatures in both samples (∼37 GPa, 449 K), suggesting the possibility of a reaction between the Eu and the diamonds, or Eu and the gasket material, in this region of P-T space. Similar behaviour was observed in K and Te when they melted [126, 127], and so this introduces the possibility of a minimum in the melting curve of Eu in this region of P-T space. Future high-temperature studies should therefore be performed using different different gasket materials in order to investigate this further.

Chapter 7

Samarium

7.1 Introduction

The high-pressure behaviour of divalent Eu has typically been compared with that of its neighbouring trivalent elements, samarium (Sm) and gadolinium (Gd), with the aim of producing a unified phase diagram of all the lanthanide elements. Gd and Sm both exhibit the common series of phase transitions observed in the trivalent lathanide elements under pressure [hcp $\rightarrow$ Sm-type $\rightarrow$ dhcp $\rightarrow$ fcc $\rightarrow$ distorted-fcc (dfcc) $\rightarrow$ low-symmetry]. However, despite the fact that the dfcc and post-dfcc phases of Sm can be accessed at reasonably low pressures, in particular when compared with the heavy lanthanide elements, there have been surprisingly few studies on its high pressure structural behaviour.

Sm adopts the Sm-type structure at ambient pressure, transforming to the dhcp phase at around 1 GPa [9], although slightly higher transition pressures of $\sim$4 and 6 GPa have also been reported [129,130]. On further compression, Sm transforms to the fcc phase at 14(3) GPa [9], and to the dfcc phase above 20 GPa [14]. Unlike the rest of the trivalent lanthanide elements, in which the dfcc phase has been determined to have the $hR24$ structure, the structure of the dfcc phase of Sm has not yet been determined. Krüger *et al.* [14] indexed their dfcc diffraction patterns based on a hexagonal structure structure with space group $P3_121$ ($hP6$), and Zhao *et al.* [18] indexed their patterns based on fcc. Olsen *et al.* [130] indexed their patterns based on the $hP6$ structure below 32 GPa, and based on a monoclinic structure with space group $C2/m$ at higher pressures, although they commented

that some of the authors thought that the lower-pressure region should be indexed on a six-layered structure with space group $P6_3/mmc$. However, all of these studies commented that these should be considered as indexing schemes only, and not as structural assignments.

Olsen *et al.* did not report any further structural transitions up to 100 GPa, the highest pressure reached in their study. However, Zhao *et al.* reported Sm to transform to a hexagonal structure with space group $P3_121$ or $P3_221$ ($hP3$) above 37(4) GPa, where these space groups are enantiomorphic pairs. Note that it is not possible to distinguish between enantiomorphic pairs using powder diffraction due to the one-dimensional nature of the data. This phase was observed to be stable up to 77 GPa, the maximum pressure reached in this study. Zhao *et al.* also reported significant anomalies in the equation of state in the dfcc and $hP3$ phases compared to the common behaviour of the other trivalent lanthanides, which was taken as evidence for the onset of $4f$ electron delocalisation. A later study be Errandonea *et al.* [131] reported a minimum in the melt curve at ∼70 GPa, which was also interpreted as resulting from the onset of $4f$ electron bonding.

Above 91 GPa, Sm was initially reported to be body-centred tetragonal (bct) [132], but the data quality is poor, and, of the 5 observed diffraction peaks, one cannot be explained by the bct structure. Computational studies using the full potential linear muffin-tin orbital method determined the bct phase to have delocalised $4f$ electrons, and that it is a delocalised $4f$ magnet at high pressure [133]. However, this is only valid if the bct phase assignment is correct. A more recent study has claimed that Sm transforms to the monoclinic $mC4$ structure at 103(5) GPa, and that this phase is stable up to 205 GPa [9]. Details of the $hR24$, $hP3$ and $mC4$ structures were given in section 3.2.3.

These previous studies all relied on energy-dispersive x-ray diffraction, and consequently the overall quality of the diffraction data is relatively poor. Integrated diffraction patterns of Sm in the dfcc, $hP3$ and $mC4$ phases, taken from references [18] and [9], are shown in figure 7.1. In particular, structural solution is complicated by the presence of fluorescence and escape peaks, as well as peaks from the gasket. Energy-dispersive x-ray diffraction does not offer the same resolution as angle-dispersive diffraction, which is essential in order to be able to resolve the closely-spaced reflections that are characteristic of distorted-fcc structures.

In order to investigate the high-pressure structural behaviour of Sm, angle-

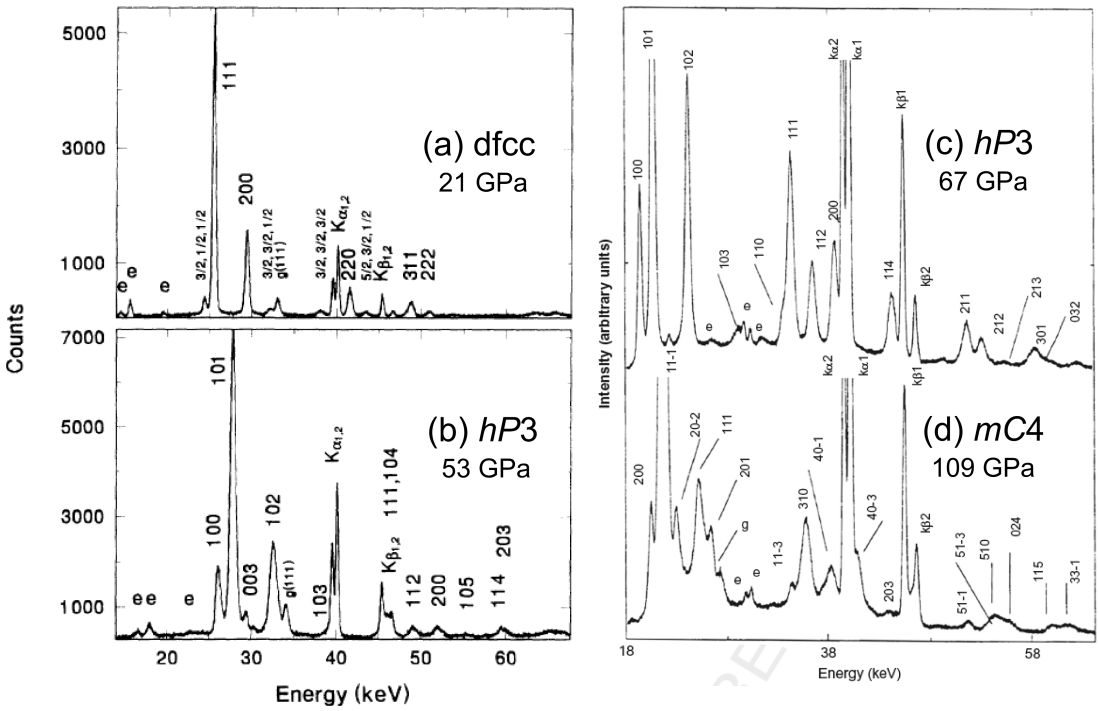

Figure 7.1: Integrated diffraction profiles of (a) dfcc Sm at 21 GPa, (b) $hP3$ Sm at 53 GPa, (c) $hP3$ Sm at 67 GPa and (d) $mC4$ at 109 GPa, from previous diffraction studies. (a) and (b) are taken from reference [18] and (c) and (d) are taken from reference [9] The label e indicates an escape peak, g indicates a peak from the gasket material, and K indicates a fluorescence peak.

dispersive x-ray diffraction x-ray powder diffraction experiments have been performed up to 50 GPa. The distorted-fcc phase of Sm has been found to have the same $hR24$ structure observed in Pr. However, Sm does not undergo a transition to a second distorted-fcc phase such as the $oI16$ phase observed in Pr, and instead $hR24$-Sm distorts to a greater extent than $hR24$-Pr. Above 40.4 GPa, Sm undergoes a sluggish transition to the $hP3$ phase in agreement with previous studies. Additionally, a path-dependent transition to a new phase, Sm-VII, which occurred on annealing followed by pressure decrease, is reported. A similar transition to another new phase, Sm-VII′, is observed on heating. However, although the diffraction patterns of these phases are extremely similar, subtle differences suggest that different structural solutions will be required for each phase. The majority of this work has been published in J. Phys.: Conf. Ser. [2].

7.2 Experimental Details

High-purity Sm samples, supplied by U. Schwarz at the Max-Planck-Institut für Chemische Physik fester Stoffe in Dresden, were loaded in diamond anvil pressure cells equipped with tungsten gaskets in a dry argon atmosphere ($<$ 1 ppm O_2 and $<$ 1 ppm H_2O). Three samples were loaded into DXR pressure cells without a pressure-transmitting medium (PTM), and small amounts of Ta powder were included as a pressure marker. These samples subsequently will be referred to as samples 1, 2 and 3. A further sample was loaded into a DXR pressure cell with a mineral oil PTM for comparison. A small ruby sphere was included for pressure determination in this sample, and the pressure was determined using the ruby fluorescence method. This sample will subsequently be referred to as sample 4.

For high-temperature studies, one sample was loaded into a MB pressure cell without a PTM, and a small grain of Ta powder included as a pressure marker. This sample will subsequently be referred to as sample 5. The cell was heated *in situ* using an external ring heater. The temperature was measured using a thermocouple placed on the back of one of the diamonds, and the uncertainty in temperature was estimated to be no more than 10 K.

Angle-dispersive x-ray powder diffraction data on samples 1 and 2 were collected at beamline ID09a using a beam of monochromatic x-rays of wavelength of $\sim$0.41 Å, collimated to a diameter of 15 μm. Some additional data on sample 1 were collected at beamline P02.2 using an x-ray beam of wavelength of $\sim$0.29 Å focused to $\sim 2 \times 2$ μm^2. Data on samples 3, 4 and 5 were collected at beamline I15 using an x-ray beam with a wavelength of $\sim$0.41 Å, collimated to a diameter of 30 μm. In all cases, the 2D diffraction images were integrated using Fit2D, and Le Bail and Rietveld refinements were performed using the Jana software.

7.3 Experimental Results

7.3.1 Contaminant Phases

Despite loading high-purity samples in a dry argon atmosphere, trace amounts of contaminants were present in all of our samples. Due to the their relatively large beam size ($\sim$10 μm and $\sim$30 μm, respectively), it was not possible to avoid

the contaminants on beamlines ID09a and I15, and contaminant reflections were present in all of the diffraction patterns collected on these beamlines. However, the small beam size on beamline P2.02 ($\sim 2 \times 2$ μm^2) made it possible to avoid small amounts of sample contaminant, and it was possible to obtain non-contaminated diffraction profiles. Two contaminant phases were then identified, each of which can be indexed based on a fcc lattice. The impurity phase with the larger fcc unit cell will subsequently be referred to as contaminant 1, and the phase with the smaller fcc unit cell will be referred to as contaminant 2. At least one of the impurity phases was present in each of the samples.

Integrated diffraction patterns of hR24-Sm plus contaminant 1 at 21.3 GPa and hR24-Sm plus contaminant 2 at 31.5 GPa are shown in figure 7.2(a) and (b), respectively. Details of this structure will be discussed later in this chapter. The volume per Sm atom against pressure for hR24-Sm and contaminants 1 and 2 are shown in figure 7.3, as determined from samples 2 and 5.

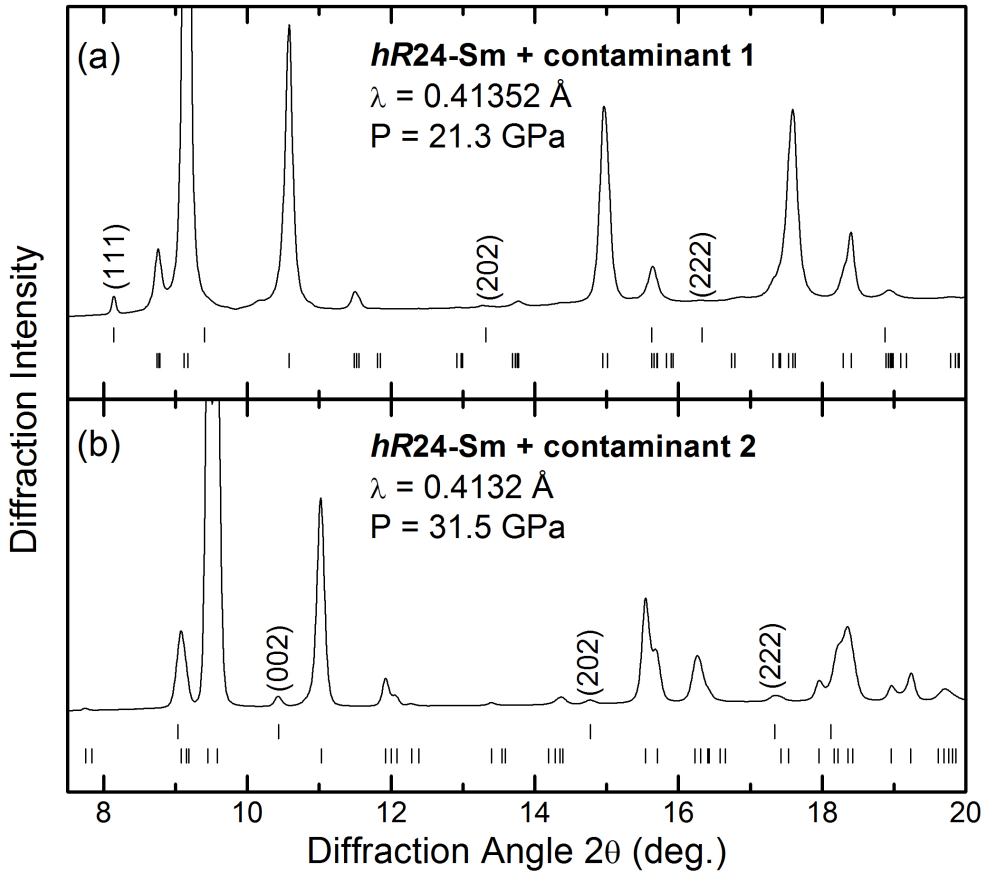

Figure 7.2: Integrated diffraction patterns of (a) hR24-Sm plus contaminant 1 at 21.3 GPa and (b) hR24-Sm plus contaminant 2 at 31.5 GPa. The tick marks below each pattern show the calculated peak positions of the contaminant phase (upper) and hR24-Sm (lower) as determined from a two-phase Rietveld refinement.

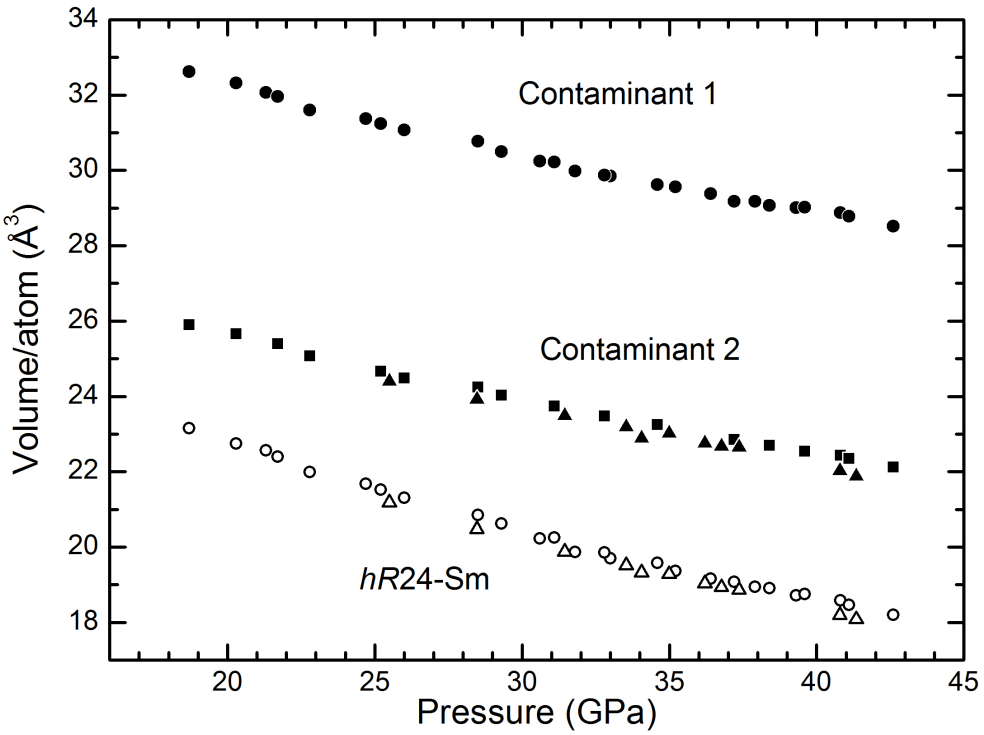

Figure 7.3: Volume per Sm atom against pressure for $hR24$-Sm and contaminants 1 and 2. The solid circles show data for contaminant 1, the solid squares show data for contaminant 2, and the open circles show data for $hR24$-Sm, as determined from mixed-phase profiles collected on sample 2. Peaks from contaminant 2 were not observed in all profiles. The solid triangles show data for contaminant 2 and the open triangles show data for $hR24$-Sm, as determined from mixed-phase profiles collected on sample 4. The lattice parameters for contaminant 1 were determined from the position of the (111)-fcc reflection, and the lattice parameters for contaminant 2 were determined from the position of the (200)-fcc reflection.

7.3.2 Lower-Pressure Phases

The lowest-pressure diffraction pattern was collected at 3.4 GPa from sample 1. Although the majority of the peaks in this pattern could be indexed based on the Sm-type structure, 4 additional reflections were observed that could not be described by this structure. The intensity of these reflections was observed to increase when the pressure of the sample was increased to 3.7 GPa, and on further compression to 7.5 GPa we found that the pattern could be indexed as single-phase dhcp. The additional reflections in 3.4 GPa pattern can therefore be identified as reflections from the dhcp phase, suggesting that the Sm-type $\rightarrow$ dhcp transition had already began at this pressure. This is illustrated in figure 7.4, which shows the integrated diffraction profiles of Sm at 3.4 GPa, where the sample is predominantly in the Sm-type phase, in the mixed-phase region at 3.7 GPa,

and in the dhcp phase at 7.5 GPa.

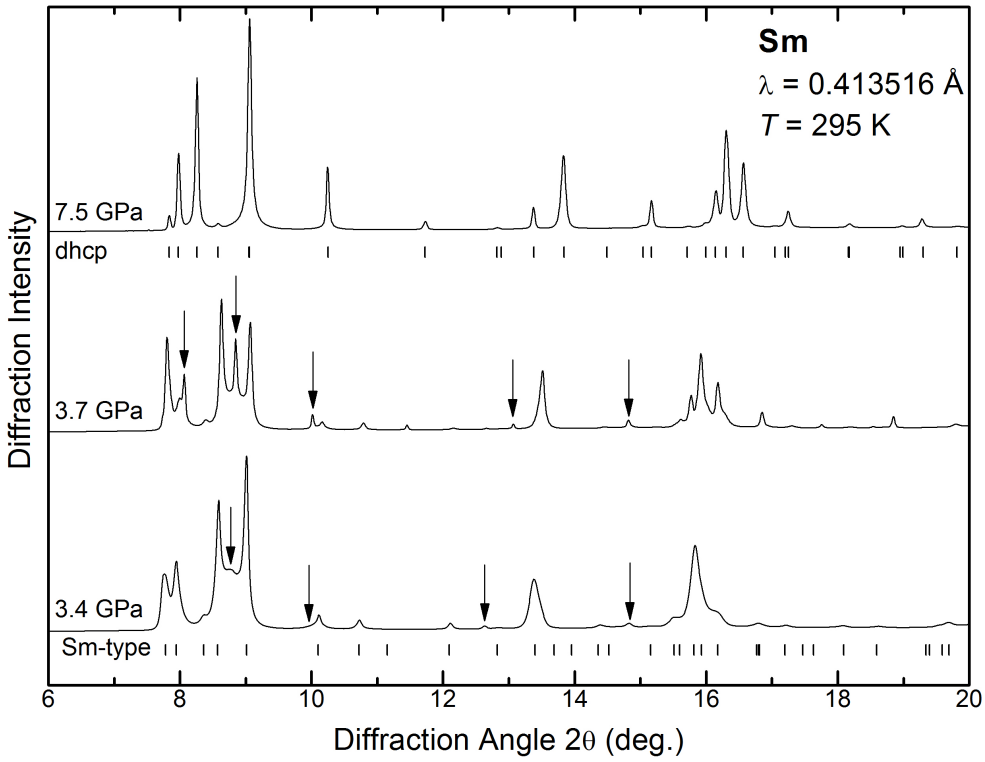

Figure 7.4: Integrated diffraction profiles of Sm at 3.4, 3.7 and 7.5 GPa, illustrating the transition from Sm-type to dhcp. The 3.4 GPa profile is predominantly Sm-type, the 3.7 GPa pattern is a two-phase mixture, and the 7.5 GPa pattern is single-phase dhcp. The tick marks below the 3.7 GPa pattern show the calculated peak positions of the Sm-type reflections, and the tick marks below the 7.5 GPa pattern show the calculated peak positions of the dhcp reflections. The arrows indicate the dhcp reflections that are present in the 3.7 and 3.7 GPa profiles.

The peaks in the 3.4 GPa pattern are very broad, which is most likely due to the presence of stacking faults. That is, where the stacking stacking sequence (in this case ABABCBCAC...) is interrupted. These broad peaks correspond to smooth arcs in the 2D diffraction image. In sample 1, the Sm-type $\rightarrow$ dhcp transition was accompanied by a significant change in the texture of the Debye-Scherrer rings. In the 2D diffraction image corresponding to the mixed-phase region at 3.7 GPa, the reflections from the dhcp phase consisted of sharp single-crystal like spots. In the single-phase dhcp diffraction image at 12.6 GPa, the peaks that are common to both the Sm-type and dhcp phases remained as smooth rings, and the new reflections that are only present in the dhcp phase are single-crystal like arcs. However, after the transition to the dfcc phase further changes in texture are observed, and the Debye-Scherrer rings are sharp and smooth. This is illustrated in figure 7.5, which shows the 2D diffraction images of Sm at 3.4 GPa, where it is predominantly in the Sm-type phase, at 3.7 GPa in the mixed-phase region, at

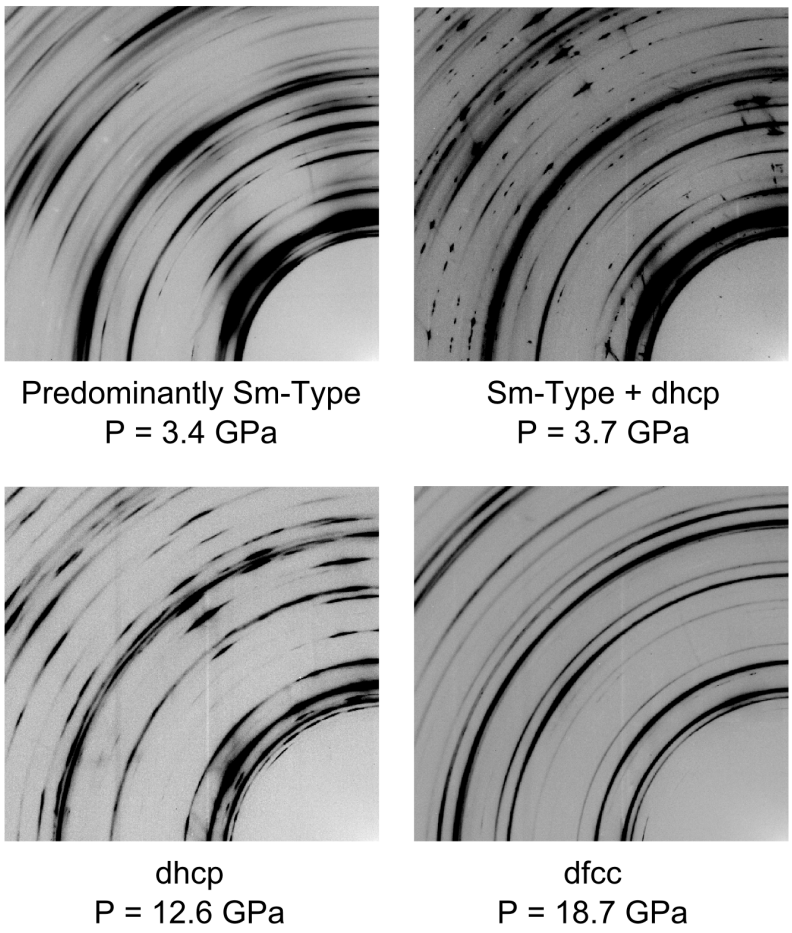

Figure 7.5: 2D diffraction images of Sm (a) predominantly in the Sm-type phase at 3.4 GPa, (b) in the the mixed-phase region at 3.7 GPa, (c) in the dhcp phase at 12.6 GPa and (d) in the dfcc phase at 18.7 GPa. The Sm-type $\rightarrow$ dhcp transition involves a significant change in texture, with new reflections appearing as single-crystal like spots. However, the Debye Scherrer rings from the higher-pressure dfcc phase are smooth and sharp.

12.6 GPa in the dhcp phase, and at 18.7 GPa in the dfcc phase.

In the other samples, the patterns from the dhcp phase did not have the same single-crystal like texture as in sample 1. Instead, the Debye-Scherrer rings were smooth, and the peaks in the diffraction pattern were broad. Again, it is likely that this is due to stacking faults. In order to investigate the effect of temperature, sample 4 was heated *in situ* while the sample was in the dhcp phase. Integrated diffraction profiles and the corresponding 2D diffraction images of Sm in the dhcp phase at 323 and 423 K are shown in figure 7.6(a) and (b), respectively. On heating to 323 K at 8 GPa, the sample reflections remained broad, and additional

peaks from the Sm-type phase are still present. However, on heating to 423 K at 3 GPa, significant changes in the texture of the Debye Scherrer rings were observed, with the rings becoming much sharper. This enabled us to resolve the majority of the individual reflections in the pattern, in particular the set of reflections between 16 and 18 degrees. Despite the fact that the pressure of the sample dropped on heating, we no longer observe any of the Sm-type reflections that were present in the 323 K patterns, and the pattern can be indexed as a single-phase dhcp pattern. This is in agreement with the results of Jayaraman and Sherwood [129], who found that heating to 350°C aided the Sm-type → dhcp transition at 4 GPa. They commented that as Sm-type → dhcp transition involves a shift of two-thirds of the atomic layers, then temperature must provide the activation energy for the transition.

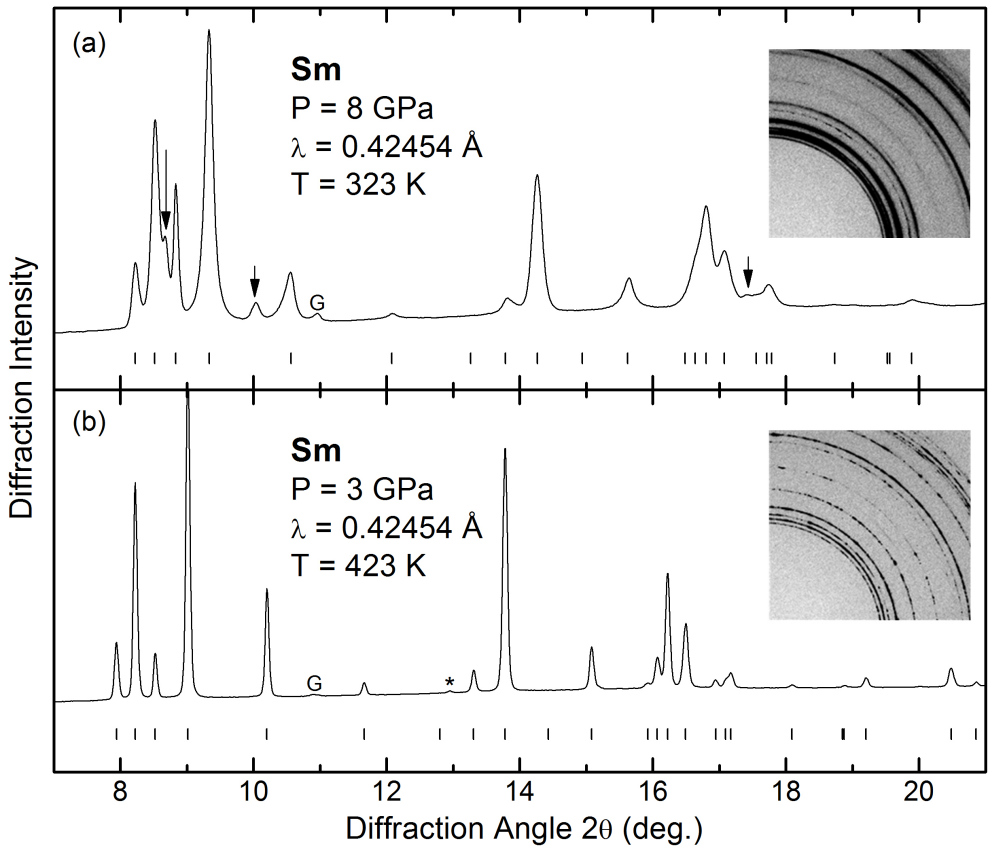

Figure 7.6: Integrated diffraction profiles and the corresponding 2D diffraction images of Sm in the dhcp phase at (a) 8 GPa and 323 K, and (b) 3 GPa and 423 K. The arrows indicate reflections from the Sm-type phase that are also present in the 323 K profile. No evidence of any peaks from the Sm-type phase are observed in the 423 K pattern, despite the fact that the pressure dropped on heating. The asterisk indicates a peak from contaminant 1, and the G indicates peaks from the W gasket. Although the sample reflections in the 323 K pattern are very broad, the 423 K pattern is considerably sharper. This change in texture can also be seen in the corresponding 2D images.

7.3.3 The Distorted-fcc Phase

In order to be able to definitively determine the structure of the dfcc phase, it is necessary to be able to resolve the closely-spaced split-fcc reflections that occur as the unit cell distorts away from cubic symmetry, as well as being able to clearly identify the superlattice reflections that occur as the atoms move away from their fcc positions. Due to the longer wavelengths (≈ 0.41 Å) used at ID09a and I15, we were able to resolve the split-fcc reflections in data collected at these beamlines to a much greater extent than in the data collected at P02.2, in which a shorter wavelength was used (≈ 0.29 Å). For this reason, the unit cell dimensions and atomic positions were determined using the data collected at ID09a and I15.

Although mixed-phase dhcp-fcc patterns were observed, no single-phase fcc patterns were seen in any of our samples, and the first single-phase dfcc pattern was first observed at 18.7 GPa. At this pressure, the dfcc phase could be clearly identified by the presence of the non-fcc superlattice reflections. Although the splitting of the lower-angle fcc reflections could not be resolved at this pressure, some of the higher-angle fcc reflections, such as the (222) reflection, were clearly split. Note that this behaviour is different to that previously reported for $hR24$-Pr, in which the superlattice reflections were observed *before* there was any evidence of a distortion from cubic symmetry [11]. On further compression, the splitting of the fcc reflections increased with pressure, allowing the lower-angle split reflections also to be resolved. Above 42.6 GPa, significant changes in the diffraction pattern were observed, indicating a transition to the higher-pressure phase. Details of this transition are discussed in section 7.3.4.

The $hR24$ structure provides an excellent fit to the the dfcc patterns over the entire pressure range in which this phase was observed (18.7-42.6 GPa), and the weak reflections that rule out the monoclinic $mC4$ structure can clearly be identified in all of the patterns. A Rietveld refinement of the $hR24$ structure based on the diffraction profile of Sm at 41.4 GPa is shown in figure 7.7. The refined structural parameters are $a = 5.891(1)$ Å, $c = 14.748(3)$ Å, with atomic coordinates $z_1 = 0.273(1)$, $x = 0.509(2)$ and $z_2 = 0.244(1)$ and residuals of $R_p = 5.2\%$ and $R_{wp} = 9.6\%$. The inset highlights the (104), ($2\bar{1}6$) and ($1\bar{1}8$) reflections, which cannot be described by the $mC4$ structure.

In Pr, the $hR24 \rightarrow oI16$ transition was identified by a gradual change in the relative intensity of the (006)/(202) doublet, and in the ($2h$,$2k$,$2l$) equivalent,

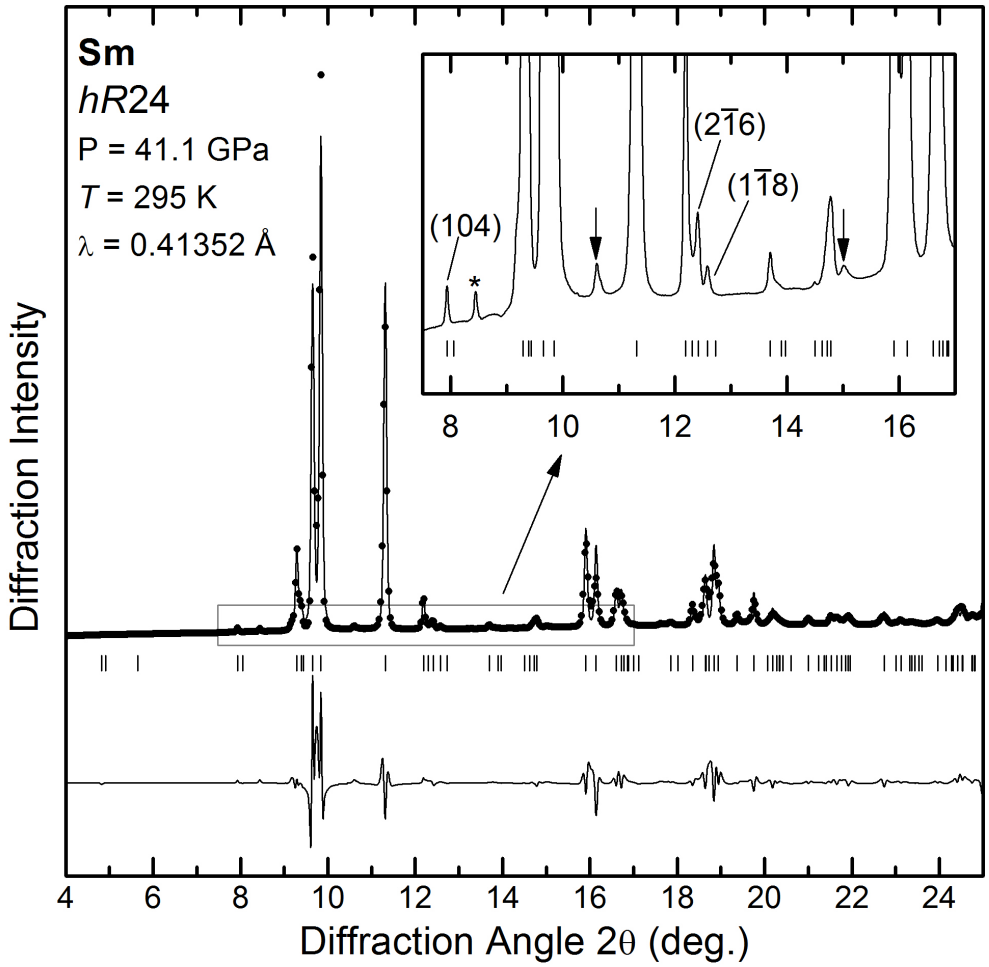

Figure 7.7: Rietveld refinement of the $hR24$ structure based on the diffraction profile of Sm at 41.1 GPa. The symbols show the experimental data, and the solid line shows the fit. The tick marks show the calculated peak positions, and the residuals are shown below the tick marks. The reflections that cannot be described by the $mC4$ structure are indicated in the inset, the asterisk identifies a reflection from contaminant 1, and the arrows identify reflections from contaminant 2.

(0,0,12)/(404), which result from the splitting of the (111) and (222)-fcc reflections, respectively. These intensity changes arise from the disappearance of the (006) and (0,0,12)-$hR24$ reflections, and the simultaneous growth of new reflections from the $oI16$ phase with very similar d-spacings. The identification of a similar transition in Sm is greatly simplified by the fact that the splitting of the (111) and (222)-fcc reflections is much greater than in Pr. Consequently, the (006) and (0,0,12) can be clearly identified as two distinct reflections for almost the entire pressure range in which this phase is observed, and the appearance of any additional reflections would be easily noticeable. This is illustrated in figure 7.8, which shows the pressure dependence of the (006)/(202) and (0,0,12)/(404) reflections for $hR24$-Sm in the 27.7–38 GPa region. It is clear that there is

no sign of any new reflections up to the maximum pressure. This then confirms that at ambient temperature, Sm does not transform to the $oI16$ structure on pressure increase, and instead it remains in the $hR24$ phase up to 42.6 GPa.

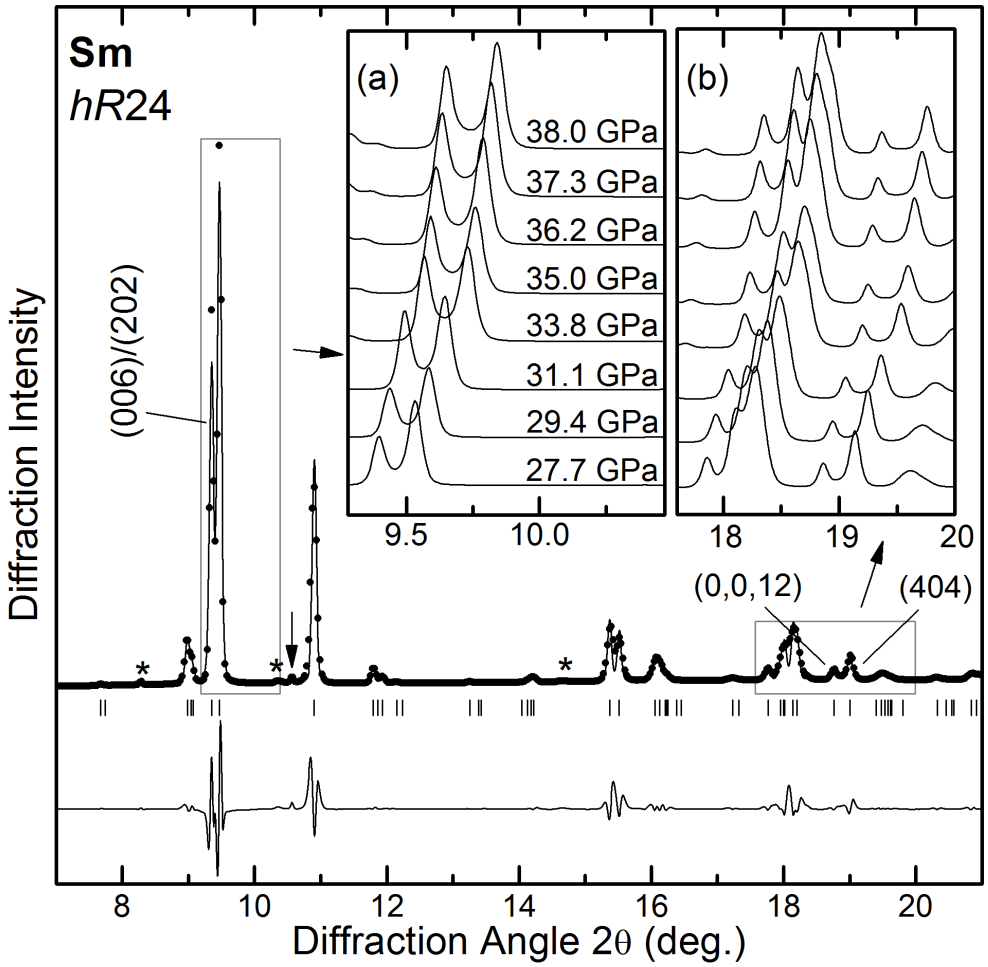

Figure 7.8: Diffraction profile of $hR24$-Sm at 29.3 GPa. The insets show the pressure evolution of the (a) (006) and (202) reflections and (b) (0,0,12) and (404) reflections. The asterisks identify the reflections from the two contaminant phases, and the arrow indicates a reflection from the Ta pressure calibrant.

The $hR24$ structure is identical to fcc when $c/a = \sqrt{6}\approx 2.449$ and refineable atomic coordinates are equal to $z_1 = \frac{1}{4}$, $x = \frac{1}{2}$, and $z_2 = \frac{1}{4}$. The distortion of the $hR24$ structure from fcc can then be quantified in terms of the departure of these structural parameters away from these values. The pressure-dependence of the c/a axial ratio for all three samples is shown in figure 7.9. The c/a ratio was observed to increase continuously from 2.463(7) at 18.7 GPa, reaching a maximum value of 2.507(8) at 42.6 GPa. No significant deviation was observed in sample 4, which was loaded with a mineral PTM.

Evans *et al.* [11] reported the c/a ratio of Pr to increase continuously from $\sqrt{6}$ to

a maximum value of 2.487 at 13.24 GPa, where the maximum value is included in figure 7.9 for comparison. This suggests that the $hR24$-Sm distorts to a much greater extent than $hR24$-Pr. This is in agreement with the results of Krüger *et al.* [14], if their data points corresponding to the pressure region in which Pr is in the $oI16$ phase are ignored. It should also be noted that a comparison with the results of Krüger *et al.* for other lanthanide elements suggests that $hR24$-Sm also distorts to a much greater extend than $hR24$-Nd, Gd and Tb.

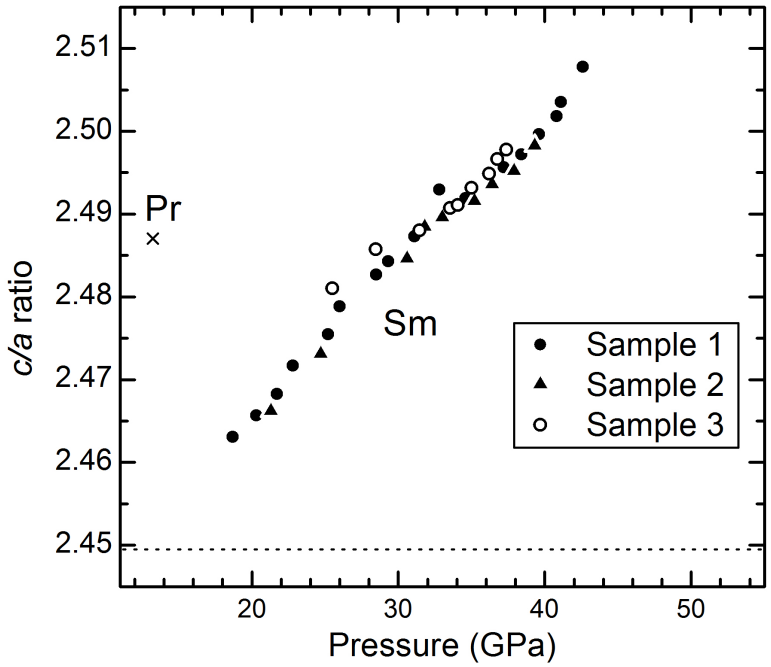

Figure 7.9: The pressure dependence of the c/a ratio of $hR24$-Sm, as determined from Rietveld refinements. The cross shows the largest c/a ratio reported for $hR24$-Pr by Evans *et al.*, and the dotted line indicates the c/a ratio of undistorted fcc ($\sqrt{6}$). The error bars are smaller than the symbol size and so have not been included.

In accordance with the analysis of $hR24$-Pr performed by Hamaya *et al.* [80], and subsequently by Evans *et al.* [11], the displacement of the atoms in the $hR24$ structure from their fcc positions can be quantified by three static displacement amplitudes, $\epsilon = x - \frac{1}{2}$, $\delta_1 = z_1 - \frac{1}{4}$ and $\delta_2 = z_1 - \frac{1}{4}$. The pressure dependence of ϵ, δ_1 and $-\delta_2$ for all three samples is shown in figure 7.10. Evans *et al.* reported that, over the stability range of $hR24$-Pr, $\epsilon \approx -\delta_2 \approx \frac{1}{3}\delta_1$. In our results for sample 1, ϵ and δ_2 have different values. However, in samples 2 and 4, $\epsilon \approx -\delta_2$, in agreement with the results for Pr, suggesting that the effect observed in the sample 1 is most likely due to the correlation between the atomic coordinates and the preferred orientation correction in the Rietveld refinement.

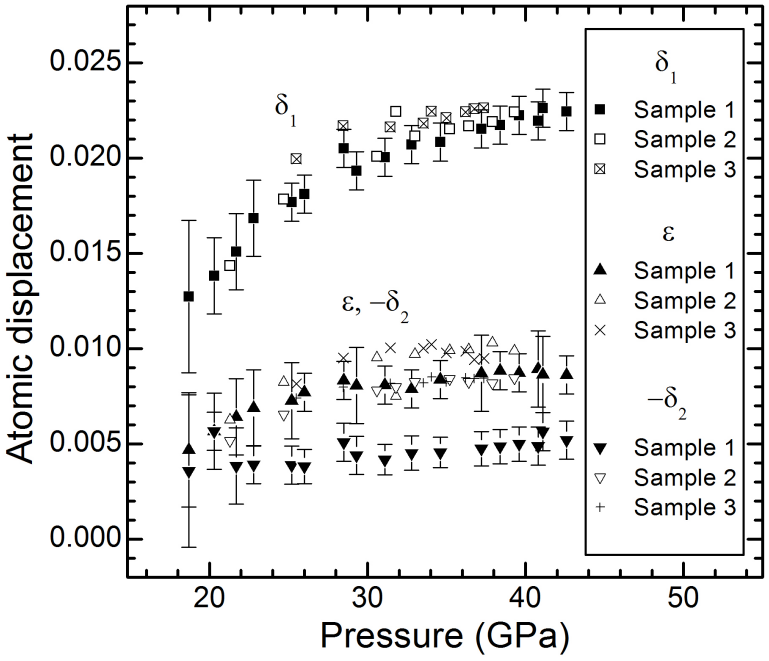

Figure 7.10: The pressure dependence of the static displacement parameters, ϵ, δ_1 and $-\delta_2$, for samples 1, 2 and 4, as determined from Rietveld refinements. The error bars are shown for sample 1. Those for samples 2 and 4 are similar, and so have not been included.

7.3.4 Higher Pressures

The $hR24 \rightarrow hP3$ transition was observed at slightly different pressures in each of the three samples. The transition is sluggish, and the onset of the transition can be identified by the observation of the (100)-$hP3$ reflection, which was first observed between 40.4 and 40.8 GPa. Additional $hP3$ reflections were not observed until 42.0–43.4 GPa, and single-phase $hP3$ patterns were first observed between 43.2 and 46.2 GPa. No correlation between the use of a PTM and the transition pressure was observed. A Rietveld refinement of this structure based on a diffraction profile collected from sample 1 at 47.4 GPa is shown in figure 7.11. The corresponding refined structural parameters are $a = 2.9717(3)$ Å, $c = 6.879(3)$ Å, with atoms at $(0,0.513(5),\frac{1}{3})$ and residuals of $R_p = 5.9\%$ and $R_{wp} = 9.6\%$. However, although this structure can account for all the reflections that are observed, a number of the reflections, in particular the (103), (104), (113) and (105) reflections, are broader than would be expected from this structure. Similar behaviour was observed in all samples. On further compression, the $hP3$ structure gives an good fit to the patterns collected up to 50 GPa, the highest pressure reached in this study. Data were also collected on decompression from 50.3 to 43.1 GPa, and the sample remained in the $hP3$ phase.

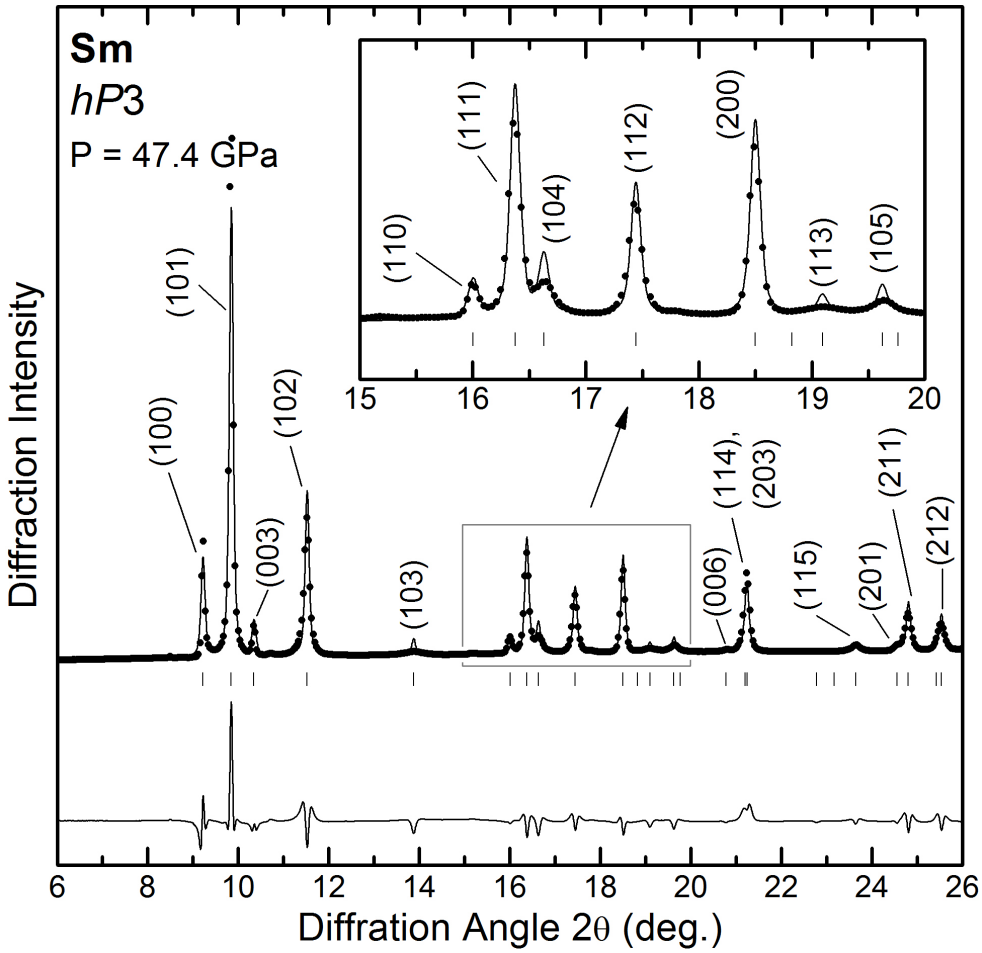

Figure 7.11: Rietveld refinement of the $hP3$ structure based on the diffraction profile of Sm at 47.4 GPa. The symbols show the experimental data and the solid line shows the fit. The tick marks below the profile show the calculated peak positions, and the residuals are shown below the tick marks.

The compressibility of Sm from 3.4 to 50.4 GPa at 295 K is shown in figure 7.12. A small volume change is observed at the $hR24 \rightarrow hP3$ transition, and $\Delta V/V_0$ is estimated to be $\sim$0.4%. This was not noted in other studies [18, 118, 130, 132]. However, our measured $\Delta V/V_0$ is very small, and previous studies did not index the dfcc phase based on $hR24$. Zhao *et al.* [18] reported significant anomalies in the equation of state in the dfcc and $hP3$ phases compared to the common behaviour of the other trivalent lanthanides, which was taken as evidence for the onset of $4f$ electron delocalisation. However, it is not possible to comment on the compressibility of the $hP3$ phase over the small pressure range in which data have been collected in this study.

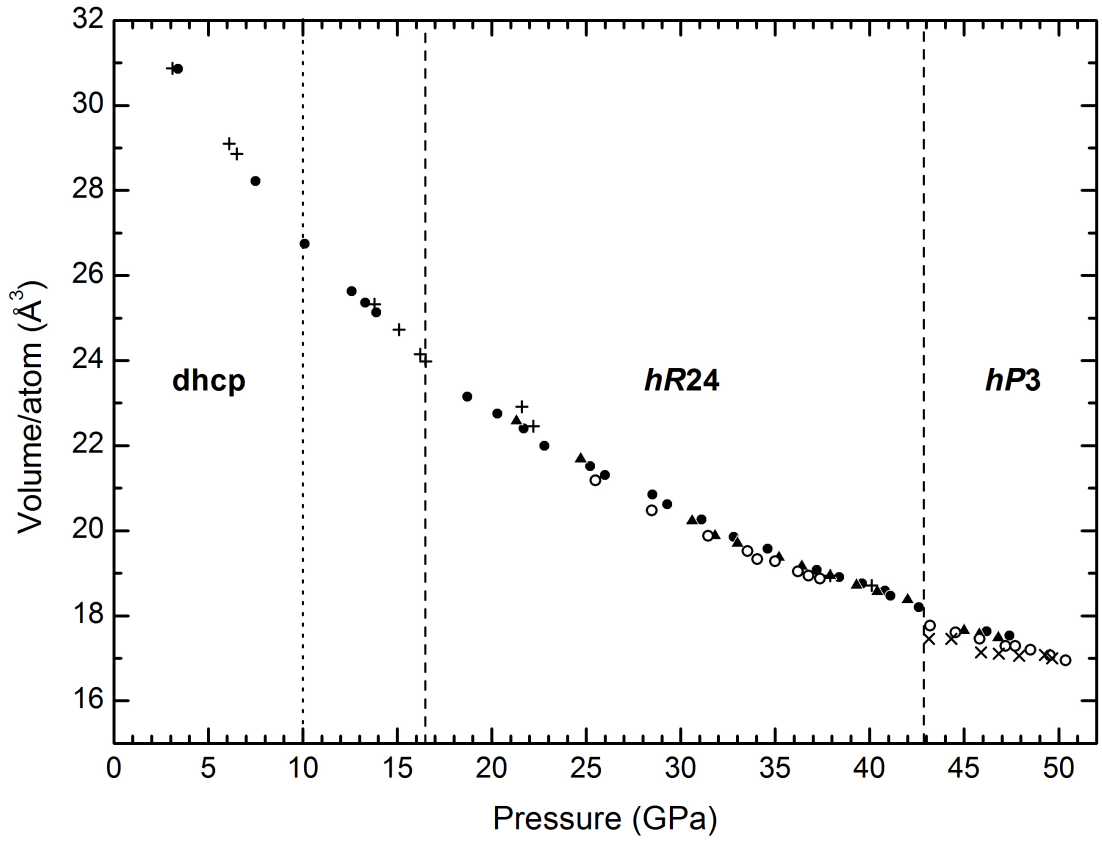

Figure 7.12: The compressibility of Sm from 3.4 to 50.4 GPa at 295 K. The solid circles show data collected on sample 1 on compression, the solid triangles show data collected on sample 2 on compression, and the open circles show data collected from sample 4 on compression. The crosses (×) show data collected from sample 1 on decompression and the plus symbols (+) show data collected from sample 3 on decompression. The dashed lines show the midpoint of the dhcp → $hR24$ and $hR24$ → $hP3$ transitions on compression, and the dotted line shows midpoint of the $hR24$ → dhcp transition on decompression.

7.3.5 Path-Dependence Structural Transition

An attempt was made to collect data on sample 1 on decompression. The $hP3 \rightarrow hR24$ transition was observed as expected, and the first single-phase $hR24$ pattern collected at 40.1 GPa. However, in this case only one single $hR24$ pattern was collected at 37.9 GPa before the pressure of the sample dropped to 22.2 GPa. A second data set was collected on this sample on compression at beamline P2.02. However, as discussed previously, the data collected at P2.02 is not included in the analysis due to the reduced resolution as a result of the shorter wavelength used on this beamline.

Sample 1 was then heated for 12 hours at 373 K at 32 GPa. After annealing,

the pressure of the sample increased slightly to 32.4 GPa. However, although the diffraction pattern could still be described by the $hR24$ structure, significant changes in the relative intensity of a number of closely-spaced reflections was observed. In particular, the intensity of the (107), (208), $(1\bar{1}1)$ and (00,12) reflections were observed to decrease with respect to their neighbouring reflections. The pressure of the sample was then subsequently decreased in small pressure steps (< 1 GPa). The intensity changes were observed to become more pronounced, until some of the reflections disappeared completely by 28.5 GPa. However, on further pressure decrease to 27.7 GPa, the changes in the relative intensity reversed, so that the pattern resembled the pattern collected before annealing.

This is illustrated in figure 7.13, which shows the integrated diffraction profiles of Sm (a) before annealing at 32 GPa, (b) after annealing at 32.4 GPa and on subsequent pressure decrease at (c) 28.5 GPa and (d) 27.7 GPa. Note that due to the small x-ray beam at P02.2, the intensity of the reflections from contaminant 2 was observed to vary between patterns, and their intensity in the 28.5 GPa pattern is significantly greater than in the other patterns shown in the figure.

Changes in the relative intensities of different peaks can be due to changes in the preferred orientation of the crystallites in the sample. However, the fact that these changes reversed on further pressure decrease suggests that this is not the case. This was therefore taken as evidence of a transition to a new phase, which was complete by 28.5 GPa. In accordance with the naming system used by Zhao *et al.* [18], this phase will subsequently be referred to as Sm-VII.

On further pressure decrease, no significant changes in the relative intensities of the sample reflections were observed. Instead, the splitting of the split-fcc reflections decreased continuously until the could no longer be resolved at 17.9 GPa. At this point, the pattern could be described by cubic $hR24$. That is, $c/a = \sqrt{6}$ but with the atoms displaced from their fcc positions so that superlattice reflections are still observed. On further pressure decrease, a single fcc pattern was collected at 13.8 GPa, and the first single-phase dhcp pattern was collected at 6.5 GPa. The dhcp phase was observed to remain stable down to 3.1 GPa, the lowest pressure reached with this cell. This is in agreement with Jayaraman and Sherwood [129], who found that the dhcp phase can be retained metastably at ambient pressure.

The transition to Sm-VII occurred after annealing at 32 GPa followed by pressure

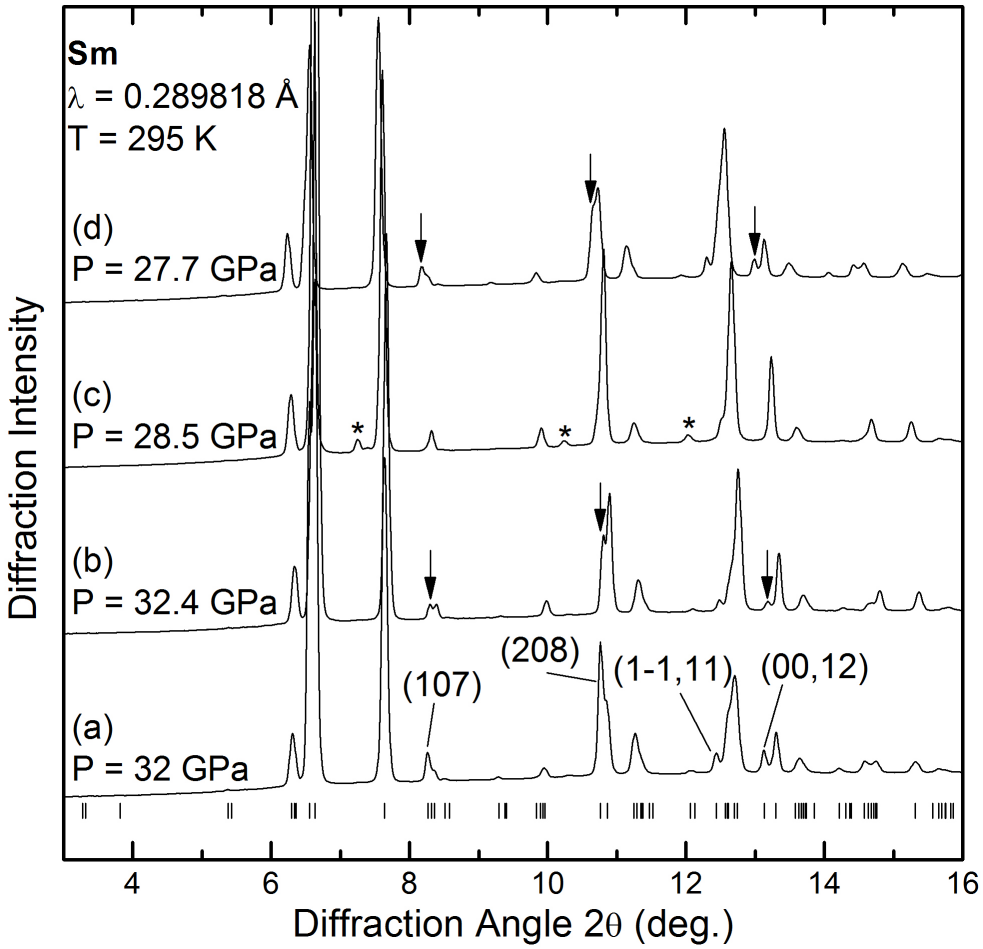

Figure 7.13: X-ray powder diffraction profiles of Sm at (a) 32, (b) 32.4, (c) 28.5 and (d) 27.7 GPa, which were collected in that order. The sample was annealed for 12 hours at 373 K between the collection of profiles (a) and (b). The tick marks below profile (a) show the calculated peak positions of $hR24$.

decrease. In order to determine if this effect is reproducible, additional data on sample 5 were collected on beamline I15. The pressure of was increased to 30.2 GPa, and the sample was annealed for 20.5 hours at 473 K. After annealing, the pressure had decreased slightly to 30.5 GPa. On subsequent pressure decrease to 29.0 GPa, the changes in the relative intensity of closely-spaced reflections, characteristic of the transition to Sm-VII, were observed, although no reflections disappeared completely. On further pressure decrease to 28.8 GPa, the intensity changes reversed slightly, suggesting that Sm was transforming back to $hR24$. The sample was then heated for 16.5 hours at 473 K, after which the sample had transformed back completely to $hR24$. Consequently, although the onset of the transition to Sm-VII was observed in this sample, it did not fully transform.

Following the three heating cycles described in section 7.3.7, sample 5 was heated

for a few hours at 358 K. On subsequent pressure decrease, the changes in the relative intensity of the closely-spaced reflections were again observed, until some reflections had completely disappeared by 22.5 GPa. The resulting diffraction pattern is identical to the Sm-VII pattern described previously, determining that this behaviour is reproducible.

7.3.6 Sm-VII

Having identified the transition to Sm-VII, an attempt was made to try to determine the structure of this new phase. Due to the longer wavelength used at DLS, the diffraction data collected from sample 5 was used for indexing purposes.

The transition from $hR24$ to Sm-VII involves the disappearance of a large number of the $hR24$ reflections, and no new reflections appear. Consequently, the Sm-VII diffraction patterns are similar to those from $hR24$, but without any split reflections. The possibility of describing the pattern as cubic $hR24$ was therefore considered. The diffraction pattern from this structure consists of intense fcc reflections and weaker superlattice reflections. However, fixing the c/a ratio to its cubic value means that a large number of the cubic $hR24$ reflections have the same d-spacing. For convenience, it is therefore easier to index cubic $hR24$ based on fcc. Alternative indexing schemes of equivalent reflections in the fcc and cubic $hR24$ settings are shown in table 7.1. Reflections with integer values of h, k and l in the fcc setting correspond to main reflections, and those with fractional values correspond to satellite reflections.

A Rietveld refinement of the cubic $hR24$ structure based on the 22.5 GPa Sm-VII diffraction pattern is shown in figure 7.14. The refined lattice parameter is $a = 6.2725(4)$ Å, with residuals of $R_p = 5.9\%$ and $R_{wp} = 10.9\%$. However, although this structure can account for all of the reflections in the pattern, significant misfits are observed in both main and satellite reflections, as illustrated for selected reflections in the insets. Note that the Rietveld refinement results in a good fit to the intense (111) reflection, while sacrificing the quality of the fit to the less-intense higher-order reflections.

The poor fit of the cubic $hR24$ structure can also be seen in the plot of the lattice parameter a, as determined from the d-spacings of each individual reflection, against 2θ. This is shown in figure 7.15(b). Significant peak shifts are observed in both the main and superlattice reflections, in comparison with the expected

fcc	$hR24$
$(\frac{1}{2},\frac{1}{2},\frac{3}{2})$	$(2\bar{2}1)$, $(1\bar{1}5)$, $(2\bar{1}3)$
(111)	(202), (006)
(002)	$(2\bar{2}4)$
$(\frac{3}{2},\frac{1}{2},\frac{3}{2})$	(107), $(3\bar{1}1)$, (205)
$(\frac{1}{2},\frac{1}{2},\frac{5}{2})$	$(3\bar{2}5)$, (009), (303), $(3\bar{3}3)$, $(2\bar{2}7)$
(202)	(208), $(4\bar{2}0)$
$(\frac{3}{2},\frac{1}{2},\frac{5}{2})$	$(2,\bar{1}9)$, $(4\bar{3}1)$, $(4\bar{2}3)$, $(3\bar{1}7)$
$(\frac{3}{2},\frac{3}{2},\frac{5}{2})$	$(4\bar{1}5)$, (401), $(1,\bar{1},11)$
(113)	$(4\bar{2}6)$, $(4\bar{4}2)$, $(2,\bar{2},10)$
(222)	(404), (0,0,12)
$(\frac{5}{2},\frac{1}{2},\frac{5}{2})$	(2,0,11), $(4\bar{3}7)$, $(3\bar{3}9)$, $(5\bar{2}1)$, (309), $(4\bar{4}5)$
$(\frac{5}{2},\frac{3}{2},\frac{5}{2})$	(407), $(5\bar{3}5)$, $(3,\bar{2},11)$, (1,0,13), $(4\bar{2}9)$, $(5,\bar{4},3)$, $(5\bar{1}3)$
(004)	$(4\bar{4}8)$
$(\frac{3}{2},\frac{3}{2},\frac{7}{2})$	$(2,\bar{2},13)$, $(5\bar{5}1)$, $(5\bar{2}7)$
$(\frac{5}{2},\frac{5}{2},\frac{5}{2})$	$(3,\bar{1},13)$, (505), (0,0,15), $(6\bar{3}3)$, $(6\bar{4}1)$, $(4,\bar{1},11)$
(313)	(2,0,14), (3,0,10), $(6\bar{4}4)$
(402)	$(4,\bar{2},12)$, $(6\bar{4}4)$

Table 7.1: Alternative indexing schemes of equivalent reflections in the fcc and $hR24$ settings. Reflections with integer values of h, k and l in the fcc setting correspond to main reflections, and those with fractional values correspond to satellite reflections.

peak positions of cubic $hR24$. The lattice parameter a_c of contaminant 2, as determined from the d-spacings of individual reflections in the same pattern, is plotted against diffraction angle 2θ in figure 7.18(b) for comparison. The overall fit is excellent, and so the poor fit of the cubic $hR24$ structure cannot be due to a calibration issue. It also suggests that it is not due to the presence of deviatoric stress, which would also be observed in the peaks from the contaminant phase. It should also be noted that the same misfits are observed in the Sm-VII patterns collected from sample 1 at beamline P02.2, where the direction and magnitude of the peak shifts are the same in both sets of data.

The possibility that these misfits could be due to the presence of stacking faults was also considered. In the fcc structure, the presence of stacking faults results in a shifts in diffraction peaks from their expected positions. The effect of a random

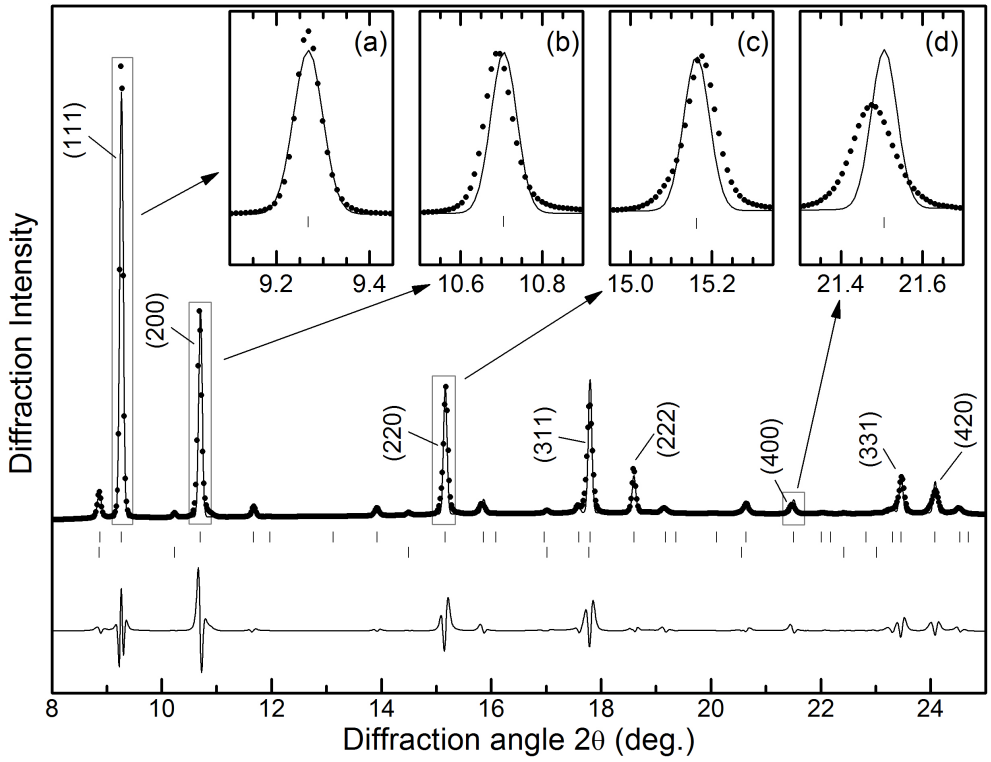

Figure 7.14: Rietveld refinement of the cubic $hR24$ structure to the Sm-VII integrated diffraction profile at 22.5 GPa. The tick marks show the peak positions of the cubic $hR24$ reflections (upper) and the reflections from contaminant 2 (lower), and the residuals are shown below the tick marks. The indices label the main reflections. Although this structure can account for all of the reflections in the pattern, significant misfits are observed in both main and satellite reflections. This is illustrated for the (111), (200), (220) and (400)-fcc reflections in insets (a)–(d).

distribution of deformation and twin faults along one of the sets of {111} planes is discussed in detail in chapter 13.5 of reference [134]. This determined that the (111) and (400)-fcc reflections are shifted to *higher* angles, and the (200) and (222) reflections are shifted to *lower* angles. However, although the shift of the (222) and (400) reflections can describe what is observed in our own patterns, it cannot account for the behaviour of the (111) and (200) reflections, which are observed to be shifted to lower and higher angles, respectively.

It is possible to describe cubic $hR24$ using a $2 \times 2 \times 2$ supercell of the fcc structure, which can describe both the fcc and superlattice reflections. However, the superlattice reflections in which h,k and l are all even ($h, k, l = 2n$) are *not* observed, which does not correspond to the allowed reflection conditions of any of the cubic space groups. It is necessary to describe this structure using the rhombohedral description.

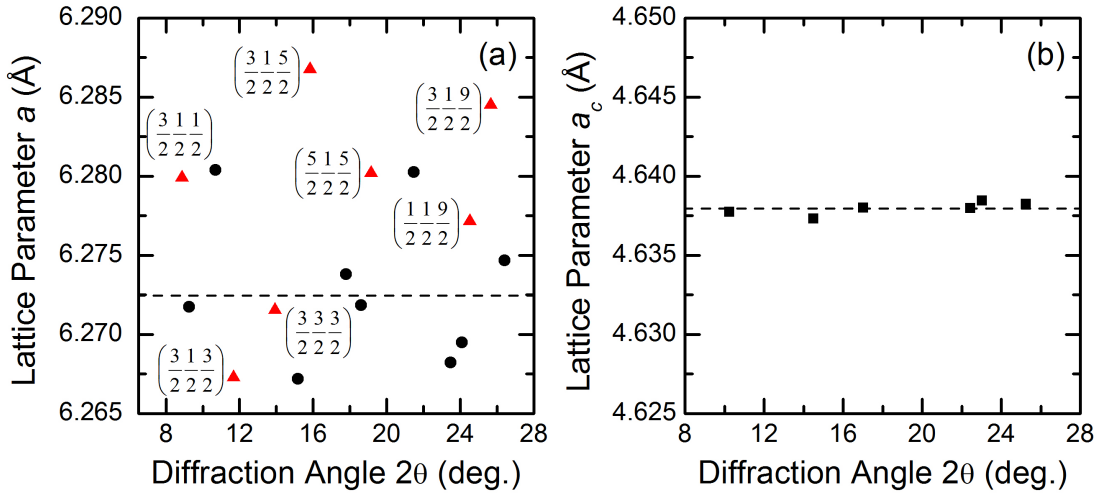

Figure 7.15: (a) Lattice parameter a of the cubic $hR24$ structure, determined from the d-spacing of individual reflections in the Sm-VII diffraction pattern at 22.5 GPa at 295 K, against diffraction angle 2θ. The black circles show data determined from the main reflections, and the red triangles show data determined from the superlattice reflections. The Miller indices of the superlattice reflections are labeled, and the dotted line indicates the value of a determined from the Rietveld refinement of the cubic $hR24$ structure to the diffraction profile.
(b) Lattice parameter a_c of contaminant 2, determined from the d-spacing of individual reflections in the Sm-VII diffraction pattern at 22.5 GPa and 295 K, against diffraction angle 2θ. The dotted line indicates the value of a_c determined from a Rietveld refinement of the cubic $hR24$ structure to the diffraction profile.

In Pr, the transition from $hR24$ to $oI16$ was identified by subtle changes in the diffraction pattern. The possibility of a transition to a different distorted-fcc structure should therefore also be considered in this case. The obvious starting point is to consider the different distorted-fcc structures proposed for the dfcc phases of Pr, which are given in table 3.2. However, these structures all predict splitting of a subset of the fcc reflections. Despite the fact that the diffraction peaks in the Sm-VII patterns are extremely sharp, no peak splittings are resolved. In particular, the (111) and (200)-fcc reflections, and the $(2h,2k,2l)$ equivalents, (222) and (400), are all very sharp and appear to be singlets. There is no possible way to distort the fcc structure without resulting in a splitting of either the (111) or the (200) reflections, or both. In order to be described by a distorted-fcc unit cell, the splitting of the reflections would have be be smaller than could be resolved in our patterns. Although it is possible to constrain the lattice parameters these structures so that they are cubic, or close to cubic, this results in the same peak misfit issue discussed for cubic $hR24$.

This suggests that a new solution is required. The diffraction pattern from this

phase is extremely simple, and the absence of any low-angle reflections rules out the possibility of large, low-symmetry unit cells. Attempts to index this new phase using DICVOL were unsuccessful, as all solutions predicted a large number of reflections that are not observed. The possibility of indexing this pattern based on an incommensurately-modulated crystal structure was also considered. However, the main reflections from incommensurately-modulated structures can be indexed based on a regular three-dimensional crystal structure. As *all* of the reflections are shifted from their expected cubic positions, and by different amounts, attempts to index a subset of reflections were unsuccessful. Further work is therefore required in order to determine the structure of this new phase.

7.3.7 High Temperature

The Sm-VII patterns were observed after annealing followed by pressure decrease. In order to investigate if this phase is stable at high temperatures, powder x-ray diffraction data were collected on sample 5 up to 450 K. Data were collected over three heating cycles, which started at 34, 27.9 and 27.8 GPa. These will be referred to as heating cycles 1, 2 and 3, respectively. The pressure was only adjusted once during the heating cycles, which is explicitly mentioned in the text, and data were collected in ∼50 K steps. In all of the temperature cycles, the pressure was observed to drop on heating. The temperatures and pressures at which diffraction data were collected in each heating cycle are shown in figure 7.16. Reflections from contaminant 2 were observed in all of the diffraction patterns, but were easily identified.

In heating cycle 1, the pressure was dropped from 34.0 to 24.5 GPa on heating to 449 K. All of the patterns collected on heating can be described by the $hR24$ structure, and the changes in the relative intensity of closely-spaced reflections which are characteristic of the transition to Sm-VII were not observed. However, the splitting of the closely-spaced reflections were observed to decrease on heating, indicating that the structure is becoming less distorted from cubic. This corresponds to a decrease in the the c/a ratio from 2.4966(7) at 295 K to 2.4773(7) at 406 K. On heating to 449 K, the splitting could only be identified by peak asymmetry, and so it was not possible to determine an accurate c/a ratio. On cooling to 428 K at 24.0 GPa, a single fcc pattern was collected. On further temperature decrease, the splitting of the closely-spaced reflections increased, with the c/a ratio increasing from $\sqrt{6} = 2.4495$ in fcc to 2.4743(7) at 27.2 GPa

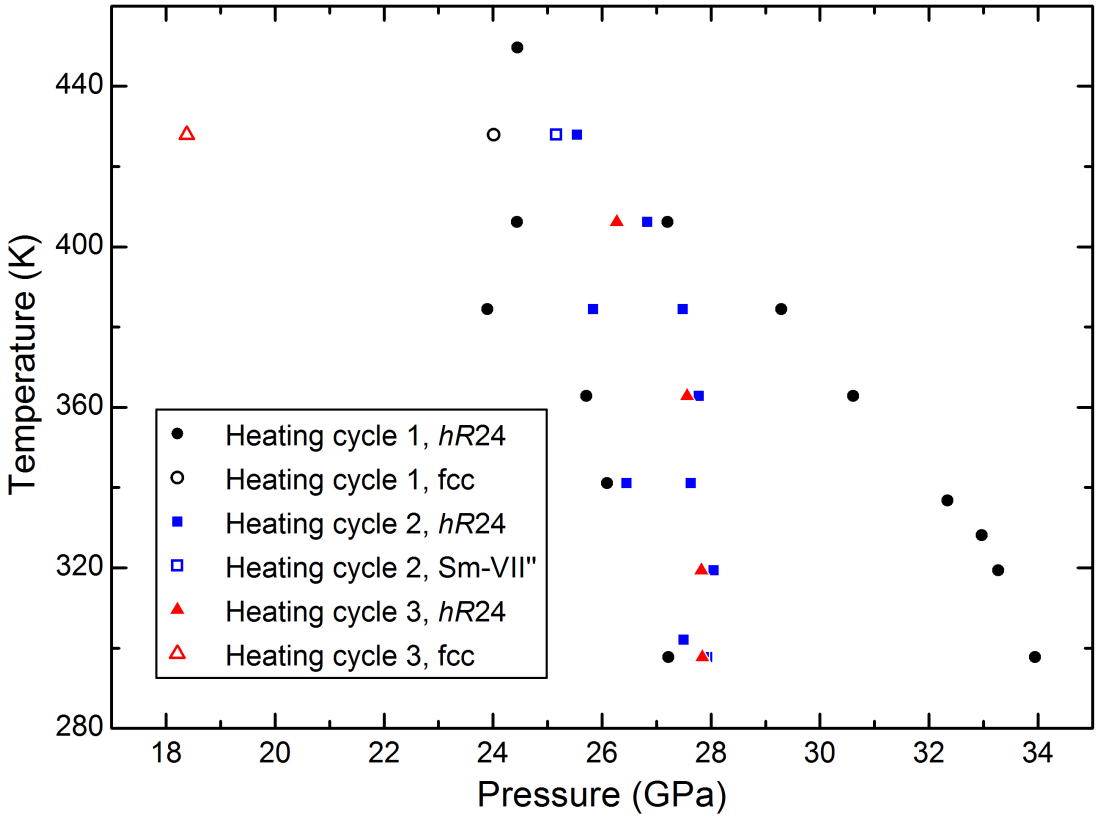

Figure 7.16: Pressure and temperature corresponding to the diffraction data collected during the three heating cycles.

at 295 K.

In heating cycle 2, the pressure dropped from 27.9 to 25.5 GPa on heating to 428 K. Similar to heating cycle 1, the splitting of the closely-spaced reflections was observed to decrease on heating, and the c/a ratio decreased from 2.4793(7) at 295 K to 2.4655(7) at 406 K. Again, on heating to 429 K the distortion from cubic could only be identified by peak assymetry, and so it is not possible to determine an accurate c/a ratio. The pressure was then decreased slightly from 25.5 to 25.2 GPa at 428 K, and the splitting of the reflections could no longer be resolved. This can be seen in figure 7.17, which shows the integrated diffraction patterns of Sm at 28 GPa and 319 K, 28 GPa and 363 K, 27 GPa and 406 K, and at 25 GPa and 428 K. Although the 428 K diffraction pattern is *extremely* similar to that of Sm-VII, there are a number of differences between the patterns. This pattern will therefore be referred to as Sm-VII′, and it will be discussed in more detail later in this section. On subsequent cooling, the splitting of the closely-spaced reflections increased, with the c/a ratio increasing to 2.4777(4) at 27.9 GPa at 295 K.

In heating cycle 3, the pressure dropped from 27.8 to 26.3 K on heating to 406 K, and the c/a ratio decreased from 2.4782(7) to 2.4660(7). Unfortunately, when the sample was heated to 428 K, the pressure of the sample dropped to 18.4 GPa. Due to the large pressure drop, no data were collected on cooling.

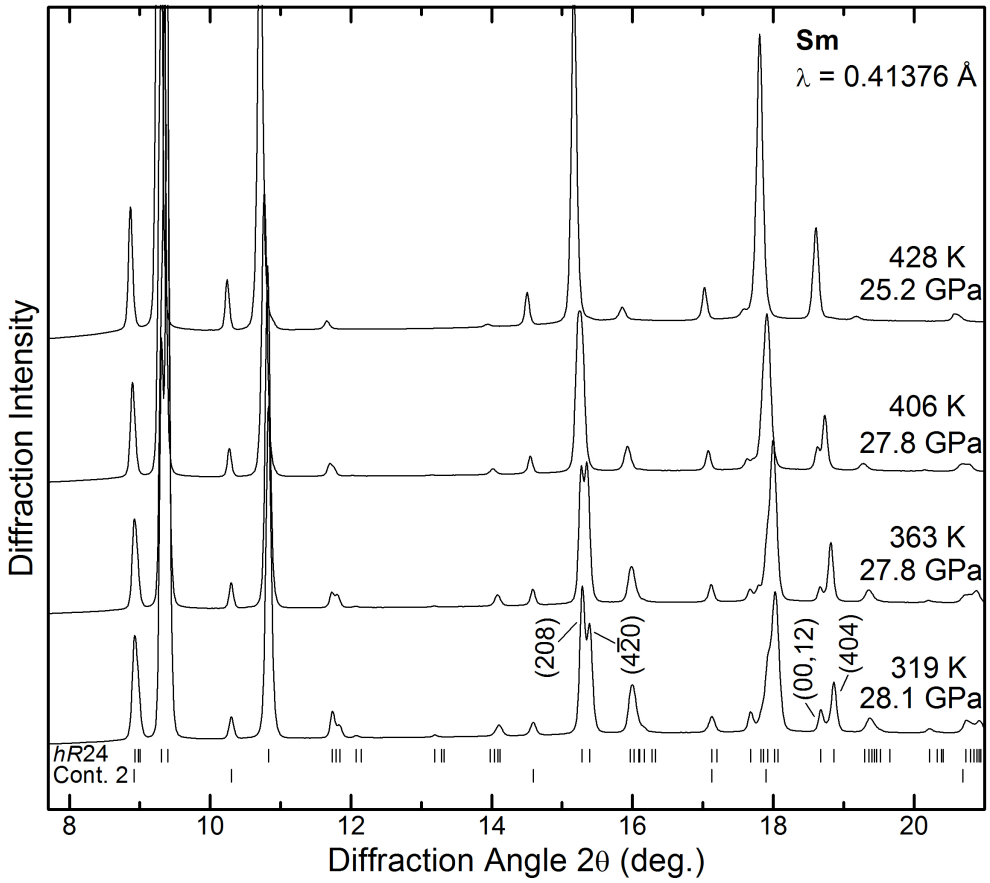

Figure 7.17: Integrated diffraction patterns of Sm plus contaminant 2 at 28.1 GPa and 318 K, 27.8 GPa and 363 K, 26.8 GPa and 406 K and 25.2 GPa and 428 K, illustrating the transition from $hR24$ to Sm-VII′. The tick marks below the lower profile show the calculated peak positions of $hR24$-Sm (upper) and contaminant 2 (lower).

The lattice parameter a of the cubic $hR24$ structure, as determined from the d-spacing of individual reflections, is plotted against diffraction angle 2θ in figure 7.18(a). This is clearly different from the same plot for the Sm-VII pattern, which is shown in figure 7.15(a). In Sm-VII, significant peak misfits are observed in both main and satellite reflections. However, in Sm-VII′, an excellent fit is observed to the main reflections, and significant misfits are only observed in the satellite reflections. Although the direction of the peak shifts are the same for the majority of the superlattice reflections in Sm-VII and Sm-VII′, the $(\frac{3}{2},\frac{1}{2},\frac{3}{2})$ is observed to be shifted to *higher* angles (smaller d-spacing) in Sm-VII and to *lower* angles (longer d-spacing) in Sm-VII′. The lattice parameter a_c of contaminant

2, determined from the d-spacing of individual reflections, is plotted against diffraction angle 2θ in figure 7.18(b) for comparison. Again, the overall fit is excellent, confirming that the peak misfits cannot be due to a calibration issue.

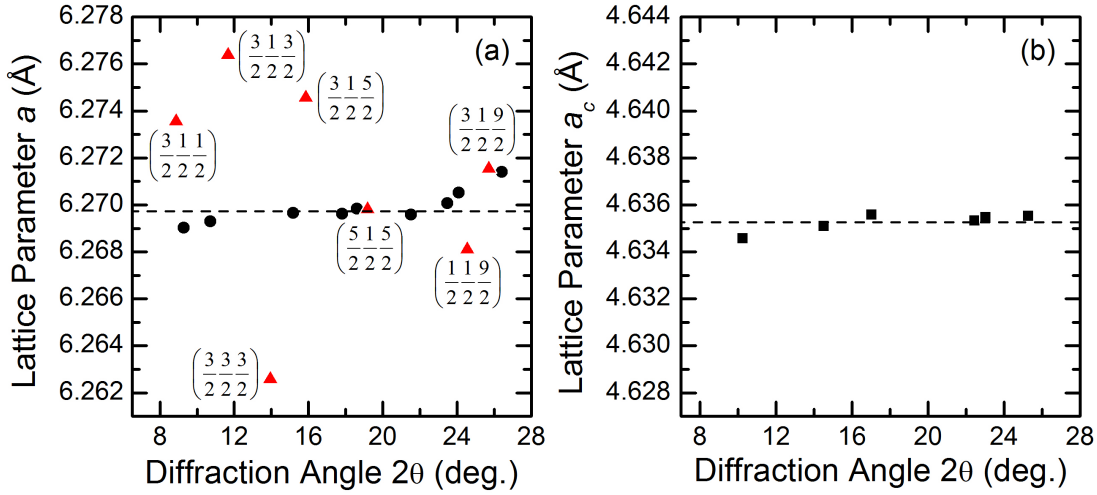

Figure 7.18: (a) Lattice parameter a of the cubic $hR24$ structure, determined from the d-spacing of individual reflections in the Sm-VII′ diffraction pattern at 428 K and 25.2 GPa, against diffraction angle 2θ. The black circles show data determined from the main reflections, and the red triangles show data determined from the superlattice reflections. The Miller indices of the superlattice reflections are labeled, and the dotted line indicates the value of a determined from the Rietveld refinement of the cubic $hR24$ structure to the diffraction profile.
(b) Lattice parameter a_c of contaminant 2, determined from the d-spacing of individual reflections in the Sm-VII′ diffraction pattern at 428 K and 25.2 GPa, against diffraction angle 2θ. The dotted line indicates the value of a_c determined from a Rietveld refinement of the cubic $hR24$ structure to the diffraction profile.

The $hR24 \rightarrow$ Sm-VII transition is identified by a change in the relative intensity of closely-spaced reflections, until a set of reflections disappear completely. However, this is not the case in the $hR24 \rightarrow$ Sm-VII′ transition, in which the splitting of closely-spaced reflections decreases until they can no longer be resolved. This can be seen in the evolution of the (0,0,12) and (404)-$hR24$ reflections, which result from the splitting of the (222)-fcc reflection. The behaviour these reflections across the $hR24 \rightarrow$ Sm-VII transition is shown in figure 7.19(a). The (0,0,12) reflection can clearly be seen to decrease in intensity, before it completely disappears by 22.5 GPa, while no significant change in the splitting of the reflections are observed. The behaviour of the same reflections across the $hR24 \rightarrow$ Sm-VII′ transition in heating cycle 2 is illustrated in figure 7.19(c). In this case, the splitting of the reflections decreases until they can no longer be resolved, and no significant changes in intensity are observed. Similar behaviour is observed in the $hR24 \rightarrow$ fcc transitions observed in heating cycles 2 and 4,

which are illustrated in figures 7.19(b) and (d), respectively.

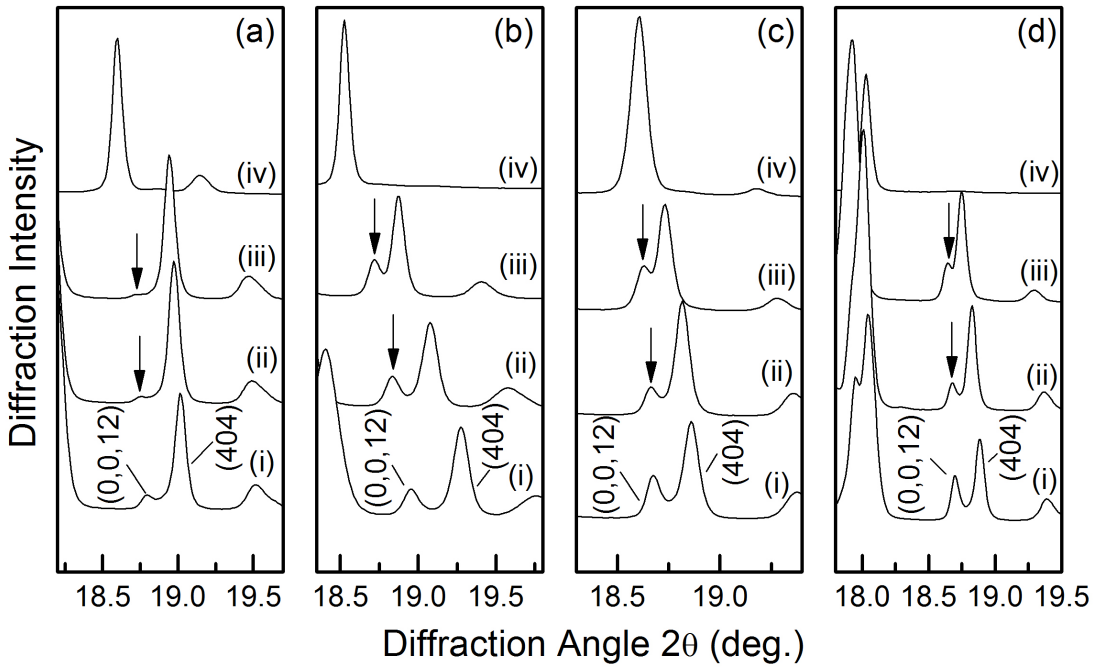

Figure 7.19: The behaviour of the (0,0,12) and (404)-$hR24$ reflections in the x-ray powder diffraction profiles of Sm (a) accross the $hR24 \rightarrow$ Sm-VII transition at (i) 28.3, (ii) 27.8, (iii) 27.3 and (iv) 22.5 GPa at 295 K, (b) in heating cycle 1 at (i) 33.3 GPa and 319 K, (ii) 30.6 GPa and 363 K, (iii) 27.2 GPa and 406 K, and (iv) 27.2 GPa and 406 K, (c) in heating cycle 2 at (i) 28.1 GPa and 319 K, (ii) 27.8 GPa and 363 K, (iii) 26.8 GPa and 406 K, and (iv) 25.2 GPa and 428 K, and (d) in heating cycle 3 at (i) 27.8 GPa and 319 K, (ii) 27.6 GPa and 363 K, (iii) 26.3 GPa and 406 K, and (iv) 18.4 GPa and 428 K. Sm transforms from $hR24$ to fcc in heating cycles 1 and 3, and from $hR24$ to Sm-VII′ in heating cycle 2. In (a), the intensity of the (0,0,12) reflection decreases on decompression until it can no longer be observed at 22.5 GPa, whereas in (b), (c) and (d), the splitting of the reflections decreases until they can no longer be resolved at 428 K.

7.4 Conclusions

Angle-dispersive powder x-ray diffraction experiments have been performed on Sm metal up to 50 GPa. The distorted-fcc phase has been found to have the same $hR24$ structure that has been reported for all of the other trivalent lanthanide elements. However, Sm does not undergo a transition to a second distorted-fcc phase such as the $oI16$ phase observed in Pr, and instead $hR24$-Sm distorts to a greater extent than $hR24$-Pr. Therefore, although the high-pressure structural behaviour of the trivalent lanthanides is often thought to be similar, there appear to be subtle structural differences between the different elements.

In situ high-pressure high-temperature experiments have been performed on $hR24$-Sm up to 450 K. The c/a ratio was observed to decrease with increasing temperature, corresponding to a decrease in the distortion away from cubic. A path-dependent transition to a new phase, Sm-VII, has been observed, which occurred on annealing followed by pressure decrease. A similar transition to another new phase, Sm-VII′, was observed on heating to 428 K at 25.5 GPa. The diffraction patterns from these two phases are extremely similar. However, subtle differences between their diffraction patterns suggest that they correspond to two subtly different structures. The structures of these new phases have not yet been determined, and further work is required.

Chapter 8

Conclusions and Future Work

8.1 Europium

Previous x-ray diffraction studies reported Eu to undergo a transition to the Eu-III phase above ∼17 GPa [13–15]. This transition is characterised by the appearance of a number of weak reflections in the diffraction patterns in addition to those from the hcp phase. In order to investigate the high-pressure structural behaviour of Eu above ∼17 GPa, angle-dispersive x-ray powder diffraction data have been collected on high-purity Eu samples up to ∼70 GPa.

Initially, the appearance of the additional reflections was observed in the diffraction patterns collected above ∼17 GPa, in agreement with previous work. However, this was determined to be due to a pressure-induced reaction, resulting in the sample becoming a mixture of hcp-Eu and a rhombohedral contaminant, $hR6$, with 6 Eu atoms per rhombohedral unit cell. The contaminant is also observed to undergo a pressure-induced transition to a cubic phase, $cI12$, at 34.8(12) GPa. Consideration of the volume per Eu atom of the two contaminant phases at the same pressure suggests that they have different stoichiometries. Comparison of the volume per Eu atom with that reported recently for EuH_2 [16] suggests that the $cI12$ phase might be a Eu hydride, EuH_x, with $x \approx 1.2$, and that $hR6$ may be a subhydride, with $x \approx 0.3$.

When high-purity Eu samples were loaded quickly in a high-quality glovebox (< 0.1 ppm O_2 and < 0.1 ppm H_2O) without a pressure-transmitting medium and without a pressure marker, no additional reflections were observed in the

diffraction patterns collected above ∼17 GPa. Instead, Eu remained in the hcp phase up to 31.5 GPa. This confirmed that the previously-reported transition to Eu-III is in fact due to changes in a contaminant phase, and not due to changes in Eu itself.

Above 31.5 GPa, Eu transforms to the Eu-IV phase. The diffraction patterns from this phase are extremely complex, with a large number of closely-spaced reflections and numerous weak reflections. However, collecting high-resolution diffraction data on non-contaminated samples made it possible to determine this phase to have an incommensurately-modulated crystal structure, i-$mC4$, which has a C-centred average structure and a modulation vector in the $a - c$ plane. This is the first observation of an incommensurate structure in the lanthanide elements at high pressure.

Above 38 GPa, Eu transforms to another new phase, Eu-V. This phase was also determined to have an incommensurately-modulated crystal structure, i-$mC4(2)$. Eu-V has the same superspace group as Eu-IV, but the modulation wave vector has a different direction and magnitude. Discontinuities were observed in both the lattice parameters and wave vector components across the Eu-IV → Eu-V transition, determining it to be first-order. This is the first observation of an incommensurate-incommensurate (non-host-guest) transition in the elements at high pressure.

Following the transition to Eu-V, no dramatic changes were observed in the diffraction patterns collected up to ∼70 GPa, the highest pressure reached in these studies. However, significant peak broadening was observed in the patterns collected above ∼50 GPa, making it increasingly more difficult to determine accurate structural parameters. Subtle changes in the diffraction patterns collected above 47.1 GPa introduced the possibility of a further structural transition. However, the diffraction patterns collected from this sample contain reflections from at least one impurity phase in addition to those from the $cI12$ contaminant. High-resolution diffraction data collected on a non-contaminated samples should therefore be collected in order to determine if the changes in the diffraction profiles are due to a structural transition in Eu itself, or simply due to pressure-induced changes in one of the contaminant phases. In particular, to determine the structure of Eu above 84 GPa, in the superconducting region [111].

The peak broadening observed in the diffraction patterns collected above ∼50 GPa mean that unless Eu transforms to a higher-symmetry structure, the

determination of the structural behaviour above this pressure will be extremely challenging. However, it is noted that no evidence of any of the structures observed in the 'regular' trivalent lanthanide elements have been observed up to the maximum pressure, suggesting that Eu has not become fully trivalent up to ∼70 GPa.

In situ high-pressure high-temperature x-ray diffraction measurements on Eu have performed up to 449 K and 61.2 GPa. This has enabled an initial estimate of the bcc, hcp, Eu-IV and Eu-V phases to be made. The bcc → hcp phase boundary is determined to be roughly vertical, and the pressure range over which the hcp phase is stable is observed to increase on heating. Two attempts were made to cross the hcp → Eu-IV phase boundary at 449 K. However, in both cases diamond failure was observed at similar pressures and temperatures (∼37 GPa and 449 K), suggesting the possibility of a reaction between Eu and the diamonds, or Eu and the gasket material. Similar behaviour was observed in previous studies on K and Te when the sample melted [126, 127]. This then introduces the possibility of a low melting temperature in Eu at this pressure. The melt curve of Eu has only been determined up to 7 GPa [119], where a maximum was observed at bcc phase at about 3.5 GPa and 722 K. Future resistive-heating studies using a different gasket material are required in order to investigate this further. In particular, future resistive heating studies should be performed in vacuum, so that higher temperatures can be reached without resulting in damage to the diamonds due to oxidation.

The lanthanide elements are known be challenging for density-functional theory calculations due to the difficulty in describing the highly-localised $4f$ electrons. Accurate modeling of the electronic structure of Eu at high pressure, in particular in the incommensurately-modulated Eu-IV and Eu-V phases, remains a challenge for future computational studies. In particular, to investigate the origin of the modulation wave by looking for phonon-softening in the unmodulated structure, and the presence of Fermi-surface nesting.

8.2 Samarium

Angle-dispersive x-ray powder diffraction experiments on Sm have been performed up to ∼50 GPa. The dfcc phase has been confirmed to have the same $hR24$ structure observed in Pr [11]. However, unlike Pr, Sm does not undergo

a transition to a second distorted-fcc phase, and instead $hR24$-Sm distorts to a greater extend than $hR24$-Pr. The post-dfcc phase has been confirmed to have the $hP3$ structure reported in previous work [18].

The diffraction patterns were observed to become much sharper following the dhcp $\rightarrow$ dfcc transition, which was accompanied by a change in the texture of the Debye-Scherrer rings. In our experience, the diffraction patterns obtained from the dfcc phase of Sm are *significantly* sharper than those obtained from La, Nd, Gd and Tb. The broadness of the patterns from these phases, combined with the fact that these structures distort less than Sm, makes it much more difficult to identify subtle changes in their diffraction patterns. In particular, if mixed-phase patterns are obtained over a relatively large pressure range, as was observed in the $hR24 \rightarrow oI16$ transition in Pr. In one of our samples, the diffraction pattern from the dhcp phase was observed to become significantly sharper when heated to 423 K. This technique may be useful when looking at higher-pressure phases of other lanthanide elements.

Evidence of a path-dependent structural transition to a new phase, Sm-VII, was observed on annealing followed by pressure-decrease. The diffraction pattern from this phase is similar to that of 'cubic' $hR24$. That is, when the c/a ratio is equal to $\sqrt{6}$. However, significant peak misfits in both main and satellite reflections determine that an alternative structural solution is required. In order to determine if this phase is stable above room temperature, *in situ* high-pressure high-temperature x-ray diffraction data were collected in the dfcc phase over three heating cycles. The c/a ration of $hR24$-Sm was observed to increase on heating, indicating that the structure is becoming less distorted from cubic. A transition to another new phase, Sm-VII′, is observed on heating to 428 K at 25.2 GPa. The diffraction pattern from this phase is *extremely* similar to that of Sm-VII. However, a Rietveld refinement of the 'cubic' $hR24$ structure to the Sm-VII′ diffraction profile found that, unlike in Sm-VII, peak misfits are only observed in the satellite reflections, and *not* in the main reflections. This suggests that the structures of Sm-VII and Sm-VII′ are subtly different. Attempts to determine the structures of these phases using conventional indexing methods were unsuccessful, and further work is required. Overall, this suggests that, despite the fact that the high-pressure structural behaviour of the trivalent lanthanide elements is often thought to be well known, surprises still remain.

Bibliography

[1] R. J. Husband, I. Loa, K. A. Munro, E. E. McBride, S. R. Evans, H. P. Liermann, and M. I. McMahon, "Incommensurate-incommensurate phase transition in Eu metal at high pressure," *Phys. Rev. B*, vol. 90, p. 214105, 2014.

[2] R. J. Husband, I. Loa, G. W. Stinton, G. J. Ackland, and M. I. McMahon, "The distorted-fcc phase of samarium," *J. Phys. Conf. Ser.*, vol. 500, p. 032009, 2014.

[3] R. J. Husband, I. Loa, G. W. Stinton, G. J. Ackland, and M. I. McMahon, "Phase transitions in europium at high pressures," *High Pressure Res.*, vol. 33, pp. 158–164, 2013.

[4] R. J. Husband, I. Loa, G. Stinton, S. R. Evans, G. J. Ackland, and M. I. McMahon, "Europium-IV: An incommensurately modulated crystal structure in the lanthanides," *Phys. Rev. Lett.*, vol. 109, p. 095503, 2012.

[5] R. J. Husband, I. Loa, G. W. Stinton, S. R. Evans, G. J. Ackland, and M. I. McMahon, "The structure of Eu-III," *J. Phys. Conf. Ser.*, vol. 377, p. 012030, 2012.

[6] R. Boehler and K. de Hantsetters, "New anvil designs in diamond-cells," *High Pressure Res.*, vol. 24, pp. 391–396, 2004.

[7] S. van Smaalen, *Incommensurate Crystallography*. Great Clarendon Street, Oxford OX2 6DP: Oxford University Press, 2007.

[8] N. W. Ashcroft and N. D. Mermin, *Solid State Physics*. Berkshire House, 168-173 High Holborn, London WC1 V7AA, UK: Thomson Learning, 1976.

[9] G. K. Samudrala and Y. K. Vohra, *Handbook on the Physics and Chemistry of Rare Earths*, vol. 43. North-Holland, Elisevier, 2003.

[10] L. Gerward, J. S. Olsen, and U. Benedict, "On the use of distorted fcc structures for describing high-pressure phases," *Physica B*, vol. 144, pp. 72–78, 1986.

[11] S. R. Evans, I. Loa, L. F. Lundegaard, and M. I. McMahon, "Phase transitions of praseodymium up to 23 GPa: An x-ray powder diffraction study," *Phys. Rev. B*, vol. 80, p. 134105, 2009.

[12] M. I. McMahon and R. J. Nelmes, "Different results for the equilibrium phases of cerium above 5 GPa," *Phys. Rev. Lett.*, vol. 78, pp. 3884–3887, 1997.

[13] K. Takemura and K. Syassen, "Pressure-volume relations and polymorphism of europium and ytterbium to 30 GPa," *J. Phys. F: Met. Phys.*, vol. 15, pp. 543–559, 1985.

[14] T. Krüger, B. Merkau, W. A. Grosshans, and W. B. Holzapfel, "Kinetics and systematics of structural phase transitions in the regular lanthanide metals under pressure," *High Pressure Res.*, vol. 2, pp. 193–236, 1990.

[15] W. Bi, Y. Meng, R. S. Kumar, A. L. Cornelius, W. W. Tipton, R. G. Hennig, Y. Zhang, C. Chen, and J. S. Schilling, "Pressure-induced structural transitions in europium to 92 GPa," *Phys. Rev. B*, vol. 83, p. 104106, 2011.

[16] T. Matsuoka, H. Fujihisa, N. Hirao, Y. Ohishi, T. Mitsui, R. Masuda, M. Seto, Y. Yoda, K. Shimizu, A. Machida, and K. Aoki, "Structural and valence changes of europium hydride induced by application of high-pressure H_2," *Phys. Rev. Lett.*, vol. 107, p. 025501, 2011.

[17] M. Winzenick and W. B. Holzapfel, "Refinement of the P–T phase diagram of barium," *Phys. Rev. B*, vol. 55, pp. 101–104, 1997.

[18] Y. C. Zhao, F. Porsch, and W. B. Holzapfel, "Intermediate $4f$ bonding structure for samarium under pressure," *Phys. Rev. B*, vol. 50, pp. 6603–6608, 1994.

[19] T. Hahn, ed., *International Tables for Crystallography, Volume A, Space-group symmetry*. Dordrecht, Holland: J. Wiley, 1983.

[20] A. J. C. Wilson and E. Prince, eds., *International Tables for Crystallography, Volume C, Mathematical, Physical and Chemical Tables*. Dordrecht: Kluwer Academic Publishers, 1999.

[21] M. I. McMahon and R. J. Nelmes, "High-pressure structures and phase transformations in elemental metals," *Chem. Soc. Rev.*, vol. 35, pp. 943–963, 2006.

[22] E. Gregoryanz, L. F. Lundegaard, M. I. McMahon, C. Guillaume, R. J. Nelmes, and M. Mezouar, "Structural diversity of sodium," *Science*, vol. 320, pp. 1054–1057, 2008.

[23] M. I. McMahon, R. J. Nelmes, U. Schwarz, and K. Syassen, "Composite incommensurate K-III and a commensurate form: Study of a high-pressure phase of potassium," *Phys. Rev. B*, vol. 74, p. 140102, 2006.

[24] M. I. McMahon, S. Rekhi, and R. J. Nelmes, "Pressure dependent incommensuration in Rb-IV," *Phys. Rev. Lett.*, vol. 87, p. 055501, 2001.

[25] M. I. McMahon, T. Bovornratanaraks, D. R. Allan, S. A. Belmonte, and R. J. Nelmes, "Observation of the incommensurate barium-IV structure in strontium phase V," *Phys. Rev. B*, vol. 61, pp. 3135–3138, 2000.

[26] R. J. Nelmes, D. R. Allan, M. I. McMahon, and S. A. Belmonte, "Self-hosting incommensurate structure of barium IV," *Phys. Rev. Lett.*, vol. 83, pp. 4081–4084, 1999.

[27] O. Degtyareva, M. I. McMahon, and R. J. Nelmes, "Pressure-induced incommensurate-to-incommensurate phase transition in antimony," *Phys. Rev. B*, vol. 70, p. 184119, 2004.

[28] M. I. McMahon, O. Degtyareva, and R. J. Nelmes, "Ba-IV-type incommensurate crystal structure in group-V metals," *Phys. Rev. Lett.*, vol. 85, pp. 4896–4899, 2000.

[29] H. Fujihisa, Y. Akahama, H. Kawamura, Y. Gotoh, H. Yamawaki, M. Sakashita, S. Takeya, and K. Honda, "Incommensurate composite crystal structure of scandium-II," *Phys. Rev. B*, vol. 72, p. 132103, 2005.

[30] O. Degtareva, E. Gregoryanz, M. Somayazulu, H. Mao, and R. J. Hemley, "Crystal structure of the superconducting phases of S and Se," *Phys. Rev. B*, vol. 71, p. 214104, 2005.

[31] I. Loa, M. I. McMahon, and A. Bosak, "Origin of the incommensurate modulation in Te-III and Fermi-surface nesting in a simple metal," *Phys. Rev. Lett.*, vol. 102, p. 035501, 2009.

[32] T. Kume, T. Hiraoka, Y. Ohya, S. Sasaki, and H. Shimizu, "High pressure raman study of bromine and iodine: Soft phonon in the incommensurate phase," *Phys. Rev. Lett.*, vol. 94, p. 065506, 2005.

[33] H. F. K. Takemura, K. Sato and M. Onoda, "Modulated structure of solid iodine during its molecular dissociation under high pressure," *Nature*, vol. 423, pp. 971–974, 2003.

[34] H. Fujihisa, Y. Akahama, H. Kawamura, Y. Ohishi, Y. Gotoh, H. Yamawaki, M. Sakashita, S. Takeya, and K. Honda, "Incommensurate structure of phosphorus phase IV," *Phys. Rev. Lett.*, vol. 98, p. 175501, 2007.

[35] A. L. Ruoff, H. Xia, H. Luo, and Y. K. Vohra, "Miniaturization techniques for obtaining static pressures comparable to the pressure at the center of the earth: Xray diffraction at 416 GPa," *Rev. Sci. Instrum.*, vol. 61, pp. 3830–3833, 1990.

[36] L. Dubrovinsky, N. Dubrovinskaia, V. B. Prakapenka, and A. M. Abakumov, "Implementation of micro-ball nanodiamond anvils for high-pressure studies above 6 Mbar," *Nat. Commun.*, vol. 3, p. 1163, 2012.

[37] M. I. McMahon, "High-pressure X-ray science on the ultimate storage ring," *J. Synchrotron Rad.*, vol. 21, pp. 1077–1083, 2014.

[38] O. Shimomura, K. Takemura, H. Fujihisa, Y. Fujii, Y. Ohishi, T. Kikegawa, Y. Amemiya, and T. Matsushi, "Application of an imagine plate to high-pressure x-ray study with a diamond anvil cell," *Rev. Sci. Instrum.*, vol. 63, pp. 967–973, 1992.

[39] R. J. Nelmes and M. I. McMahon, "High-pressure powder diffraction on synchrotron sources," *J. Synchrotron Rad.*, vol. 1, pp. 69–73, 1994.

[40] B. Johansson and A. Rosengren, "Generalized phase diagram for the rare-earth elements: Calculations and correlations of bulk properties," *Phys. Rev. B*, vol. 11, pp. 2836–2857, 1975.

[41] L. Merrill and W. A. BAssett, "Miniature diamond anvil pressure cell for single crystal x-ray diffraction studies," *Rev. Sci. Instrum.*, vol. 45, pp. 290–294, 1975.

[42] J. Zsolt, H. Cynn, K. Visbeck, and W. J. Evans, "High-temperature experiments using a resistively heated high-pressure membrane diamond anvil cell," *Rev. Sci. Instrum.*, vol. 84, p. 095114, 2013.

[43] R. A. Forman, G. J. Piermarini, J. D. Barnett, and S. Block, "Pressure measurement made by the ulilization of ruby sharp-line luminescence," *Science*, vol. 176, pp. 284–285, 1972.

[44] H. K. Mao, J. Xu, and P. M. Bell, "Calibration of the ruby pressure gauge to 800 kbar under quasihydrostatic conditions," *J. Geophys. Res.*, vol. 91, pp. 4673–4676, 1986.

[45] H. K. Mao, P. M. Bell, J. W. Shaner, and D. J. Steinberg, "Specific volume measurements of Cu, Mo, Pd, Ag and calibration of the ruby R_1 fluorescence pressure gauge from 0.06 to 1 MBar," *J. Appl. Phys.*, vol. 49, pp. 3276–3283, 1978.

[46] A. D. Chijioke, W. J. Nellis, A. Soldatov, and I. Silvera, "The ruby pressure standard to 150 GPa," *J. Appl. Phys.*, vol. 98, p. 114905, 2005.

[47] G. J. Piermarini, S. Block, and J. D. Marnett, "Hydrostatic limits in liquids and solids to 100 kbar," *J. Appl. Phys.*, vol. 44, pp. 5377–5382, 1973.

[48] F. Datchi, A. Dewaele, P. Loubeyre, R. Letoullec, Y. L. Godec, and B. Canny, "Optical pressure sensors for high-pressure-high-temperature studies in a diamond anvil cell," *High. Pressure Res.*, vol. 27, pp. 447–463, 2007.

[49] M. Hanfland, K. Syassen, and J. Köhler, "Pressure-volume relationship of Ta," *J. Appl. Phys.*, vol. 91, pp. 4143–4148, 2002.

[50] P. I. Dorogokupets and A. R. Oganov, "Ruby, metals, and MgO as alternative pressure scales: A semiempirical description of shock wave, ultrasonic, x-ray, and thermochemical data at high temperatures and pressures," *Phys. Rev. B*, vol. 75, p. 024115, 2007.

[51] M. Taxak, S. Kumar, N. Krishnamurthy, A. K. Suri, and G. P. Tiwari, "Change in lattice parameter of tantalum due to dissolved hydrogen," *Processing and Application of Ceramics*, vol. 6, pp. 73–76, 2012.

[52] K. Takemura and A. Dewaele, "Isothermal equation of state for gold with a He-pressure medium," *Phys. Rev. B*, vol. 78, p. 104119, 2008.

[53] S. Klotz, J.-C. Chervin, P. Munsch, and G. L. Marchand, "Hydrostatic limits of 11 pressure transmitting media," *J. Phys. D: Appl. Phys.*, vol. 42, p. 075413, 2009.

[54] C. Giacovazzo, H. L. Monaco, G. Artioli, D. Viterbo, M. Milanesio, G. Ferraris, G. Gilli, P. Gilli, G. Zanotti, and M. Catti, *Fundamentals of Crystallography.* Great Clarendon Street, Oxford OX2 6DP: Oxford University Press, 2011.

[55] R. A. Young, ed., *The Rietveld Method.* Great Claredon Street, Oxford OX2 6DP: Oxford University Press, 1993.

[56] P. M. de Wolff, "The pseudo-symmetry of modulated crystal structures," *Acta Cryst.*, vol. A30, pp. 777–785, 1974.

[57] J. R. Hook and H. E. Hall, *Solid State Physics.* The Atrium, Southern Gate, Chichester, West Sussex PO19 8SQ, England: John Wiley & Sons, 2010.

[58] M. I. McMahon, E. Gregoryanz, L. F. Lundegaard, I. Loa, and C. Guillaume, "Structure of sodium above 100 GPa by single-crystal x-ray diffraction," *PNAS*, vol. 104, pp. 17297–17299, 2007.

[59] I. Loa, E. I. Isaev, M. I. McMahon, D. Y. Kim, B. Johansson, A. Bosak, and M. Krisch, "Lattice dynamics and superconductivity in cerium at high pressure," *Phys. Rev. Lett.*, vol. 108, p. 045502, 2012.

[60] P. J. Duke, *Synchrotron Radiation: Production and properties.* Great Clarendon Street, Oxford OX2 6DP: Oxford University Press, 2000.

[61] A. P. Hammersley, "FIT2D: An introduction and overview," tech. rep., ESRF, 1997.

[62] A. P. Hammersley, S. O. Svensson, M. Hanfland, A. N. Fitch, , and D. Häusermann, "Two-dimensional detector software From real detector to idealised image or two-theta scan," *High Press. Res.*, vol. 14, pp. 235–248, 1996.

[63] A. Boultif and D. Louër, "Powder pattern indexing with the dichotomy method," *J. Appl. Cryst.*, vol. 37, pp. 724–731, 2004.

[64] J. Rodrìguez-Carvajal, "Recent advances in magnetic structure determination by neutron powder diffraction," *Physica (Amsterdam)*, vol. 192B, p. 55, 1993.

[65] A. L. Bail, H. Duroy, and J. L. Fourquet, "Ab-initio structure determination of $LiSbWO_6$ by x-ray powder diffraction," *Mat. Res. Bull.*, vol. 23, pp. 447–452, 1988.

[66] H. M. Rietveld, "A profile refinement method for nuclear and magnetic structures," *J. Appl. Cryst.*, vol. 2, pp. 65–71, 1969.

[67] P. Thompson, D. E. Cox, and J. B. Hastings, "Rietveld refinement of Debye-Scherrer synchrotron x-ray data from Al_2O_3," *J. Appl. Cryst.*, vol. 20, pp. 79–83, 1987.

[68] W. A. Dollase, "Corrections of intensities for preferred orientation in powder diffractometry: Application of the March model," *J. Appl. Cryst.*, vol. 19, pp. 267–272, 1986.

[69] V. Petríicek, M. Dusek, and L. Palatinus, "Crystallographic computing system JANA2006: General features," *Z. Kristallogr.*, vol. 229, pp. 345–352, 2014.

[70] H. G. Smith and G. H. Lander, "Neutron scattering investigations of α-uranium in the charge-density-wave state," *Phys. Rev. B*, vol. 30, pp. 5407–5415, 1984.

[71] L. Fast, O. Eriksson, B. Johansson, J. M. Wills, G. Straub, H. Raeder, and L. Nordström, "Theoretical aspects of the charge density wave in uranium," *Phys. Rev. Lett.*, vol. 81, pp. 2978–2981, 1998.

[72] C. Hejny and M. I. McMahon, "Large structural modulations in incommensurate Te-III and Se-IV," *Phys. Rev. Lett.*, vol. 91, p. 215502, 2003.

[73] O. Degtyareva, M. Magnitskaya, J. Kohanoff, G. Profeta, S. Scandolo, M. Hanfland, M. I. McMahon, and E. Gregoryanz, "Competition of charge-density waves and superconductivity in sulphur," *Phys. Rev. Lett.*, vol. 99, p. 155505, 2007.

[74] T. Ishikawa, H. Nagara, K. Kusakabe, and N. Suzuki, "Determining the structure of phosphorus in phase IV," *Phys. Rev. Lett.*, vol. 96, p. 095502, 2006.

[75] J. C. Duthie and D. G. Pettifor, "Correlation between *d*-band occupancy and crystal structure in the rare earths," *Phys. Rev. Lett.*, vol. 38, pp. 564–567, 1977.

[76] N. C. Cunningham, W. Qiu, K. M. Hope, H.-P. Liermann, and Y. K. Vohra, "Symmetry lowering under high pressure: Structural evidence for f-shell delocalization in heavy rare earth metal terbium," *Phys. Rev. B*, vol. 76, p. 212101, 2007.

[77] R. Patterson, C. K. Saw, and J. Akella, "Static high-pressure structural studies on Dy to 119 GPa," *J. Appl. Phys.*, vol. 95, pp. 5443–5446, 2004.

[78] N. C. Cunningham, W. Qiu, and Y. K. Vohra, "Observation of complete regular trivalent rare earth sequence in heavy lanthanide metal holmium under high pressure," *High Pressure Res.*, vol. 26, pp. 43–50, 2006.

[79] G. K. Samudrala, S. A. Thomas, J. M. Montgomery, and Y. K. Vohra, "High pressure phase transitions in the rare earth metal erbium to 151 GPa," *J. Phys.: Condens. Matter*, vol. 23, p. 315701, 2011.

[80] N. Hamaya, Y. Sakamoto, H. Fujihisa, Y. Fujii, J. Takemura, T. Kikegawa, and O. Shimomura, "Crystal structure of the distorted fcc high-pressure phase of praseodymium," *J. Phys.: Condens. Matter*, vol. 5, pp. L369–L374, 1993.

[81] H. K. Mao, R. M. Hazen, P. M. Bell, and J. Wittig, "Evidence for $4f$ shell delocalization in praseodymium under pressure," *J. Appl. Phys.*, vol. 52, pp. 4572–4574, 1981.

[82] Y. K. Vohra, V. Vijayakumar, B. K. Godwal, and S. K. Sikka, "Structure of the distorted fcc high-pressure phase of the trivalent rare-earth metals," *Phys. Rev. B*, vol. 30, pp. 6205–6207, 1984.

[83] W. A. Grosshans, Y. K. Vohra, and W. B. Holzapfel, "F bonding in praseodymium under high pressure," *J. Phys. F: Met. Phys.*, vol. 13, pp. L147–L149, 1983.

[84] F. Porsch and W. B. Holzapfel, "Symmetry change at the fcc–distorted-fcc phase transition of lanthanides under pressure," *Phys. Rev. B*, vol. 50, pp. 16212–16218, 1994.

[85] V. P. Dmitriev, A. Y. Kuznetsov, O. Bandilet, P. Bouvier, L. Dubrovinsky, D. Machon, and H.-P. Weber, "Stability of the high-pressure monoclinic phases in Ce and Pr metals: Comparative diffraction study and phenomenological theory," *Phys. Rev. B*, vol. 70, p. 014104, 2004.

[86] K. A. Munro, R. J. Husband, R. Briggs, M. I. McMahon, and S. G.Macleod, "Diffraction study of the high pressure distorted-fcc phases of lanthanum metal," Tech. Rep. HC-1338, ESRF Report, 2014.

[87] M. Seipel, F. Porsch, and W. B. Holzapfel, "Characterisation of the fcc-distorted fcc-structural transition in lanthanum in an extended pressure and temperature range," *High Pres. Res.*, vol. 15, pp. 321–330, 1997.

[88] D. Errandonea, R. Boehler, B. Schwager, and M. Mezouar, "Structural studies of gadolinium at high pressure and temperature," *Phys. Rev. B*, vol. 75, p. 014103, 2007.

[89] J. M. Montgomery, G. K. Samudrala, G. M. Tsoi, and Y. K. Vohra, "High-pressure phase transitions in rare earth metal thulium to 195 GPa," *J. Phys.: Condens. Matter*, vol. 23, p. 155701, 2011.

[90] G. K. Samudrala and Y. K. Vohra, "Crystallographic phases in heavy rare earth metals under megabar pressures," *J. Phys. Conf. Ser.*, vol. 377, p. 012111, 2012.

[91] Y. R. Shen, R. S. Kumar, A. L. Cornelius, and M. F. Nicol, "High-pressure structural studies of dysprosium using angle-dispersive x-ray diffraction," *Phys. Rev. B*, vol. 75, p. 064109, 2007.

[92] A. W. Lawson and T.-Y. Tang, "Concerning the high pressure allotropic modification of cerium," *Phys. Rev.*, vol. 76, pp. 301–302, 1949.

[93] M. J. Lepp, D. Jackson, H. Cynn, C. Aracne, W. J. Evans, and A. K. McMahon, "Thermal signatures of the Kondo volume collapse in cerium," *Phys. Rev. Lett.*, vol. 101, p. 165703, 2008.

[94] J. W. Allen and R. M. Martin, "Kondo volume collapse and the $\gamma \rightarrow \alpha$ transition in cerium," *Phys. Rev. Lett.*, vol. 49, pp. 1106–1110, 1982.

[95] G. Fabbris, T. Matsuoka, J. Lim, J. R. L. Margegan, K. Shimizu, D. Haskel, and J. S. Schilling, "Different routes to pressure-induced volume collapse transitions in gadolinium and terbium metals," *Phys. Rev. B*, vol. 88, p. 245103, 2013.

[96] B. Johansson and S. Li, "Itinerant f-electron elements," *Philos. Mag.*, vol. 89, pp. 1793–1799, 2009.

[97] Y. K. Vohra, B. R. Sangala, A. K. Stemshorn, and K. M. Hope, "High pressure phase transformations in heavy rare earth metals and connections to actinide crystal structures," *Mater. Res. Soc. Symp. Proc.*, vol. 1104, pp. NN01–04, 2004.

[98] G. N. Chesnut and Y. K. Vohra, "Phase transformation in lutetium metal at 88 GPa," *Phys. Rev. B*, vol. 57, pp. 10221–10223, 1998.

[99] J. Lim, G. Fabbris, D. Haskel, and J. S. Schilling, "Origin of the volume collapse under pressure in elemental Dy," *J. Phys. Conf. Ser.*, vol. 500, p. 192009, 2014.

[100] F. Porsch and W. B. Holzapfel, "Novel reentrant high pressure phase transition in lanthanum," *Phys. Rev. Lett.*, vol. 70, pp. 4087–4089, 1993.

[101] G. K. Samudrala, G. M. Tsoi, and Y. K. Vohra, "Structural phase transitions in yttrium under ultrahigh pressures," *J. Phys.: Condens. Matter*, vol. 24, p. 362201, 2012.

[102] G. N. Chesnut and Y. K. Vohra, "Phase transformations and equation of state of praseodymium metal to 103 GPa," *Phys. Rev. B*, vol. 62, pp. 2965–2968, 2000.

[103] B. J. Baer, H. Cynn, V. Iota, C.-S. Yoo, and G. Shen, "Phase diagram and equation of state of praseodymium at high pressures and temperatures," *Phys. Rev. B*, vol. 67, p. 134115, 2003.

[104] B. I. Min, H. J. F. Jansen, T. Oguchi, and A. J. Freeman, "Electronic and structural properties of rare earth metals at normal and high pressures: Eu and Yb," *J. Magn. Magn. Mater.*, vol. 59, pp. 277–286, 1986.

[105] S. Rosengren and B. Johansson, "Alloy theory of the intermediate valence state: Application to europium metal," *Phys. Rev. B*, vol. 13, pp. 1468–1472, 1976.

[106] N. G. Nereson, C. E. Olsen, and G. P. Arnold, "Magnetic structure of europium," *Phys. Rev.*, vol. 135, pp. A176–A180, 1964.

[107] F. P. Bundy and J. K. Dunn, "Electrical behaviour of eu at very high pressures and low temperatures," *Phys. Rev. B*, vol. 24, pp. 4136–4141, 1981.

[108] J. Röhler, "The valence of Eu under high pressure," *Physica B*, vol. 144, pp. 27–31, 1986.

[109] J. N. Farrell and R. D. Taylor, "Coexistence of intermediate valence and antiferromagnetic ordering in europium metal," *Phys. Rev. Lett.*, vol. 58, pp. 2478–2481, 1987.

[110] W. Bi, N. M. Souza-Neto, D. Haskel, G. Fabbris, J. Z. E. E. Alp, R. G. Hennig, M. M. Abd-Elmeguid, Y. Meng, R. W. McCallum, K. Dennis, and J. S. Schilling, "Synchrotron x-ray spectroscopy studies of valence and magnetic state in europium metal to extreme pressures," *Phys. Rev. B*, vol. 85, p. 205134, 2012.

[111] M. Debessai, T. Matsuoka, J. J. Hamlin, and J. S. Schilling, "Pressure-induced superconducting state of europium metal at low temperatures," *Phys. Rev. Lett.*, vol. 102, p. 197002, 2009.

[112] P. Söderlind, P. E. A. Turchi, A. Landa, and V. Lordi, "Ground-state properties of rare-earth metals: an evaluation of density-functional theory," *J. Phys.: Condens. Matter*, vol. 26, p. 416001, 2014.

[113] L. W. Nixon and D. A. Papaconstantopoulos, "Electronic structure and superconductivity of europium," *Physica C*, vol. 470, pp. 709–715, 2010.

[114] G. N. Chesnut and Y. K. Vohra, "Structural and electronic transitions in ytterbium metal to 202 GPa," *Phys. Rev. Lett.*, vol. 82, pp. 1712–1715, 1999.

[115] K. Syassen, G. Wortmann, J. Feldhaus, K. H. Frank, and G. Kaindl, "Mean valence of Yb metal in the pressure range 0 to 340 kbar," *Phys. Rev. B*, vol. 26, pp. 4745–4748, 1982.

[116] H. L. Skriver, "Calculated structural phase transitions in the alkaline earth metals," *Phys. Rev. Lett.*, vol. 49, pp. 1768–1772, 1982.

[117] W. A. Grosshans and W. B. Holzapfel, "On structural systematics of the lanthanides under pressure," *J. Phys-Paris*, vol. 45, pp. C8–141, 1984.

[118] W. A. Grosshans and W. B. Holzapfel, "Atomic volumes of rare-earth metals under pressures to 40 GPa and above," *Phys. Rev. B*, vol. 45, pp. 5171–5178, 1992.

[119] A. Jayaraman, "Fusion curve of europium fusion, and fcc–bcc transformation in ytterbium at high pressures," *Phys. Rev.*, vol. 135, pp. A1056–A1059, 1964.

[120] N. M. Souza-Neto, J. Zhao, E. E. Alp, G. Shen, S. V. Sinogeikin, G. Lapertot, and D. Haskel, "Reentrant valence transition in EuO at high pressures: Beyond the bond-valence model," *Phys. Rev. Lett.*, vol. 109, p. 026403, 2012.

[121] S. Jiang, L.-G. Bai, J. Lui, W.-S. Xiao, X.-D. Li, Y.-C. Li, L.-Y. Tang, Y.-F. Zhang, D.-C. Zhang, and L.-R. Zheng, "The phase transition of Eu_2O_3 under high pressure," *Chin. Phys. Lett.*, vol. 26, p. 076101, 2009.

[122] D. B. McWhan, P. C. Souers, and G. Jura, "Magnetic and structural properties of europium metal and europium monoxide at high pressure," *Phys. Rev.*, vol. 143, pp. 385–389, 1966.

[123] Y. M. Polovov and L. G. Maistrenko, "Specific heat of europium," *Zh. Eksp. Teor. Fiz.*, vol. 68, pp. 1418–1422, 1975.

[124] T. Kenichi, "High-pressure structural study of barium to 90 GPa," *Phys. Rev. B*, vol. 50, pp. 16238–16246, 1994.

[125] I. Loa, R. J. Nelmes, L. F. Lundegaard, and M. I. McMahon, "Extraordinarily complex crystal structure with mesoscopic patterning in barium at high pressure," *Nature Materials*, vol. 11, pp. 627–632, 2012.

[126] O. Narygina, E. E. McBride, G. W. Stinton, and M. I. McMahon, "Melting curve of potassium to 22 GPa," *Phys. Rev. B*, vol. 84, p. 054111, 2011.

[127] C. Hejny and M. I. McMahon, "Phase transitions in tellurium at high pressure and temperature," *Phys. Rev. B*, vol. 74, p. 174119, 2006.

[128] G. Fabbris, J. Lim, L. S. I. Veiga, D. Haskel, and J. S. Schilling, "Electronic and structural ground state of heavy alkali metals at high pressure," *preprint arXiv:1412.0768v2*, 2014.

[129] A. Jayaraman and R. C. Sherwood, "Phase transformation in samarium induced by high pressure and its effect on the antiferromagnetic ordering," *Phys. Rev.*, vol. 134, pp. A691–A692, 1964.

[130] J. S. Olsen, S. Steenstrup, L. Gerward, U. Benedict, J. Akella, and G. Smith, "X-ray diffraction studies on samarium up to one megabar pressure," *High Press. Res.*, vol. 4, pp. 366–368, 1990.

[131] D. Errandonea, R. Boehler, and M. Ross, "Melting of the rare earth metals and f-electron delocalization," *Phys. Rev. Lett.*, vol. 85, pp. 3444–3447, 2000.

[132] Y. Vohra, J. Akella, S. Weir, and G. S. Smith, "A new ultra-high pressure phase in samarium," *Phys. Lett. A*, vol. 158, pp. 89–92, 1991.

[133] P. Söderlind, O. Eriksson, J. M. Wills, and B. Johansson, "Local-moment collapse in compressed samarium metal," *Phys. Rev. B*, vol. 48, pp. 9212–9215, 1993.

[134] B. E. Warren, *X-ray Diffraction*. London U. K.: Constable and Company, Ltd., 1990.

Journal of Physics: Conference Series **377** (2012) 012030 doi:10.1088/1742-6596/377/1/012030

The Structure of Eu-III

R J Husband[1], I Loa[1], G W Stinton[1], S R Evans[2], G J Ackland[1] and M I McMahon[1]

[1]SUPA, School of Physics and Astronomy and Centre for Science at Extreme Conditions, The University of Edinburgh, Edinburgh, EH9 3JZ, UK
[2]European Synchrotron Radiation Facility, 38043 Grenoble, France

E-mail: R.J.Husband@sms.ed.ac.uk

Abstract. Previous x-ray diffraction studies have reported Eu to transform from the *hcp* structure to a new phase, Eu-III, at 18 GPa. Using x-ray powder diffraction we have determined that Eu remains *hcp* up to 33 GPa, and that the extra peaks that appear at 18 GPa are from an impurity phase with space group $R\bar{3}c$. Above 33 GPa the diffraction pattern becomes very much more complex, signalling a transition to a phase with a distorted *hcp* structure.

1. Introduction

The majority of the lanthanide elements are trivalent due to their $4f^n5d^16s^2$ outer electronic structure. The two exceptions are europium (Eu) and ytterbium (Yb), which are divalent due to their half-filled and filled 4f shells, respectively. As a result, Eu and Yb both exhibit a significantly larger atomic volume than would be expected to be consistent with the general trend observed within the lanthanide series [1]. They also do not follow the general trend of phase transitions under pressure or with increasing atomic number observed in the trivalent lanthanides: *hcp*-(Sm-type)-*dhcp*-*fcc* [2].

Under pressure, the valence of Eu undergoes a continuous transition to a mixed-valence state, and L_{III} x-ray absorption studies indicate that the valence increases to 2.64 at 18 GPa, and is then pressure independent up to 33 GPa [3]. Very recently, Eu has been found to be superconducting at a pressure of approximately 80 GPa, with T_c = 1.8 K [4].

Initial high-pressure x-ray diffraction studies by Takemura and Syassen found that Eu exhibits the same body-centred cubic (*bcc*) structure as the divalent alkaline metals at ambient pressure, which transforms to a hexagonal close-packed (*hcp*) structure at 12.5 GPa and then to a new phase (Eu-III) at 18 GPa [1]. Eu-III was initially and tentatively assigned a hexagonal structure closely related to a superstructure of *hcp*.

Krüger *et al.* subsequently performed energy-dispersive x-ray diffraction up to 40 GPa [5]. At pressures exceeding 32 GPa, they found the diffraction pattern to become more complex, with the appearance of new reflections in addition to those observed in the 18–32 GPa region. It was noted that the additional reflections were weak in comparison to the *hcp* peaks, and it was suggested that they could be attributed to superlattice distortions of the *hcp* lattice, or to phase mixing.

Despite this interesting behaviour, very little further attention has been paid to the high-pressure behaviour of Eu until this year, when, prompted by the observation of superconductivity, Bi *et al.* reported results from an x-ray diffraction study up to 92 GPa [6]. They attributed the complex diffraction patterns observed above 18 GPa to arise from a sluggish transition to a mixture of *hcp* and

a monoclinic phase with space group *C2/c*. Bi *et al.* did not observe a transition at 33 GPa, but at pressures above 41 GPa, changes in the diffraction pattern were attributed to a mixture of the *C2/c* phase and an orthorhombic phase with the space group *Pnma*, followed by a transition to a pure *Pnma* phase at pressures exceeding 66 GPa. These diffraction results were supported by *ab initio* structure prediction calculations.

In this paper, we present angle-dispersive x-ray diffraction data to illustrate that the Eu-III phase does not consist of pure Eu, but in fact consists of *hcp*-Eu plus a rhombohedral phase, the atomic volume of which suggests it is an impurity.

2. Experimental

Angle-dispersive x-ray diffraction was performed at the SRS and ESRF synchrotron sources using monochromatic x-rays of wavelengths 0.44397 Å and 0.4161 Å, respectively. The x-ray beams were collimated to diameters of 50 μm and 15 μm, and the data were collected using MAR345 and MAR555 detectors, respectively.

High-purity Eu samples, supplied by U. Schwarz at the Max-Planck-Institut für Chemische Physik fester Stoffe in Dresden, were loaded into diamond-anvil pressure cells in a dry oxygen-free environment (<1 ppm O_2 and <1 ppm H_2O) using rhenium and tungsten gaskets. A small piece of ruby was included for pressure calibration. Samples were loaded using helium, mineral oil and no pressure-transmitting media (PTM). The diffraction patterns were integrated using Fit2D and analysed using Rietveld and Le Bail methods with the JANA2006 software [7-9].

3. Discussion

In our initial samples, including those loaded using a PTM (helium, mineral oil) and those loaded without a PTM, we observed the appearance of weak non-*hcp* reflections at 18 GPa, in agreement with all previous studies [1,5,6]. In these samples we found that as the pressure is increased further, the intensity ratio between the strong *hcp* peaks and the weak extra peaks remains constant all the way to a phase transition at 33 GPa. This behaviour was also noted by Takemura and Syassen [1]. However, we found that the relative intensity of the *hcp* and extra peaks varies between different samples. Additionally, we left one sample of Eu in mineral oil at 26.1 GPa for one month in order to investigate changes over time. The intensity of the non-*hcp* reflections grew significantly, and many further peaks could be identified. In addition, we found that the Debye-Scherrer rings on the diffraction image corresponding to the non-*hcp* reflections had become spotty, while those from the *hcp* phase remained smooth. This is illustrated in figure 1. All of this behaviour strongly indicated that there were two phases present, and we therefore attempted to index the non-*hcp* peaks as a separate phase.

The extra phase was indexed as having a rhombohedral unit cell with a = 9.293(4) Å, and c = 5.381(4) Å at 26.1 GPa. The lattice parameters of the *hcp* phase at the same pressure are a = 3.159(1) Å and c = 4.869(1) Å. Analysis of the systematic absences of the rhombohedral phase showed the spacegroup to be $R\bar{3}c$ or *R3c*, while density considerations restricted the number of Eu atoms per hexagonal unit cell to 18. Trial refinements showed an excellent fit could be obtained with atoms occupying the 18e (x,0,¼) Wyckoff sites of $R\bar{3}c$, with x = 0.800(4). An identical structure was obtained in spacegroup *R3c*. A two-phase *hcp*/ $R\bar{3}c$ Rietveld refinement at 26.1 GPa is shown in figure 2.

The volume per Eu atom of the *hcp* phase at 26.1 GPa is 21.05(1) Å^3, while the $R\bar{3}c$ phase at the same pressure is *less* dense, with a volume/atom of 22.36(1) Å^3. The decrease in density of 5.86(6) % suggests that the $R\bar{3}c$ phase is not pure Eu, but rather results from a pressure-induced reaction, and due to the small difference in the vol/atom, is perhaps a hydride. The quality of the Rietveld fit shown in figure 2 is excellent, suggesting that whatever the contaminant atoms are, they are weakly-scattering in comparison with europium atoms.

In order to confirm that the $R\bar{3}c$ phase was not pure Eu, we loaded samples with no pressure-transmitting medium and no ruby spheres in a very-high quality glovebox (<0.1 ppm O_2 and <0.1 ppm

H_2O) in order to obtain contaminant-free samples. In such samples, we observed no additional peaks appearing at 18 GPa, but only a single-phase *hcp* pattern from 12.5 – 33 GPa (see figure 3). However, heating such a sample for 2.5 hours at 100 °C resulted in the reappearance of the spotty Debye-Scherrer rings from the *R–3c* phase.

Peaks corresponding to the Eu-III impurity phase have been observed in all previous x-ray diffraction studies performed to pressures above 18 GPa [1,5,6], and we observed the same peaks in all of our samples loaded with a pressure medium, or pressure calibrant, or loaded in a non-optimum glovebox (>1 ppm O_2 and >1 ppm H_2O). Indeed, diffraction patterns shown in Ref [5] from the *hcp* phase at 14 GPa show evidence of a contaminant phase at this lower pressure. This illustrates the extreme reactivity of Eu, and the difficulty in loading clean, contaminant-free samples. Our experience suggests that it is more difficult to load contaminant-free Eu samples than it is to load contaminant-free Rb and Cs. The present study also suggests that future studies investigating the pressure-induced superconductivity or valence change of Eu should be combined with x-ray diffraction studies of the same samples to ensure that they are free from contaminant phases.

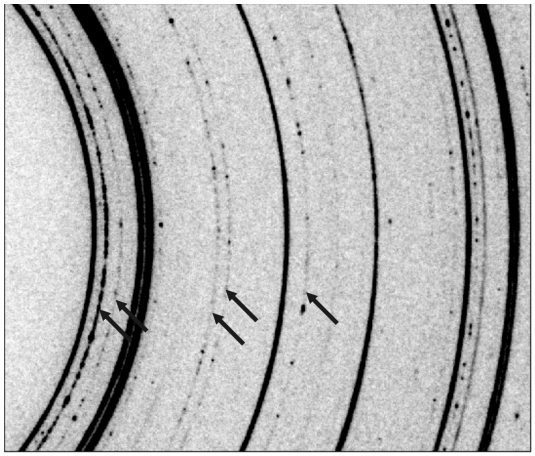

Figure 1. A 2D diffraction image from Eu at 26.1 GPa. The Debye-Scherrer (D-S) rings corresponding to the non-*hcp* reflections are spotty, whereas the *hcp* D-S rings are smooth. The arrows mark the five additional reflections observed by Takemura and Syassen [1].

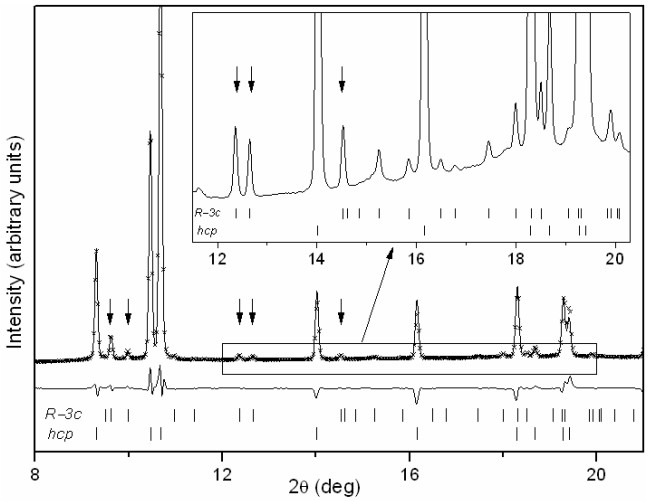

Figure 2. A two-phase *hcp*/ $R\bar{3}c$ Rietveld refinement of Eu-III at 26.1 GPa. The experimental data are shown by the crosses and the fit by the solid line. The residuals are shown under the fit and the tick marks show the calculated peak positions. The arrows indicate the Eu-III reflections observed by Takemura and Syassen [1]. The inset shows an enlarged view of the high-angle part of the profile.

Using a contaminant-free sample is also vital for understanding the structural behaviour of europium above 33 GPa, in order to determine which diffraction peaks result from pure-Eu alone. Increasing the pressure of our contaminant-free sample to 33 GPa, we observed the appearance of many additional weak peaks in agreement with Krüger *et al.* [5]. Our data also clearly show splittings of the *hcp* peaks which have not been resolved in previous studies [1,5]. These splittings suggest that the new phase has a distorted-*hcp* structure, and we initially considered the orthorhombic *Pnma* structure proposed by Bi *et al.* for pressures exceeding 41 GPa. A refinement of this structure using the Le Bail method to a profile collected from Eu at 34 GPa is shown in figure 4. The best-fitting lattice parameters are a = 5.291(1) Å, b = 4.713(1) Å, and c = 3.085(1) Å. Although this structure is an orthorhombic distortion of *hcp*, and results in a splitting of the *hcp* diffraction peaks, it cannot account for the observed splittings, and the overall fit is very poor, as illustrated by the inset. There are also a

large number of extra peaks not accounted for by this structure. More complex structures must therefore be considered to obtain the correct solution.

In conclusion, we have made high-resolution powder diffraction studies of europium to 37 GPa. These reveal that the long-reported phase transition at 18 GPa to the Eu-III phase is, in fact, a pressure-induced reaction, resulting in the sample becoming a mixture of *hcp*-Eu and a rhombohedral contaminant, perhaps a hydride. Very careful sample preparation and pressure cell loading is required to obtain samples without the contaminant phase. The reasons for the reaction to occur at 18 GPa are unclear, but may be related to the valence of Eu become close to 2.666 at this pressure, perhaps aiding the creation of a stochiometric compound.

Acknowledgements
We thank the European Synchrotron Radiation Facility (ESRF) and Daresbury Laboratory (SRS) for provision of synchrotron time and support. We thank M. Hanfland of ID09a (ESRF) and A. Lennie of 9.5HPT (SRS) for their help with the experiments. This work was supported by a research grant and a fellowship (I.L.) from the UK Engineering and Physical Sciences Research Council.

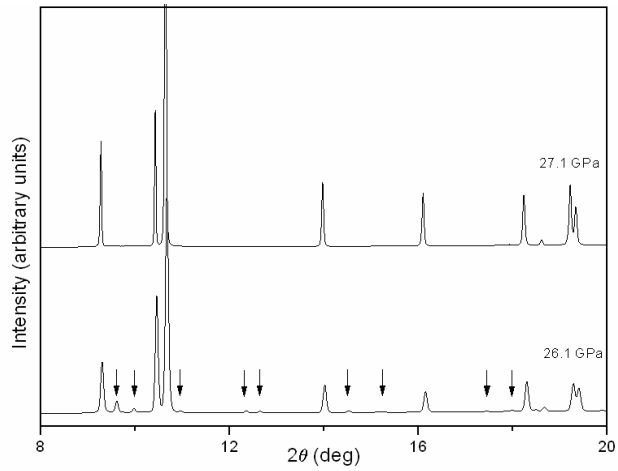

Figure 3. Integrated diffraction patterns from a contaminant-free sample of Eu at 27.1 GPa (upper) and a contaminated sample of Eu at 26.1 GPa (lower). Arrows in the lower profile mark the positions of the most intense $R\bar{3}c$ peaks.

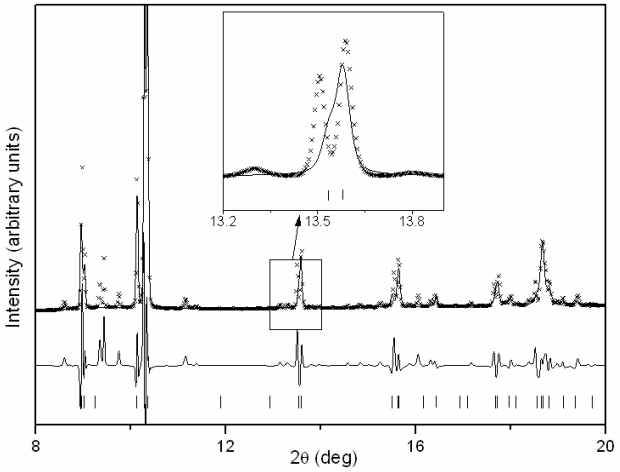

Figure 4. Le Bail refinement of a diffraction profile from a contaminant-free sample of Eu at 34 GPa, using the *Pnma* structure proposed by Bi *et al.* [5] for Eu above 41 GPa. The residuals are shown under the fit and the tick marks show the calculated peak positions. The inset shows an enlarged view of the fit to the split (102) peak from the *hcp* phase.

References

[1] Takemura K and Syassen K 1985 *J. Phys. F.* **15** 543
[2] Jayaraman A and Sherwood R C 1964 *Phys. Rev.* **134** A691-A692
[3] Rohler J 1986 *Physica* **144B** 27-31
[4] Debessai M, Matsuoka T, Hamlin J J and Schilling J S 2009 *Phys. Rev. Lett.* **102** 197002
[5] Krüger T, Merkau B, Grosshans W A and Holzapfel W B 1990 *High Pressure Research* **2** 193
[6] Bi W, Meng Y, Corneluis A L, Tipton W W, Hennig R G, Zhang Y, Chen C, Schilling J S 2011 *Phys. Rev. B.* **83** 104106
[7] Petrícek V, Dusek M and Palatinus L 2006 *The crystallographic computing system JANA2006*. Institute of Physics, Prague, Czech Republic
[8] Hammersley A P 1997 *ESRF Internal Report* **ESRF97HA02T**
[9] Hammersley A P, Svensson S O, Hanfland M, Fitch A N and Häusermann D 1996 *High Pressure Research* **14** 235-248

Europium-IV: An Incommensurately Modulated Crystal Structure in the Lanthanides

R. J. Husband,[1] I. Loa,[1] G. W. Stinton,[1] S. R. Evans,[2,*] G. J. Ackland,[1] and M. I. McMahon[1]
[1]SUPA, School of Physics and Astronomy and Centre for Science at Extreme Conditions, The University of Edinburgh, Mayfield Road, Edinburgh, EH9 3JZ, United Kingdom
[2]European Synchrotron Radiation Facility, 38043 Grenoble, France
(Received 18 May 2012; published 27 August 2012)

High-resolution x-ray powder-diffraction experiments were performed on europium metal at high pressure up to 50 GPa. At variance with previous reports, the hcp phase of Eu was observed to be stable not only to 18 GPa, but to 31.5 GPa. At 31.5(5) GPa, europium transforms to a phase (Eu-IV) with an incommensurately modulated monoclinic crystal structure with superspace group $C2/c(q_1 0 q_3)00$. This new phase was observed to be stable to ~37.0 GPa, where another phase transition was observed. Eu-IV is the first phase in the lanthanide elements with an incommensurate crystal structure.

DOI: 10.1103/PhysRevLett.109.095503 PACS numbers: 61.50.Ks, 62.50.−p, 64.70.Rh

Because of its half-filled $4f^7$ electron shell, europium is a divalent metal at ordinary conditions and, therefore, unlike the majority of the lanthanide elements, which are trivalent. As a result, Eu has a significantly larger atomic volume at ambient pressure, and a larger compressibility, than the neighboring lanthanides [1,2], and the high-pressure phase transitions of Eu are also different from those observed in the trivalent lanthanides [1–3].

In the x-ray diffraction study by Takemura and Syassen [2], Eu was observed to transform from its ambient-pressure body-centered cubic (bcc) phase to hexagonal close-packed (hcp) near 12.5 GPa, a transition that also occurs in divalent barium [4]. At pressures exceeding 18 GPa, the same authors observed the appearance of several diffraction lines in addition to those from the hcp phase. This was attributed to a transition to a new phase, Eu-III, with a structure thought to be closely related to hcp, possibly based on a large supercell. The additional weak reflections were also observed in a subsequent study by Krüger *et al.* [5], who reported further changes in the diffraction patterns of Eu above 32 GPa, but little effort was made over the following two decades to determine the crystal structures of Eu at high pressure.

Interest in the high-pressure behavior of Eu has been rekindled only very recently by the discovery of superconductivity in Eu above 80 GPa, with a critical temperature of $T_c \approx 1.8$ K [6]. In an x-ray diffraction study to 92 GPa, supported by *ab initio* structure prediction calculations, Bi *et al.* [7] confirmed the appearance of additional reflections above 18 GPa and concluded that two regions of phase mixture exist from 18 to 66 GPa: A mixture of hcp and a monoclinic phase from 18 to ~35 GPa and a mixture of the same monoclinic phase and an orthorhombic phase from ~35 to 66 GPa. The phase with the orthorhombic crystal structure was reported to be stable up to at least 92 GPa.

However, we have recently shown that the changes at ~18 GPa are in fact due to the appearance of diffraction peaks from a rhombohedral contaminant phase, and not due to a transition in Eu itself [8]. This raises concerns about the above structure assignments, and leaves us in a situation, where—50 years after the first high-pressure studies on Eu—we are lacking a basic understanding of the crystal structures of this element at pressures as low as 35 GPa. In view of this, we have made an effort to obtain contaminant-free samples of Eu at high pressure and to perform powder x-ray diffraction experiments with very high angular resolution up to a pressure of 50 GPa. We confirm that there is no phase transition in Eu at 18 GPa, and that Eu remains in the hcp phase up to ~31.5 GPa, at which point it transforms to a phase (Eu-IV) with a complex, incommensurately modulated monoclinic crystal structure. This structure is unique among all of the elemental modulated high-pressure structures in that it has a two-dimensional modulation, and it is the first incommensurate structure to be observed in the lanthanide elements.

High-purity Eu samples, supplied by U. Schwarz at the Max-Planck-Institut für Chemische Physik fester Stoffe in Dresden, were loaded into diamond-anvil pressure cells equipped with rhenium gaskets in a dry argon atmosphere (< 0.1 ppm O_2 and < 0.1 ppm H_2O). Due to the history of contamination issues, and because we had observed Eu to discolor even in the argon atmosphere of well-maintained glove boxes, we loaded Eu samples without a pressure-transmitting medium and without a pressure marker, in order to minimize the chances of contamination. The pressure was determined from the position of one or two sample Bragg reflections, using a calibration obtained from high-pressure diffraction experiments on two samples that were loaded with helium as a pressure-transmitting medium and where the pressure was determined with the standard ruby fluorescence method [9].

Angle-dispersive x-ray powder diffraction data were collected on station ID09a at the European Synchrotron Radiation Facility (ESRF), Grenoble, using a beam of monochromatic x rays of wavelength 0.4161 Å collimated

to a diameter of 15 μm. The data were collected using a mar555 area detector placed either 300 mm, or, in order to improve the angular resolution of the very complex diffraction patterns, 510 mm from the sample. Additional experiments were performed on beam line I15 of the Diamond Light Source, UK, using an x-ray wavelength of 0.338 Å and a mar345 image plate detector. The diffraction patterns were integrated using Fit2D [10,11] and analyzed using the Rietveld method with the JANA2006 software [12]. Once the Eu-IV structure was solved, we were also able to fit the numerous diffraction patterns collected from over 10 different samples both at the ESRF and at the former Synchrotron Radiation Source (SRS), Daresbury—including those where helium was used as a pressure transmitting medium (but all of these samples showed additional contaminant peaks [8]).

We observed the bcc–hcp transition in Eu at 12.5 GPa on pressure increase, in excellent agreement with previous studies [2,5,7]. On further pressure increase, no transition was observed at 18 GPa. Rather, Eu remained in the hcp phase up to a pressure of 31.5 GPa, above which significant changes in the diffraction profiles were observed. This is illustrated in Fig. 1(a), which shows the diffraction patterns of Eu at 30.6 GPa in the hcp phase and at 33.9 GPa after the transition. Note that, unlike in previous studies, the 30.6-GPa pattern comprises only peaks from the hcp phase, and no other. The transition to the new phase, Eu-IV, has been observed in all of our samples that were compressed to above 31.5 GPa.

Two distinct changes were observed in the diffraction patterns at the transition from hcp to Eu-IV. Firstly, our high-resolution data enabled us to observe the splitting of many of the hcp reflections into doublets or triplets, which were not resolved in previous studies. In particular, the intense hcp (101) reflection splits into a triplet, as shown in Fig. 1(d). Secondly, we observed the appearance of more than 30 additional weak reflections, as illustrated in Fig. 1(b).

The splitting of the hcp reflections suggests a transition to a distorted-hcp structure. We first considered the crystal structure with space group *Pnma* (*oP*4 in the Pearson notation) proposed by Bi *et al.* for pressures above 35 GPa [7], as this corresponds to an orthorhombic distortion of the hcp structure. However, we found the overall fit to the split-hcp peaks to be poor. Crucially, the *oP*4 structure does not account for the splitting of the hcp (101) reflection into a triplet. It also cannot account for the large number of weak reflections that appear at 31.5 GPa.

However, an excellent description of the split-hcp reflections was obtained with a monoclinic unit cell. Analysis of the systematic absences showed that all the split-hcp reflections could be indexed based on a structure with space group $C2/c$ and 4 atoms per unit cell (denoted *mC*4 in the Pearson notation) with the atoms in the 4*e* positions at $(0, y, \frac{1}{4})$. At 33.9 GPa, a Rietveld refinement gives lattice parameters of $a = 3.0838(5)$ Å, $b = 5.3002(7)$ Å, $c = 4.7239(4)$ Å, and

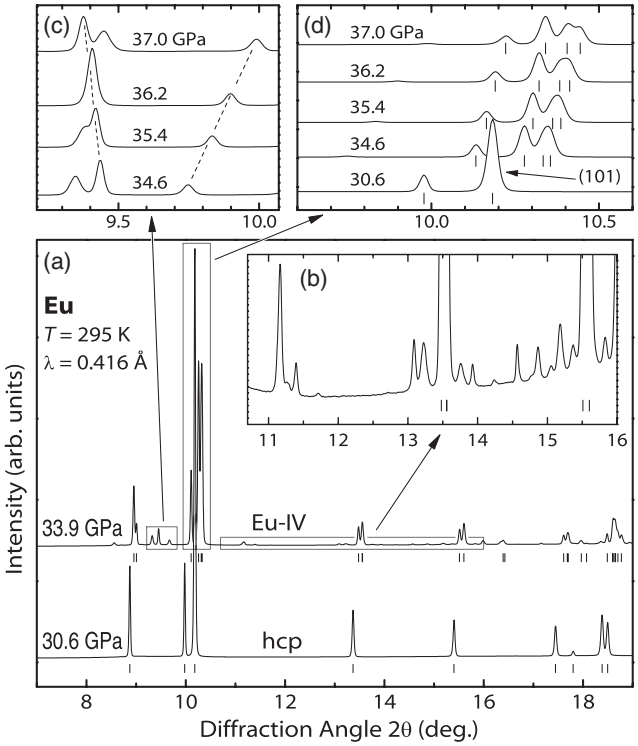

FIG. 1. X-ray powder diffraction patterns of Eu at the transition from hcp to Eu-IV. (a) Diffraction profiles of Eu in the hcp phase at 30.6 GPa and at 33.9 GPa after the transition to Eu-IV. Tick marks indicate the calculated peak positions for the hcp structure (30.6 GPa) and the *mC*4 structure (33.9 GPa). (b) A large number of weak reflections appears at the transition, which the unmodulated *mC*4 structure does not account for. (c) Movement of one of the weak reflections to lower angles (larger *d*-spacings) with increasing pressure. (d) Splitting of the hcp (101) reflection into a triplet, which originates from the monoclinic distortion, as shown by the *mC*4 tick marks.

$\beta = 90.39(1)°$, and the atomic coordinate $y = 0.341(2)$. This represents a small distortion of the hcp structure in the orthohexagonal description, where $b/a = \sqrt{3}$, $\beta = 90°$, and $y = 1/3$.

In Fig. 1, the positions of the *mC*4 reflections are shown by tick marks for the patterns recorded at $P > 31.5$ GPa. It is clear from Fig. 1(d) that the *mC*4 structure correctly accounts for the triplet splitting of the hcp (101) reflection highlighted above. However, it must be stressed that although this structure can account for all the split-hcp reflections, it does not explain any of the additional weak reflections [Fig. 1(b)].

Our attempts to index these weak peaks as a separate phase were unsuccessful. We therefore considered the possibility of indexing them using a superlattice of the *mC*4 structure. We noticed, however, that several of the weak additional reflections move to *lower* angles (longer *d*-spacings) with increasing pressure, whereas all of the split-hcp peaks move to higher angles (smaller *d*-spacings). One such peak is

illustrated in Fig. 1(c). This, combined with the absence of low-angle reflections that would be expected for a larger unit cell, suggested that the many weak additional peaks did not arise from a superstructure of the $mC4$ structure.

We then considered the possibility of an incommensurate structure, with the weak peaks being satellite reflections. The program SUPERCELL [13] was used to index the weak peaks, and we found them to be satellite reflections corresponding to a 2-dimensional modulation vector $\mathbf{q} = (q_1, 0, q_3)$, with $q_1 \approx 0.8$ and $q_3 \approx 0.6$. The resulting superspace group is $C2/c(q_1 0 q_3)00$ (i-$mC4$ in the Pearson notation, where 'i' indicates that the structure is incommensurate).

All of the Bragg peaks observed in the diffraction patterns from Eu above 31.5 GPa can be indexed using four Miller indices, $(hklm)$, according to $\mathbf{H} = h\mathbf{a}^* + k\mathbf{b}^* + l\mathbf{c}^* + m\mathbf{q}$, where $\mathbf{a}^*$, $\mathbf{b}^*$, $\mathbf{c}^*$ define the reciprocal lattice of the $mC4$ structure and $\mathbf{q}$ is the modulation vector. Only first-order ($m = \pm 1$) satellite reflections have been observed. The displacement of an atom in the modulated structure from its average position is given by the modulation function $\mathbf{u}(\bar{x}_4)$, where $\bar{x}_4 = \mathbf{q} \cdot \mathbf{r}_0$ is the fourth superspace component and $\mathbf{r}_0$ is the position of the atom in the average (unmodulated) crystal structure [14]. Taking into account the superspace group symmetry [12], and retaining only the first-order Fourier components, the modulation function for Eu-IV is then given by $\mathbf{u}(\bar{x}_4) = B_{1a}\sin(2\pi\bar{x}_4)\mathbf{a} + A_{1b}\cos(2\pi\bar{x}_4)\mathbf{b} + B_{1c}\sin(2\pi\bar{x}_4)\mathbf{c}$.

Figure 2 illustrates that a Rietveld refinement using the i-$mC4$ structure gives an excellent fit to the diffraction pattern from Eu at 33.9 GPa, with residuals of $R_p = 2.5\%$ and $R_{wp} = 4.2\%$. The satellite reflections account for all of the large number of weak peaks that appear at 31.5 GPa, as illustrated in panel (c), including those that move to lower angles with increasing pressure, such as the $(002\bar{1})$ reflection shown in panel (b). The refined structure at 33.9 GPa is given by $a = 3.0835(1)$ Å, $b = 5.2994(2)$ Å, $c = 4.7239(1)$ Å, $\beta = 90.400(2)$ Å, and $y = 0.342(1)$, with a modulation vector $\mathbf{q} = (0.8095(2), 0, 0.5908(2))$ and modulation amplitudes of $B_{1a} = -0.034(2)$, $A_{1b} = 0.016(1)$, and $B_{1c} = 0.040(1)$.

The i-$mC4$ structure of Eu-IV is the first incommensurately modulated crystal structure observed in the elements at high pressure in which the modulation vector is not in the direction of one of the lattice vectors. Figure 3 shows the unmodulated $mC4$ and the modulated i-$mC4$ structures in comparison. The very close relation to the hcp structure can clearly be seen in the views down the crystallographic c axis in Figs. 3(a) and 3(b).

The i-$mC4$ structure provides an excellent fit to all patterns observed for Eu between 31.5 and 37 GPa. The pressure dependences of the lattice parameters, modulation wave vector and modulation amplitudes are given in the Supplemental Material [15]. In essence, both q_1 and q_3 were observed to decrease with increasing pressure

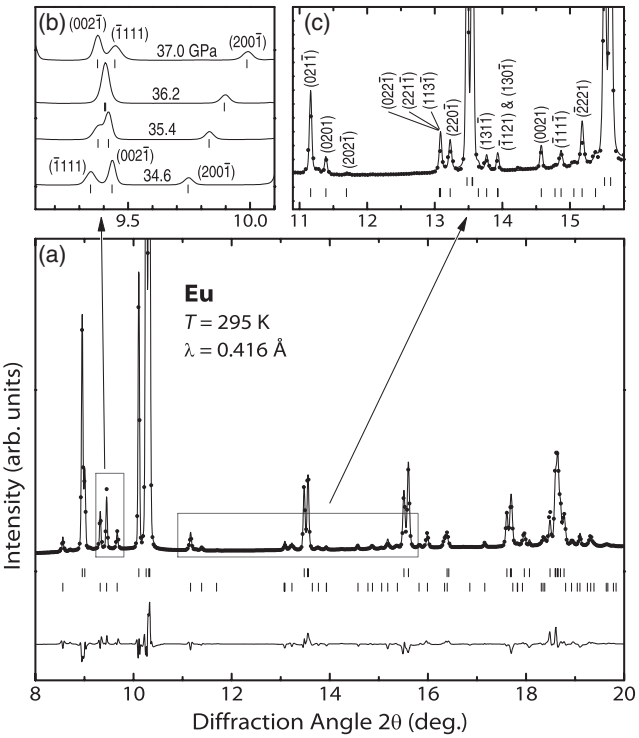

FIG. 2. (a) Rietveld refinement of the Eu i-$mC4$ structure at 33.9 GPa. The symbols show the experimental data and the solid line shows the fit. The upper and lower tick marks show the positions of the main and satellite peaks, respectively, and the residuals are given below the tick marks. Inset (c) illustrates the excellent fit to the large number of weak peaks observed above 31.5 GPa. (b) Movement of the $(002\bar{1})$ reflection to lower angles (larger d-spacing) with increasing pressure.

between 32.4 and 37.0 GPa, and q_1 passes smoothly through $q_1 = 0.8 = 4/5$, which corresponds to a commensurate modulation in this direction. The modulation amplitudes ($|B_{1a}|$, A_{1b}, and B_{1c}) were all found to increase with increasing pressure. In particular, B_{1c} increases from 0.034(3) to 0.055(8) over the 32.4–37.0 GPa pressure range. The increase in the modulation amplitudes entails an increase in the maximum atomic displacements, and as a consequence, the closest-contact distance in the i-$mC4$ structure decreases more rapidly with increasing pressure than it would in the hcp and the unmodulated $mC4$ structure [15]. Overall, this behavior is reminiscent of that of the incommensurately-modulated high-pressure phase phosphorus-IV [16] and different from that of incommensurately-modulated tellurium-III, where the closest-contact distances remain remarkably constant with increasing pressure [17].

We would like to note that Krüger *et al.* [5] reported the appearance of additional peaks in the diffraction patterns of Eu above 32 GPa, and it appears likely that these were evidence of the phase transition to the incommensurate phase. The extra reflections observed in that study are in the correct positions to be the most intense satellite

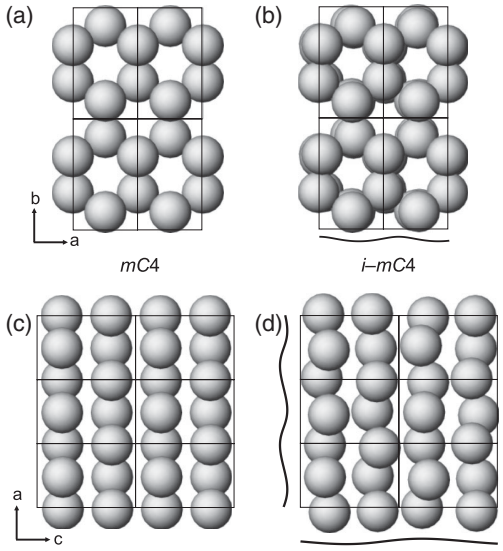

FIG. 3. Schematic views of the hypothetical $mC4$ and the experimentally observed i-$mC4$ crystal structures at 33.9 GPa. Four unit cells viewed along the c direction of (a) unmodulated $mC4$ and of (b) modulated i-$mC4$. Six unit cells viewed along the b direction of (c) unmodulated $mC4$ and of (d) modulated i-$mC4$. Projections of the modulation function $\mathbf{u}(\bar{x}_4)$ onto the ab and ac planes, evaluated along the crystallographic axes, are shown besides the crystal structures in (b) and (d), respectively. The modulation function along the b axis is 0 and therefore not shown.

reflections of Eu-IV, but the limited resolution in this energy-dispersive x-ray diffraction study made it impossible to resolve the splitting of the hcp reflections and other details. Bundy and Dunn observed a step in the electrical resistance of Eu near 28 GPa at room temperature [18], and this may also be related to the transition from hcp to the i-$mC4$ phase at 31.5 GPa.

Upon compression to above 37.0 GPa, we observed further changes in the diffraction profiles of Eu that indicate a transition to another new phase. The complexity of the diffraction patterns suggests that this phase may also have a modulated crystal structure, but this remains to be determined in detail.

It is highly desirable to identify the mechanism that leads to the formation of the incommensurate modulation in Eu-IV, presumably via strong electron-phonon coupling or extreme Kohn anomalies, but europium is well known to be among the elements that are the most difficult to treat in electronic structure calculations in the framework of density functional theory (DFT). The challenge is to describe the properties of the half-filled shell of relatively localized $4f$ electrons accurately. Treating the $4f$ states as regular valence states in the local density approximation leads to a significant overbinding: The calculated equilibrium volume is too small by 15% and 33% in the spin-polarized and the nonpolarized case, respectively, which is far more than the few percent typical in DFT calculations [19].

In a recent computational search for the crystal structures of Eu metal at high pressure [7], the $4f$ electrons were treated as core states, and the projector-augmented wave (PAW) method [20] was used together with the generalized gradient approximation (GGA); this reduced the underestimation of the equilibrium volume to slightly less than 10% for both the spin-polarized and the nonpolarized case. We used the same approach (as implemented in the ABINIT code [21]) in an initial attempt to identify the origin of both the monoclinic distortion and the incommensurate modulation, but found the variation of the calculated axial ratio in the hcp phase, c/a, to be inconsistent with the experimental results (see the Supplemental Material [15] for details). For example, these calculations yielded $c/a = 1.34$ at 20 GPa, which is much smaller than the experimental value of 1.56. Treating the $4f$ states as core states is therefore not an adequate approximation for modeling the properties of Eu metal at high pressure.

To test an alternative approach, we have also performed spin-polarized calculations in the generalized gradient approximation with additional treatment of on-site Coulomb repulsion for the $4f$ states, using the DFT + U scheme [22] as implemented in the "full-potential augmented plane-wave plus local orbital" code, WIEN2K [15,23]. This yielded a calculated equilibrium volume in good agreement with the experiment, i.e., 3% larger than the experimental value, which is typical for GGA-based DFT calculations. In addition, the calculated decrease in c/a with increasing pressure leveled off at 1.55, which is also in good agreement with the experiment. However, the calculation yields the rapid reduction in c/a only at a higher pressure (by $\sim$13 GPa) than observed experimentally. Overall, a better description of Eu at high pressure is obtained with the DFT + U approach than by treating the $4f$ states as core states, but there is clearly a need for further improvement.

In future computational work, the possible pressure-dependence of the effective on-site Coulomb repulsion [24] should be considered, but it may prove necessary to go beyond the DFT + U scheme, with dynamical mean field theory (DMFT) being a possible alternative [25]. The accurate modeling of the electronic structure of Eu at high pressure remains a great challenge, and the present detailed experimental results on the structural evolution of Eu metal under pressure provide stringent tests for future work in this direction.

In summary, we have determined that Eu-IV, which is stable from 31.5 to 37 GPa, has an incommensurately modulated crystal structure, the first of this type to be observed in a lanthanide element. Eu-IV is also the first high-pressure incommensurate elemental structure in which the modulation vector is not in the direction of one of the crystallographic axes. Eu is well known to be challenging for DFT calculations. These experimental observations warrant new, dedicated electronic structure calculations aimed

at uncovering the mechanism that leads to Eu's unusual high-pressure behavior.

This work was supported by grants and a fellowship (I. L.) from the UK Engineering and Physical Sciences Research Council, and facilities were made available by the European Synchrotron Radiation Facility, Diamond Light Source, and SRS Daresbury. We thank L. F. Lundegaard and O. Degtyareva for their help with the experiments in the early stage of this study, U. Schwarz for providing Eu samples, and M. Hanfland, A. Lennie, and N. Casati for their support on the beam lines.

*Present address: Departement für Chemie und Biochemie, Universität Bern, Switzerland and Swiss Light Source, PSI, Villigen, Switzerland.

[1] B. Johansson and A. Rosengren, Phys. Rev. B **11**, 2836 (1975).
[2] K. Takemura and K. Syassen, J. Phys. F **15**, 543 (1985).
[3] A. Jayaraman and R. Sherwood, Phys. Rev. **134**, A691 (1964).
[4] J. D. Barnett, R. B. Bennion, and H. T. Hall, Science **141**, 534 (1963).
[5] T. Krüger, B. Merkau, W. A. Grosshans, and W. B. Holzapfel, High Press. Res. **2**, 193 (1990).
[6] M. Debessai, T. Matsuoka, J. J. Hamlin, J. S. Schilling, and K. Shimizu, Phys. Rev. Lett. **102**, 197002 (2009).
[7] W. Bi, Y. Meng, R. S. Kumar, A. L. Cornelius, W. W. Tipton, R. G. Hennig, Y. Zhang, C. Chen, and J. S. Schilling, Phys. Rev. B **83**, 104106 (2011).
[8] R. J. Husband, I. Loa, G. W. Stinton, S. R. Evans, G. J. Ackland, and M. I. McMahon, J. Phys. Conf. Ser. **377**, 012030 (2012).
[9] H. K. Mao, J. Xu, and P. M. Bell, J. Geophys. Res. **91**, 4673 (1986).
[10] A. P. Hammersley, computer code FIT2D, 2005.
[11] A. P. Hammersley, S. O. Svensson, M. Hanfland, A. N. Fitch and D. Häusermann, High Press. Res. **14**, 235 (1996).
[12] V. Petrícek, M. Dusek and L. Palatinus, *The Crystallographic Computing System JANA2006* (Institute of Physics, Prague, 2006).
[13] J. Rodrìguez-Carvajal, Physica (Amsterdam) **192B**, 55 (1993).
[14] S. van Smaalen, *Incommensurate Crystallography* (Oxford University, New York, 2007).
[15] See Supplemental Material at http://link.aps.org/supplemental/10.1103/PhysRevLett.109.095503 for details.
[16] H. Fujihisa, Y. Akahama, H. Kawamura, Y. Ohishi, Y. Gotoh, H. Yamawaki, M. Sakashita, S. Takeya, and K. Honda, Phys. Rev. Lett. **98**, 175501 (2007)
[17] C. Hejny and M. I. McMahon, Phys. Rev. Lett. **91**, 215502 (2003).
[18] F. P. Bundy and K. J. Dunn, Phys. Rev. B **24**, 4136 (1981).
[19] B. Min, H. Jansen, T. Oguchi, and A. Freeman, J. Magn. Magn. Mater. **59**, 277 (1986).
[20] P. E. Blöchl, Phys. Rev. B **50**, 17953 (1994).
[21] X. Gonze *et al.*, Comput. Mater. Sci. **25**, 478 (2002), http://www.abinit.org.
[22] V. I. Anisimov, I. V. Solovyev, M. A. Korotin, M. T. Czyżyk, and G. A. Sawatzky, Phys. Rev. B **48**, 16929 (1993).
[23] P. Blaha, K. Schwarz, G. K. H. Madsen, D. Kvasnicka, and J. Luitz, *WIEN2K, An Augmented Plane Wave + Local Orbitals Program for Calculating Crystal Properties* (K. Schwarz, Technische Universität Wien, Vienna, Austria, 2001).
[24] M. Cococcioni and S. de Gironcoli, Phys. Rev. B **71**, 035105 (2005).
[25] A. Georges, G. Kotliar, W. Krauth, and M. J. Rozenberg, Rev. Mod. Phys. **68**, 13 (1996).

High Pressure Research, 2013
Vol. 33, No. 1, 158–164, http://dx.doi.org/10.1080/08957959.2013.775280

Taylor & Francis
Taylor & Francis Group

Phase transitions in europium at high pressures†

R.J. Husband*, I. Loa, G.W. Stinton, G.J. Ackland and M.I. McMahon

SUPA, School of Physics and Astronomy and Centre for Science at Extreme Conditions, The University of Edinburgh, Mayfield Road, Edinburgh EH9 3JZ, UK

(*Received 4 October 2012; final version received 7 February 2013*)

For several decades, x-ray diffraction studies on europium (Eu) metal at high pressure were complicated by the presence of a rhombo-hedral contaminant phase, *hR*6, which has been recognised as such only recently. Using x-ray powder diffraction, we have determined the *hR*6 contaminant to undergo a phase transition to a cubic phase, *cI*12, at 34.8(12) GPa. Consideration of the volume per Eu atom of the two contaminant phases at the same pressure suggests that they have different stoichiometries or chemical compositions. We also report a phase transition in pure Eu from the incommensurately-modulated Eu-IV phase to Eu-V between 38 and 42 GPa.

Keywords: europium; diamond-anvil cell; x-ray diffraction; structural transition; contaminant

Introduction

Unlike the majority of the lanthanide elements, europium (Eu) is divalent at ambient pressure due to its half-filled 4*f* shell. In addition, it has a significantly larger atomic volume, and compressibility, than would be expected to be in keeping with the general trend across the lanthanide series [1]. Eu also does not show the series of structural phase transition exhibited by the trivalent lanthanides with increasing pressure. Instead, Eu adopts the body-centred cubic (bcc) structure at ambient pressure, transforming to the hexagonal close-packed (hcp) structure at 12.5 GPa. This behaviour is very similar to that of divalent barium [2].

Previous x-ray diffraction studies reported Eu to undergo a phase transition at ∼18 GPa [1,3,4]. This was characterised by the appearance of a number of reflections in the diffraction pattern in addition to those from the hcp phase. Although this behaviour was initially reported in 1985, the crystal structures adopted by Eu above 18 GPa remained unknown until 2011 when Bi et al. [4] reported a series of phase transitions and structure assignments up to 92 GPa.

However, we recently reported that the behaviour initially attributed to a phase transition at 18 GPa is in fact due to pressure-induced changes in a contaminant phase, and not due to changes in Eu itself [5]. This contaminant was determined to have a rhombohedral structure with 18 Eu atoms per hexagonal unit cell (*hR*6 in Pearson notation, where the 6 refers only to the number of Eu atoms).

*Corresponding author. Email: R.J.Husband@ed.ac.uk
†This paper was presented at the Lth European High Pressure Research Group (EHPRG 50) Meeting at Thessaloniki (Greece), 16–21 September 2012.

When great care is taken to minimise the chances of contamination by quickly loading samples in a high-quality glove box without a pressure-transmitting medium (PTM) and without a pressure marker, we found that it is possible to obtain 'clean' Eu samples. In these samples, we did not observe the appearance of the additional reflections above 18 GPa, and instead Eu remained in the hcp phase up to 31.5 GPa. Working with clean samples removed the possibility of misidentifying diffraction peaks from the contaminant as coming from pure Eu, and therefore enabled us to identify a transition at 31.5 GPa to an incommensurately modulated monoclinic structure, Eu-IV [6]. This is the first structure of this type to be observed in the lanthanide series, and the first elemental incommensurately modulated crystal structure to be observed at high pressure in which the modulation vector is not along one of the crystallographic axes.

High pressure diffraction studies of Eu are complicated by the fact that it is only possible to determine whether the sample is contaminated by compressing it to above 18 GPa, where the rhombohedral phase appears. The intensity of the contamination peaks can vary across the sample, and relative to the Eu peak intensities, indicating that the contaminant is not evenly distributed. Understanding the behaviour of the contaminant is essential in order to be able to determine the structural behaviour of Eu at higher pressures. In this paper, we report that the *hR*6 contaminant undergoes a pressure-induced transition at 34.8(12) GPa to a new bcc contaminant phase, *cI*12. The diffraction profile from the *cI*12 phase is much simpler than that of the *hR*6 phase, and its most intense reflections can easily be identified over the whole pressure region in which the Eu-IV phase is observed. The identification of this cubic phase has enabled us to determine which diffraction peaks arise from Eu alone above 34.8(12) GPa, and thereby observe a phase transition in Eu between 38 and 42 GPa.

Experimental details

High-purity, distilled samples of Eu, supplied by U. Schwarz at the Max-Planck-Institut für Chemische Physik fester Stoffe in Dresden, were loaded into diamond-anvil cells in a dry argon environment (<1 ppm O_2, <1 ppm H_2O) using rhenium or tungsten gaskets. Gaskets were pre-indented to an initial thickness of 25–35 μm, and a sample chamber of diameter 100–150 μm was drilled using spark erosion.

A total of 10 contaminated samples were considered, 7 of which were loaded with a mineral oil pressure-transmitting medium (PTM), two of which were loaded with helium as the PTM and one which was loaded without any PTM. In the majority of the samples, a small ruby sphere was included as a pressure calibrant, and the pressure was determined using the standard ruby fluorescence method and the calibration of Mao et al. [7]. The sample that was loaded without any PTM did not contain a ruby sphere, and the pressure was, therefore, determined using the position of one or two sample Bragg reflections, using a calibration established from the two samples loaded in He.

Our non-contaminated samples were loaded quickly in a well-maintained glove box (<0.1 ppm O_2, <0.1 ppm H_2O) without a PTM and without a pressure calibrant, in order to minimise any sources of contamination. The pressures of these samples were also determined from the position of one or two sample Bragg reflections, using the calibration established from the two samples loaded in He.

Angle-dispersive x-ray diffraction data were collected at the European Synchrotron Radiation Facility (ESRF), the Synchrotron Radiation Source (SRS) and the Diamond Light Source (DLS). The size of the x-ray beam varied between 15 μm (ESRF) and 30 μm (SRS and Diamond). The 2D diffraction images were integrated using Fit2D [8,9] to produce standard 1D diffraction profiles, which were subsequently analysed using the Le Bail and Rietveld methods with the JANA2006 software [10].

Results and discussion

In order to investigate the pressure dependence of the *hR*6 contaminant phase, we increased the pressure on one of our contaminated samples of Eu in mineral oil. When the pressure was increased to 33.5 GPa, we observed the transition from hcp Eu to Eu-IV, as expected. The reflections from the *hR*6 phase were also still observed in the diffraction profiles from Eu-IV. However, on further pressure increase to 36 GPa, although the Eu-IV reflections were still present and unchanged, those from the *hR*6 phase had disappeared and a smaller number of new reflections were observed. The appearance of the new reflections was most noticeable at low diffraction angles, due to a high degree of overlap with Eu-IV reflections at higher angles. The transition in the contaminant is illustrated in Figure 1, which shows the low-angle sections of the diffraction profiles of Eu-IV plus *hR*6 at 33.6 GPa, and Eu-IV plus the new reflections at 36 GPa.

On pressure decrease below 31.5 GPa, we observed the reverse transition from Eu-IV to hcp Eu, as expected. However, we did not observe the reappearance of the *hR*6 reflections, and the new reflections were still present. The simplification of the diffraction pattern from Eu in transforming back to the hcp phase meant that a large number of additional reflections from the new contaminant phase could now be identified, and these were straightforwardly indexed on a cubic unit cell. All of the observed reflections satisfied the condition $h + k + l = 2n$, showing that the structure is body-centred, and further consideration of the systematic absences allowed the spacegroup to be identified uniquely as $I\bar{4}3d$. An excellent fit to diffraction profiles from the *hR*6 phase was obtained using only Eu atoms, and so the same approach was used for the cubic phase. The number of Eu

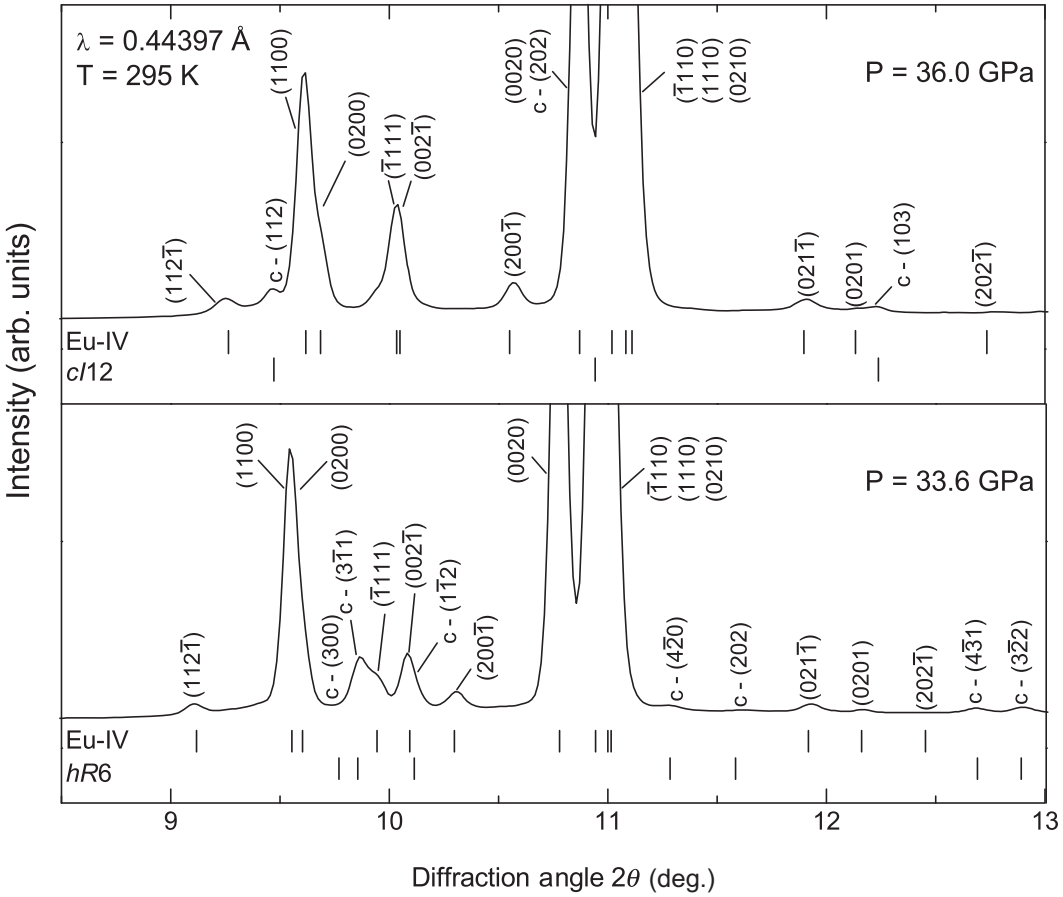

Figure 1. X-ray powder diffraction profiles of Eu-IV plus the *hR*6 contaminant at 33.6 GPa (lower profile), and Eu-IV plus the *cI*12 contaminant at 36.0 GPa (upper profile). The tick marks beneath the profiles show the calculated peak positions of the three phases. The corresponding Miller indices are given above the profiles, using (hklm) 4-dimensional notation for the incommensurate phases. 'c' indicates reflections from the contaminant phase.

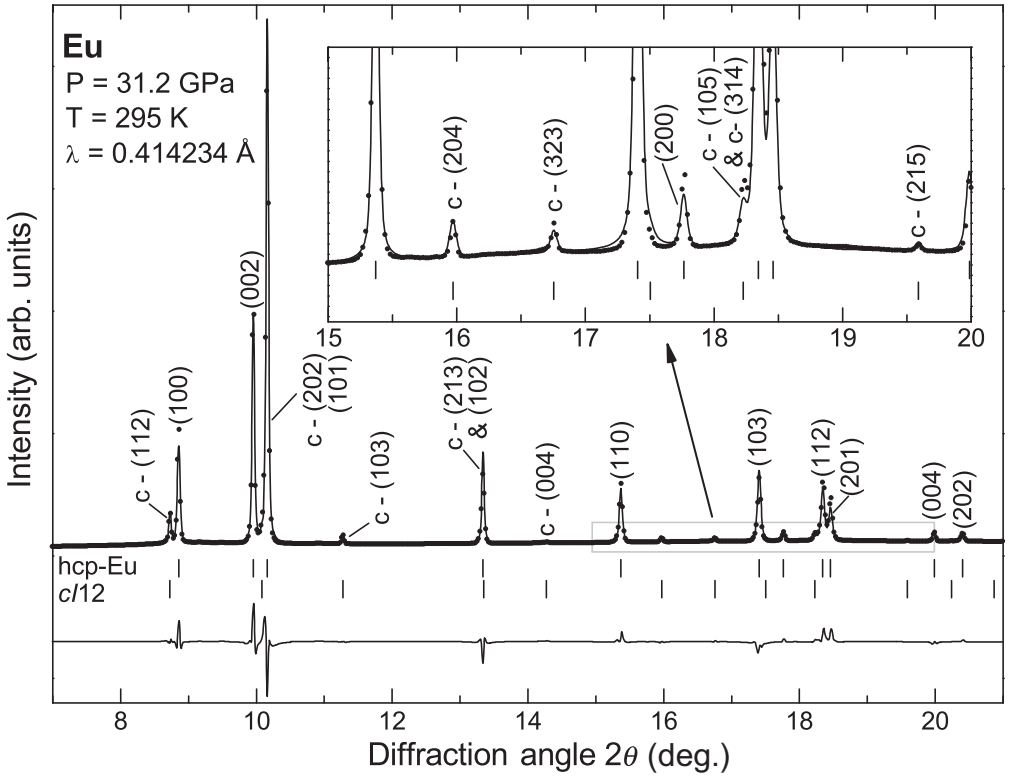

Figure 2. Two-phase Rietveld refinement of a diffraction profile from hcp Eu plus the *cI*12 contaminant at 31.2 GPa. The symbols show the experimental data and the solid line shows the fit. The tick marks beneath the profile show the calculated peak positions of the hcp (upper) and the *cI*12 (lower) phases. The residuals are shown under the tick marks. The inset illustrates the excellent fit to the weak *cI*12 reflections. The corresponding Miller indices are given above the profile, where 'c' indicates reflections from the contaminant phase.

atoms was restricted to 12, the lowest site multiplicity in this spacegroup, as higher multiplicities corresponded to a considerably larger density than that of hcp Eu. An excellent fit was obtained with the Eu atoms in the 12a Wyckoff positions (*cI*12, where 12 refers to the number of Eu atoms). Tick marks indicating the calculated peak positions of the *cI*12 reflections, along with the Eu-IV tick marks, are shown on the higher pressure profile in Figure 1.

A Rietveld refinement of the pattern from hcp Eu plus the *cI*12 contaminant at 31.2 GPa is shown in Figure 2. The refined lattice parameters of the hcp phase are $a = 3.0978(2)$ Å and $c = 4.7744(4)$ Å, corresponding to a volume per atom of $19.840(3)$ Å^3. The refined lattice parameter of the *cI*12 phase at the same pressure is $a = 6.667(2)$ Å, corresponding to a volume per Eu atom of $24.69(2)$ Å^3. If only the Eu atoms were present, this would imply that the cubic phase is 19.7% *less* dense than the hcp phase at the same pressure. This confirms that the *cI*12 phase does not consist of pure Eu, but is a second impurity phase formed from a pressure-induced transition of the *hR*6 phase.

The Rietveld refinement using Eu atoms alone is excellent, suggesting that the additional atoms must be very weakly scattering in comparison with Eu. The difference in the volume per Eu atom between hcp and *cI*12 is $4.85(2)$ Å^3 at 31.2 GPa, which suggests that the impurity atom(s) must be very small.

A plot of the volume per Eu atom against pressure for Eu and the *hR*6 and *cI*12 contaminant phases is shown in Figure 3. It is clear from the figure that the volume per Eu atom of *cI*12 is significantly larger than that of *hR*6: the *cI*12 phase is 19.7% less dense than hcp Eu at 31.2 GPa, whereas the *hR*6 phase is only 6.7% less dense at 30.7 GPa. This suggests that the stoichiometry or chemical composition of the two contaminant phases is not the same. However, neither the *hR*6 nor the *cI*12 phases correspond to phases that have previously been reported for Eu hydrides under pressure. The volume per Eu atom for EuH_2, taken from reference [11], is also plotted in Figure 3.

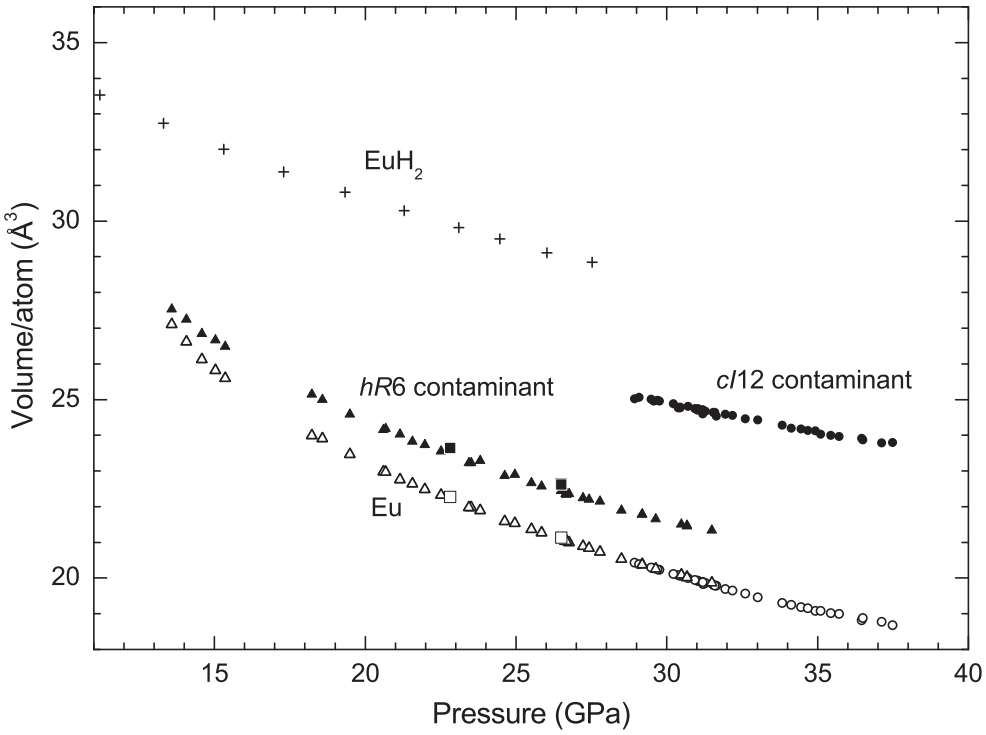

Figure 3. Volume per Eu atom against pressure for Eu and the *hR*6 and *cI*12 contaminant phases. The Eu volumes were obtained by Rietveld fits to the diffraction patterns, and the volumes for the contaminant phases were determined from the *d*-spacings of 4 to 11 reflections. The solid triangles show data for the *hR*6 phase measured on samples loaded with a pressure-transmitting medium, and the open triangles show data for the hcp phase at the same pressures, as obtained from mixed-phase profiles. The solid circles show data for the *cI*12 phase measured on samples loaded with a pressure-transmitting medium, and the open circles show data for the hcp phase at the same pressures, as obtained from mixed-phase profiles. The solid squares show data for the *hR*6 phase measured on the sample loaded without a PTM, and the open squares show data for the hcp phase at the same pressures, as obtained from mixed-phase profiles. The estimated uncertainties in the atomic volumes as obtained from the least-squares fits are smaller than the equivalent of the symbol size. The uncertainties in pressure are typically 0.5 GPa, as estimated from pressure readings taken before and after the data collections. The crosses show data for EuH_2, as taken from reference [11].

Extrapolating these data to 30 GPa gives a volume per H atom of 4.1 Å^3. Comparing this with the difference in the volume per Eu atom of 4.8 Å^3 between *cI*12 and hcp Eu at the same pressure, suggests that the density of the *cI*12 phase could be explained by it being EuH_x, with $x \approx 1.2$ at 30.5 GPa. A similar comparison gives a value of $x \approx 0.3$ for *hR*6 at the same pressure. Figure 3 also suggests that both contaminant phases are less compressible than Eu, which is consistent with results on Eu hydrides by Matsuoka et al. [11].

Although our analysis suggests that it is likely that there was a hydride present in our samples, it is unclear where the hydrogen came from in the loading process. We used distilled Eu metal, which we believe not to contain any significant amount of hydrogen. Both 'clean' and 'contaminated' samples were loaded from the same Eu bulk sample, and there is no evidence of any diffraction peaks from additional crystalline or amorphous phases in the as-loaded samples. However, the *hR*6 contaminant phase is always observed above 18 GPa in samples loaded in mineral oil, and is also observed in samples loaded without a PTM above the same pressure. However, such samples were not pressurised above 31.5 GPa, and so the transition to the *cI*12 phase was not observed in these samples. On pressure decrease, we find that the *hR*6 contaminant phase is stable below 18 GPa, and we have observed it down to pressures as low as 11 GPa, at which point the Eu has returned to the ambient-pressure bcc phase.

The identification of the *hR*6 and *cI*12 contaminant phases was essential in order for us to determine the Eu-IV structure and its pressure dependence. In particular, the transition pressure of 34.8(12) GPa between the *hR*6 and *cI*12 phases is very similar to that in Eu (31.5 GPa), and

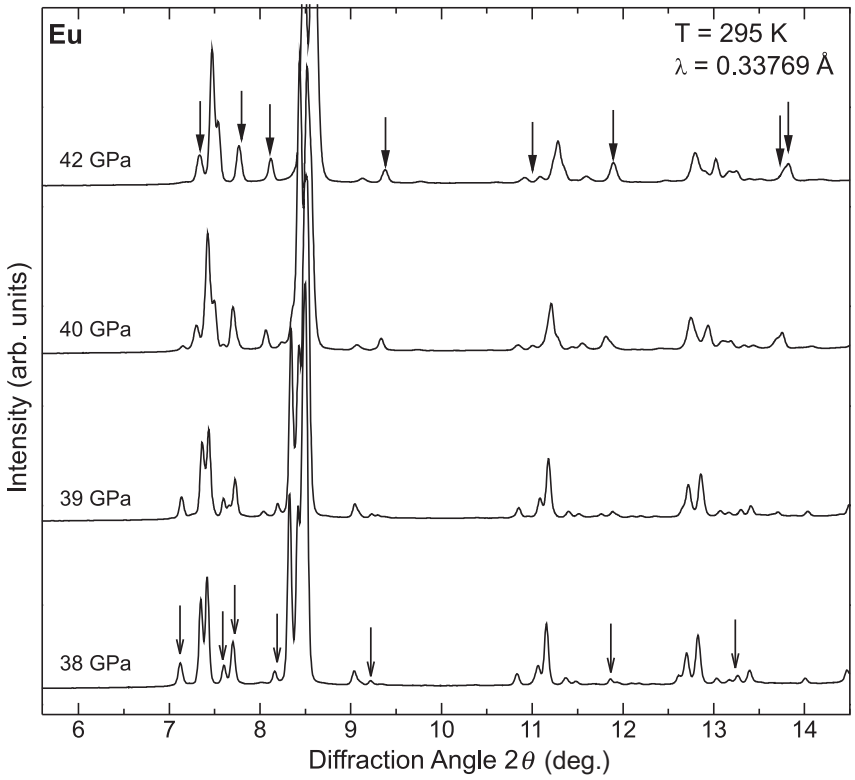

Figure 4. X-ray powder diffraction profiles of Eu at 38, 39, 40 and 42 GPa illustrating the transition from Eu-IV to Eu-V. The 38 GPa profile can be indexed as single-phase Eu-IV, the 39 and 40 GPa profiles are from a mixed-phase region, and the 42 GPa profile is single-phase Eu-V. The arrows above the 38 GPa profile indicate the most intense Eu-IV satellite reflections which disappear with increasing pressure, and the arrows above the 42 GPa profile indicate the new reflections that appear and which cannot be explained by the Eu-IV structure.

this greatly complicated our initial analysis. Although it is possible to load clean samples that do not show the *hR6* phase above 18 GPa, of the large number of samples loaded over the course of our studies, the majority were contaminated. In addition, diffraction profiles from a 'clean' sample at 37 GPa which did not initially contain diffraction peaks from the *hR*6 phase did contain very strong diffraction peaks from this phase after the sample was heated for 2.5 h at 100°C. This suggests that what may initially appear to be a pure Eu sample may in fact still contain impurities. Understanding the behaviour of such contaminant phases is vital for high pressure studies, in particular for work carried out at high temperatures.

Further increasing the pressure in non-contaminated Eu samples to above 38 GPa revealed that they could no longer be indexed on the incommensurate Eu-IV structure. As the pressure was increased to above 38 GPa, we observed the appearance of a number of new reflections that did not belong to Eu-IV, while, simultaneously, the intensity of incommensurate satellite reflections from Eu-IV decreased until they were no longer observed. This indicates a transition to a new phase, Eu-V.

The transition is illustrated in Figure 4, which shows diffraction profiles from Eu at 38, 39, 40 and 42 GPa. The profile at 38 GPa can be indexed as Eu-IV, whereas the profiles at 39 and 40 GPa correspond to a mixed-phase region. The transition to Eu-V is complete at 42 GPa. The most obvious features that signify the transition can be seen in the 7.5–8.25° region of the profiles, where the triplet of satellite peaks from Eu-IV, which is clearly visible at 38 GPa, can be seen to disappear and be replaced by a doublet at 42 GPa. The Eu-V phase was observed up to 45 GPa, the highest pressure reached in these studies.

The diffraction profile from Eu-V retains a strong similarity to that from Eu-IV and the change in the positions of the satellite reflections suggests the possibility of a transition to a second

modulated structure. However, several of the new reflections are very strong, and so it is not clear if these also correspond to new satellite reflections, or if they arise from a further distortion of the average structure. The analysis of this new structure is ongoing.

In conclusion, we have reported the *hR*6 contaminant to undergo a transition to a body-centred cubic phase, *cI*12, above 34.8(12) GPa. The volume per Eu atom of the *cI*12 contaminant is significantly larger than that of the *hR*6 contaminant at the same pressure, suggesting that the two phases have different stoichiometries or chemical compositions. Comparison of the volume per Eu atom with that reported recently for EuH_2 suggests that the *cI*12 phase might be a Eu hydride, EuH_x, with $x \approx 1.2$, and that *hR*6 may be a subhydride, with $x \approx 0.3$. We also reported a phase transition from incommensurate Eu-IV to Eu-V between 38 and 42 GPa, and the crystal structure of the latter phase remains to be determined.

Acknowledgements

This work was supported by grants and a fellowship (I. L.) from the UK Engineering and Physical Sciences Research Council, and facilities were made available by the ESRF, DLS, SRS and the Research Complex at Harwell. We thank N. Casati, A. Lennie and M. Hanfland for their support on the beam lines, U. Schwarz of the MPI für Chemische Physik fester Stoffe for providing the Eu samples and L.F. Lundegaard and O. Degtyareva for their help with the experiments in the early stages of this study.

References

[1] Takemura K, Syassen K. Pressure-volume relations and polymorphism of europium and ytterbium to 30 GPa. J Phys F. 1985;15:543–559.
[2] Barnett JD, Bennion RB, Hall HT. High pressure x-ray diffraction studies on barium. Science. 1963;141:534–535.
[3] Krüger T, Merkau B, Grosshans WA, Holzapfel WB. Kinetics and systematics of structural phase transitions in the regular lanthanide metals under pressure. High Press Res. 1990;2:193–236.
[4] Bi W, Meng Y, Kumar RS, Cornelius AL, Tipton WW, Hennig RG, Zhang Y, Chen C, Schilling JS. Pressure-induced structural transitions in europium to 92 GPa. Phys Rev B. 2011;83:104106.
[5] Husband RJ, Loa I, Stinton GW, Evans SR, Ackland GJ, McMahon MI. The structure of Eu-III. J Phys Conf Ser. 2012;377:012030.
[6] Husband RJ, Loa I, Stinton GW, Evans SR, Ackland GJ, McMahon MI, Europium-IV: an incommensurately modulated crystal structure in the lanthanides. Phys Rev Lett. 2012;109:095503.
[7] Mao HK, Xu J, Bell PM. Calibration of the ruby pressure gauge to 800 kbar under quasi-hydrostatic conditions. J Geophys Res. 1986;91:4673–4676.
[8] Hammersley AP. Computer code FIT2D, 2005.
[9] Hammersley AP, Svensson SO, Hanfland M, Fitch AN, Häusermann D. Two-dimensional detector software: from real detector to idealised image or two-theta scan. High Press Res. 1996;14:235–248.
[10] Petrícek V, Dusek M, Palatinus L. The crystallographic computing system JANA2006. Prague: Institute of Physics; 2006.
[11] Matsuoka T, Fujihisa H, Hirao N, Ohishi Y, Mitsui T, Masuda R, Seto M, Yoda Y, Shimizu K, Machida A, Aoki K. Structural and valence changes of europium hydride induced by application of high-pressure H_2. Phys Rev Lett. 2011;107:025501.

The distorted-fcc phase of samarium

R J Husband[1], I Loa[1], K Munro[1] and M I McMahon[1,2]

[1] SUPA, School of Physics and Astronomy and Centre for Science at Extreme Conditions, The University of Edinburgh, Edinburgh, EH9 3JZ, UK
[2] Research Complex at Harwell, Didcot, Oxon, OX11 0FA, UK

Email: R.J.Husband@ed.ac.uk

Abstract. Angle-dispersive x-ray powder diffraction experiments were performed on samarium metal up to 50 GPa. We report that the high-pressure distorted-fcc phase has the same *hR*24 structure observed in praseodymium, but, unlike praseodymium, samarium does not undergo a transition to a second distorted-fcc phase. We also report a path-dependent transition to a new phase, the structure of which has not yet been determined, which occurs on annealing followed by pressure decrease.

1. Introduction

The trivalent lanthanide elements exhibit a common series of structural phase transitions under pressure: hcp → Sm-type → dhcp → fcc → distorted-fcc (dfcc), which have long been associated with pressure-induced changes in their electronic structure. Due to this common structural trend, the structures of these high-pressure phases are often thought to be well known. However, the diffraction patterns generated by several distinct distorted-fcc structures can be very similar, and great care has to be taken in order to definitively determine the structure of these phases. Despite this fact, in many cases structural assignments were performed by analogy with other elements in the series. Previous work on praseodymium (Pr) has shown that this method is not sufficient. Evans *et al.* [1] showed that the dfcc phase of Pr has a rhombohedral structure with 24 atoms per hexagonal unit cell (*hR*24 in Pearson notation), and that a *C*-centred monoclinic structure (*mC*4) could only be ruled out due to the observation of a small number of weak reflections. The same study also showed that Pr transforms from *hR*24 to a second dfcc phase, a body-centred orthorhombic structure with space group *Ibam* and 16 atoms in the unit cell (*oI*16). This subtle transition was identified by the observation of a change in the relative intensity of the (006)/(202) and (0,0,12)/(404) doublets. This transition is also most likely observed in neodymium (Nd), raising the question of whether this transition may occur in all the trivalent lanthanide elements.

While it was possible to obtain very high quality diffraction data from the dfcc phase of Pr, this has not always been possible at the higher pressures required to access this phase in the other trivalent lanthanide elements. Although the dfcc phases of the majority of the trivalent lanthanides have been reported to have the same *hR*24 structure observed in Pr [2], these assignments rely heavily on analogy with Pr, and Rietveld refinements have only been shown for erbium and gadolinium [3,4]. Samarium (Sm) transforms to the dfcc phase above 20 GPa [5], but its structure has not yet been definitively determined: it has been indexed as either trigonal (*hP*6) [6], or *hP*6 at lower pressures and monoclinic at higher pressure [5]. At 37(4) GPa, Sm transforms to a hexagonal structure (*hP*3) [7], which is also observed in ytterbium (Yb) above 91 GPa [8]. Significant anomalies in the equation of state of Sm

were observed in the dfcc and *hP*3 phases compared to the common behaviour of the other trivalent lanthanides, and this has been taken as evidence for the onset of 4*f* electron delocalization [7].

In this paper, we report the results of our angle-dispersive powder x-ray diffraction experiments on Sm up to 50 GPa. We have found that the dfcc phase of Sm has the same *hR*24 structure observed in Pr. However, unlike Pr, Sm does not undergo a transition to a second dfcc phase, and instead the *hR*24 structure distorts to a much greater extent than in Pr. Above 40.4 GPa, Sm undergoes a sluggish transition to the *hP*3 phase in agreement with previous studies. In addition, we report the onset of a path-dependent structural phase transition, which is observed on annealing at 32 GPa followed by subsequent pressure decrease. This transition is characterised by large intensity changes in the diffraction profile, with some of the *hR*24 reflections disappearing completely. On further pressure decrease, the intensity changes reverse back to that of *hR*24 before annealing, suggesting that the intensity changes are not due to preferred orientation.

2. Experimental Methods

High-purity Sm samples, supplied by U. Schwarz at the Max-Planck-Institut für Chemische Physik fester Stoffe in Dresden, were loaded in diamond anvil pressure cells equipped with tungsten gaskets in a dry argon atmosphere (<1 ppm O_2 and <1 ppm H_2O). Two samples were loaded without a pressure-transmitting medium (PTM) and small amounts of Ta powder were included as a pressure marker. These samples subsequently will be referred to as samples 1 and 2. The pressure was determined using the calibration by Hanfland *et al*. [9]. A further sample was loaded with a mineral oil PTM for comparison. A small ruby sphere was included for pressure determination, and the pressure was determined using the standard ruby fluorescence method using the calibration by Mao *et al*. [10]. This sample will subsequently be referred to as sample 3.

Angle-dispersive x-ray powder diffraction data were collected at the European Synchrotron Radiation Facility (ESRF), Diamond Light Source (DLS) and the PETRA III synchrotron source at DESY. Data on samples 1 and 2 were collected at beamline ID09a at the ESRF using a beam of monochromatic x-rays of wavelength of 0.41352 Å, collimated to a diameter of 15 μm, and a Mar555 area detector. Some additional data on sample 1 were collected at beamline P02.2 at PETRA III using an x-ray beam of wavelength of 0.289818 Å and a diameter of ~2 μm, and data on sample 3 were collected at beamline I15 at DLS using an x-ray beam of wavelength of 0.4132 Å with a diameter of 30 μm. Data from DLS and PETRA were collected on Mar345 image plate detectors. In all cases, the 2-d diffraction images were integrated using Fit2D [11,12] and Rietveld refinements were performed using the Jana software [13].

Despite loading high-purity samples in a dry, oxygen-free atmosphere, trace amounts of contaminants were present, and reflections from these contaminant phases were observed in the data collected at the ID09a and I15. However, due to its very small beam size, P02.2 is excellent for avoiding small amounts of sample contaminant. The data collected at this beamline then enabled us to obtain non-contaminated diffraction profiles, enabling us to identify two contaminant phases, both with an fcc lattice. However, due to the short wavelength used at P02.2, the closely-spaced Sm reflections could not be fully resolved. For this reason, the unit cell dimensions and atomic positions were determined using the data collected at ID09a and I15, where a longer wavelength was used.

3. Results and Discussion

In all of our samples, we observe the Sm-type → dhcp transition in agreement with previous studies. Although mixed-phase dhcp-fcc patterns were observed, no single-phase fcc patterns were seen in any of our samples, and a single-phase dfcc pattern was first observed at 18.7 GPa. The dfcc phase could clearly be identified by the appearance of non-fcc superlattice reflections, and although the splitting of the lower-angle fcc reflections could not be resolved at 18.7 GPa, some of the higher-angle fcc reflections, such as the (222) reflection, were clearly split at this pressure. On further compression, the splitting of the fcc reflections increased, allowing the lower-angle split reflections also to be resolved.

The *hR*24 structure provides an excellent fit to the dfcc patterns over the entire pressure range in which this phase was observed (18.7-42.6 GPa), and the weak reflections that rule out the *mC*4 structure [1] were present in all patterns. A Rietveld refinement of the *hR*24 structure based on the diffraction profile of Sm obtained at 41.4 GPa is shown in figure 1. The refined structural parameters are a = 5.891(1) Å, c = 14.748(3) Å, with atoms at (0,0,0.273(1)) and (0.509(2),-0.509(2),0.244(1)). The (104), ($2\bar{1}6$) and ($1\bar{1}8$) reflections that cannot be accounted for by the *mC*4 structure are identified in the inset, and the strongest reflections from the two impurity phases are indicated by the asterisks.

The transition from *hR*24 to *oI*16 in Pr can be identified by a gradual change in the relative intensity of the (006)/(202) doublet, and in the (2*h*,2*k*,2*l*) equivalent, (0,0,12)/(404), which result from the splitting of the (111) and (222) reflections in the fcc phase. These intensity changes arise from the disappearance of the (006) and (0,0,12)-*hR*24 reflections, and the simultaneous growth of new reflections from the *oI*16 phase with very similar *d*-spacings. The identification of a potential similar transition in Sm is greatly simplified by the fact that the splitting of the (111) and (222)-fcc reflections is much greater than in Pr. Consequently, the (006) and (0,0,12) can be clearly identified as two distinct reflections for almost the entire pressure range in which this phase is observed, and the appearance of any additional reflections would be easily noticeable. The pressure dependence of the (006)/(202) and (0,0,12)/(404) reflections for *hR*24-Sm are shown in insets (a) and (b) of figure 2. It is clear from these figures that there is no sign of any new reflections up to the maximum pressure. We therefore conclude that there is no transition in Sm to the *oI*16 structure on pressure increase at ambient temperature, and instead Sm remains in the *hR*24 phase up to 42.6 GPa.

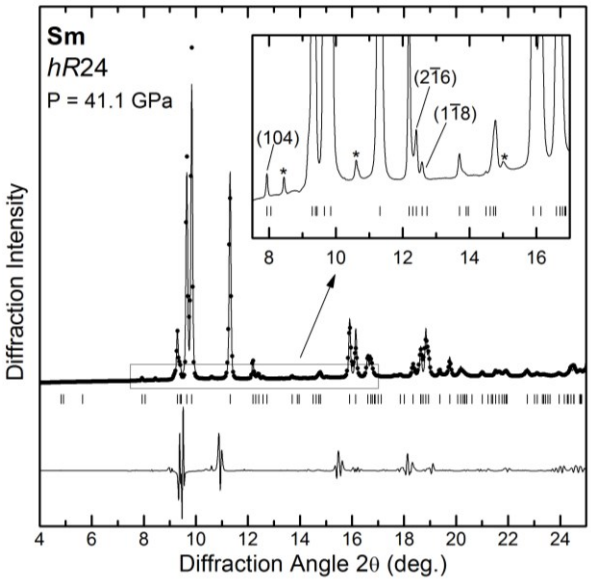

Figure 1. Rietveld fit of the *hR*24 structure for the diffraction profile of Sm at 41.1 GPa. The symbols show the experimental data, and the solid line shows the fit. The tick marks show the calculated peak positions, and the residuals are shown below the tick marks. Non-*mC*4 peaks are indicated in the inset, and the asterisks identify the reflections from the two contaminant phases.

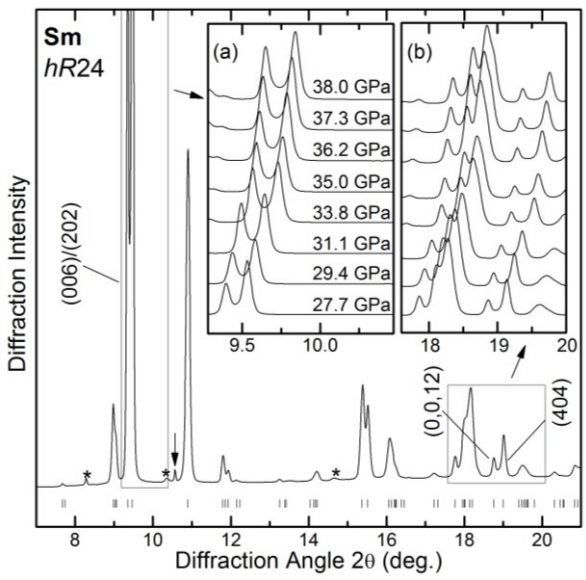

Figure 2. Diffraction profile of *hR*24-Sm at 29.3 GPa. The insets show the pressure evolution of the (a) (006) and (202) reflections and (b) (0,0,12) and (404) reflections. The asterisks identify the reflections from the two contaminant phases and the arrow indicates a reflection from the Ta pressure calibrant.

The *hR*24 structure is identical to fcc when $c/a = \sqrt{6} \approx 2.449$ and the atoms located at (0, 0, z_1) and (x, $-x$, z_2) have z_1 = ¼ , x = ½, and z_2 = ¼. The departure of the structural parameters from these values then quantifies the distortion of the structure from fcc. The c/a ratio increases continuously from 2.463(7) at 18.7 GPa, reaching a maximum value of 2.507(8) at 42.6 GPa, as shown in figure 3.

Krüger *et al.* [6] reported the pressure dependence of the *c/a* ratio of the dfcc phase for all the trivalent lanthanides up to Tb, although this phase was indexed using a trigonal structure in all cases. The *c/a* ratio of Sm was reported to reach a value of about $1.015\times\sqrt{6}$ (2.486), which is a significantly larger distortion than that reported for La, Gd and Tb, in which the distortion from fcc is almost negligible. The *c/a* ratios of Pr and Nd were reported to reach values similar to that of Sm. However, if the data points from these latter two elements that occur in the pressure regions after the transition to the *oI*16 structure are disregarded, the remaining points would suggest that the *c/a* distortion of these elements is similar to that of La, Gd, and Tb. Evans *et al.* [1] subsequently reported the *c/a* ratio of Pr to increase continuously from $\sqrt{6}$ to a maximum value of 2.487 at 13.24 GPa. Comparison with our data therefore suggests that the *hR*24-Sm distorts to a much greater extent than *hR*24-Pr.

In accordance with the analysis of Pr performed by Hamaya *et al.* [14], and subsequently by Evans *et al.* [1], the displacement of the *hR*24 atomic positions from those in the fcc structure can be expressed by amplitudes of three static displacements, $\varepsilon = x - \frac{1}{2}$, $\delta_1 = z_1 - \frac{1}{4}$ and $\delta_2 = z_1 - \frac{1}{4}$. The pressure dependence of ε, δ_1 and $-\delta_2$ for all three samples is shown in figure 4. In sample 1, ε and δ_2 have different values. However, in samples 2 and 3, $\varepsilon \approx \delta_2$, suggesting that the effect observed in the sample 1 is most likely due to the correlation between the atomic coordinates and the preferred orientation correction in the Rietveld refinement.

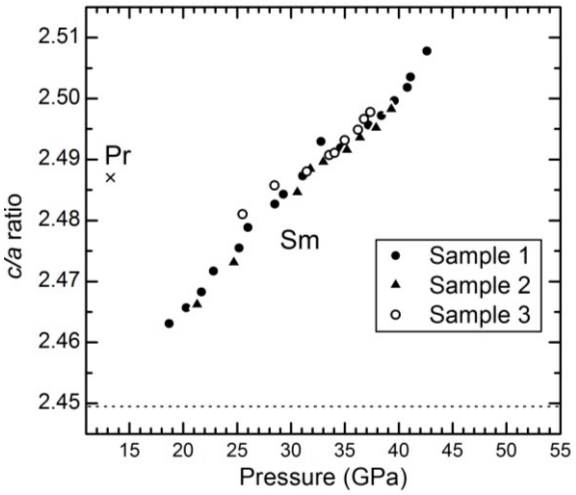

Figure 3. The pressure dependence of the *c/a* ratio of *hR*24-Sm. The cross shows the largest *c/a* ratio reported for *hR*24-Pr by Evans *et al.* The dotted line indicates the *c/a* ratio of undistorted fcc ($\sqrt{6}$). Error bars have not been included as they are smaller than the symbol size.

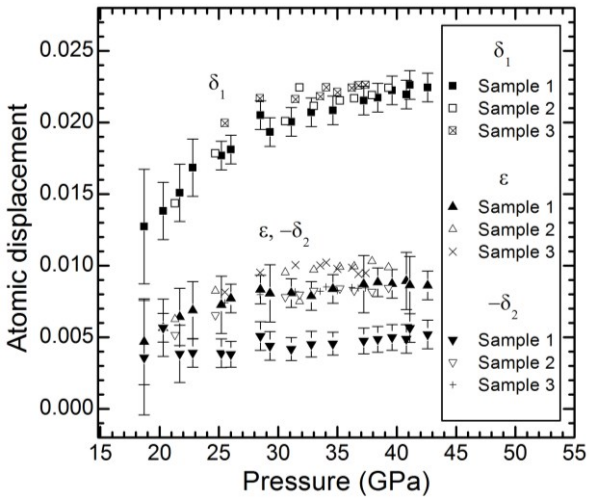

Figure 4. The pressure dependence of the static displacement parameters, ε, δ_1 and $-\delta_2$ for samples 1, 2 and 3. The error bars obtained from the Rietveld refinements are shown for sample 1, and those for samples 2 and 3 are similar.

We observed the *hR*24 → *hP*3 transition at slightly different pressures in each of the three samples. The transition is sluggish, and the onset of the transition can be identified by the observation of the (100)-*hP*3 reflection, which was first observed between 40.4 and 40.8 GPa. Additional *hP*3 reflections were not observed until 42.0-43.4 GPa, and single-phase *hP*3 patterns were first observed between 43.2 and 46.2 GPa. No correlation between the use of a PTM and the transition pressure was observed. The *hP*3 structure can account for all the reflections observed in our diffraction profiles. A Rietveld refinement of this structure based on a diffraction profile collected at 47.4 GPa is shown in figure 5. The corresponding refined structural parameters are $a = 2.9717(3)$ Å, $c = 6.879(3)$ Å, with atoms at (0,0.513(5),⅓). Sm remained in this phase up to 50 GPa, the highest pressure reached in this study.

An attempt was made to collect diffraction data from sample 1 on decompression. The *hP*3 → *hR*24 transition was observed, and the first single-phase dfcc pattern was observed at 40.1 GPa.

However, only one more data point was collected at 37.9 GPa before the pressure of the cell dropped to 22.2 GPa. The *hR*24 structure gave an excellent fit to these patterns. Additional compression data from the same sample up to 32 GPa, the maximum pressure that could be reached after pressure cycling, were collected at beamline P02.2. The integrated diffraction profiles were in agreement with those collected previously.

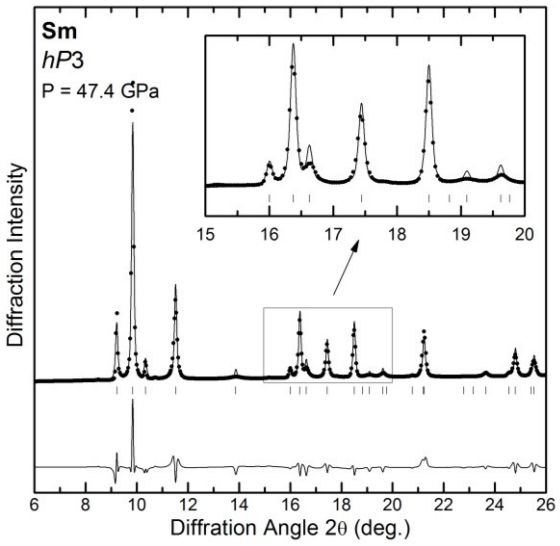

Figure 5. Rietveld refinement of the *hP*3 structure to the diffraction profile of Sm obtained at 47.4 GPa. The symbols show the experimental data and the solid line shows the fit. The tick marks below the profile show the calculated peak positions, and the residuals are shown below the tick marks.

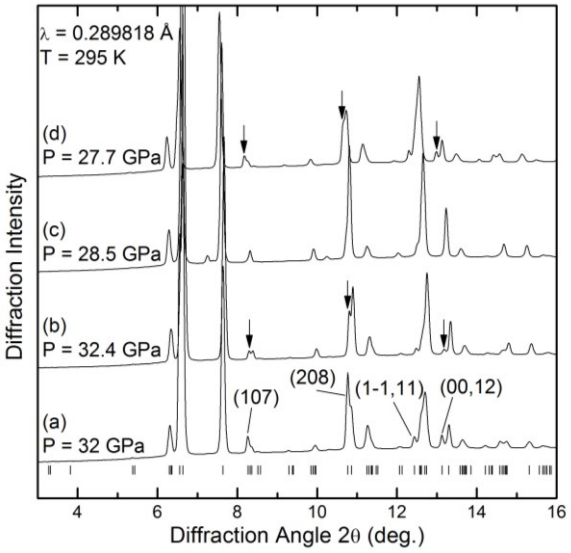

Figure 6. X-ray powder diffraction profiles of Sm at (a) 32, (b) 32.4, (c) 28.5 and (d) 27.7 GPa, which were collected in that order. The sample was annealed for 12 hours at 100°C between the collection of profiles (a) and (b). The tick marks below profile (a) show the calculated peak positions of *hR*24.

This sample was then annealed at 100°C for 12 hours at 32 GPa. After annealing, the pressure of the sample had increased slightly to 32.4 GPa. Although the subsequent diffraction pattern could still be described by the *hR*24 structure, there was a significant change in the relative intensity of many of the *hR*24 reflections. This effect became more pronounced when the pressure on the cell was subsequently decreased, with the intensity of some reflections decreasing further until they had disappeared completely. However, on further decompression the intensity changes reversed and the diffraction profiles strongly resemble those taken before annealing.

This is illustrated in figure 6, which shows the diffraction profiles observed (a) before annealing at 32 GPa, (b) after annealing at 32.4 GPa, and on subsequent pressure decrease to (c) 28.5 GPa and then (d) 27.7 GPa. The *hR*24 structure no longer gives a good fit to profile (c) as it predicts reflections that are no longer observed. In particular, the (107), (1,$\bar{1}$,11) and (0,0,12) reflections from *hR24* have completely disappeared, and the intensity of the (208) reflection has significantly decreased. On further pressure decrease, the intensity changes are reversed and intensities in profile (d) strongly resemble those in profile (a). This suggests that the intensity changes were not due to preferred orientation effects, as we would not expect them to reverse. Instead, this suggests that what we observed is the onset of a transition to a new phase. This behaviour was also observed in two other samples in subsequent experiments at DLS.

Further work will be required in order to determine the origin of this transition. In particular, it is not clear whether it will be observed on decompression at ambient temperature, or if the new phase is only stable at high temperatures. Many distorted-fcc structures have extremely similar diffraction patterns, and so high-resolution diffraction data will be required in order to resolve any closely-spaced

doublets and triplets. Subsequent data will therefore be collected using a longer x-ray wavelength in order to maximise the angular resolution.

4. Conclusion

We have reported the results of our angle-dispersive powder x-ray diffraction experiments on samarium metal up to 50 GPa. We report that the high-pressure distorted-fcc phase has the same *hR*24 structure observed in Pr. However, Sm does not undergo a transition to a second distorted-fcc phase such as the *oI*16 phase observed in Pr, and instead *hR*24-Sm distorts to a greater extent than *hR*24-Pr. We also report a path-dependent transition to a new phase, the structure of which has not yet been determined, which occurred on annealing followed by pressure decrease.

Acknowledgments

This work was supported by a research grant from the UK Engineering and Physical Sciences Research Council, and facilities were provided by the ESRF and DLS. We would like to thank L. Bezacier of ID09a (ESRF) and H. Wilhelm of I15 (DLS) for their support on the beamlines, and U. Schwarz at the Max-Planck-Institut für Chemische Physik fester Stoffe in Dresden for the providing the samarium samples. Portions of this research were carried out at the light source PETRA III at DESY, a member of the Helmholtz Association (HGF). We would like to thank H. P. Liermann and Z. Konopkova for assistance in using beamline P02.2.

References

[1] Evans S R, Loa I, Lundegaard L F and M I McMahon 2009 *Phys. Rev.* B **80** 134105
[2] Samudrala G K and Vohra Y K 2013 *Handbook on the Physics and Chemistry of Rare Earths* vol 43, Ed J G Bünzli and V K Pecharsky (Elsevier) p 575
[3] Samudrala G K, Thomas S A, Montgomery J M and Vohra Y K 2011 *J. Phys.: Condens. Matter* **23** 315701
[4] Errandonea D, Boehler R, Schwager B and Mezouar M 2007 *Phys. Rev.* B **75** 014103
[5] Staun Olsen J, Streenstrup S, Gerward L, Benedict U, Akella J and Smith G 1990 *High Pressure Res.* **4** 366-368
[6] Krüger T, Merkau B, Grosshans W A and Holzapfel W B 1990 *High Pressure Res.* **2** 193
[7] Zhao Y C, Porsch F and Holzapfel W B 1994 *Phys. Rev.* B **50** 6603
[8] Chesnut G N and Vohra Y K 1999 *Phys. Rev. Lett.* **82** 1712
[9] Hanfland M, Syassen K and Köhler J 2002 *J. Appl. Phys.* **91** 4143
[10] Mao H K, Xu J, and Bell P M 1986 *J. Geophys. Res.* **91** 4673
[11] Petricek V, Dusek M and Palatinus L 2006 *The crystallographic computing system JANA2006.* Institute of Physics, Praha, Czech Republic
[12] Hammersley A P 1997 *ESRF Internal Report* **ESRF97HA02T** **"**http://www.esrf.eu/computing/scientific/FIT2D/FIT2D_INTRO/"
[13] Hammersley A P, Svensson S O, Hanfland M, Fitch A N and Häusermann D 1996 *High Pressure Res.* **14** 235
[14] Hamaya N, Sakamoto Y, Fujihisa H, Fujii Y, Takemura K, Kikegawa T and Shimomura O 1993 *J. Phys.: Condens. Matter* **5** L369

Incommensurate-to-incommensurate phase transition in Eu metal at high pressures

R. J. Husband,[1] I. Loa,[1] K. A. Munro,[1] E. E. McBride,[1,*] S. R. Evans,[3] H.-P. Liermann,[2] and M. I. McMahon[1,4]

[1]*SUPA, School of Physics and Astronomy and Centre for Science at Extreme Conditions, The University of Edinburgh, Mayfield Road, Edinburgh, EH9 3JZ, United Kingdom*

[2]*Photon Sciences, Deutsches Elektronen Synchrotron (DESY), Notkestrasse 85, D-22607 Hamburg, Germany*

[3]*European Synchrotron Radiation Facility, 38043 Grenoble, France*

[4]*Research Complex at Harwell, Didcot, Oxon, OX11 0FA, United Kingdom*

(Received 11 September 2014; revised manuscript received 5 November 2014; published 8 December 2014)

High pressure x-ray powder-diffraction experiments were performed on europium metal up to ∼70 GPa. Above 38 GPa, europium transforms from the incommensurately modulated Eu-IV phase to a second phase with an incommensurately modulated crystal structure, Eu-V. This is a previously unseen incommensurately modulated to incommensurately modulated transition in the elements at high pressure. High-pressure high-temperature experiments were also performed up to 449 K in order to make an initial estimate of the positions of the phase boundaries of the incommensurate phases.

DOI: 10.1103/PhysRevB.90.214105 PACS number(s): 61.50.Ks, 62.50.−p

I. INTRODUCTION

Europium (Eu), which is divalent at ambient pressure due to its half-filled $4f$ electron shell, is an anomalous member of the lanthanide elements, the majority of which are trivalent. Consequently, Eu does not exhibit the common series of structural phase transitions observed in the trivalent lanthanide elements on compression (hcp–Sm-type–dhcp–fcc–distorted-fcc–low-symmetry phase) [1], but instead its behavior is much more complex.

Eu transforms from the ambient-pressure body-centred cubic (bcc) structure to the hexagonal close-packed (hcp) structure at 12.5 GPa. Initial high-pressure x-ray diffraction studies [2–5] reported a transition to a new phase Eu-III above 17 GPa. This was identified by the appearance of a number of weak reflections in the diffraction pattern in addition to those from the hcp phase. However, we have shown that if great care is taken to minimize any possible sources of contamination during the preparation and pressure cell loading process, no additional peaks are observed above 17 GPa, and instead Eu remains in the hcp phase up to 31.5 GPa [6]. We therefore concluded that the behavior initially attributed to a transition to Eu-III was not due to changes in Eu itself, but was instead due to pressure-induced changes in a contaminant phase that was present in previous studies.

The presence of this contaminant phase in early x-ray diffraction studies greatly complicated the analysis of data collected above 17 GPa. Collecting diffraction data on non-contaminated samples allowed us to determine a transition to a new phase, Eu-IV, above 31.5 GPa [7]. The diffraction patterns from this phase are complex, and high-resolution diffraction data were required in order to resolve the large number of closely spaced reflections, and to identify the large number of weak reflections that appear at the transition. This enabled us to unambiguously determine Eu-IV to have an incommensurately modulated crystal structure (denoted i-$mC4$ in Pearson's notation, where i indicates that the structure is incommensurate and $mC4$ is the Pearson symbol for the average structure) [7]. This structure has a modulation vector in the a-c plane (q_1, 0, q_3), with superspace group $C2/c(q_1 0 q_3)00$ and atoms in the (0, y, 0.25) Wyckoff positions. We found that the i-$mC4$ structure can describe all of the diffraction patterns of Eu collected between 31.5 and 37 GPa, the highest pressure reached in our previous study. Eu-IV is currently the only incommensurate crystal structure to have been observed in the lanthanide elements at high pressure.

In our subsequent study [8], further changes were observed in the diffraction patterns of Eu collected above 38 GPa and we found that these patterns could no longer be described by the i-$mC4$ structure. This was taken as evidence of a transition to a new phase Eu-V, which was thought to be incommensurate, although we were unable to determine the structure at that time.

Despite the fact that europium exhibits possibly the most interesting high-pressure phases of any lanthanide element, there have been surprisingly few studies on its high-pressure behavior. With the exception of our earlier work [8], only one previous study has reported the results of x-ray diffraction experiments on Eu at pressures greater than 40 GPa. Bi *et al.* [5] reported a series of phase transitions and structural assignments in Eu up to 92 GPa. However, reflections from the contaminant phase can clearly be identified in their diffraction profiles collected above 18 GPa. Consequently, we found that none of the structures proposed by Bi *et al.* could describe our own data collected at pressures exceeding 18 GPa.

In this paper we report the results of powder x-ray diffraction experiments on Eu up to ∼70 GPa. We show that Eu transforms from i-$mC4$ to a second incommensurately modulated crystal structure Eu-V above 38 GPa. This transition is an example of an incommensurate-to-incommensurate transition in a non-host-guest structure, previously unseen in the elements at high pressure. The diffraction patterns from Eu-V are complex, and high-quality data are required in order to resolve the large number of closely spaced diffraction peaks. Significant peak broadening was observed in the diffraction profiles collected above ∼40 GPa, making it increasingly more difficult to analyze the patterns above this pressure.

We also report the results of our high-pressure high-temperature experiments up to ∼450 K and 42 GPa, in an

*Present address: Photon Sciences, Deutsches Elektronen Synchrotron (DESY), Notkestrasse 85, D-22607 Hamburg, Germany.

initial attempt to expand the phase diagram of Eu away from only room temperature studies. We find that the pressure range in which the hcp phase is stable is larger than in our room temperature experiments, with the hcp phase remaining stable up to higher pressures.

II. EXPERIMENTAL DETAILS

High-purity Eu samples, provided by U. Schwarz of the MPI für Chemische Physik fester Stoffe, were loaded into diamond-anvil cells equipped with tungsten or rhenium gaskets in a dry argon environment. Initial room temperature studies were performed on two samples, one of which was loaded without a pressure-transmitting medium (PTM), whereas the other was loaded with a helium PTM. In both of these samples, a small ruby sphere was included as a pressure marker, and the pressure was determined with the ruby fluorescence method using the calibration by Mao *et al.* [9].

Eu is extremely reactive, and great care must be taken in the loading procedure in order to minimize any possible sources of contamination. Reflections of the most common contaminant phase are not observed at pressures below 17 GPa, and so single-phase hcp Eu patterns must be collected in the 17–31.5 GPa region in order to confirm that the sample is "clean" [6]. We previously found that loading samples quickly without a PTM and without a pressure marker was the most effective way of obtaining noncontaminated samples [6,7]. The majority of the room-temperature data were therefore collected from a third sample loaded according to this method. The pressure of this sample was subsequently determined from the position of one or more sample reflections using a calibration established from the sample loaded in He and with a ruby pressure marker.

Two additional Eu samples were loaded in cells equipped with W gaskets for the high-temperature experiments. In one of these samples, a small grain of Ta powder was included as a pressure marker, and in the other sample a piece of 1 μm thick Ta foil was placed between the sample and one of the diamond anvils. The pressures of both samples were determined using the ambient-temperature pressure-volume relation of Ta measured by Hanfland *et al.* [10,11], and a thermal correction based on the results of Dorogokupets and Oganov [12] was applied for the high-temperature experiments. The cells containing these samples were heated using external resistive heaters, and the temperature was measured using a K-type thermocouple placed on the back of one of the diamonds. The uncertainty in temperature was estimated to be no more than 10 K.

Angle-dispersive powder x-ray diffraction data were collected on station ID09a at the European Synchrotron Radiation Facility (ESRF) and on beamline I15 at Diamond Light Source (DLS), using monochromatic x-ray beams of wavelength $\sim$0.41 and $\sim$0.34 Å and with diameters of 10 and 30 μm, respectively. Data were collected using a mar555 area detector (ID09a) and a mar345 image plate detector (I15). Additional data were collected on the Extreme Conditions Beamline (P02.2) at the PETRA III synchrotron, DESY, using an x-ray beam of wavelength $\sim$0.29 Å focused to $\sim 2 \times 2$ μm^2. Data were collected at Petra-III using an Perkin Elmer XRD 1621 area detector. In all cases, the 2D diffraction images were integrated using Fit2D [13,14] to produce 1D diffraction profiles, which were then indexed using the DICVOL [15] and SUPERCELL [16] indexing programs, and subsequently analyzed using the Le Bail and Rietveld methods with the JANA2006 software [17].

III. RESULTS

A. Transition to Eu-V

In all of our samples we observed the bcc–hcp transition in agreement with previous studies [2–7], and Eu transformed to the incommensurately modulated i-$mC4$ structure at 31.5 GPa. Preliminary studies performed on station ID09a found that although the i-$mC4$ structure gives an excellent fit to the diffraction profiles collected in the 31.5–38 GPa region, it could not explain the patterns collected at higher pressures. This suggested a transition to a new crystal structure above 38 GPa. This behavior was observed in both the sample loaded with a He pressure-transmitting medium and a sample loaded without a PTM.

Initial attempts to index this new phase were unsuccessful. However, analysis of data from these samples was complicated by the presence of contaminant reflections, the details of which have been reported previously [6,8]. The diffraction profiles from Eu above 31.5 GPa are extremely complex, and great care must be taken in order to find a unique structural solution for the new phases. It was therefore essential to collect data on noncontaminated samples to avoid misidentification of contaminant peaks as those from pure Eu, particularly as the behavior of the contaminant phase has only been established up to 38 GPa [8].

We therefore loaded a sample without a pressure marker and without a PTM with the aim of obtaining a noncontaminated sample. Data from this sample were collected on beam line I15 up to a maximum pressure of 46 GPa, the highest pressure that could be reached with the pressure cell. In this sample we did not observe the appearance of any contaminant reflections above 17 GPa, and instead Eu remained in the hcp phase up to 31.5 GPa. Above this pressure, data were collected in $\sim$1 GPa steps so that subtle changes in the diffraction patterns could be identified. The i-$mC4$ structure gives an excellent fit to the diffraction patterns collected in the 31.5–38 GPa region. The highest-pressure single-phase i-$mC4$ pattern at 38 GPa is shown in Fig. 1. The Bragg reflections can be indexed using four Miller indices (h,k,l,m) according to $\mathbf{H} = h\mathbf{a}^* + k\mathbf{b}^* + l\mathbf{c}^* + m\mathbf{q}$, where $\mathbf{a}^*,\mathbf{b}^*,\mathbf{c}^*$ define the reciprocal lattice of the $mC4$ average structure and $\mathbf{q}$ is the modulation vector, according to the 4D superspace formalism [18] as described in our previous work [7,19]. Only first-order ($m = \pm 1$) satellite reflections were observed. In our previous work we described the i-$mC4$ structure in the $C2/c(q_1 0 q_3)00$ superspace group setting in order to allow a direct comparison with the hcp structure in the orthohexagonal setting, and so the same superspace group will be used here. A Rietveld refinement of the i-$mC4$ structure based on the diffraction profile of Eu at 38 GPa gives lattice parameters of $a = 3.0508(4)$ Å, $b = 5.2196(4)$ Å, $c = 4.6524(4)$ Å, and $\beta = 90.541(9)^\circ$, and the atomic coordinate $y = 0.3264(9)$, with wave vector components $q_1 = 0.7684(5)$ and $q_3 = 0.5864(4)$ and modulation amplitudes of $B_{1a} = -0.048(4)$, $A_{1b} = 0.0292(15)$, and $B_{1c} = 0.0557(14)$. All other first-order Fourier components are equal to zero due to the superspace group symmetry conditions. These are

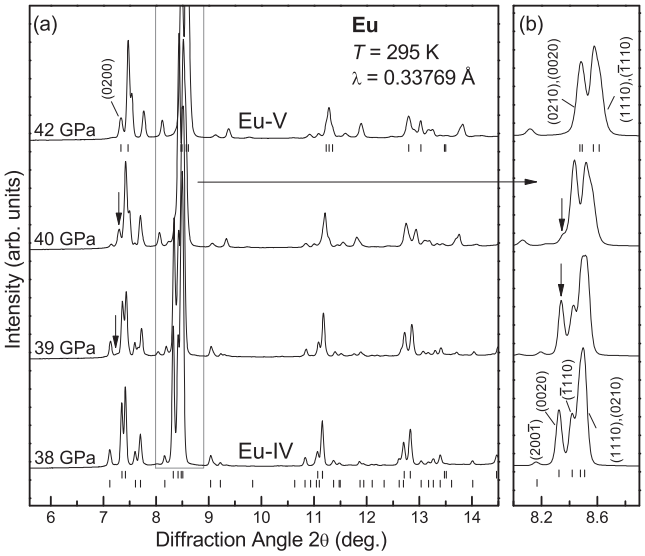

FIG. 1. (a) X-ray powder diffraction profiles of Eu at 38, 39, 40, and 42 GPa illustrating the transition from Eu-IV to Eu-V. The 38 GPa profile can be indexed as single-phase Eu-IV, the 39 and 40 GPa profiles are mixed-phase, and the 42 GPa profile is single-phase Eu-V. The upper and lower tick marks below the 38 GPa pattern indicate the calculated peak positions of the main and satellite reflections from i-$mC4$, respectively, and the tick marks below the 42 GPa pattern indicate the positions of $mC4(2)$, the average structure of Eu-IV. The arrows indicate the growth of the (0200) $mC4(2)$ reflection. (b) Enlargement showing the behavior of the (0020), ($\bar{1}110$), (1110), and (0210) i-$mC4$ reflections across the transition. The arrows indicates the disappearance of the (0020) i-$mC4$ reflection. The indices above the 42 GPa profile correspond to describing the $mC4(2)$ structure in the $\beta < 90^\circ$ setting.

in agreement with the structural parameters we previously determined for the i-$mC4$ structure [7].

Above 38 GPa we observed changes in the diffraction profiles which meant that they could no longer be described by the i-$mC4$ structure. This was taken as evidence of a transition to a new phase Eu-V, which was complete by 42 GPa. This is illustrated in Fig. 1(a), which shows diffraction patterns from Eu in the Eu-IV phase at 38 GPa, in the mixed-phase region at 39 and 40 GPa, and in the Eu-V phase at 42 GPa. The changes in the diffraction profiles during the transition can be characterized by three distinct features. First, we observed the appearance of a set of new reflections that cannot be accounted for by the i-$mC4$ structure. Second, the intensity of the i-$mC4$ satellite reflections began to decrease until they had completely disappeared by 42 GPa. Finally, subtle changes in the main i-$mC4$ reflections were also observed. In particular, the intense (0020) main reflection was observed to decrease in intensity until it had completely disappeared by 42 GPa, as illustrated in Fig. 1(b).

Additional data from this sample were collected on beamline P02.2 and in a second experimental run on I15, where the pressure was first decreased in order to observe the transition back into the Eu-IV phase, and then increased again to transform back into the Eu-V phase. In this case we observed the Eu-IV–EuV transition at a slightly lower pressure, and the lowest-pressure single-phase Eu-V pattern was collected at 40.3 GPa. These additional data sets were considered alongside the original data collected on I15 during the process of indexing the patterns from the new phase.

Attempts to index all of the reflections from Eu-V based on a crystal structure with a 3D space group were unsuccessful. However, as we noted previously [8], the fact that the overall diffraction profile of the new phase is very similar to that of Eu-IV suggested the possibility that Eu had transformed to a second incommensurately modulated crystal structure. In addition, a large number of weak reflections appear at the transition to Eu-V, which may be a new set of satellite reflections.

In order to index the Eu-V patterns based on an incommensurately modulated crystal structure, it is necessary to identify the main diffraction peaks so as to determine the average structure. However, although there is clear distinction between main ($m = 0$) and satellite ($m \neq 0$) reflections in the diffraction patterns from the Eu-IV phase, the reflections in the Eu-V patterns could not be distinguished with the same certainty. The main i-$mC4$ reflections in Eu-IV can be identified by two distinct features. First, they are much more intense than the surrounding satellite reflections. Second, they result from a continuous splitting of the hcp reflections as Eu transforms from hcp Eu-II to the lower-symmetry monoclinic Eu-IV structure. However, these features are not so easily identifiable in the Eu-V patterns. The positions of some of the main i-$mC4$ reflections can be clearly identified over the course of the transition, and we therefore assumed these also to correspond to main reflections of the new phase. As noted previously, at least one of the main i-$mC4$ reflections, (0020), disappears at the transition, suggesting that there is a change in the average structure. In addition, some of the new reflections that appear at the transition have an intensity comparable to that of the main Eu-IV reflections, and it is not immediately obvious if these are main or satellite reflections from the new phase.

However, the changes in the main i-$mC4$ reflections at the transition to Eu-V are subtle, and so we made the initial assumption that the average structures of both phases are similar. The DICVOL program was therefore used to index a subset of the reflections based on a similar monoclinic unit cell, ensuring that all of the reflections previously identified as main Eu-V reflections were accounted for. The best fit was obtained using a monoclinic structure with space group $C2/c$ with the atoms in the 4e (0, y, 0.25) Wyckoff positions. We denote the average structure as $mC4(2)$, where the 2 distinguishes it from the average Eu-IV structure, $mC4$. Please note that although both the $mC4$ and $mC4(2)$ structures have the $C2/c$ space group, they are not related to the $C2/c$ structure proposed by Bi *et al.*. A Rietveld refinement of this structure at 42 GPa gives lattice parameters of $a = 2.9756(18)$ Å, $b = 5.278(6)$ Å, $c = 4.564(4)$ Å, and $\beta = 89.66(7)^\circ$, with the atomic coordinate $y = 0.337(5)$. The positions of the main $mC4(2)$ reflections are shown by the tick marks under the diffraction profile of Eu at 42 GPa in Fig. 1. This structure can account for the set of reflections originally identified as the main Eu-IV reflections, and also at least one of the new reflections that appeared at the transition. This is illustrated in Fig. 1(a), which shows the growth of the (0200) reflection, which cannot be related to any of the peaks in the Eu-IV pattern.

The program SUPERCELL was then used to index the remaining reflections as satellite reflections corresponding to

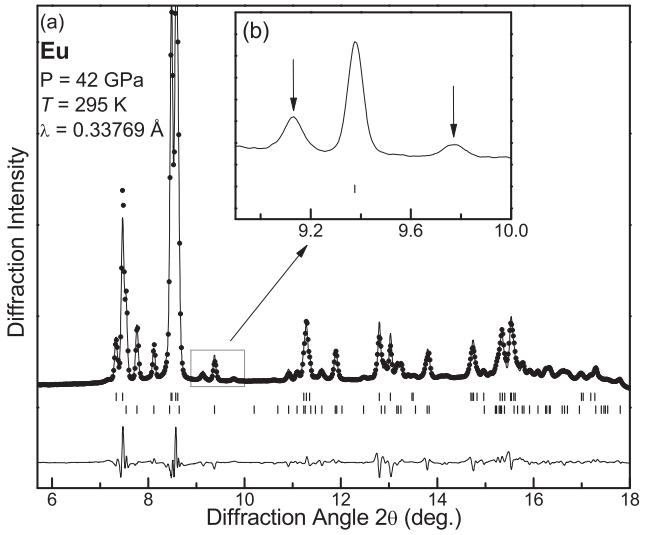

FIG. 2. Rietveld refinement of the *i*-*mC*4(2) structure based on the diffraction profile of Eu at 42 GPa, where only first order ($m = \pm 1$) satellite reflections have been considered. (a) The points show the experimental data, and the solid line shows the fit. The tick marks below the profile show the calculated peak positions of the main (upper) and satellite (lower) reflections, and the residuals are shown below the tick marks. Inset (b) illustrates the most intense reflections that cannot be accounted for by main or first-order satellite reflections, which are indicated by the arrows above the profile. In this case, the solid line shows the experimental data.

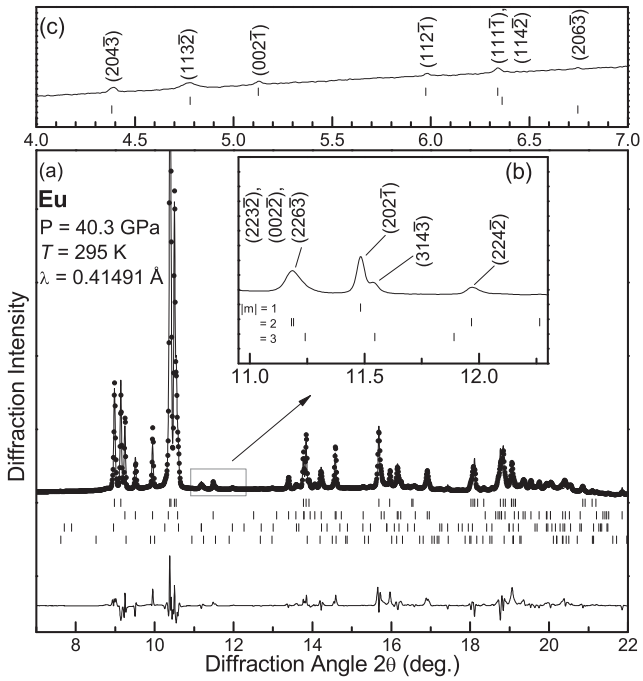

FIG. 3. Rietveld refinement of the *i*-*mC*4(2) structure based on the diffraction profile of Eu obtained at 40.3 GPa, where up to third-order ($m = \pm 3$) satellite reflections have been considered. The points show the experimental data, and the solid line shows the fit. The tick marks below the profile show the calculated peak positions of the main (upper) and satellite (lower) reflections, and the residuals are shown below the tick marks. Inset (b) illustrates weak reflections that cannot be described as main or first-order satellite reflections, but can be accounted for when up to third-order satellite reflections are considered. Inset (c) illustrates a number of extremely weak low-angle satellite reflections that can be described by this structure. In insets (b) and (c), the solid line shows the experimental data. The indices correspond to describing the structure with $\beta > 90^\circ$.

a modulation wave vector (q_1,0,q_3), with $q_1 \approx 0.6$ and $q_3 \approx 0.4$. Analysis of systematic absences showed the superspace group to be $C2/c(q_1 0 q_3)00$ [*i*-*mC*4(2), where again the (2) distinguishes this from the Eu-IV *i*-*mC*4 structure]. The *i*-*mC*4 and *i*-*mC*4(2) structures therefore have the same superspace groups, with very similar lattice parameters, but with different modulation vectors. However, we described *i*-*mC*4 with $\beta > 90^\circ$ and *i*-*mC*4(2) with $\beta < 90^\circ$. In order to compare the two structures, it is necessary to also describe *i*-*mC*4(2) with $\beta > 90^\circ$. This involves the transformations $\beta' = 180^\circ - \beta$ and $q_3' = 2 - q_3$. The *i*-*mC*4(2) structure will be described in this setting from now on. A Rietveld refinement of the *i*-*mC*4(2) structure at 42 GPa is shown in Fig. 2, where only first-order ($m = \pm 1$) satellite reflections have been considered. The refined structural parameters are $a = 2.9761(3)$ Å, $b = 5.2809(7)$ Å, $c = 4.5613(6)$ Å, $\beta' = 90.372(10)^\circ$, and the atomic coordinate $y = 0.3371(9)$, with wave vector components $q_1 = 0.5869(3)$ and $q_3' = 1.5877(4)$ and modulation amplitudes of $B_{1a} = 0.061(3)$, $A_{1b} = -0.041(2)$, and $B_{1c} = 0.0667(15)$. As with Eu-IV, all other first-order Fourier components are equal to zero due to the superspace group symmetry conditions.

The *i*-*mC*4(2) structure with first-order satellite reflections gives a reasonable fit to the diffraction pattern at this pressure. However, there are a small number of weak reflections that are not accounted for, the most intense of which are highlighted in Fig. 2(b). In order to test if these arise from higher-order satellite reflections, we collected a single exposure of our sample at ID09a following pressure cycling, as described previously. A Rietveld refinement of the *i*-*mC*4(2) structure to this single pattern at 40.3 GPa is shown in Fig. 3(a), where satellite reflections up to third order have now been considered. The inclusion of second- and third-order satellite reflections results in an improved fit ($R_p = 5.6\%$ and $R_{wp} = 8.9\%$) in comparison with a refinement in which only first-order satellite reflections are considered ($R_p = 6.5\%$ and $R_{wp} = 10.3\%$). A larger number of second-order satellite reflections (≈12) are observed in this pattern, as well as a number of third-order satellite reflections, as illustrated in Fig. 3(b). Crucially, this structure can also explain a number of extremely weak satellite reflections at low angles, as illustrated in Fig. 3(c), which were not observed in the original data collected at I15 and which were therefore not used in the determination of the *i*-*mC*4(2) structure model. The parameters of our final solution for the *i*-*mC*4(2) structure at 40.3 GPa are $a = 2.9886(3)$ Å, $b = 5.2987(3)$ Å, $c = 4.5720$ Å, $\beta' = 90.328(8)^\circ$, and $y = 0.3365(9)$, with a modulation vector of [0.5863(3),0,1.5865(2)]. The refined modulation amplitudes are $B_{1a} = 0.042(5)$, $A_{1b} = -0.0363(2)$, $B_{1c} = 0.0693(19)$, $B_{2a} = -0.035(6)$, $A_{2b} = -0.008(3)$, $B_{2c} = 0.019(3)$, $B_{3a} = 0.018(11)$, $A_{3b} = -0.008(4)$, and $B_{3c} = 0.004(4)$. We

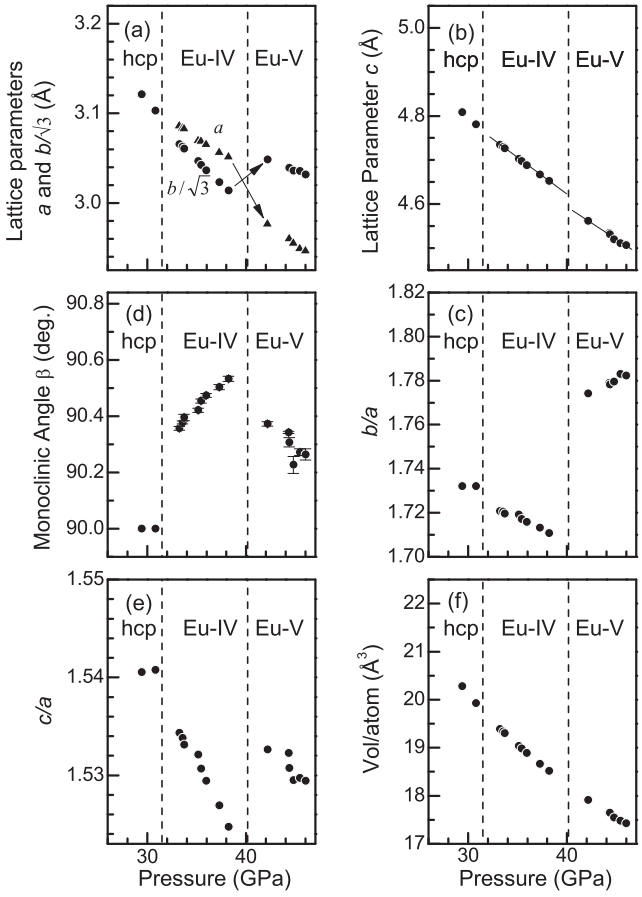

FIG. 4. Lattice parameters of Eu as a function of pressure, across the transition from hcp to i-$mC4$ (Eu-IV) and then to i-$mC4(2)$ (Eu-V). The hcp structure is described in the orthohexagonal setting, where the b/a axial ratio is equal to $\sqrt{3}$. For this reason, the pressure dependence of a (solid triangles) and $b/\sqrt{3}$ (solid circles) are both shown in (a), in order to illustrate the distortion of the structure from hcp. The arrows in (a) and the lines in (b) are added as guides to the eye. The lattice parameters were obtained from Rietveld fits to the diffraction profiles. With the exception of the monoclinic angle β, the error bars are smaller than the symbol size and so have been omitted.

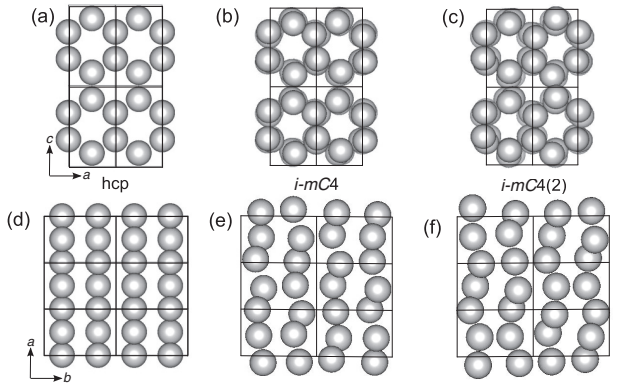

FIG. 5. Schematic views of the hcp, i-$mC4$ (Eu-IV), and i-$mc4(2)$ (Eu-V) structures at <31.5, 38, and 41 GPa, respectively. Four unit cells viewed along the b direction of the (a) hcp, (b) i-$mC4$, and (c) i-$mC4(2)$ structures, and six unit cells viewed along the c direction of the (d) hcp, (e) i-$mC4$, and (f) i-$mC4(2)$ structures. The modulation amplitudes are drawn to scale.

therefore conclude that Eu undergoes a transition to a second incommensurately modulated crystal structure at 38 GPa.

The i-$mC4(2)$ structure gives an excellent fit to the diffraction patterns collected up to 46 GPa, the highest pressure reached with this sample, when up to second-order satellite reflections are considered. Although this is an insufficient number of data points in order to be able to comment on the pressure dependence of the structural parameters of i-$mC4(2)$, we can consider the changes in the structural parameters of Eu across the transition from hcp to i-$mC4$ and then to i-$mC4(2)$. The pressure dependencies of the lattice parameters (a, $b/\sqrt{3}$, c, c/a, b/a, and volume/atom) are shown in Fig. 4. The hcp structure is described in the orthohexagonal setting, where the b/a axial ratio is equal to $\sqrt{3}$. For this reason, the pressure dependence of a and $b/\sqrt{3}$ are shown in the same panel for comparison. Discontinuities were observed in the c/a and b/a axial ratios, and also in the monoclinic angle β, across the transition from i-$mC4$ to i-$mC4(2)$. In particular, the b/a ratio was observed to decrease away from $\sqrt{3}$ following the transition to i-$mC4$, and then increase away from $\sqrt{3}$ following the transition to i-$mC4(2)$. The wave vector components also show discontinuous jumps across the transition from i-$mC4$ to i-$mC4(2)$, with q_1 going from $\sim$0.77 to $\sim$0.59, and q_3 going from $\sim$0.59 to $\sim$1.59. We therefore conclude that the transition is first order, with discontinuous changes in the structural parameters of the average structure, and also a rotation of the wave vector in the a-c plane.

This is the first incommensurate-incommensurate transition to be observed in a non-host-guest structure in the elements at high pressure. Schematic views of the hcp, i-$mC4$, and i-$mC4(2)$ structures along the b and c axes are shown in Fig. 5 for comparison, where the modulation amplitudes are drawn to scale.

Having solved the structure of Eu-V, we could then revisit the data collected in our initial studies. Only one single-phase Eu-V pattern was collected from the original sample loaded without a PTM, and the i-$mC4(2)$ structure gives an excellent fit to this pattern when up to $m = \pm 2$ satellite reflections were considered. Data from the sample loaded with a He PTM were collected up to much higher pressures, reaching a maximum pressure of 70.1 GPa. However, the patterns collected from this sample contained contaminant reflections from at least one additional impurity phase in addition to those from the $cI12$ impurity phase described in Ref. [8].

The i-$mC4(2)$ structure gives a good fit to the patterns collected below $\sim$50 GPa. However, this structure has six refinable lattice parameters (a, b, c, β, q_1, q_3), and so accurate peak positions of at least seven reflections are required in order to determine the unit cell dimensions and modulation vector. The diffraction profiles from this phase are very complex, with a large number of closely spaced reflections, and very high-resolution data are required in order to resolve individual peaks. Despite the use of a helium pressure medium, significant broadening of the sample reflections above $\sim$40 GPa made it increasingly difficult to determine accurate unit cell dimensions. This is illustrated in Fig. 6, which shows diffraction

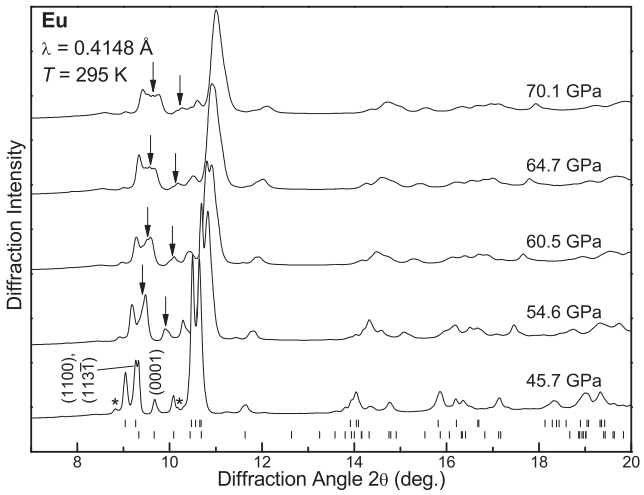

FIG. 6. (a) X-ray powder diffraction profiles of Eu at 45.7, 54.6, 60.5, 64.7, and 70.1 GPa collected from a sample loaded with a He PTM. The tick marks below the 45.7 GPa profile show the calculated peak positions of the main (upper) and first-order satellite (lower) reflections, as determined from a Rietveld refinement of the *i*-*mC*4(2) structure to this profile. The asterisks above the 45.7 GPa pattern indicate contaminant reflections from the *cI*12 contaminant phase. The arrows indicate the splitting of the (0001) reflection into a doublet, and the simultaneous change in the relative intensity of the (1100) and (113$\bar{1}$) reflections, with increasing pressure. The splitting of the (0001) reflection cannot be described by the *i*-*mC*4(2) structure.

profiles of Eu collected at 45.7, 54.6, 60.5, 64.7, and 70.1 GPa. The overall shape of the diffraction patterns are similar, and no dramatic changes are observed. However, taking into account the fact that the transition from Eu-IV to Eu-V is relatively subtle, and the overall diffraction patterns of both phases are also relatively similar, means that the possibility of similar transitions occurring at higher pressures cannot be ruled out. We note that in the patterns collected above 47.1 GPa, the (0001) satellite reflection appears to split into a doublet, with the splitting increasing at higher pressures, as highlighted in Fig. 6. This splitting cannot be accounted for by the *i*-*mC*4(2) structure when up to third-order satellites are considered. As said, the patterns from this sample contain reflections from at least one additional contaminant phase that has not been reported in previous studies, and so we cannot rule out the possibility that the apparent splitting is actually due to a contaminant reflection with a similar *d* spacing to the (0001) sample reflection. However, we simultaneously observe a change in the relative intensity of the (1100) and (113$\bar{1}$) reflections, which are also highlighted in Fig. 6. Taken together, there is thus evidence of a further structural change above 47.1 GPa, but higher resolution data are required to be more certain.

Higher pressure diffraction data on Eu were collected up to 92 GPa in the previous study by Bi *et al.* [5]. Their structural assignments are not consistent with our own data collected above 18 GPa. We note that they reported a transition from a mixed-phase region to a single-phase orthorhombic phase above 66 GPa, and so we would expect the diffraction patterns to simplify at this transition. We saw no clear evidence of any transitions in our own data, but it is possible that this transition may occur at slightly higher pressures than were reached in our studies.

Eu has been predicted to transform to a fully trivalent state at pressures of 15.5(15) or 35 GPa [20,21]. However, although initial spectroscopic studies reported Eu to undergo a continuous transition to a mixed-valence state on compression [22,23], a more recent study reported Eu to remain almost divalent up to 87 GPa [24]. Ytterbium (Yb), which is also divalent at ambient pressure, transforms to a hexagonal structure (*hP*3) at 98(5) GPa [25]. This structure is also observed in neodymium and samarium at high pressure [26], and its observation in Yb was cited as evidence of a transformation to a fully trivalent state above this pressure [25]. No evidence of any of the crystal structures that have been observed in the trivalent lanthanides at high pressures were observed in our own studies of Eu, supporting the idea that Eu has not become trivalent by ∼70 GPa.

Despite the unusual complex structures that have been observed in Eu at high pressure, it is one of the few remaining elements about which nothing is known beyond 100 GPa. But, unless it transforms to a higher-symmetry structure at higher pressures, the determination of the structural behavior at pressure exceeding ∼50 GPa will be extremely challenging due to the complexity of the diffraction patterns and the increasing broadness of the diffraction peaks. Extremely high-resolution diffraction data collected on noncontaminated samples will be required for further investigations in order to determine the structural behavior of Eu at megabar pressures.

B. High temperature studies

In order to investigate the temperature dependence of the incommensurate phases, high-temperature powder x-ray diffraction data were collected on two Eu samples on beamline I15, and additional data from one of these samples were collected on beamline ID09a. In these experiments, the pressure of the sample was increased at constant temperature with the aim of determining the position of the high-temperature phase boundaries, in particular that between the hcp and incommensurate phases. The majority of the data were collected at three different temperatures: 363, 428, and 449 K. The 363 and 428 K data were each collected during a single run, and the 449 K data were collected in one run from each of the two samples.

The results of our high-temperature studies are summarized in Fig. 7. The bcc–hcp transition, which is known to occur at 12.5 GPa at ambient temperature, was determined to occur between 11.1 and 13.6 GPa at 449 K. We can therefore tentatively suggest that the bcc–hcp phase boundary is close to vertical. The hcp–Eu-IV transition, which occurs at 31.5 GPa at ambient pressure, was determined to occur between 32.4 and 36.4 GPa at 363 K, and between 39.8 and 41.3 GPa at 428 K. This suggests that the pressure range over which the hcp phase is stable increases with increasing temperature.

At 363 K, the transition from Eu-IV to Eu-V was observed between 39.8 and 41.3 GPa at 313 K, which is again a slightly higher pressure than we observed at room temperature, where the transition was observed to start between 38 and 39 GPa. The Eu-IV–Eu-V phase boundary was also crossed at 428 K.

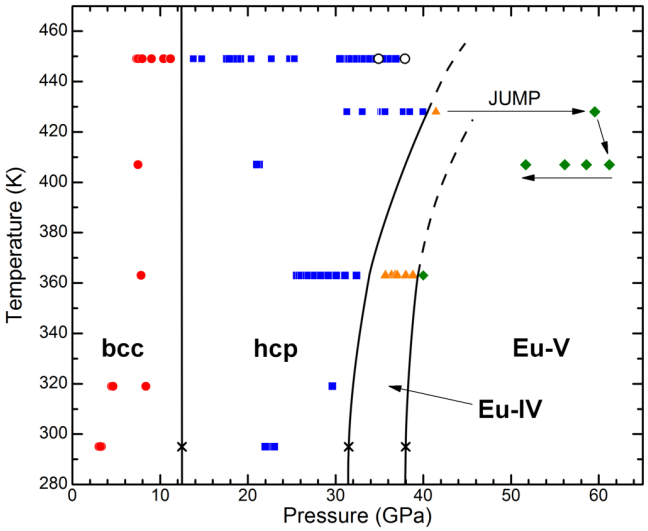

FIG. 7. (Color online) Phase diagram of Eu to 449 K. The (red) circles show the points in the bcc phase, the (blue) squares show the points in the hcp phase, the (orange) triangles show the points in the Eu-IV phase, and the (green) diamonds show the points in the Eu-V phase. The crosses show the room-temperature transition pressures, and the open circles show the points at which diamond failure occurred. The solid lines show an estimate of the phase boundaries, and the dotted lines show an extrapolation to higher temperatures. The data were collected on compression at constant temperature, with the exception of the data collected on Eu-V at 407 K, as indicated by the arrows.

However, the pressure of the sample jumped from 41.4 GPa in the Eu-IV phase to 59.5 GPa in the Eu-V phase (see Fig. 7), and so we were unable to determine the transition pressure at this temperature. However, this does confirm that both incommensurate phases are stable up to at least 428 K.

An attempt was made to cross the hcp–incommensurate phase boundary at 449 K in both of our samples. However, somewhat surprisingly, in both cases gasket failure leading to diamond failure was observed before we observed the transition to the incommensurate phase. The highest pressure hcp patterns were collected at 34.9 and 37.9 GPa, respectively, in the two samples.

There has been only one study of the high-pressure, high-temperature behavior of Eu, in which the melting curve was determined, although only to 7 GPa [27], and large areas of the phase diagram of Eu remain completely unknown. In the small pressure range in which the melting curve is known, a maximum was observed in the melting temperature of the bcc phase at about 3.5 GPa and 722 K. Similar behavior is observed in divalent Ba, which also exhibits a maximum in its melting temperature in the bcc phase [28]. At higher pressures, Ba exhibits a deep minimum in the melting curve at 7.7 GPa, close to the bcc–hcp transition. Given the similarities in their electronic structure, it is possible that this unusual melting behavior is also present in Eu. We note that in our previous high-pressure high-temperature experiments on K and Te, diamond failure was consistently observed in different sample runs on sample melting. In K, this was found to be due to a reaction between the sample and the Re gasket that occurred on sample melting [29]. Similar behavior was observed in Te on melting at ∼3 GPa and ∼750 K [30]. The fact that the diamonds failed at moderate pressures and temperatures in both of our Eu samples, and also that diamond failure was observed at very similar pressures and temperatures in each case (∼37 GPa, 449 K), suggests the possibility of a reaction between the Eu and the diamonds in this region of P-T space. This introduces the possibility of a minimum in the melting curve of Eu in this region of P-T space. Future studies using different gasket materials are required in order to investigate the behavior of Eu in this region.

IV. CONCLUSIONS

In summary, we have determined that Eu undergoes a transition from the incommensurately modulated Eu-IV to a second incommensurately modulated phase, Eu-V, above 38 GPa. Eu-IV and V have the same superspace group, but the modulation vectors differ in direction and magnitude. The transition involves discontinuous jumps in both the lattice parameters of the average structure and the wave vector components q_1 and q_3, and so we conclude that the transition is of first order. This is the first incommensurately modulated to incommensurately modulated transition to be observed in the elements at high pressure. Eu-V is stable to at least 46 GPa, and there is some evidence of another phase above that pressure. However, the sample reflections in the diffraction patterns collected above ∼50 GPa are very broad, and determining accurate structural details above this pressure will be very challenging. Despite these new results, Eu remains one of the few elements about which nothing is known above 100 GPa.

We have also performed high-pressure high-temperature studies up to 449 K in order to determine the position of the phase boundaries. The stability range of the hcp phase increases to higher pressures with increasing temperature. Further studies are required in order to determine the phase boundaries of the incommensurate Eu-IV and Eu-V phases in more detail.

ACKNOWLEDGMENTS

This work was supported by grants and a fellowship (I.L.) from the UK Engineering and Physical Sciences Research Council, and facilities were made available by the European Synchrotron Radiation Facility, Diamond Light Source, and the Research Complex at Harwell. Parts of this research were carried out at the light source PETRA III at DESY, a member of the Helmholtz Association (HGF). We thank M. Hanfland of ID09a (ESRF), and A. Kleppe and N. Casati of I15 (Diamond Light Source) for their assistance in using the beamlines, and U. Schwarz at the Max-Planck-Institut für Chemische Physik fester Stoffe in Dresden for providing the Eu samples. We would also like to thank S. MacLeod of AWE for the use of pressure cells and equipment, and we would like to acknowledge helpful discussions with Professor S. van Smaalen. M.I.M. and K.A.M. would like to thank AWE for the award of a William Penny Fellowship and a Case Studentship award, respectively, and R.J.H and E.E.M. would like to acknowledge financial support from EPSRC (UK) via the Scottish Doctoral Training Centre in Condensed Matter Physics.

[1] G. K. Samudrala and Y. K. Vohra, in *Handbook on the Physics and Chemistry of Rare Earths*, edited by J.-C. G. Bünzli and V. K. Pecharsky (North-Holland, Elsevier, Amsterdam, 2013), Vol. 43, Chap. 257, pp. 275–319.
[2] K. Takemura and K. Syassen, J. Phys. F: Met. Phys. **15**, 543 (1985).
[3] T. Krüger, B. Merkau, W. A. Grosshans, and W. B. Holzapfel, High Press. Res. **2**, 193 (1990).
[4] W. A. Grosshans and W. B. Holzapfel, Phys. Rev. B **45**, 5171 (1992).
[5] W. Bi, Y. Meng, R. S. Kumar, A. L. Cornelius, W. W. Tipton, R. G. Hennig, Y. Zhang, C. Chen, and J. S. Schilling, Phys. Rev. B **83**, 104106 (2011).
[6] R. J. Husband, I. Loa, G. W. Stinton, S. R. Evans, G. J. Ackland, and M. I. McMahon, J. Phys. Conf. Ser. **377**, 012030 (2012).
[7] R. J. Husband, I. Loa, G. W. Stinton, S. R. Evans, G. J. Ackland, and M. I. McMahon, Phys. Rev. Lett. **109**, 095503 (2012).
[8] R. J. Husband, I. Loa, G. W. Stinton, G. J. Ackland, and M. I. McMahon, High Press. Res. **33**, 158 (2013).
[9] H. K. Mao, J. Xu, and P. M. Bell, J. Geophys. Res. **91**, 4673 (1986).
[10] M. Hanfland (private communication).
[11] M. Hanfland, K. Syassen, and J. Köhler, J. Appl. Phys. **91**, 4143 (2002).
[12] P. I. Dorogokupets and A. R. Oganov, Phys. Rev. B **75**, 024115 (2007).
[13] A. P. Hammersley, ESRF Internal Report, ESRF97HA02T, "FIT2D: An Introduction and Overview" (1997).
[14] A. P. Hammersley, S. O. Svensson, M. Hanfland, A. N. Fitch, and D. Häusermann, High Press. Res. **14**, 235 (1996).
[15] A. Boultif and D. Louër, J. Appl. Crystallogr. **37**, 724 (2004).
[16] J. Rodrìguez-Carvajal, Physica (Amsterdam) B **192**, 55 (1993).
[17] V. Petříček, M. Dušek, and L. Palatinus, Z. Kristallogr. **229**, 345 (2014).
[18] S. van Smaalen, *Incommensurate Crystallography* (Oxford University Press, New York, 2007).
[19] C. Hejny and M. I. McMahon, Phys. Rev. Lett. **91**, 215502 (2003).
[20] B. Johansson and A. Rosengren, Phys. Rev. B **11**, 2836 (1975).
[21] A. Rosengren and B. Johansson, Phys. Rev. B **13**, 1468 (1976).
[22] J. Röhler, Physica B **144**, 27 (1986).
[23] R. D. Taylor and J. N. Farrell, J. Appl. Phys. **61**, 3669 (1987).
[24] W. Bi, N. M. Souza-Neto, D. Haskel, G. Fabbris, E. E. Alp, J. Zhao, R. G. Hennig, M. M. Abd-Elmeguid, Y. Meng, R. W. McCallum, K. Dennis, and J. S. Schilling, Phys. Rev. B **85**, 205134 (2012).
[25] G. N. Chesnut and Y. K. Vohra, Phys. Rev. Lett. **82**, 1712 (1999).
[26] Y. C. Zhao, F. Porsch, and W. B. Holzapfel, Phys. Rev. B **50**, 6603 (1994).
[27] Jayaraman, Phys. Rev. **135**, A1056 (1964).
[28] M. Winzenick and W. B. Holzapfel, Phys. Rev. B **55**, 101 (1997).
[29] O. Narygina, E. E. McBride, G. W. Stinton, and M. I. McMahon, Phys. Rev. B **84**, 054111 (2011).
[30] C. Hejny, S. Falconi, L. F. Lundegaard, and M. I. McMahon, Phys. Rev. B **74**, 174119 (2006).